A COMPARISON OF CONTINUUM AND DISCRETE MODELING TECHNIQUES OF THE EFFECTS OF MANUFACTURING DEFECTS COMMON TO COMPOSITE STRUCTURES

by

Jared William Nelson

A dissertation submitted in partial fulfillment
of the requirements for the degree

of

Doctor of Philosophy

in

Engineering

MONTANA STATE UNIVERSITY
Bozeman, Montana

November 2013

APPROVAL

of a dissertation submitted by

Jared William Nelson

This dissertation has been read by each member of the dissertation committee and has been found to be satisfactory regarding content, English usage, format, citation, bibliographic style, and consistency and is ready for submission to The Graduate School.

Dr. Douglas S. Cairns

Approved for the Department of Mechanical and Industrial Engineering

Dr. Christopher H.M. Jenkins

Approved for The Graduate School

Dr. Ronald W. Larsen

STATEMENT OF PERMISSION TO USE

In presenting this dissertation in partial fulfillment of the requirements for a doctoral degree at Montana State University, I agree that the Library shall make it available to borrowers under rules of the Library. I further agree that copying of this dissertation is allowable only for scholarly purposes, consistent with "fair use" as prescribed in the U.S. Copyright Law. Requests for extensive copying or reproduction of this dissertation should be referred to ProQuest Information and Learning, 300 North Zeeb Road, Ann Arbor, Michigan 48106, to whom I have granted "the right to reproduce and distribute my dissertation in and from microform along with the nonexclusive right to reproduce and distribute my abstract in any format in whole or in part."

Jared William Nelson

November 2013

ACKNOWLEDGEMENTS

There are a great many people that have helped me achieve the work herein. First, I would like to thank my committee, Dr. Douglas Cairns, Dr. John Mandell, Dr. Ladean McKittrick, Dr. David Miller, and Mr. Robb Larson, for their mentorship and support. In addition, I am deeply appreciative to Dr. Keongsik Woo for the significant direction and guidance he offered. There was great amount of help that I received from Dan Samborsky and the MSUCG; specifically thanks to Pancasatya Agastra, Patrick Flaherty, Daniel Guest, Mike Lerman, Julie Muretta, Matt Peterson, Tammy Ritchey, and all of the undergraduate students who contributed. I am also extremely grateful to Dr. Ed Adams for helping me start on this path and his support along the way. Next, I wish to acknowledge the help from Sandia contract monitors Dr. Daniel Laird (through March, 2011) and Mr. Joshua Paquette (current) while acknowledging the technical help from Mr. Mark Rumsey of Sandia. In addition, I wish to thank Mr. Scott Hughes, Mr. Michael Desmond, Mr. Derek Berry, Mr. Steve Nolet, and the entire BRC for their help and encouragement. Finally, I am extremely grateful to my entire family and especially my mother for her wonderful, diligent editing and my wife for not letting me walk away.

To Dr. Cairns and Dr. Trey Riddle, a special thanks for a special time I will never forget. I am grateful to have been a part of this with you both and appreciate your friendship.

TABLE OF CONTENTS

TABLE OF CONTENTS - CONTINUED

TABLE OF CONTENTS - CONTINUED

LIST OF FIGURES

Figure Page

LIST OF FIGURES - CONTINUED

Figure Page

LIST OF FIGURES - CONTINUED

Figure Page

LIST OF FIGURES - CONTINUED

Figure Page

LIST OF FIGURES - CONTINUED

Figure Page

LIST OF FIGURES - CONTINUED

Figure Page

LIST OF FIGURES - CONTINUED

Figure Page

LIST OF FIGURES - CONTINUED

Figure Page

LIST OF FIGURES - CONTINUED

Figure Page

LIST OF FIGURES - CONTINUED

Figure Page

LIST OF TABLES

Table Page

LIST OF TABLES - CONTINUED

ABSTRACT

Application of different damage modeling approaches for use with composite materials and composite material structures has grown with increasing computational ability. However, assumptions are often made for "worst case" scenarios with these modeling techniques resulting in approximating defects as a hole or notch in a plate instead of modeling actual flaw geometry. These analytical tools have helped bound composite material and structure capabilities, but do not allow for comprehensive understanding of the effects of defects as the characteristic parameters of the defects vary. In order to develop a tool that will allow for accurate analysis of a complete structure, including defects of different parameters, modeling approaches must be optimized. It was the optimization of these approaches that was investigated herein with specific application toward establishing a protocol to understand and quantify the effects of defects in composite wind turbine blades. A systematic, three-round study of increasing complexity was performed to understand the effects of three typical blade manufacturing defects while investigating continuum, discrete, and combined damage modeling. Through the three rounds of the benchmark material testing, significant coupon level testing was performed to generalize the effects of these defects. In addition, material properties and responses were analyzed and then utilized as material inputs and correlation criteria for each analytical technique. Parallel to the material testing, each of the three rounds increased in analytical complexity to ensure that models were only as complex as necessary to achieve acceptable correlation. Correlation was compared both qualitatively and quantitatively for an initial case and other cases were investigated only if initial correlation was acceptable. While each modeling type offered certain attributes, a combined approach yielded the most accurate analytical/experimental correlation. Thus, a unique comparison of several different analytical approaches to composites with respect to manufacturing for consistency, accuracy, and predictive capability allowing for improved blade reliability and composite structural assessment.

INTRODUCTION

Structures made from composite materials are being utilized more and more, as they typically offer significant benefits. Typically these benefits include weight reduction, fatigue resistance, corrosion resistance, and the ability to tailor structural properties as seen with the recent project by Boeing to incorporate fiber reinforced composites into the 787 Dreamliner (Barbero, 1999; Smock, 2007). While anisotropy allows laminated composites to be tailored to exhibit specific properties and responses, engineering analysis becomes more difficult compared to conventional single-phase materials. This is due not only to the heterogeneous composition and orthotropy of laminates, but also to the probabilistic nature of composite failure (MIL-HDBK-17-1F, 2002). Moreover, additional difficulties associated with manufacturing often compound the difficulty and complexity of composite analysis. Even highly controlled manufacturing procedures are prone to variances, such as fiber misalignment, inclusions, voids, and insufficient cure, which result in degradation from ideal material properties. Some of these variables are able to be controlled by ensuring consistent environmental conditions, this type of control is attainable for some portions of the composites community (e.g. aerospace, automotive) but is seen as cost-prohibitive for lower cost areas (e.g. sporting goods, wind). Regardless, it is difficult to comprehensively quantify material properties and response, given these variables (Hallett et al., 2009).

Compliance with design and safety requirements are generally attained by utilizing safety and model factors to account for load uncertainties and material damage resistance. These factors are often based on worst-case scenarios due to lack of accurate

predictive analytical tools for assessing damage progression and residual strength of a structure. These factors then potentially negate the advantages of using composites by incorrectly predicting response, especially in the lower cost areas of the industry (Long and Narciso, 1999; Lekou and Philippidis, 2008). As outlined by MIL-HDBK-17 (2002), standards have been set to determine material allowables, utilizing the approach seen in Figure 1.

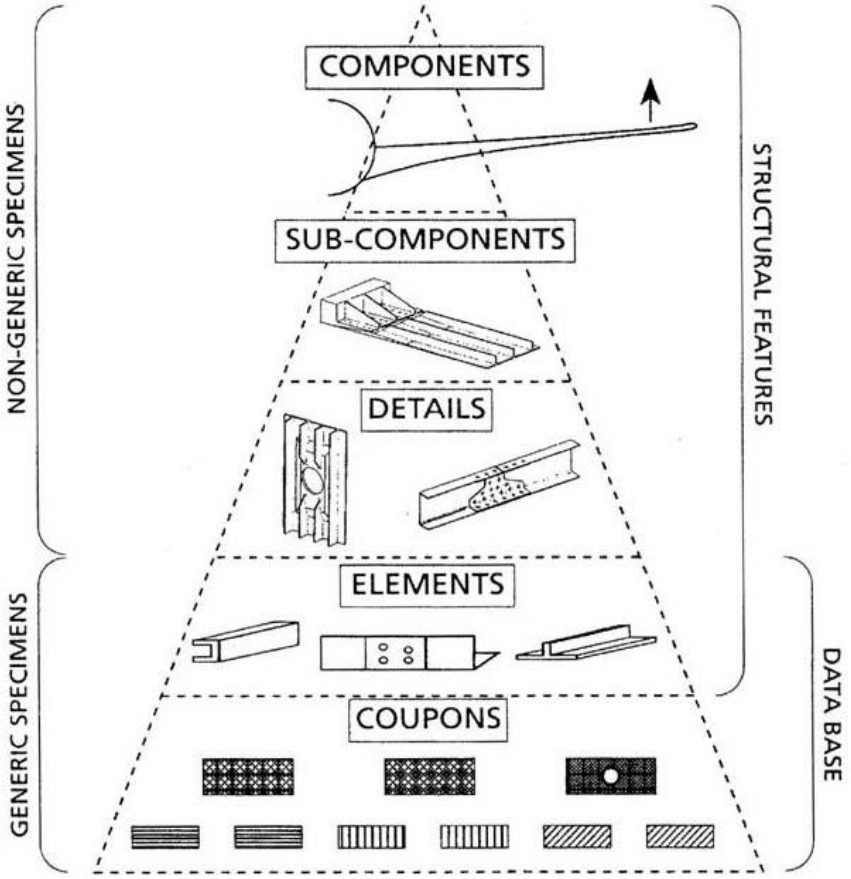

Figure 1: Approach for designing composites structures per MIL-HDBK-17 (2002).

Beginning at the bottom, coupon level testing is specified for 30 specimen from at least five independent batches of material in longitudinal compression and tension, transverse compression and tension, and in-plane shear. While less testing is required during progression from coupons to components, the testing itself becomes complex, time-consuming, and costly. Design allowables are generated from this testing which account for the variations noted above by assuming that testing a large number of specimen from a variety of batches, combined with a quality assurance plan, will account for the material response associated with such a variation. Based on the associated time and costs with generating design allowables, even in areas that can afford to meet these qualification criteria, it is very difficult to choose composite structures , and is often unattainable for lower cost areas of the composites market where design requirements are often set experientially.

A viable path around such a qualification program is to utilize analytical tools to predict material response, thereby reducing the amount of testing necessary. In short, accurate prediction would allow for factors, especially experientially based factors, and designs to be optimized. Classic laminated plate theory is an excellent tool that offers simple analysis of composite laminates and with some initial testing allows for prediction of elastic properties and initial failure (Barbero, 1999). The calculations assume uniformity and do not account for inclusion of any flaws, defects, or damage in specific areas. Instead, this approach handles these areas with simple material knockdowns. More complex approaches are being utilized including many different types of analytical tools. Typically, these tools predict material response by determining damage

progression and residual strength. Damage progression, which can also be analyzed as damage resistance, is mathematically modeled and the nature and extent of the damage are predicted (Tay et al., 2008). While damage progression models have been developed, an accurate analysis method is not currently available for damage tolerance certification due to the complex nature of damage progression and large number of influential parameters (DOT/FAA/AR-97/79, 1998).

Modeling methods have progressed significantly with increased computational ease and availability. Finite element analysis is typically used, and many models are able to predict responses up to damage initiation, but beyond initiation accuracy is limited due to the complexities associated with damage progression (Pal and Ray, 2002). As such, models are often not truly predictive from case-to-case, and the application of prediction analysis is made complex by a multitude of failure modes (Boyer et al., 1997). Often models only consider few, and in many cases only one, failure mode(s), which is insufficient for assessing structural response and integrity. Improvements have been made whereby models are able to generate stochastic loads and/or material properties that are input to an analytical model to assess material response at certain conditions (Whiteside et al, 2012). These improvements allow for generation of allowables, given known distributions of variance parameters such as load and material properties.

While these approaches potentially allow for test reduction or removal of experientially based factors, little work has been done to compare different modeling methods across a variety of design and manufacturing variances to assess consistency, accuracy, and predictive capability. This is especially true for the development of

predictive analytical tools that are often correlated with experimental results and are often tuned to minimize correlation differences, thereby reducing predictive capability (Tay et al., 2008). Predictive capability must be assessed for other flaw types, materials, and flaw geometries to ensure that these capabilities are real. In addition, it is imperative to test the notion that in order to accurately model and predict damage in a composite structure, a model must treat fiber and matrix individually (Kassapoglou, 2013).

Many facets of the composites manufacturing community would benefit from such a study, including the composite wind turbine blade industry where manufacturing quality is a more critical issue. This issue is critical due to a combination of the continually increasing large scale of the blades (Figure 2, left), the comparatively low cost manufacturing processes, and the increased demand for blades (Riddle et al., 2010). The reader may take note of the large scale of wind turbines, and the blades in particular, as seen in the left of Figure 2 where a full size pickup truck is seen at the bottom of the tower. Scale and demand are impacted by recent programs such as the DOE's 20% Wind Energy by 2030 program (DOE/GO-102008-2567, 2008) and other incentive programs designed to develop the wind energy industry rapidly. As such, more and bigger are key drivers for the wind industy, and downtime due to blade incidents are increasing (Figure 2, right). For example, focus on blade quality has been highlighted as recently as April 2012, when one of the world's largest wind turbine manufacturers experienced catastrophic failures as a result of manufacturing defects (Gebert, 2012). Failures like that call into question whether the standards designed to ensure reliability over a desired 20-year design life are accurate.

Figure 2: Typical wind turbine (left), with a blade failure (right).

The DOE-sponsored Blade Reliability Collaborative (BRC) has been formed to perform research to improve blade reliability. Led by Sandia National Laboratories, the BRC is a collaborative of wind farm owners/operators, turbine manufacturers, and third party investigators. The BRC charged the MSUCG with the goal of understanding and quantifying the effects of manufacturing discontinuities and defects with respect to wind turbine blade structural performance and reliability. As noted, two coordinated distinct tasks were established to meet this goal: Flaw Characterization and Effects of Defects. The work herein describes the latter, Effects of Defects, as a task which has focused on performing mechanical testing of flawed composite specimens and on developing

predictive progressive damage models for correlation with experimental test results. More generally, this work allows for the unique comparison of different analytical approaches to model progressive damage in composite laminates with typical manufacturing defects for consistency, accuracy, and predictive capability that will allow for improved blade reliability and composite structural assessment.

The work in this document is organized as follows. A review of the BRC goals and work scope along with relevant previous research of both flaws and progressive damage models is offered in Chapter 2. In addition, the objectives and research plan are summarized. Next, in Chapter 3, the significant combined effort to assess the response of inclusion of typical manufacturing flaws by performing benchmark testing is presented. Each of chapters 4 through 9 comprehensively outlines a specific model and assesses how well the model was able to correlate with the results from Chapter 3. A comparison of all these correlations is offered and discussed in Chapter 10, with conclusions and recommended future work outlined in Chapter 11.

BACKGROUND

While the unique comparison performed herein could be performed based on any number of composite structures with representative defects, this work was based on composite wind turbine blades with manufacturing defects typical to their processing. As such, an outline of the Blade Reliability Collaborative (BRC) and of the Effects of Defects task herein as associated with the BRC, is offered to allow the reader a better understanding of the impetus behind this task. Next, both an explanation of manufacturing-related defect types commonly found in composite blades as defined by the BRC and previous research related to mechanical response of these flaws are presented. An outline of both continuum and discrete techniques, along with related previous works, is given to provide an understanding of each analytical approach. Finally, a summary of work is offered outlining the rest of the document.

BRC Outline

It has been well established that wind turbine blades with reliability issues, such as those related to manufacturing, can be costly due to extensive downtime and expensive repairs (Paquette, 2012). To face this problem, the Blade Reliability Collaborative (BRC) was established to publicly better understand: the primary causes of premature blade failure; the ability of inspection methods to detect flaws and damage; the effects of prominent manufacturing defects on blade materials; and the adequacy of design tools and certification testing to replicate operational life. As Paquette summarized, "[The BRC's objective is to] improve the reliability of blades delivered to the field so that

remediation work before operation can be reduced and the service lifetimes can achieve the 20-year targets that are expected by wind plant operators and financiers."

The BRC has divided its work into six tasks with an experienced leader and expert taking each task:

1. Blade Defect and Damage Database: Aggregate data from blade manufacturers, service companies, and operators to determine largest sources of unreliability.
2. Inspection Validation: Evaluate the ability of inspection techniques to accurately characterize blade defects and damage in manufacturing plants and in the field.
3. Effects of Defects: Determine how common manufacturing defects affect blade strength and service life.
4. Analysis Validation: Assess the ability of design analysis tools to find and characterize potential failure modes.
5. Certification Testing: Evaluate the ability of certification testing to uncover potential reliability issues and find innovative ways for testing to provide better insight.
6. Standards and Partnerships: Interface with international standards committees and industrial partners to identify pathways to implementing improved design, manufacture, and inspection.

The BRC, led by Sandia National Laboratories, has been made up of a collaborative of wind farm owners/operators, turbine manufacturers, and third party investigators. To assist in these tasks, the MSUCG has been charged with the Effects of Defects task in order to understand and quantify the effects of manufacturing discontinuities and defects with respect to wind turbine blade structural performance and reliability. Two coordinated distinct subtasks were established to meet this goal and were originally named Flaw Characterization and Effects of Defects, though both progressed beyond this nomenclature. The Flaw Characterization subtask may be found as comprehensively addressed by Riddle (2013). As defined by Riddle, the Flaw Characterization subtask has two major objectives: (1) Acquisition of relevant defect statistics and defect laden lamina response, and (2) Development of a probabilistic model to assess the global structural response, probability of failure, and estimation of time to failure for flawed wind blades. Both of these objectives are addressed within the context of a framework called the Probabilistic Reliability Protocol. The work herein describes the Effects of Defects subtask, which has focused on performing mechanical testing of flawed composite specimen and developing predictive progressive damage models for correlation with experimental test results. The BRC has also added an investigation, similar to the research herein, to understand and model defects typically found in adhesive joints. The results of this investigation will be published by Peterson in the future who is investigating promising new techniques for common interactions between and within the isotropic adhesive and anisotropic laminates.

In this study, the following goals were proposed:

1. Understand critical flaw types.
    a. Determine critical flaw types from flaw database and probabilistic modeling.
    b. Use previous research specific to blades or from other applications.
2. Characterize the mechanical properties of common flaws deemed critical to composite blades.
3. Determine the criteria at criticality threshold of each flaw type.
    a. Determine flaw type, size, and location.
4. Use a three-round study to develop coordinated 2D analytical and experimental analogs for damage progression and residual strengths necessary for blade reliability.
    a. Develop finite element model initially at individual flaw scale.
    b. Improve model toward full blade scale with combinations of flaws.
5. Understand and model how these flaws contribute to the entire structure.
6. Complement on-going activities of the entire BRC.

While the majority of the work outlined was performed on coupon level structures, the implication that each method must ultimately allow for analysis of a full structure was considered throughout. As such, the BRC's task #5 was intended to be a culmination which was to be a BRC-wide coordinated effort performing validation tests on two 9 m blades with as-manufactured flaws. Further, the work-flow diagram shown in

Figure 3 maps out the progression necessary to achieve each of these individual goals, as a systematic path building toward improved models to be used for larger scale validation by attempting correlation. This work-flow diagram shows three distinct rounds of testing and modeling approached which systematically increase in complexity. The first round was intended to develop simple continuum models based on initial testing, once preliminary defect types and parameters had been established. Round 2 then improved upon and developed new models to more accurately predict response while increasing the complexity of the modeling technique. Correlations were performed consistently and a systematic increase in complexity was followed here as well in order to test each modeling technique as fully as possible. The third round saw development of the most complex model and attempted validation with a full scale 9 m validation wind turbine blade before the overall comparisons and publishing herein occurred.

Common Composite Structure Manufacturing Flaws

Three composite material flaw types were investigated after being deemed critical to blade function and life cycle: porosity, out-of-plane (OP) fiber waviness, and in-plane (IP) fiber waviness. These flaw types were determined by the BRC, which may be considered a Delphi Expert Panel due the amount of expertise within the group. Since these flaw types are not exclusive to wind blades but are commonly found in composite structures, extensive studies have been reported on each of the defects in relatively thin laminates utilizing varying advanced composite materials. Much less research related to these and other structural details has been performed for wind turbine blade materials.

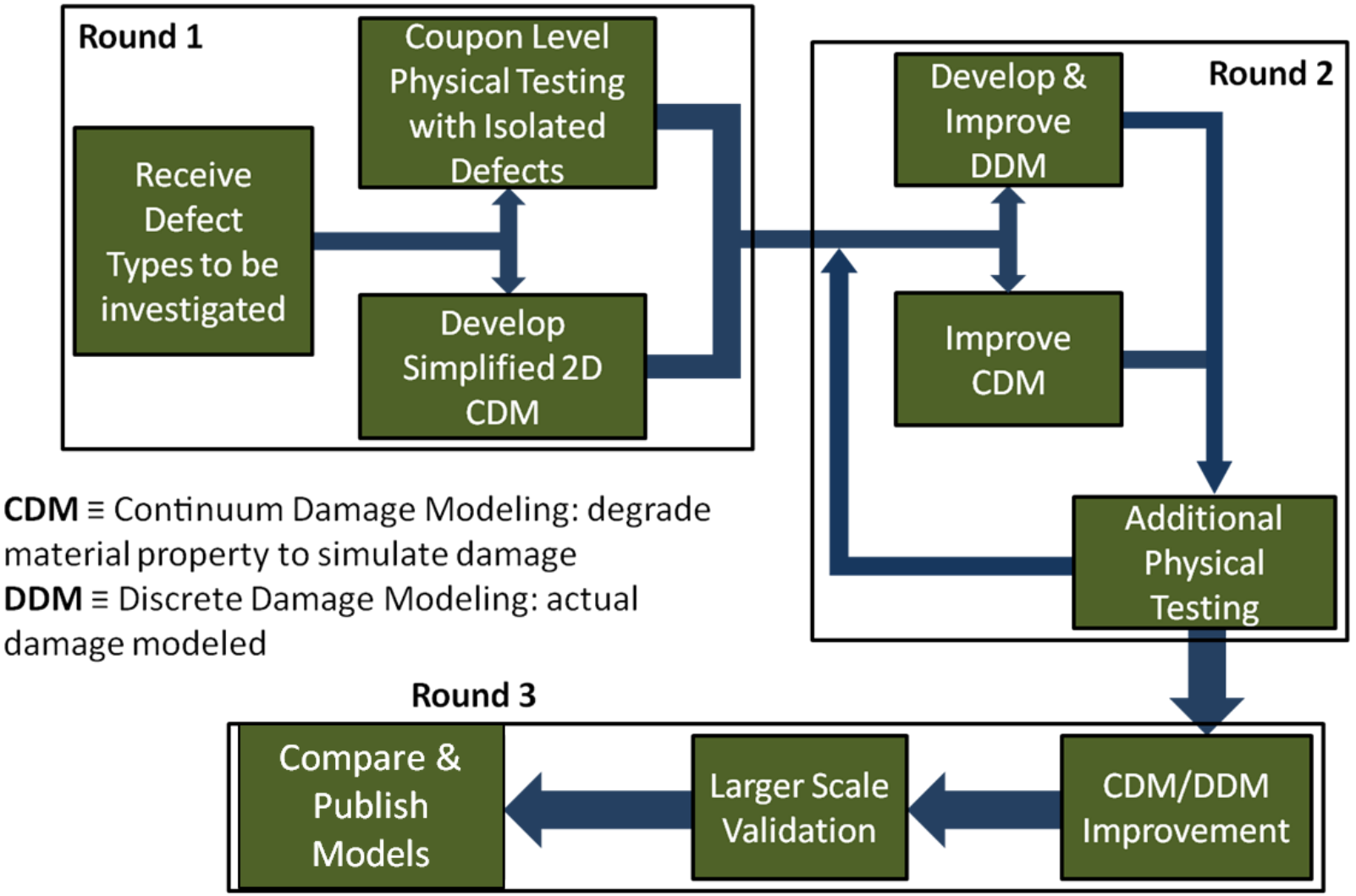

Figure 3: Effects of Defects laminate work flow diagram.

Further, it must be noted that much of this research has been performed for industries where manufacturing is on a smaller scale and expense is less critical compared to some industries, such as aerospace. Most of this prior research offers a preliminary basis for this work, but it is known that acceptable defects often included in wind turbine blades far exceed what would be acceptable in other industries. Thus, research specific to understanding the criticality of defects common to wind turbine blades was deemed necessary.

Significant research of composite manufacturing and design flaws has been performed by the MSUCG and others. In particular, Montana State University Composites Group's SNL/MSU/DOE Composite Material Database (MSU-CMD) has tested over 12,000 coupons for over 130 material systems (Mandell and Samborsky, 2013). This database has been extremely useful as most of the material systems tested are those utilized and found in composite blades. Each of the flaw types and a brief accounting of applicable research is offered. In particular, the MSUCG has a significant history analyzing misaligned fibers related to this work, but is not directly applicable. As such, each flaw type was characterized in detail as discussed below in Chapter 3.

Porosity

Porosity and voids are commonly used to describe the same phenomenon of air trapped within the laminate. For the purposes herein, porosity is used to describe uniform air inclusion, whereas voids describe large air-pockets that are large geometric discontinuities (Figure 4). Given this definition, voids are extreme porosity cases and, given the need to determine critical flaw geometries, their parameters were not

considered further herein. Unless otherwise noted, porosity is characterized as percent-by-volume, meaning the percentage of total volume of the composite laminate being evaluated.

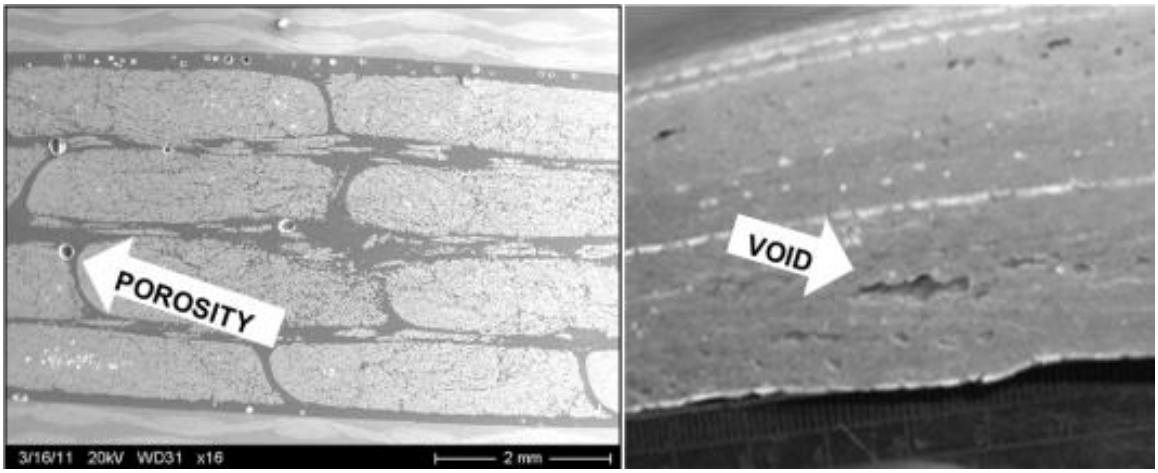

Figure 4: Comparison of porosity and voids.

Significant research has been performed to understand the effects of porosity on mechanical properties, and the research was in agreement that these properties degrade as the percent-of-volume of porosity increases. Judd (1978) provided an appraisal of research performed and methods utilized to detect porosity in composite laminates. Findings indicate that mechanical properties degrade significantly—up to 7% decrease in strength—with as little as 1% porosity. In most cases, studies only investigated up to a maximum between 5% and 12% porosity by volume, while 2% has been noted as a quality control standard by the wind industry (Riddle, 2013). However, effects of porosity on mechanical properties have been found to be influenced by void shape, location, proximity, and size, causing a difference in results within test groups of similar

porosity content (Wisnom et al., 1996; Baley et al., 2004; Costa et al., 2005; Pradeep et al., 2007; Zhu et al., 2009; Guo et al., 2009).

Wu et al. (1998) assumed homogenization of porosity within the laminate and offered graphical representations of the impacts of increasing porosity (0-8%) on mechanical properties as shown in Figure 5. It must be noted that the increasing presence of porosity only minimally affects the axial modulus (E_A). Whereas, the transverse modulus (E_T) and both axial (G_A) and transverse (G_T) shear are detrimentally affected as porosity increases. This result indicates that as the porosity increased, the matrix was more susceptible to degradation at lower loads which led to decreased material properties.

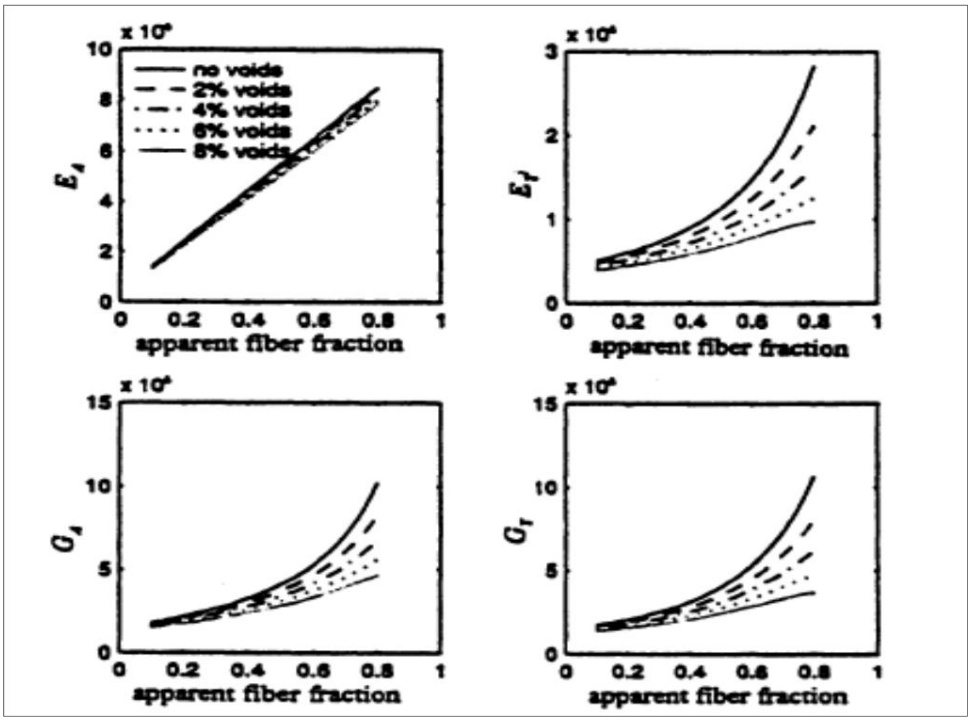

Figure 5: Effect of porosity in fiber reinforced composites (Wu et al., 1998).

Given the difficulty in understanding damage mechanisms and the inconsistent test results of the effects of porosity, modeling has been noted to be difficult. In addition, discretely modeling each case is not only extremely intensive and computationally expensive but also requires *a priori* knowledge of the flaw sizes, locations, proximity effects, and shapes. As such, generalized models have been developed for inclusions, as in this case air, in composites, beginning with Bruggeman (1937) and Kerner (1956). These initial works developed relations based elasticity solutions considering the law of mixtures. Wu et al. (1998) utilized a proven generalized self-consistent method derived from property predictions of a two-phase composite (Christensen, 1990). In particular, transverse bulk modulus k, axial modulus E_A, axial Poisson ratio ν_A, and axial shear modulus G_A are approximated by:

$$k = \frac{k_m(k_i + G_{Tm})c_m + k_i(k_m + G_{Tm})c_i}{(k_i + G_{Tm})c_m + (k_m + G_{Tm})c_i} \tag{1}$$

$$E_A = c_m E_{Am} + c_i E_{Ai} + \frac{4(\nu_{Ai} - \nu_{Am})^2 c_m c_i}{c_m/k_i + c_i/k_m + 1/G_{Tm}} \tag{2}$$

$$\nu_A = c_m \nu_{Am} + c_i \nu_{Ai} + \frac{c_m c_i (\nu_{Ai} - \nu_{Am})(1/k_m - 1/k_i)}{c_m/k_i + c_i/k_m + 1/G_{Tm}} \tag{3}$$

$$G_A = \frac{G_{Am}(1 - c_i) + G_{Ai}(1 + c_i)}{G_{Am}(1 + c_i) + G_{Ai}(1 - c_i)} G_{Am} \tag{4}$$

where the material volume ratio is c and the subscripts i and m refer to inclusion and matrix phases, respectively. This model was verified and compared to experimental

trends with good correlation noted. As such, these approximations are useful in that they can offer material properties for damage progression analysis.

Out-of-Plane (OP) Fiber Waviness

Fiber waviness studies have most commonly investigated the effects of waviness on compressive strength of OP waves. An OP wave was defined as a fiber wave that was through the thickness of the laminate as shown in Figure 6. It was evident that the fiber misorientation, or the fiber misalignment angle, varied greatly within each wave and each wave was different. Thus, averaging the misalignment angle (θ), or the amplitude (A) and wavelength (λ), was utilized to characterize each wave. The misalignment angle θ was the angle between the wavy fibers incline and the nominal fiber direction, while amplitude A is the maximum height difference at the peak of wavy fibers to the nominal fiber, and wavelength λ is the length of the span of wavy fibers in the nominal fiber direction.

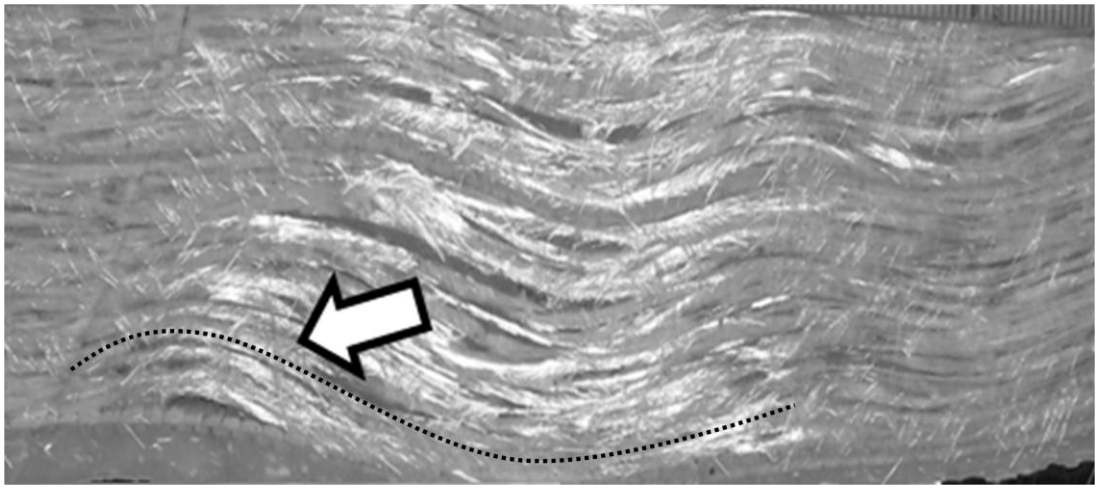

Figure 6: Example of an OP fiber waviness found in the skin section of a wind turbine blade.

In general, OP waviness has been found to decrease static compressive strength. Adams and Bell (1995) investigated OP waves isolated within a thermoplastic laminate and determined that compressive strength decreased approximately 35% when more than 33% of 0° layers contained waves. Previous research by Adams and Hyer (1996) also determined that static compressive strength decreased up to 36% with sudden, catastrophic brooming failures near the waves.

Related research has been performed within the MSUCG, not necessarily directly on OP waves but on similar geometric discontinuities. Much can be learned from these findings that allow for a basis for understanding OP waves as based on the similar fiber misalignment when comparing to an IP wave. Avery et al. (2004) noted that the geometries in Figure 7 were similar to OP fiber waviness in that, in the area of ply drops or build-ups, fibers were misaligned as nominal overall, or layer, thickness changed.

Avery et al. utilized the known sensitivity of compressive strength related to fiber straightness in order to study structural details such as ply drops and ply joints. By varying parameters such as ply thickness, fraction of ply drops, location, gap and mold geometry, and pressure, it was found that ply drops and joints can provide adequate compressive strength. However, severe knockdowns occurred where large fiber misalignments were induced. Cairns et al. (1999) determined that suppressing damage and delamination in-service emanating from ply drops was not possible, though in most cases there was a threshold loading under which little progression after initiation was noted. Based on these results, rules defining acceptable thickness and proximity were established for ply drops.

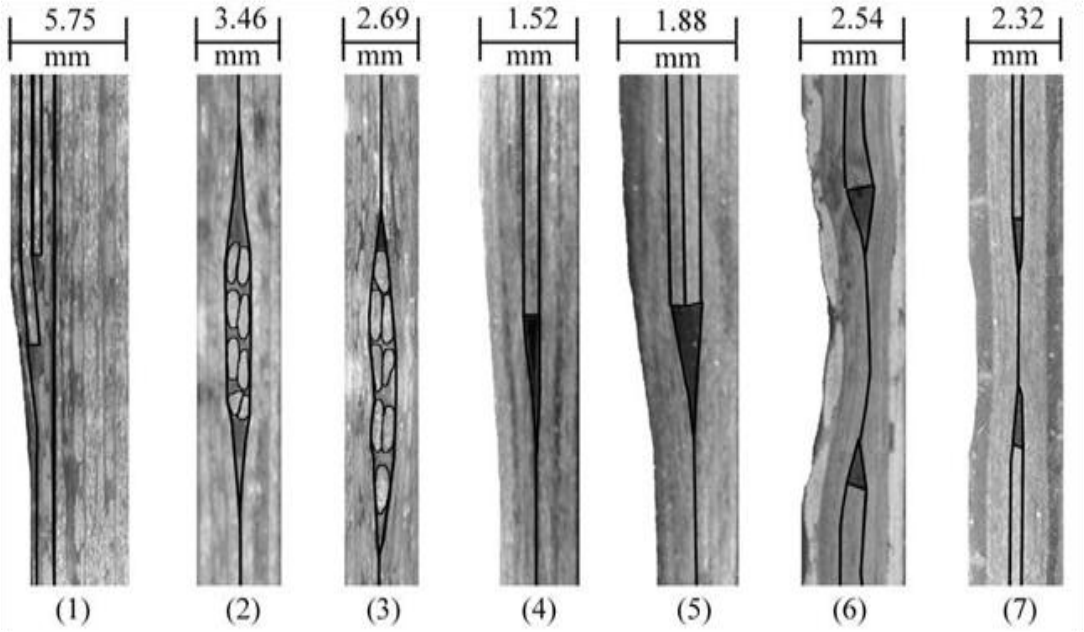

Figure 7: Examples of fiber misalignment resulting from ply drops and build-ups (Avery et al., 2004).

Wang et al. (2012) utilized ply drops to develop a manufacturing procedure for 16-layer laminates with an OP wave of varying misalignment angle (2.3-30.3°). This method was developed based on the three step process established by Adams and Bell. Two mirrored ply drops with a fiber wave in between create a laminate of consistent thickness (Figure 8). The number of plies dropped and the slope of the ply drop may be adjusted to achieve different misalignment angles. Though Lemanski et al. (2013) credit Wang et al. with experimental results in compression, the results are found only in Lemanski et al.'s work. Regardless, as expected, failure load drops significantly as fiber misalignment angle increases. This drop is worth noting because Lemanski et al.'s modeling techniques are of interest in later discussion.

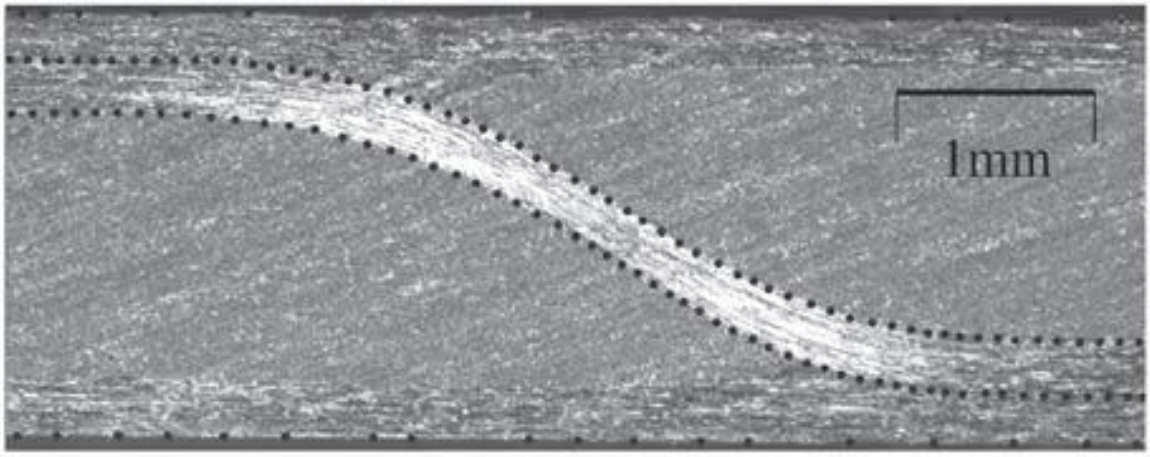

Figure 8: Wang et al. (2012) utilized a mirrored ply drops to manufacture OP waves.

In-plane (IP) Fiber Waviness

IP fiber waviness has been examined to a lesser extent due largely to the qualitative assessment that IP waves are less impactful on mechanical properties and strength. An IP wave was defined as a fiber wave in the plane of the surface that impacted the thickness very little, if at all (Figure 9). The same characterization parameters were utilized (θ, A, and λ), in the same methods as for OP waves unless otherwise noted.

As noted by Avery et al. (2004), "waviness is expected to reduce compressive strength due to two factors: (1) the fibers may be put into a geometry which exacerbates the basic fiber, strand, or layer buckling mode of failure, and (2) the waviness shifts the fiber orientation off the axis of the ply longitudinal direction, producing matrix dominated failures for plies nominally orientated in the primary load direction (0°).

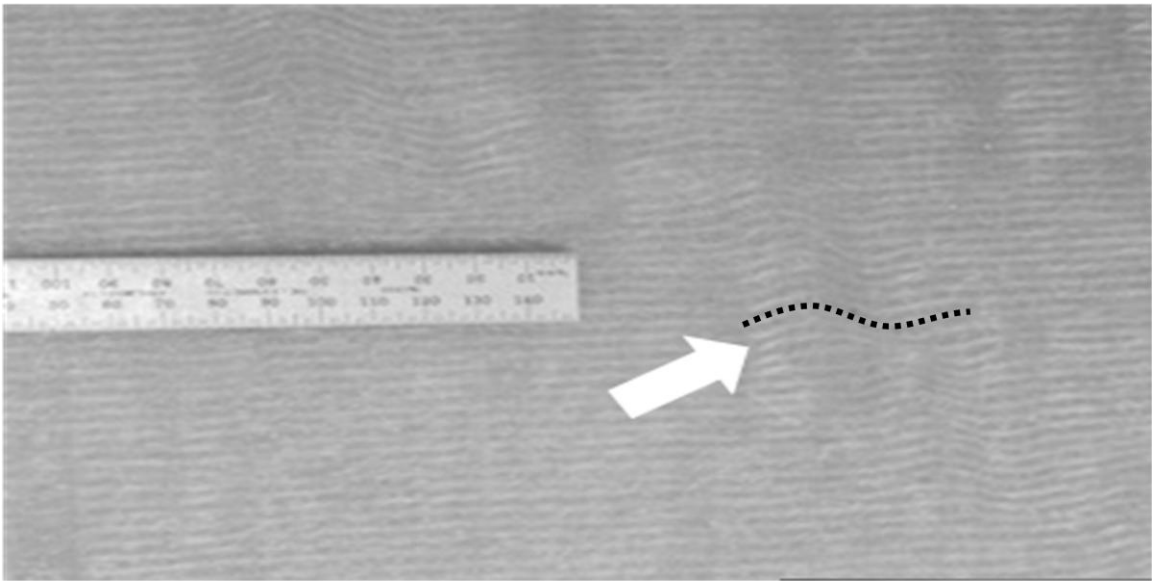

Figure 9: Example of an IP fiber waviness seen on the surface of the skin section of a wind turbine blade.

The second factor may also affect tensile strength in severe cases. Compared with typical aerospace prepreg laminates, blade prepregs are thicker, and blade fabrics tend to be both thicker and more heterogeneous, with strands of fiber either woven (usually over a small strand) or stitched together."

As noted by Wang (2004), blade manufacturing often utilizes vacuum assisted resin transfer molding (VARTM) which can induce waviness in some conditions. An example of unintended IP waviness in a large-tow carbon fiber stitched fabric induced during VARTM processing is shown in Figure 10. Based on the waviness of this type, a reduction in strength properties was compared to a laminate with straight, unflawed 0° fibers. It was interesting to note that the ultimate failure, in compression for all three cases, appeared to take place at the maximum fiber misalignment angle.

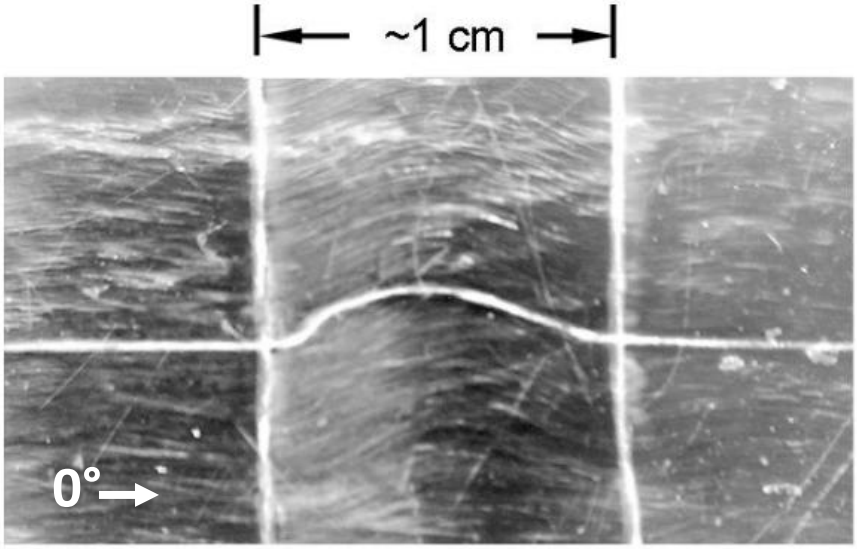

Figure 10: Examples of unintended IP waviness in coupons resulting from infusion process (Wang, 2004; Avery et al., 2004).

Wang determined that static compressive strength reductions increased as the maximum fiber misalignment angle and percentage of layers with waves in the laminate increased. Failures were noted to be at the maximum angle of fiber orientation. Further, in-plane waves were found to have a significant reduction in static tensile strength, decreasing further as wave severity increased. Tensile failures were characterized as delaminations and fiber fractures. In both compressive and tensile cases, wave severity was characterized by aspect ratio (A/λ).

Digital Image Correlation

Digital image correlation (DIC) was first introduced into mechanics as a metrology tool to determine small strains by Peters and Branson (1982). DIC is ideal for measuring an area, or volume if used stereographically, where sensitivity and non-contact are beneficial (Parker, 2009). As a subject is deformed, cameras record images. These

images are than analyzed by division into smaller sub-images from which displacements can be measured from a consistent starting point. Images and sub-images are then compared through the deformation sequence using a correlation function (Parker, 2009; Aramis, v6.2). This method deals with images as discrete, real functions where each pixel on the image has a numerical value and the images are dealt with simply as arrays of these values. Image correlation between two images is performed at user specified control points where deformations are then determined by variations in the array of these control points. Then within each image, the other sub-images are then located relative to these points allowing for individual displacements and ultimately strains to be known. It should be noted that the MSUCG has significant experience with DIC and the reader is referred to Parker (2009) for a more comprehensive explanation and detailed information.

Progressive Damage Modeling Approaches

When considering composite structures, damage is better explained as a creation and progression of a crack(s) beginning on a micro-scale and continuing through the medium (Lamaitre and Desmorat, 2009). As the damage progresses, it may be viewed as discontinuities, and in many cases the laminate still has some load-carrying capacity up to ultimate failure. Damage progression becomes even more exaggerated for laminates with as-manufactured flaws when compared to unflawed laminates. Modeling this damage progression is an especially difficult problem that has been tackled in many different ways, most traditionally with the use of micromechanics (Kassapoglou, 2013). While this method has been widely used, it is difficult to utilize with a complex geometry such

as the geometry of an unintended defect or larger scale structure. As such, continuum and discrete damage modeling techniques are often utilized to model damage with a pseudo-representation or with a direct representation, respectively. These two techniques are the basis for the comparisons performed herein and are performed on the flaws determined to meet the BRC Effects of Defects task.

There are two crucial considerations when modeling damage: the failure theory and ways to account for the damage. There are many different failure theories and a criterion may be used regardless of the modeling technique. Typical failure criteria such as the maximum stress, the maximum strain, Hashin, Tsai–Hill, and Tsai–Wu are widely used because they are simple and easy to utilize (Barbero, 2001; Christensen, 2008). The maximum stress and maximum strain criteria are typical examples of so-called non-interactive theories which have been shown to produce poor predictions in general, though maximum strain can offer easy insight into final failure. Criteria, such as the Hashin criteria, that allow interaction among stress components generally perform better (1980). In recent reviews by Daniel (2007) and Icardi (2007), wide variations in prediction by various theories were attributed to different methods of modeling the progressive failure process, the non-linear behavior of matrix-dominated laminates, the inclusion or exclusion of curing residual stresses in the analysis, and the utilized definition of ultimate failure. Unfortunately there is no clear definition of ultimate failure, and it is often defined as the maximum attained load, the occurrence of first fiber failure, or the occurrence of last ply failure. Since each of these definitions is theoretically based and difficult to determine experimentally, they all can be difficult to

implement. As such, experimentally derived failure theories which have separate predictions of fiber-dominated and matrix-dominated failures have become popular. The Hashin theory falls into this category of popular failure theories and so it is in widespread use in progressive failure modeling. Many other failure theories exist, each with its own attributes and capabilities (Christensen, 2008; Hansen, Kenik and Nelson, 2012). While it was not the case that all failure theories were able to be included in the comparisons performed herein, each criterion utilized was identified and explained in detail within its respective section. Accounting for the damage is the second key factor in indicating the difference between a continuum technique and a discrete technique, as described in more detail below.

The importance of both of these two key factors, failure method and damage accounting, may be identified in Figure 11 which outlines a typical logic tree for progressive damage. Once the model has been created with applicable model inputs, a stress analysis is performed followed by a failure analysis where the specified failure criteria are implemented. A check for failure then occurs, and if failure is noted, then damage has occurred and must be accounted for in some way before ultimate failure is checked and the model stops or iterates. While each of these two key factors may be adjusted independently, each of the various models utilized herein investigates one specified combination.

Significant prior work has been performed in this area with many investigations looking at various damage progression schemes. Many different failure criteria and damage accounting approaches have been utilized with various continuum methods, with

fewer utilizing discrete methods based on their direct approach. Based on the considerations noted above, a brief background on each is offered below with special consideration paid to the failure theory and method of accounting for damage.

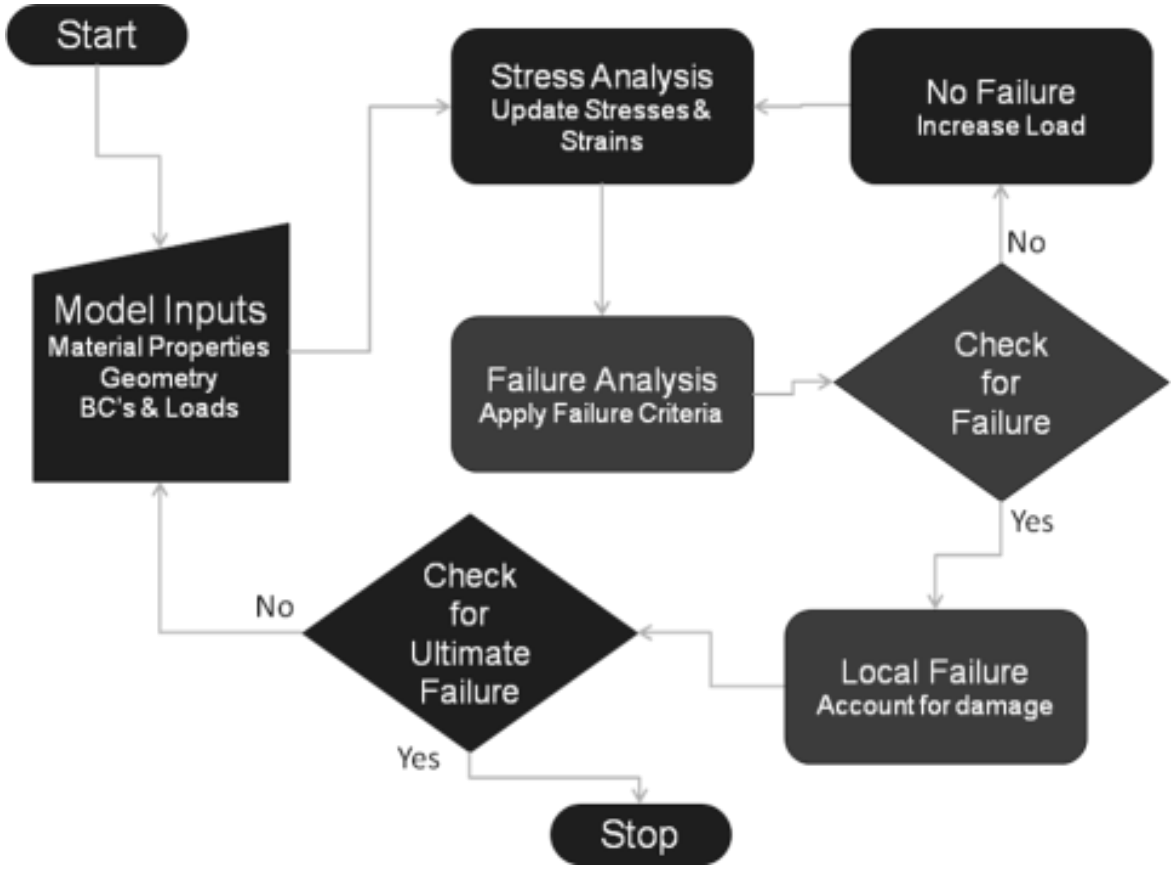

Figure 11: Typical decision tree for progressive damage logic.

Continuum Damage Modeling (CDM)

Continuum damage modeling (CDM) derives from the assumption that a material is continuous and fills an entire region of space. From this region, the material is broken into representative volume element (RVE) unit cells as shown in Figure 12 such that constitutive equations relate the RVE to the entire structure. This breaking down allows

for the relating of equations to heterogeneous micro-processes that occur during strain of materials locally, and during strain of structures globally, insofar as they are to be described by global continuum variables given their non-homogeneity (Chaboche, 1988). Simply put, actual description of damage is difficult, especially when the damage is on a grain, cell, or micro scale; however, a change in global material response is rather easily noted from the onset of damage. As such, it is often useful to homogenize, or smear, the material properties of the RVE, a process which is not always feasible when studying composites. In some instances, the two different materials cannot be represented accurately in such a way, especially when damage accumulation occurs independently in one of the constituents. Thus, care must be given to the failure modes and types when accounting for the changes in constitutive properties through the damage phases.

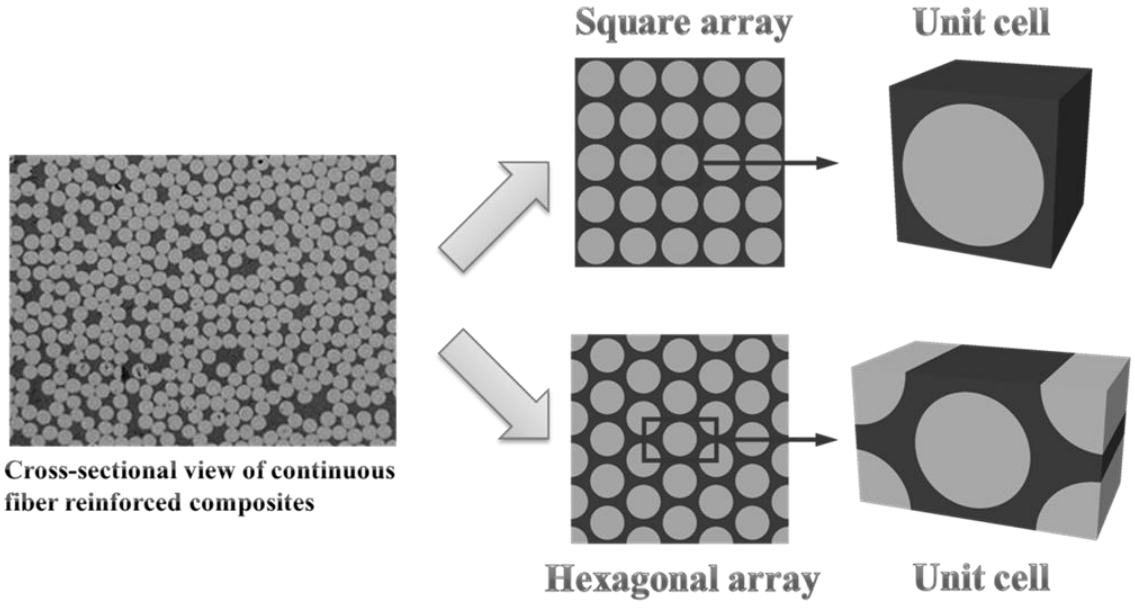

Figure 12: Schematic illustration of idealized fiber arrays and their corresponding unit cells (Sungkha777, 2013).

This constitutive type of analysis is rooted in an approach developed by Kachanov (1958, 1986) for isotropic solids. Kachanov developed mathematical damage descriptions for changing material structures based on their increasing entropy during damage. As damage occurs, the elastic properties are irreversibly affected in ways that are similar to those in a general framework of an irreversible thermodynamic process. As shown in Figure 13, this takes place by reducing the elastic properties (E_1, E_2, v_{12}, v_{32}, and G_{12}) in the stiffness matrix (C) of the stress-strain relationship. While such damage is not directly measurable from this approach, the damage is estimated for the continuum as an increasing mathematical entity by altering observable properties: strength, stiffness, toughness, stability, and residual life. As noted above, damage may be viewed as the creation of discontinuities, and Kachanov suggested a single scalar variable as a measure of the effective surface density of these discontinuities. His approach assumes that load redistribution to undamaged areas or ligaments occurs, and effective stresses increase, until all ligaments are severed at failure. This tensorial representation can take any

$$\begin{Bmatrix} \sigma_{xx} \\ \sigma_{yy} \\ \sigma_{zz} \\ \sigma_{yz} \\ \sigma_{zx} \\ \sigma_{xy} \end{Bmatrix} = \begin{bmatrix} C_{11} & C_{12} & C_{13} & 0 & 0 & 0 \\ & C_{11} & C_{13} & 0 & 0 & 0 \\ & & C_{33} & 0 & 0 & 0 \\ & & & C_{44} & 0 & 0 \\ & \text{sym} & & & C_{44} & 0 \\ & & & & & (C_{11} - C_{12}) \end{bmatrix} \begin{Bmatrix} \varepsilon_{xx} \\ \varepsilon_{yy} \\ \varepsilon_{zz} \\ \varepsilon_{yz} \\ \varepsilon_{zx} \\ \varepsilon_{xy} \end{Bmatrix}$$

Figure 13: Stress-strain relation for a transversely isotropic laminate where the stiffness matrix, C, is made up of five elastic constants: E_1, E_2, v_{12}, v_{32}, and G_{12} (Barbero, 1998).

direction in the continuum, but it must be expanded to at least a second order tensor for utility of an orthotropic material, or to a fourth order tensor in order to remove all material symmetries, thus generalizing this procedure (Chaboche, 1995; Carol et al., 2001; Luccioni and Oller, 2003; Ortiz, 1985; Simo and Ju, 1987; Cauvin and Testa, 1999).

Application of CDM in orthotropic or transversely isotropic materials, such as fiber-reinforced plastics, results in additional difficulties due to the morphology of the material which induces some preferred directions for crack progression (Maimi et al., 2007). That is, crack orientations are not only induced by the loads, geometry, and/or boundary conditions, but also by the morphology of the material. The interface between fiber and matrix is weaker than the surrounding material, meaning that many modeling techniques have to attempt to model these constituents separately. In addition, interfacial debonding is thought to normally be the first damage mechanism. Typically, when a ply fails, its elastic properties are set to zero and the failure analysis is then repeated with the modified laminate, based on updated stiffness matrices until the next initiation of failure is reached. As such, the ply discount method is based on this assumption, whereby the entire set of stiffness properties of a ply is removed from consideration if the ply is deemed to have failed (Pal and Ray; 2002; Prusty, 2005). This approach works in laminated plate theories because even after leaving out the stiffness of entire failed plies, the assembled laminate stiffness matrix is still diagonally dominant. Different ply-discount strategies that assume only chosen material properties of the failed plies are reduced depending on whether the failure mechanisms responsible for the ply failure

have been implemented (Chu and Sun; 1993; Kim et al, 1996; Chang et al.., 1996). A comparison of the analytical/experimental results indicated that the predicted failure occurred at a substantially lower load than the experimentally determined failure load. In short, it was generally observed that the ply-discount method underestimates laminate strength and stiffness due to an overestimation that the entire ply was damaged and removed instead of an estimation that damage was being localized with additional load-carrying capacity.

Another method to address these issues common to modeling composite materials was the use of multiscale modeling. Using homogenization laws, multiscale models define relations between a mesoscale, normally the scale of the finite elements or RVE, where material is considered homogeneous, and the microscale, which is the scale of the fiber and matrix constituents. This technique allows for the progression outlined in Figure 1 to be followed with models accounting for local damage while assessing the global impact on the larger scale structure. The constitutive models are defined at the microscale, and the strain and stress fields at both the microscale and the mesoscale are solved using finite elements (Car et al., 2002; Oller et al., 2005). Matzenmiller et al. (1995) attempted to address these issues by developing a simple model for the nonlinear analysis of composite material within the framework of continuum damage mechanics that reduced the complicated process of damage progression down to a few essential features. This method included the specification of elastic and inelastic range of deformation, failure planes, and damage modes. To deal with the phenomenological treatment of the state of defects and the implications on the degradation of the stiffness

properties damage variables were introduced. Consistent wtih the work herein, all material properties and damage progression functions were taken or estimated from quasi-static, monotonic, uniaxial testing. The model allowed for consideration of refined loading criteria or evolution laws, especially with respect to interaction terms. However, the model involved issues with stability due to strain softening, a fairly common issue that may not be overlooked, especially with consideration of the geometric discontinuities associated with manufacturing flaws.

In the literature overall, progressive damage models of composite structures range from the fairly simple material property degradation methods (MPDM) as shown above in Figure 13 to more complex MPDM that combine CDM and fracture mechanics (Tay et al., 2005). The idea of MPDM is that the material goes through several stages up to final failure. First, the material is fully intact and all material properties are normal. Once damage initiation occurs, which is often defined as failure of an element, a reduction in material properties, usually stiffness, is enacted. This reduction continues through the damage evolution phase up to final failure where no additional load-carrying is achieved; all the ligaments have been severed. This method has been widely used, and typical examples of MPDM utilize a 2D progressive damage model for laminates containing central holes subjected to in-plane tensile or compressive loading (Chang and Chang, 1991; Tan et al., 2005). Internal state variables, commonly called degradation factors, D_i , are used to simulate the stiffness degradation of failed elements. In these cases, the material properties are degraded such that D_i is a value between zero and 1 that is factored with the original stiffness values. The result is that the material properties are

knocked-down as elements fail, in some cases all the way to zero, which knock-down then may be argued to be an overestimation. Tan et al. (2005) found the predicted damage progression patterns agreed with experimental results obtained from X-radiographic examination of the specimens, but the predicted ultimate strength values were very sensitive to the selected values of the internal state variables.

Similarly, Camanho and Matthews (1999) developed a 3D finite element MPDM to predict damage progression and strength of mechanically fastened joints in carbon fiber-reinforced plastics failing in bearing, net-tension, and shear-out modes. Four failure modes were assumed by using Hashin's failure theory, where each mode had a different degradation factor ranging from 0.07 for longitudinal tension to 0.4 for transverse compression. By assuming the first load drop-off as the failure load and enacting these knock-down factors, a good agreement between experimental results and numerical predictions was obtained.

These results imply that the agreement of MPDM's such as these mentioned above may be effective, but they are difficult to use confidently in a predictive fashion. This difficulty is due to the degradation factors utilized being a constant value, often approximately 0.1, and as such the material response is binary though it is not seen experimentally. In turn, degradation factors must essentially be tuned to reach agreement, meaning that while they agree for one set of circumstances, the MPDM may not be universal even within the same material. Several studies have been performed attempting to generalize this procedure by replacing the constant degradation factor with a gradual stiffness reduction scheme (Reddy et al., 1995). In this case, when element

failure is indicated by a failure criterion, the stiffness properties of that element are reduced gradually only to a level at which the failure criterion is no longer satisfied. This gradual stiffness reduction scheme results in the partial unloading of elements and allows repeated failures, or damage accumulation, for the same element. In order to simulate this gradual degradation, an assumption is made that the degraded elastic properties of equivalent damaged elements are constant multiples of the elastic properties before any failure. In short, the degradation factor is replaced with what Reddy et al. called "the stiffness reduction coefficient" which may have an adjustable value between 0 and 1. These values still required tuning in order for agreement to be achieved. Successful attempts have been made to reduce the tunable parameters, such as Barbero et al.'s (2002) approach, where a second-order damage tensor was proposed with eigenvalues representing the density of distributed damage. Additionally, a fourth-order damage tensor was defined with the damage variables. The damage parameters were calibrated from experiments in order to determine the damage evolution laws.

With recent computational advances and continued decreasing computational expense, MPDM schemes are often implemented in FE codes where common implementation is achieved through user-defined subroutines such as UMAT for Abaqus (Chen et al., 1999; Xiao and Ishikawa, 2002; Goswami, 2005; McCarthy et al. 2005; Basu et al., 2007). To most accurately model all damage modes, it is thought that 3D elements should be used because damage in composites is 3D in nature, with strong and complex interactions. For example, delamination propagation in composite structures is a 3D phenomenon because a delamination frequently propagates in a non-self-similar

fashion and may kink into other plies and propagate along another ply interface (Tao and Sun, 1998). Furthermore, the presence of microcracks often interferes with the direction and shape of delamination progression. Unfortunately, modeling this usually means that the computational time and resources needed are quite substantial, and analyses based on 2D plate or shell elements are still widely used to save computational expense (Reddy et al., 1995; Pal and Ray, 2002; Xiao and Ishikawa, 2002; Basu et al., 2007; Laurin et al., 2007).

Simple CDM's have been utilized with finite element analysis that account for damage in the fiber and matrix, independently. Utilizing a simple material property degradation model, Chang and Chang (1987) presented a progressive damage model for laminated composites with a circular hole in tension (Figure 14). Convergence between stress and failure analyses were performed utilizing classical lamination theory considering material nonlinearity and property degradation resulting from damage, respectively. Nonlinear finite element analysis was performed and agreement was found between the analytical and experimental data. In the stress analysis, the equilibrium equation and stress-strain relations were derived. The equilibrium equation took into account that once the laminate was damaged, a redistribution of the stresses and strains resulted in degraded material properties. Thus, the equilibrium equation was solved at each step utilizing a Newton-Raphson iteration scheme. The failure criteria were defined based on the failure mechanism's resulting from damage, namely, from matrix cracking, fiber-matrix shearing, and fiber breakage. Based on these criteria, a property reduction model was implemented reducing certain properties to zero upon failure. Using a logic

structure similar to that in Figure 11, Chang and Chang's results were in agreement with respect to the analytical and experimental data for seven independent laminates. Later, Chang and Lessard (1991) performed similar work on damage tolerance of laminated composites in compression with a circular hole.

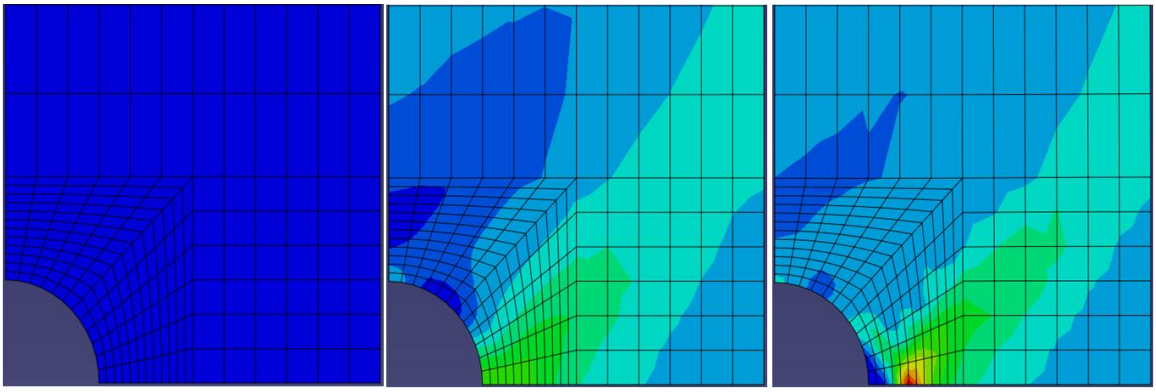

Figure 14: Continuum progressive damage of a laminated composites with a circular hole in tension where no actual damage is physically noted but is accounted for with a material property degradation.

Additional research in this area has been performed by others for many different conditions (e.g. material, matrix, loading, fastening, etc.). Eveil (2008) developed a 3D failure analysis methodology for composite laminates. This analysis utilizes a similar logic to Chang above with failure criteria based on Hashin and Yeh. Utilization of this advancement to 3D improved error from 25-30% to as low as 2.6%. Tay et al. (2005) have compared material property degradation models, element failure methods, and strain invariant failure theory. Material property degradation is the method used in each of the papers above where the element failure method modifies nodal forces to reflect damage and is employed with micromechanics based failure criteria. It is suggested that these

and other alternative approaches may be superior when translating results from specimen level to component and structural levels.

While these simplified versions show reasonable correlation to experimental data, the accuracy with which they can predict damage beyond initial fiber or matrix failure is dubious. This is largely due to the oversimplified property degradation and failure criteria, though these simplified methods do attempt to account for the constituents independently. Furthermore, these simple models are utilizing a uni-directional material. Hansen et al. (1994) presented a multicontinuum technique that keeps each constituent independent and allows for the introduction of additional constituents for more complex materials such as woven fabrics. By utilizing a volume fraction mixture theory, the composite average stress or strain may be estimated by summing the stresses, or strains, of each constituent based on the volume ratio of that constituent. By decomposing the average composite stress/strain state into constituent average stress/strain states, a basis is formed from which damage evolution may be predicted at a point of interest. Thus, constituent failure criteria may be based on the constituent average stress which potentially increases the level of accuracy of the model. This has been the foundation for the multicontinuum theory that is the basis for recent composites analysis software packages.

In summary, many different approaches have been attempted to model the damage progression of composite laminates and structures with CDM's. While they are largely based on utilization of experimentally determined properties, some properties, such as degradation factors, are generally found iteratively, which impacts the predictive

capability of the model. Increasing model complexity has been one avenue around this issue but comes at the expense of computational intensity. As such, there is no clear, identifiable CDM that generalizes progressive damage in composite materials. While it is likely that there exists a reasonable option depending on the exact case being analyzed, few options were found for the type of manufacturing defects investigated herein.

Discrete Damage Modeling (DDM)

Discrete damage modeling (DDM) is considered by many to be more consistent with the physical damage of thermosetting polymer reinforced composites. As noted, a continuum approach relies on representing the damage as a change in material properties, whereas observed damage is typically local failure of the constituents (matrix and/or fiber). Constitutive properties do not physically change in a continuum sense and the degradation is a consequence of a local failure. As such, DDM attempts to directly model damage as it would actually occur within a structure (Figure 15). It must be noted however, that this method is generally more expensive computationally and is more mesh dependent than CDM (Breitzman et al., 2010). In addition, knowledge *a priori* of the damage location is very helpful as an initial crack may have to be placed depending on the type of model.

A form of discrete damage modeling is the Virtual Crack Closure Technique (VCCT), which has been used with great success for delamination progression in composite materials and structures. VCCT calculates the fracture energy at the crack tip by calculating the energy required to close the crack (Krueger, 2002). The work required to bring nodes together is utilized to calculate strain energy release rates. This technique

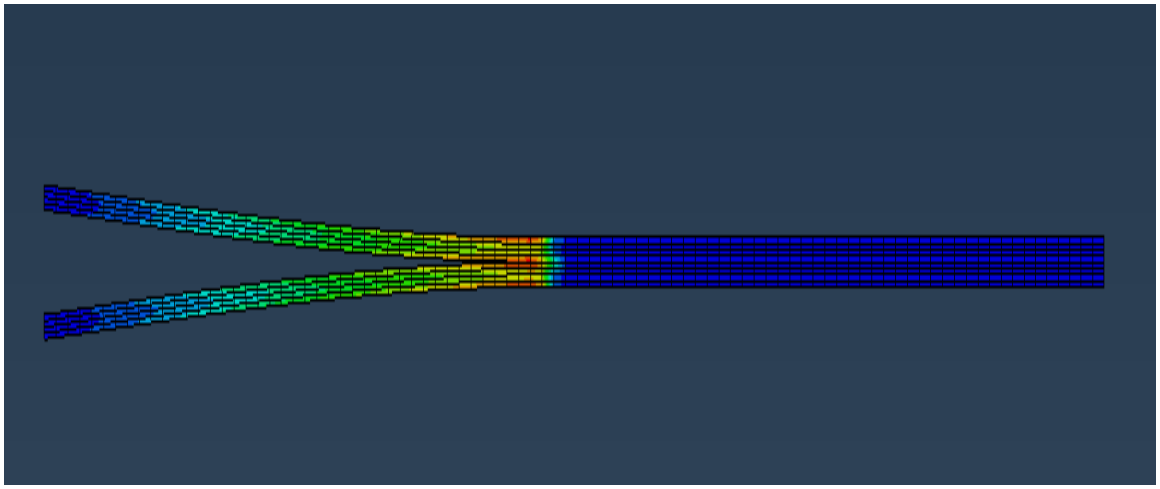

Figure 15: Discrete damage modeling (DDM) where damage is actually modeled as shown with crack growth and separation mid-laminate.

is particularly useful for establishing or confirming critical strain energy release rates in either Mode I or II, G_{Ic} and G_{IIc}, respectively. The authors have used this technique for delamination progression modeling, but VCCT is a relatively mature procedure, and as such, the results are not presented herein, nor is this method considered for use.

Several other techniques for discrete modeling exist such that crack development and path may be modeled. Originally, DDMs followed a discrete crack propagation by a re-meshing with the new geometry including the crack in future increments. This cycle was repeated until ultimate failure was reached based on one of several crack propagation criteria (Bouchard et al., 2000). The discontinuity created by the crack can make re-meshing difficult, and extended finite element modeling (XFEM) allows for a crack to propagate without having to re-mesh at each step (Areias and Belytschko, 2005). While significant work has been performed in this area, XFEM has been left out of this

investigation as it is currently being considered by others within the MSUCG in areas where it is more applicable.

Cohesive elements, as described in detail below, have gained attention as they are able to discretely model damage within composite materials. The idea of cohesive elements is based on the Dugdale–Barenblatt cohesive zone approach, which can be related to Griffith's theory of fracture when the cohesive zone size is negligible compared with other characteristic dimensions (Dugdale, 1960; Barenblatt, 1962). The intent of the cohesive zone is to add an area of vanishing thickness ahead of the crack tip to describe more realistically the fracture process without the use of the stress singularity utilized in linear elastic fracture mechanics. Barenblatt (1962) theorized that a cohesive zone, that is much smaller that the crack length, exists near the crack tip and has a cohesive traction on the order of the theoretical strength of the solid. In addition, the parameters defining size of the zone and traction at onset are independent of crack size and extremal loads. Finally, no stress singularity exists because stresses are finite everywhere including a the crack tip. It is important to note that energy dissipation is an intrinsic mechanism of fracture with the cohesive approach in contrast to classic continuum fracture mechanics.

Cui and Wisnom (1993) used this type of element to predict delamination progression in specimens under three-point bending and in specimens with cut central plies. Duplicate nodes were used along the interface between distinct plies, and two independent, zero thickness springs, horizontal and vertical, were used to connect them. As may be expected, the cohesive elements used showed a sudden discontinuous change in stiffness when the failure criterion was reached. Wisnom (1996) and Petrossian and

Wisnom (1998) further developed this process and created an element that provided a smoother transition from linear elastic behavior to plastic behavior. A quasi-3D model was proposed by Wisnom and Chang (2000) to predict, with reasonable results, both delamination and intra-ply damage prior to ultimate failure in a cross-ply laminate with a center crack loaded in tension.. Planar elements were used on the surface of each ply and were then connected together with non-linear springs, as above, to model delamination between different plies. A similar technique was used to model longitudinal splitting along the fibers by means of spring interface elements across the line perpendicular to the notch where splitting is expected.

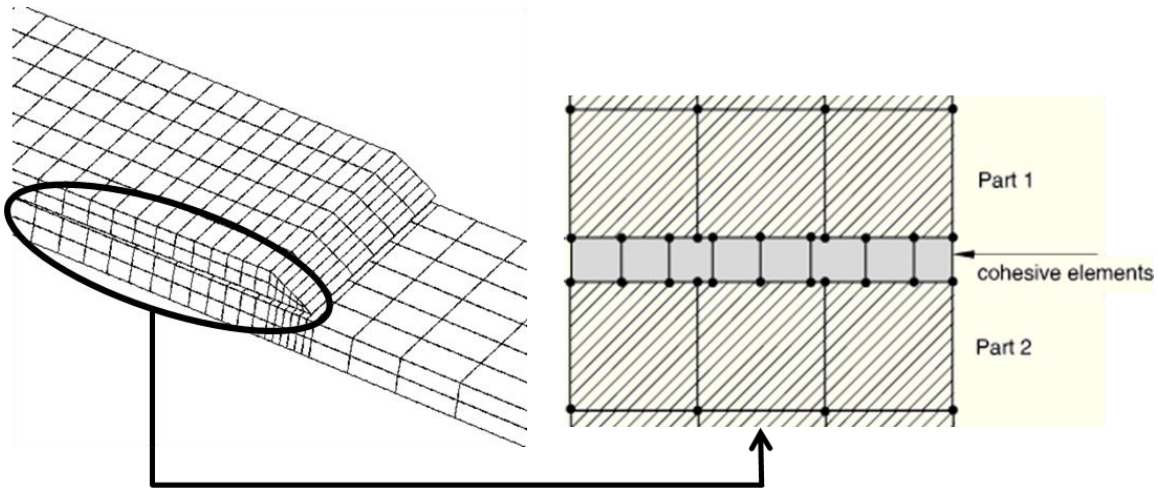

Figure 16: Cohesive elements placed in a stringer where discrete, physical separation may be noted (Daussault Systems, Abaqus v6.12, 2012).

Common configurations that often utilize DDM's, and in many cases cohesive elements, are double cantilever beam (DCB), and end notched flexure (ENF), as these tests are commonly performed to determine the Mode I and II loadings (Figure 17). Meo

and Thieulot (2005) studied Mode I fracture for a double cantilever beam using shell elements for the composite plies and non-linear springs for the interface. Borg et al. (2001) extended the work of Crisfield et al. (1997) using three orthogonal springs to connect the interface in order to develop a 3D model which allowed for Mode I, II, III, and combined loading. In this model, the dissipated work was used to control the unloading path in the cohesive zone, similar to the traction-separation above. Xie and Waas (2006) created a 2D DDM with cohesive elements to simulate fracture initiation and progression in each of these configurations. Simulation results were found to be in agreement with experimental results for DCB and ENF tests.

For 2D plain strain conditions, lines of cohesive elements have been used to analyze fracture in DCB (Chen and New, 2001; Alfano and Crisfield, 2001) and in free edge delaminations (Schellekens and Borst, 1994). In short, a layer of zero thickness cohesive elements with specific traction-separation criteria are placed in areas of interest such as areas between layers of the laminate. A bi-linear criterion is then used as shown in Figure 18 where the initial stiffness, K, of the cohesive element is linear up to the damage initiation point at maximum traction, T_{max}. From this point to the failure separation, Δ_c, the slope estimates the damage evolution of each of the cohesive elements up to failure, Δ_{fail}. At this point, the traction-separation criterion is met for a specific cohesive element, a separation occurs resulting in crack propagation, and the element is deleted.

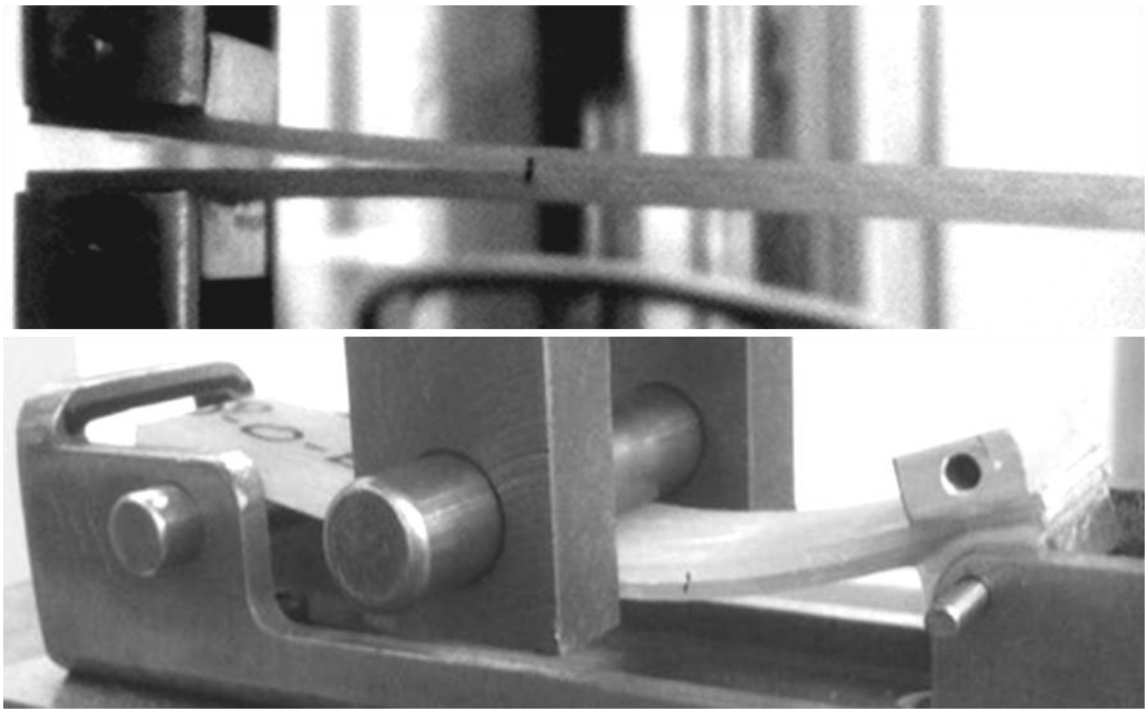

Figure 17: Double Cantilever Beam (DCB) specimen just prior to first Mode I crack propagation (top) and End-Notch Flexure (ENF) specimen just after Mode II crack propagation (bottom).

As such, damage evolution is able to be modeled discretely. It must be noted that to achieve accurate results, significant time up-front may be needed to build meshes, as models can become very detailed. In turn, this can potentially result in high computation expense to run these models. The exact values for this bi-linear response may not be known and must be adjusted in an iterative approach that results in multiple model analyses to establish reasonable experimental/analytical correlations. However, once correlations are determined, they are thought to be consistent for a specific composite material system.

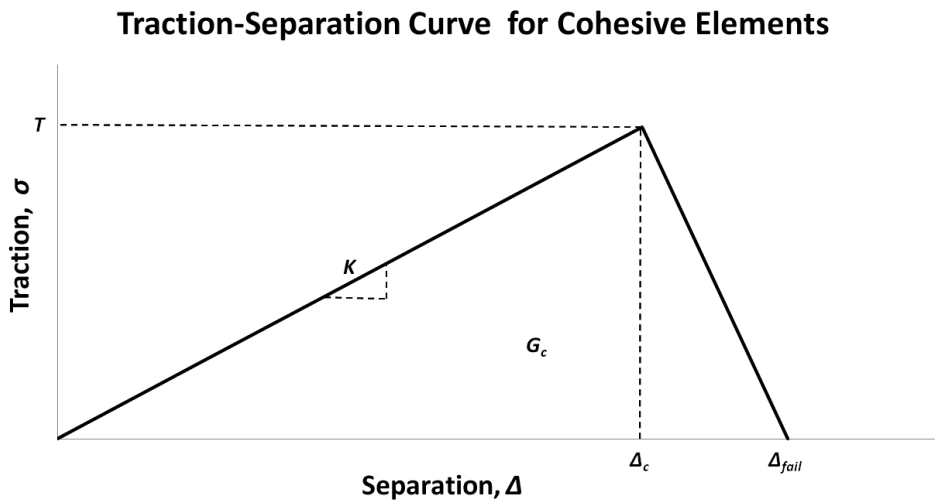

Figure 18: Representation of a cohesive element's bi-linear traction-separation response.

Recently, the use of cohesive elements in this way has proven to be a viable option for modeling laminated composites and does not require an initial crack be placed in the model (Karayev et al, 2012; Lemanski et al., 2013). The work of Lemanski et al. is of particular interest as it utilizes cohesive elements to model an out-of-plane fiber wave in compression. Progressing from the work of Wang et al. (2012), four different configurations were modeled utilizing cohesive elements placed in areas around the misaligned fibers. It was noted that both the qualitative results, location and shape of failed specimen, and quantitative results, failure load, predicted by the models correlated well to the experimental results in all cases.

In summary, like the CDM's above, many different types of DDM exist and have been utilized for composite materials. Cohesive element methods have shown promise and have progressively improved in their ability to accurately predict damage in

composite structures. In particular, they have shown promise when utilized in composites with defects and, as such, cohesive elements are utilized herein.

Overview of Work

While the BRC and this Effects of Defects study are the impetus for this work, the benefits of this work are applicable to composite structures universally. The work was begun with Benchmark Material Testing (BMT) to determine material properties and to characterize damage progression in coupons both flawed and unflawed. Several different analytical models were created and generated utilizing these results, and were correlated to the BMT effort while allowing for the prediction accuracy of each model to be determined and for overall comparisons among model types to be ascertained. To ensure accuracy, efficiency, and development of worthwhile predictive tools, a systematic approach was taken throughout this study whereby consistent, simple cases were correlated and modeling techniques became more complex..

Benchmark Material Testing (BMT)

As noted above, three composite material defect types are currently being investigated after each was deemed critical to blade function and life cycle: in-plane (IP) waviness, out-of-plane (OP) waviness, and porosity. While extensive studies have reported on each of the defect types in thin laminates utilizing varying advanced composite materials, less research has been performed for wind turbine blade materials. Furthermore, it must be noted that much of this research has been performed for industries where manufacturing is on a smaller scale and where expense is less critical.

Most of this prior research offers a preliminary basis for the work herein, but it is known that acceptable defects often included in wind turbine blades far exceed what would be acceptable in other industries, such as aerospace. Thus, testing specific to understand the criticality of defects common to blades is necessary. Test groups in particular were utilized, each more complex than the previous, as outlined in Chapter 3 and in Riddle (2013). As such, many different cases for each flaw type are tested herein, allowing for progressive damage quantification, material property definition, and development of many correlation points in this work.

Systematic Approach

A systematic approach was employed to compare different modeling methods discussed herein (Figure 19) for each of the models generated and run in Chapters 4-9. All of these models utilized material properties and responses generated in the Benchmark Material Testing (BMT) effort discussed in Chapter 3. For each different model method, flaw complexity was increased, starting with a consistent unflawed case and initial IP wave case, until the correlation was deemed acceptable or unacceptable. Acceptable modeling methods were able to predict and match flawed material response for multiple flaw types utilizing unflawed material properties and flaw geometries. It is worth noting that a qualitative/quantitative approach was utilized herein that is similar to that utilized by Lemanski et al. (2013), though strains at peak stress were also considered. In short, acceptable models correlated well both qualitatively, as matching failure location and shape, and quantitatively, as matching peak stress at failure strain.

As shown in Figure 19, if correlation was not achieved by a model at any point during the systematic increase in flaw complexity, the model was deemed unacceptable and was discarded. Unless otherwise noted, the increase in flaw complexity in each case went from unflawed controls to porosity to the IP wave baseline case to the initial OP wave case, and then to other IP and OP geometries. Acceptable models were able to accurately and consistently predict each of these cases, and with this consistent systematic approach, the different techniques were able to be compared easily.

Acceptance criteria was defined to allow for consistent analysis at each decision point of Figure 19. First, a qualitative assessment was performed and correlation was deemed acceptable if strain accumulation and damage progression visually matched the BMT results. While this assessment method may seem crude, it allows for quick analysis of several key factors including an energy comparison. An energy comparison ensured that the energy is conserved between the strain energy available and energy dissipated. Qualitative comparison of the unrecoverable energy, or area under the curves, was deemed sufficient for the work herein as models that do not conserve energy were evident and were not considered acceptable. While conservation may be inherent in finite element analysis, it was shown that this comparison gave rapid indication when a model was unrealistic as seen with the non-linear shear approach in Chapter 7 below. As such, qualitative assessment provided a rapid go/no-go gage. It is also interesting to note that classical fracture mechanics approaches would not allow for this comparison to be easily made, reinforcing the use of cohesive zone modeling as the discrete method.

If the qualitative criteria are met, a quantitative assessment was performed. First, the strain at peak stress was compared and deemed acceptable if it was within 10% of BMT results. If acceptable, peak stress was compared and also deemed acceptable if it was within 10% of BMT results. While these acceptance criteria were beyond the variability noted in the BMT, if these criteria were outside 10%, but within 20%, correlation was considered moderate. It is important to note that this consideration was only made for correlation with other flaws and/or materials after acceptable correlation had been achieved for the initial IP wave case. As such, models were considered predictive if correlation was achieved with these other cases utilizing the same input parameters as the initial IP wave case.

Overview of Analytical Approaches

Several different CDM methods were used to generate and run models with increasing computational difficulty in order to prove the capabilities and expose the deficiencies of each model type. In this case, computational difficulty refers to a combination of complexity of model type, one which requires more user time to setup and more overall model computational expense. First, linear elastic models were run with neither damage criteria, nor non-linear material response, nor any sort of material defect to confirm accurate correlation to initial stiffness response as outlined in Chapter 4. Once this was achieved, Hashin failure criteria (Barbero, 1999) were added to porosity, IP, and then OP wave models as shown in Chapter 5. This Abaqus (Daussault Systems, v6.12, 2012) built-in capability allowed for prediction of damage onset based on fiber and matrix properties before following an energy based damage evolution law.

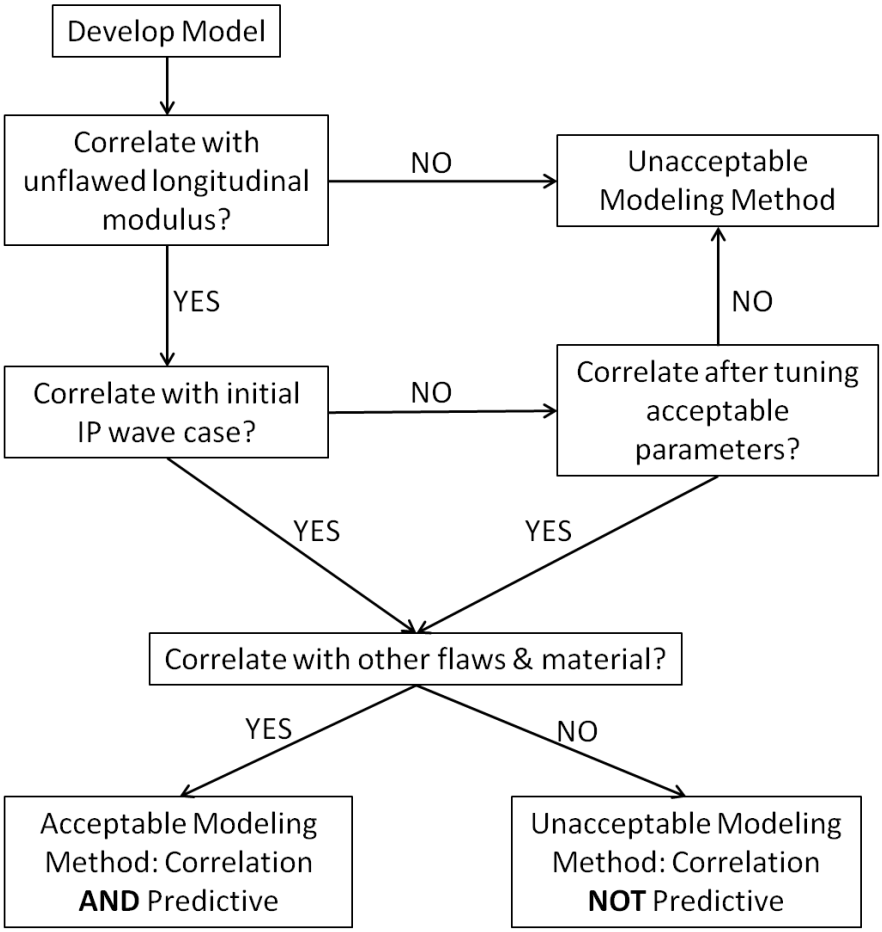

Figure 19: Flow chart depicting systematic approach to determine correlation acceptance and predictive capability.

Next, in Chapter 6, the linear elastic model was modified with user-defined failure criteria where mixed stress/strain based failure criteria were implemented. Instead of following a damage evolution law, material properties were directly degraded once failure had occurred in order to reduce material properties. Several different property reduction schemes were investigated with varying degrees of correlation though, in short, it was found that degrading properties to zero was an overestimation. In Chapter 7, a user-defined material card was implemented to match the non-linear shear response.

Given the fiber misalignment found in both IP and OP waves, shear between the tows and layers, respectively, was observed to be the critical failure mode. Thus, generation of a non-linear response possibly allowed for better approximation than the standard linear approximation.

The DDM effort was utilized, as discussed in Chapter 8, focusing on the use of cohesive elements placed in all areas of possible damage progression (e.g. between fiber tows and between plies). The use of cohesive elements has proven to be a viable option for modeling laminated composites and does not require an initial crack be placed in the model (Karayev et al., 2012). In short, a layer of zero thickness cohesive elements with specific traction-separation criteria are placed in areas of interest such as between layers of the laminate. As the traction-separation criterion is met for a specific cohesive element, a separation occurs resulting in crack propagation. Thus, damage evolution is able to be modeled discretely. Models are generated with cohesive elements between the fiber tows for the baseline IP wave case.

Finally, a combined CDM/DDM approach was implemented that incorporated a CDM non-linear shear user-subroutine with DDM cohesive elements placed between the fiber tows as discussed in Chapter 9. This combination of approaches allowed for damage to progress between the fiber tows, as initially seen in the BMT damage progression, while then allowing for fiber degradation to occur, thereby reducing the load-carrying capacity of the composite.

In summary, these models were created, run, and correlated to responses outlined in the BMT effort and modified to improve correlation. Flaw complexity and

computational difficulty were both increased within and between model types, respectively. While correlation was found rather easily in some cases, other cases required significant modification, or tuning, of input parameters. In some cases, correlation was able to be achieved by small amounts of acceptable parameter tuning, such as viscous regularization, maximum element degradation, and shear stress coefficients. These acceptable tuning parameters, in most cases, were adjusted to assist with convergence, and the effects on the model, or element section, were able to be tracked. In other cases, material properties were modified as a final approach to attempt correlation. Adjustment of these types of parameters was considered to be unacceptable tuning, and while correlation may have been achieved, the model type was considered to be a failure for unbiased prediction efforts. It must be noted that these unacceptable tuning methods were performed only to better understand the effects on modeling and are not included herein. Below, each case is presented, a discussion is offered for each correlation, and either modification of input parameters is justified or the model type is found to be inaccurate.

BENCHMARK MATERIAL TESTING

Introduction

In order to meet the purpose of comparing different modeling methodologies, baseline information was needed to establish and understand the material properties, failure points and modes, and damage progression of both unflawed and flawed specimens. As noted above, a three round benchmark material testing (BMT) program was implemented to provide this information for typical wind turbine blade flaws and materials. For each step in the three rounds, additional variations of the critical flaw parameters were tested, as well as additional materials. It should be noted that all three rounds of testing were a shared effort between the two MSUCG tasks listed above with results being necessary for both tasks. As such, the portions of the BMT led by the author are included herein, namely Round 1 and portions of the BRC validation blades, while the Round 2 and remainder of the validation blades efforts may be found as detailed by Riddle (2013). Results from all three rounds were utilized herein establishing material properties, response, and damage progression.

To ensure testing accuracy, controls were directly compared to previous results listed in the Montana State University Composites Group's SNL/MSU/DOE Composite Material Database (MSU-CMD) (http://www.coe.montana.edu/composites/, v22). In some cases, material response of the unflawed controls did not adequately match these existing results and MSU-CMD or other published results were utilized. These cases are investigated completely and the logical process for utilizing this data source is justified.

The flawed specimens were not able to be compared to database values as the database does not include flawed materials. However, it was clearly evident that once a flaw was introduced, the material response in the flawed area dominated the overall response in most cases. In some cases, such as OP waves in compression, material response was inconsistent due to eccentricity and did not allow for correlation data to be attained. These variant cases are also noted.

Round 1 BMT Coupon Testing

Coupon testing was performed utilizing a vacuum infused PPG-Devold fiberglass with a Hexion resin system representative of the materials commonly found in wind turbine blades. Unflawed controls and flawed specimens with waves, porosity, or delamination were tested in tension and compression with several different ply orientations. Material response was measured with digital image correlation (DIC) for at least one representative sample from each test group. DIC data was not gathered for all samples given the time necessary for each test, the extensive number of test variations, and the large number of tests performed.

Flaw Characterization

In order to ensure the applicability of the specimen tested in Round 1, coordination with the Flaw Characterization portion was necessary. In this vein, Riddle et al. (2011) determined the priorities and characterized both the IP and OP waves to be analyzed in this study based on a survey of wind turbine blades containing these defects. Digital images were analyzed and waves were discretized and mathematically

characterized using a sinusoidal curve fit to determine wavelength, amplitude, and fiber misalignment angles as shown below in Figure 20. Statistical analysis of these parameters and scaling were performed to determine the values to be tested as outlined in Table 1 for the initial round of testing. For more information regarding this topic, the reader is referred to the companion work performed by Riddle where this work is addressed comprehensively.

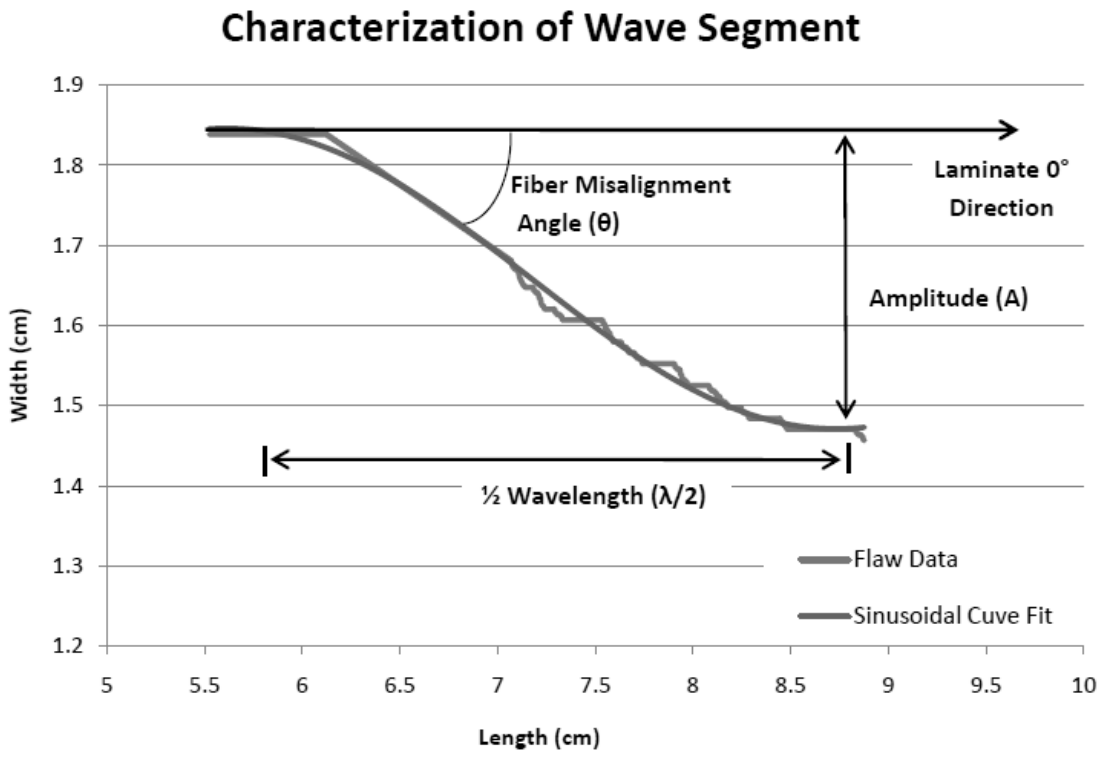

Figure 20: Explanation of parameters used in wave characterization as outlined below in Table 1 for in-plane and out-of-plane waves (Riddle et al., 2011).

Table 1: Parameters for each of the OP and IP waves used in Round 1 of the BMT (Riddle et al., 2011).

OP1 Wave [mm]	As-Built	Scaled
Max Amplitude	8.5	**2.9**
Mean Wavelength	67.4	**22.8**
Angle [deg]	34.9	**36.8**

IP1 Wave [mm]	As-Built	Scaled
Mean Amplitude	3.7	**1.9**
Mean Wavelength	47.5	**23.8**
Angle [deg]	24.8	**24.8**

OP2A Wave [mm]	As-Built	Scaled
Mean Amplitude	1.9	**0.7**
Min Wavelength	15.8	**5.4**
Angle [deg]	35.0	**34.8**

IP2 Wave [mm]	As-Built	Scaled
99% Amplitude	9.0	**4.5**
Mean Wavelength	47.5	**23.8**
Angle [deg]	48.9	**48.9**

OP4A Wave [mm]	As-Built	Scaled
Mean Amplitude	1.9	**0.7**
Mean Wavelength	7.4	**2.28**
Angle [deg]	9.7	**9.4**

IP3 Wave [mm]	As-Built	Scaled
Mean Amplitude	3.7	**1.9**
10% Wavelength	20.0	**10.0**
Angle [deg]	47.8	**47.8**

Test Manufacturing and Methods

Four layer panels containing a single defect and defect-free control panels were infused under vacuum with one layer of peel-ply on the top and bottom surfaces, and one layer of flow medium on the top surface of the laminate. Mostly uni-directional PPG-Devold 1250 gsm areal weight E-glass was infused using a vacuum assisted resin transfer molding (VARTM) technique with a Hexion RIM 135 resin system in all cases (Figure 21). Laminates for each case were manufactured with fiber directions of both 0° and ±45°. The cure profile for each panel was 48 hours at room temperature followed by 8 hours at 80°C. The nominal fiber volume fraction of the panels was 55% with a nominal thickness of 3.2 mm.

Figure 21: Materials and VARTM process utilized in making plates through entire BMT.

The manufacturing process was adapted to include each of the three defect types with significant assistance from many of the members of the MSUCG including Julie Muretta and Daniel Guest. For Round 1, air bubbles were introduced into the resin directly by inducing cavitations during the mixing process prior to infusion. IP waves were introduced by pulling the fibers manually for one entire wavelength as outlined below. OP waves, also for one entire wavelength, were created initially by placing a resin form of the proper amplitude and wavelength under the laminate. After it was determined that bonding issues prevented proper adhesion, a method was created whereby discontinuous fibers were placed transversely to build up the waveform as outlined below. Among the wavelengths, amplitudes, and estimated fiber misalignment

angles that were tested are listed in Table 1 above. It is important to note that for correlation purposes a 29° IP wave was used for initial correlations, while 16° and 48° cases were used for additional cases given an increment of approximately 15°. In addition, fiber misalignment angles were deemed a more consistent method of wave severity characterization than aspect ratio for this study (Riddle et al, 2011).

Porosity Methods: Manufacturing composite laminates with a specified amount of porosity is extremely difficult, and inclusion of specific size and shape is near impossible. Thus, content was controlled as much as possible with measurement of these parameters after laminate manufacture to fully characterize the porosity of samples next to those that were tested. As exact values of the amount of porosity commonly included in wind turbine blades is unknown, it is known that greater than 2% is undesirable based on information given to the BRC from blade manufacturers. In this initial Round 1 of testing, porosity was introduced by cavitating the resin while mixing resulting in a 2% porosity by volume inclusion. Techniques were later developed to created isolated areas of porosity for Rounds 2 and 3 (Riddle, 2013).

IP Wave Manufacturing Instruction: IP waves were formed manually one ply at a time. The first step in the method of forming IP waves was to lay the fabric over a piece of polyethylene tubing oriented transversely to the 0° fiber angles in order to form a wave of approximately the desired amplitude and wavelength OP with the fabric. This was accomplished by pressing the ply gently over the tubing by hand, using only enough force to cause the tows to form around the tube. To ensure fiber integrity, this must be

performed slowly due to the stiffness of the tows. Next, steel bars were placed on either side of the tubing to act as an anchor for the fabric when the hose was removed (Figure 22). With these steel bars in place by hand, the hose was then unclamped and removed (Figure 23). It was essential that the steel bars remain in place to constrain the wave through the entire process.

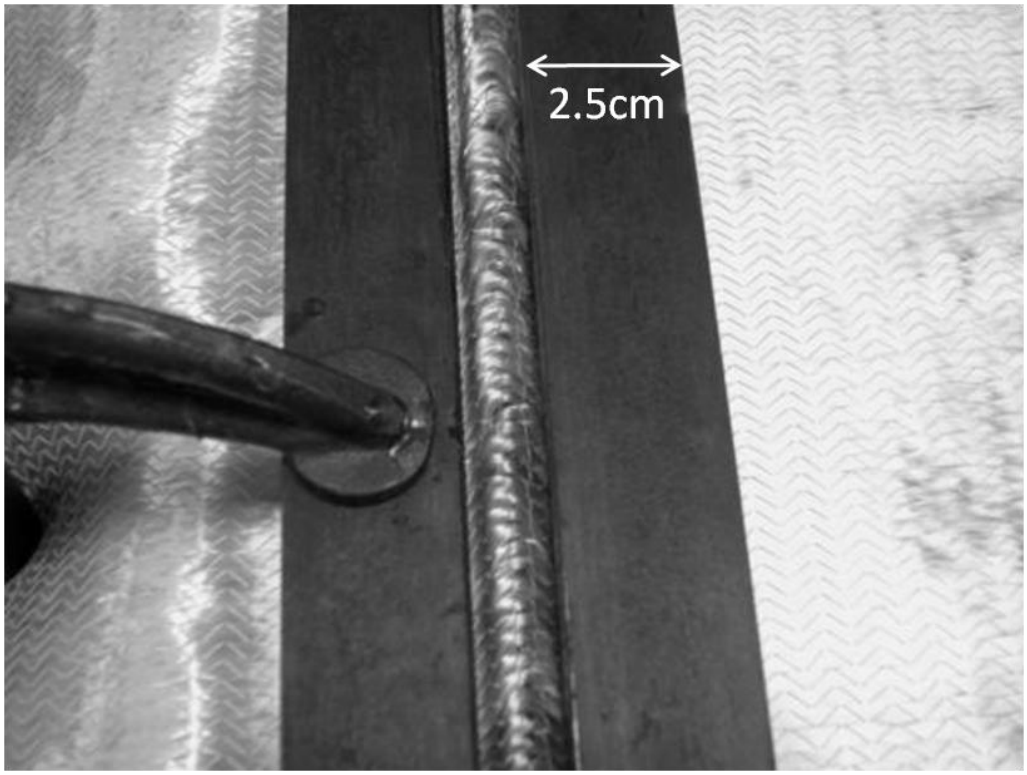

Figure 22: Fabric over polyethylene tubing constrained by steel bars.

Once the polyethylene tubing was removed the process of transforming the as-formed OP wave into an IP wave began. First, the waves were manually pressed over, or essentially rotated, to lay at approximately 45° to their initial OP orientation. Then the steel bars were removed and placed at a distance apart on the work table such that the

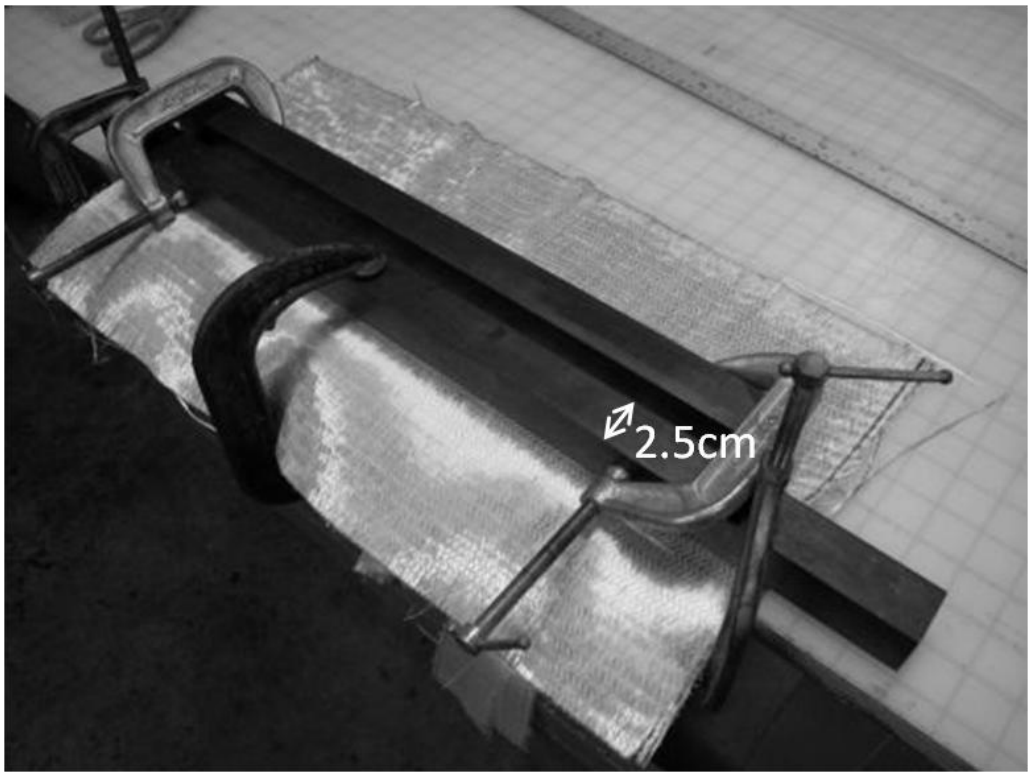

Figure 23: After the tubing was removed, the wave is ready to be pressed over into an IP wave.

fabric layer was laid between them while using them as end constraints for the tows (Figure 24). The partially formed waves were then manipulated further by hand, with care taken to keep the peaks of the waves aligned transversely to the 0° fiber angle. Once the wave form had the approximate desired dimensions, the fabric was covered with 3/8" thick glass, while still remaining constrained by the steel bars (Figure 25). The fabric rested in this configuration for at least two hours, allowing stresses in the fibers to be relieved and wave measurements to be taken through the glass. Once this was complete, the plies were stacked on the mold for the standard vacuum assists resin injection process.

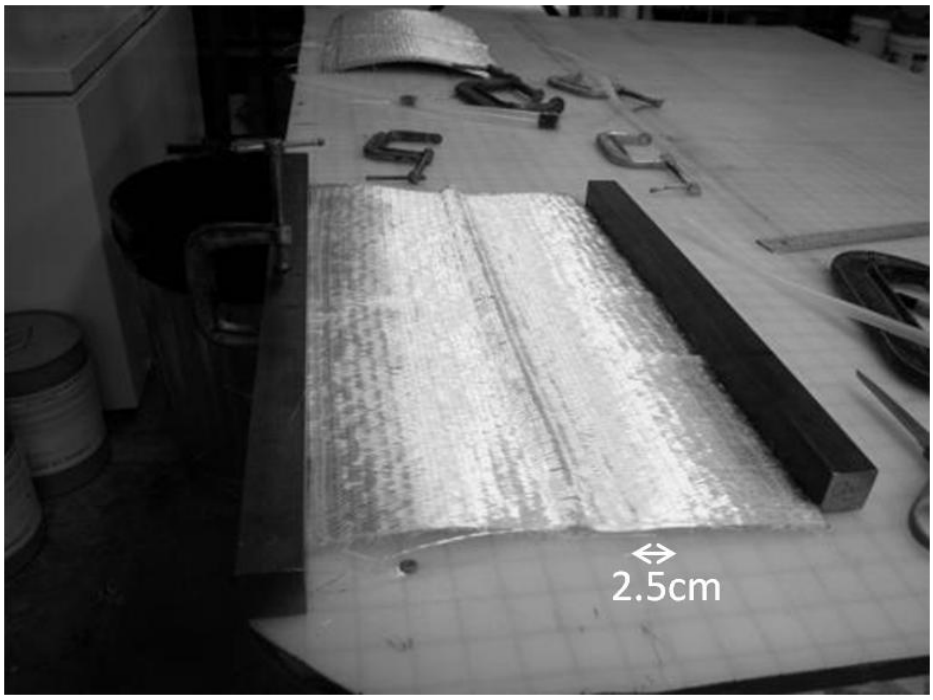

Figure 24: Partially formed wave constrained between steel bars.

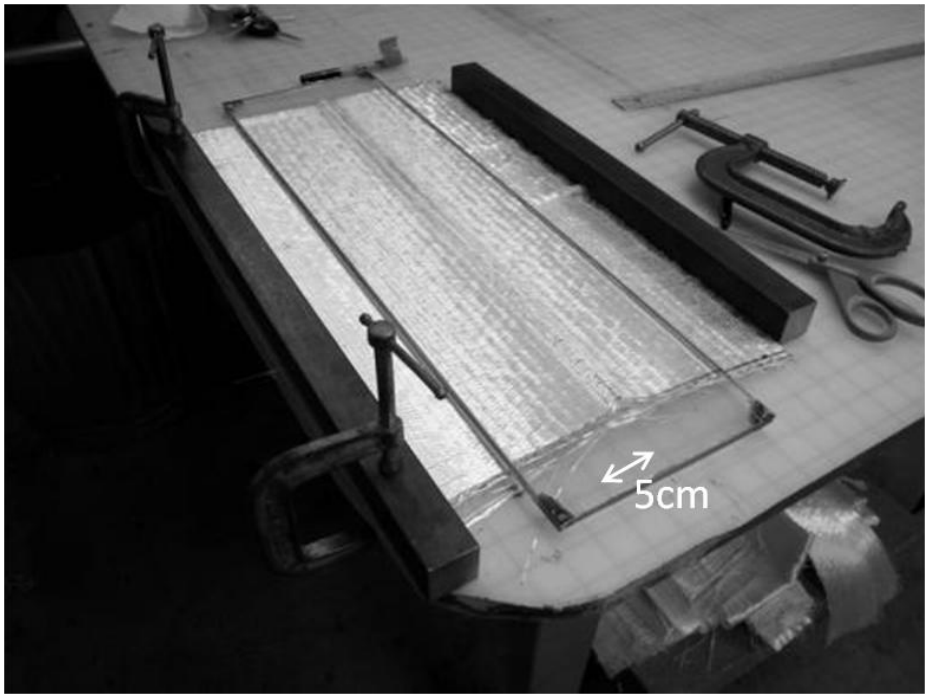

Figure 25: Finished wave relaxing under glass ready to be measured.

OP Wave Manufacturing Instruction: The first step in building a plate with OP waves was to secure the bottom layer of peel ply to the mold tool to ensure it did not shift during the infusion process. A form for the OP wave was then constructed using individual fiber tows. The fiber tows used for the wave build-up were cut to the width of the laminate. The wave build-up was created by stacking fiber tows in a pyramid fashion until the desired amplitude and wave length values were approximately reached (Figure 26). The OP wave sections were then placed onto the secured peel ply perpendicular to the direction of resin flow and to the orientation of the laminate fiber tows.

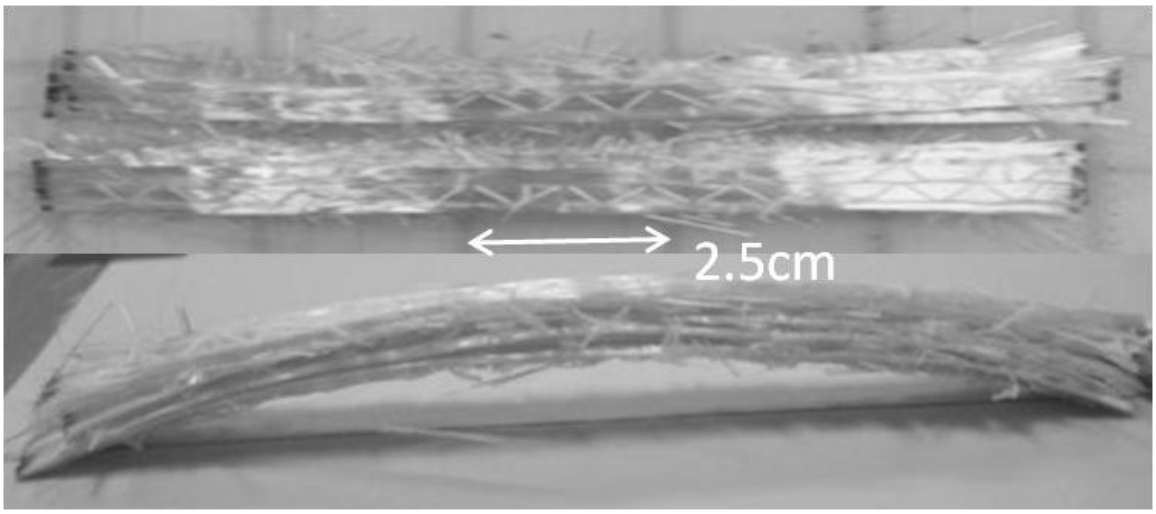

Figure 26: Chopped wave perturbation tows (top) and chopped tows as implemented for creation of OP waves (bottom)

Layers of fiberglass sheets were then placed on top of the mold while ensuring that the OP wave build-ups did not shift and remain perpendicular to the fiber direction. The buildup was completed by securing the top layer of peel ply and flow media. Once a

vacuum was pulled, the OP wave buildups are rolled to ensure that no air pockets or voids have formed. Infusion was then completed using a VARTM method (Figure 27).

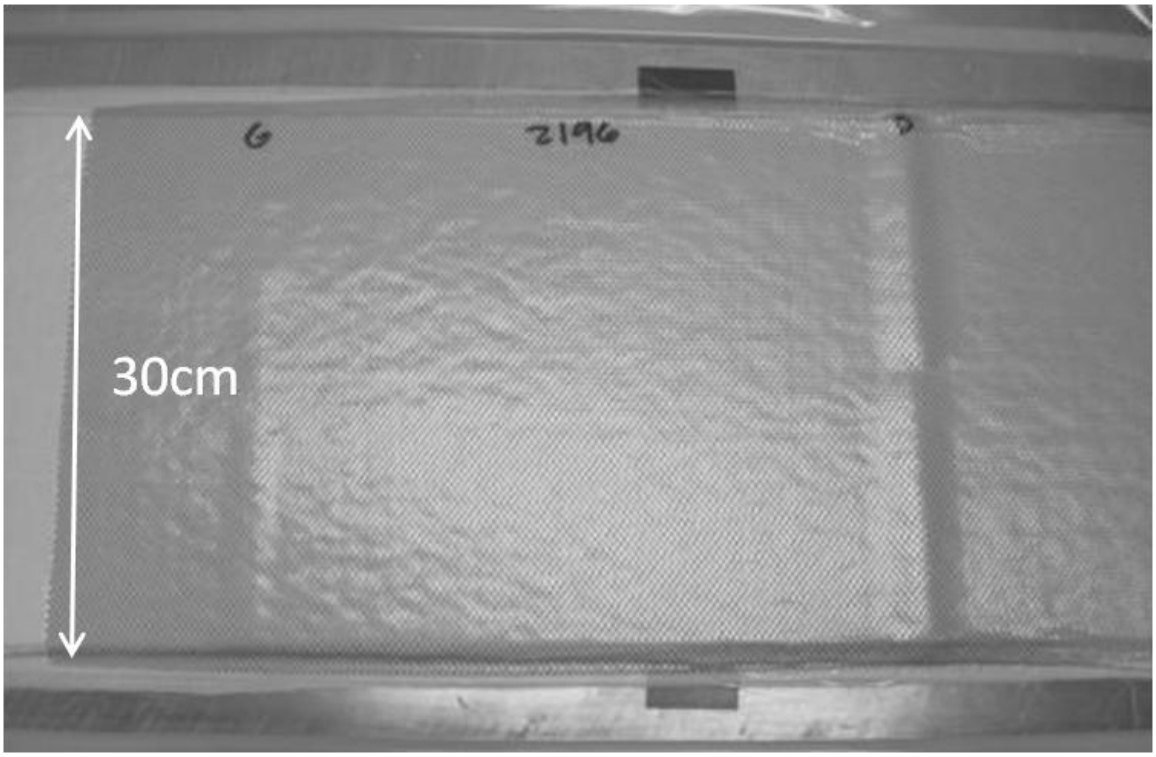

Figure 27: Plate under vacuum with OP waves

Coupon Geometry and Test Setup

Test coupons were cut from the panels for use in tension and compression testing. Tensile coupons were cut to approximately 50 mm wide by 200 mm long and were tabbed resulting in a gage length of 100 mm. Compression coupons were cut to approximately 25 mm wide by 150 mm with an nominal gage length of 25 mm, which was extended to 38 mm where the wavelengths were greater than 25 mm. The control and porosity samples were symmetric, while each of the wave samples lacked symmetry along the axis in the direction of the particular wave. Test methodology was considered

when determining lay-up and coupon dimensions. Coupons were constructed with representatives of blade materials and construction processes though scale was reduced. Scaling was required to achieve compatibility with the Instron 8802 250 kN testing machine and grip capacity (Figure 28). Static ramp tests on the specimens were conducted at a rate of 0.05 and 0.45 mm/s for tension and compression, respectively. A complete listing of all the combinations tested in Round 1 of the BMT are shown in Table 2 below. Overall, more than 150 coupons were tested with 3 to 5 in each test group depending on the consistency of the results.

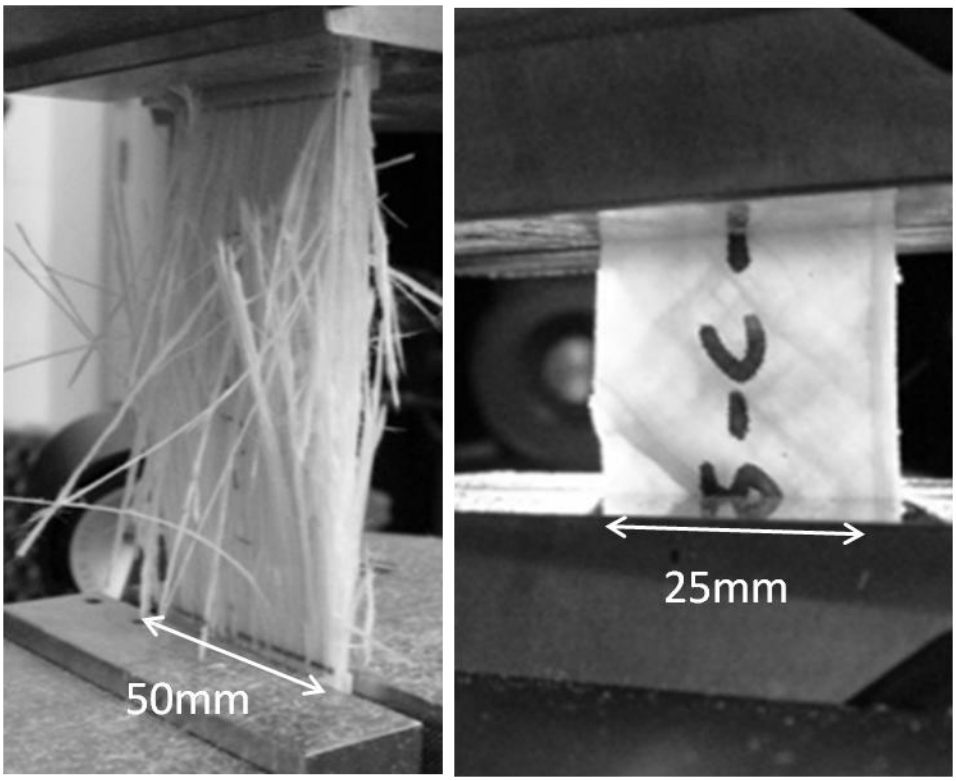

Figure 28: Representative 0° tensile (left) and ±45° compressive (right) samples being tested.

Table 2: Round 1 BMT matrix.

	Defect	Parameter 1		Parameter 2		Test	Layers	Samples	Properties
Group A: Control	Control	--	--	--	--	Tension	4	5	Axial (Tensile)
	Control	--	--	--	--	Compression	4	5	Axial (Compressive)
	Control	--	--	--	--	45° Tensile	4	5	Shear
	Control	--	--	--	--	45° Compression	4	5	Shear
Group B: Initial Properties (OP Waves)	OP Waves	2.9	Amplitude (mm)	22.8	Wavelength (mm)	Tensile	4	5	Axial (Tensile)
	OP Waves	2.9		22.8		Compression	4	5	Axial (Compressive)
	OP Waves	2.9		22.8		45° Tensile	4	5	Shear
	OP Waves	2.9		22.8		45° Compression	4	5	Shear
	OP Waves	0.7		5.4		Tensile	4	5	Axial (Tensile)
	OP Waves	0.7		5.4		Compression	4	5	Axial (Compressive)
	OP Waves	0.7		5.4		45° Tensile	4	5	Shear
	OP Waves	0.7		5.4		45° Compression	4	5	Shear
	OP Waves	0.7		2.3		Tensile	4	5	Axial (Tensile)
	OP Waves	0.7		2.3		Compression	4	5	Axial (Compressive)
	OP Waves	0.7		2.3		45° Tensile	4	5	Shear
	OP Waves	0.7		2.3		45° Compression	4	5	Shear
Group C: Initial Properties (IP Waves)	IP Waves	1.9	Amplitude (mm)	23.8	Wavelength (mm)	Tensile	4	5	Axial (Tensile)
	IP Waves	1.9		23.8		Compression	4	5	Axial (Compressive)
	IP Waves	1.9		23.8		45° Tensile	4	5	Shear
	IP Waves	1.9		23.8		45° Compression	4	5	Shear
	IP Waves	4.5		23.8		Tensile	4	5	Axial (Tensile)
	IP Waves	4.5		23.8		Compression	4	5	Axial (Compressive)
	IP Waves	4.5		23.8		45° Tensile	4	5	Shear
	IP Waves	4.5		23.8		45° Compression	4	5	Shear
	IP Waves	1.9		1		Tensile	4	5	Axial (Tensile)
	IP Waves	1.9		1		Compression	4	5	Axial (Compressive)
	IP Waves	1.9		1		45° Tensile	4	5	Shear
	IP Waves	1.9		1		45° Compression	4	5	Shear
Group D: Initial Properties (Delam & Porosity)	Delamination	38.1	Crack Length (mm)	--	--	DCB	4	5	Out of Plane
	Delamination	38.1		--	--	45° DCB	4	5	Out of Plane
	Delamination	38.1		--	--	MMB	4	5	Out of Plane
	Porosity	2%	% Volume	--	--	Tension	4	5	Axial (Tensile)
	Porosity	2%		--	--	Compression	4	5	Axial (Compressive)
	Porosity	2%		--	--	45° Tensile	4	5	Shear
	Porosity	2%		--	--	45° Compression	4	5	Shear

All coupons were tested with the Instron 8802, and several ASTM standards were utilized as guidelines (ASTM D695, D3039, D3410, D3518, D6641; 2007). It should be noted that the geometric discontinuities associated with both wave types were non-symmetrical about at least one axis. The associated stiffness variation resulted in a bending moment where a stress variation occurs across the width for IP waves and through the thickness for OP waves. This stress variation necessitated consideration of grip fixity during testing to ensure the bending reacted out by the grips was not significant. Utilizing a similar finite element analysis to Agastra and Mandell (2010), it was noted that strains varied by less than 8% across the thickness with a fixed grip condition in tension (Figure 29). Bending due to these asymmetries was a significant issue when testing in compression, especially with an embedded OP wave as discussed below. In compression, D695 was most closely followed, as the fixturing required in the other compression standards did not allow for a large enough gage section to test either wave configuration. As such, the digital image correlation (DIC) data was analyzed to ensure minimal bending which in turn allowed for simplified assessment of material properties outlined below.

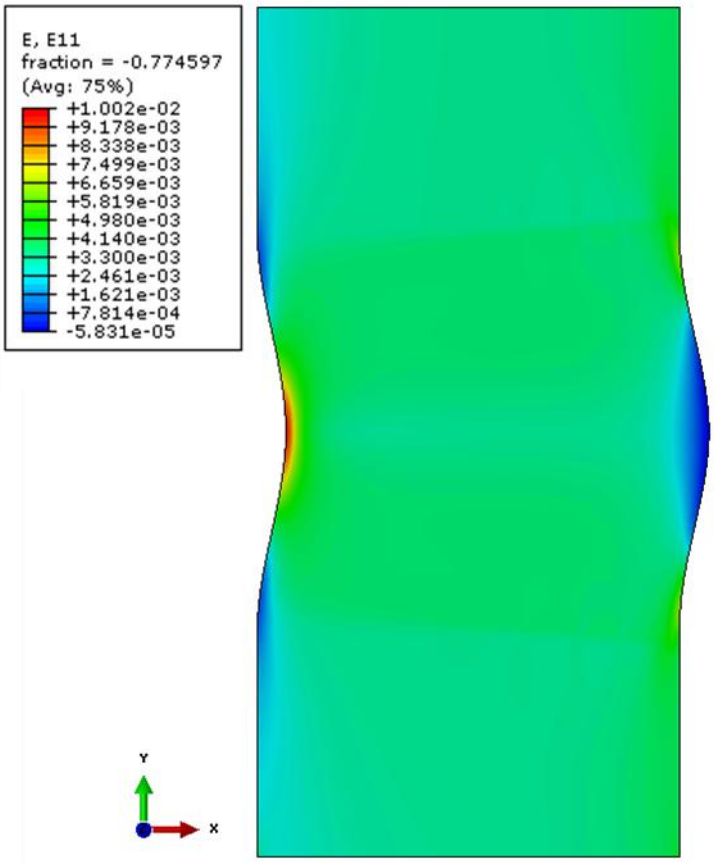

Figure 29: Axial strain distribution of a typical IP wave in tension indication minimal bending in the straight fiber area above and below the wave.

Several different ASTM standards were utilized for reference and for material property calculation definition. Material properties were calculated for each coupon and then averaged for each group. Where bending was found to be minimal enough to be disregarded, ultimate tensile or compressive strength was calculated:

$$F^{tu} = P^{max}/A \tag{1}$$

where F^{tu} is the ultimate tensile or compressive strength, P^{max} is the maximum load before failure, and A is the average cross sectional area. This equation was modified to

calculate the stress at each point (σ_i), necessary for plotting of stress-strain curves, by substituting P_i, the load at the *i*th point, for P^{max}. Similarly, ultimate shear strength was calculated for ±45° specimen:

$$\tau_{12}^{tu} = P^{max}/2A \tag{2}$$

where τ_{12}^{tu} is maximum in-plane shear.

Strain was calculated utilizing the DIC system based on the full field of the coupon such that it was calculated for the entire gage section shown in Figure 29. To ensure a consistent method that would allow for calculation for both unflawed controls and flawed specimens, strain was generalized for the entire gage length which was the same for all coupons. This allowed for consistent comparison given the different flaws, specifically the variation of fiber misalignment angles. It is worth noting that through each of the three rounds of the BMT the relation of strength and fiber misalignment angle was investigated. As suggested by Wang (2001), and further confirmed herein and by Riddle (2013), it was determined that regardless of amplitude and wavelength, ultimate strength and strain degraded as misalignment angle increased. In addition, waves with the same fiber misalignment angle, but different amplitude and wavelengths, were noted to have similar results. As such, this method of determining strain for the entire coupon field was justified for the analytical/experimental correlations performed herein since the same coupon geometry was utilized in all modeling efforts. This method of strain calculation was also utilized for the lateral strains which were then utilized with the longitudinal strains to calculate the Poisson's ratio of the unflawed controls.

Once both stress and strain were calculated, modulus of elasticity (E) was calculated for each specimen utilizing this data. Initial linear portions of each stress-strain curve (generally 0.1-0.3% strain) were chosen to ensure accuracy and consistency of the chord modulus utilized:

$$E = \Delta\sigma/\Delta\epsilon \quad (3).$$

Digital Image Correlation (DIC): A 5 mega-pixel Aramis digital image correlation system (Figure 30) was used to measure and to analyze the displacement and strain of the entire field for at least one representative sample of each specimen type (Aramis, v6.2). This system consisted of two cameras allowing for 3D stereographic measurement. A consistent measuring volume of approximately 175 mm by 150 mm was utilized with a relatively consistent depth since out-of-plane motion was minimal during these tests. As such, a set of 17 mm lenses were utilized and the resulting pixel size was approximately 0.005 mm2. Load data was recorded automatically from the load cell at a frequency of 5 Hz and tabulated by the system allowing for immediate analysis of stress and strain. Image capture rates were varied between 2 and 12 Hz throughout the testing. As noted above, strain analysis was performed for the full field and local points and cross-sections were analyzed where appropriate, though the full field results were found to be best for analytical/experimental correlations.

Figure 30: Aramis digital image correlation (DIC) system utilized during entire BMT effort (Aramis, v6.2).

Round 1 BMT Results and Discussion

Testing was performed on unflawed controls and flawed specimen of each type. Load data were obtained (Figure 31) from each test and were then utilized to calculate stress for each sample, while the DIC data were utilized to measure displacement and calculate strain. Initially, displacement data were gathered from the Instron's linear variable differential transformer (LVDT), but this data was found to be dubious. It appeared that the LVDT was influenced by elastic response in the entire system and varied by a factor related to load and stiffness of the specimen. While this factor could be

determined, it was deemed outside the scope of this work. Instead, the DIC data were utilized and within the Round 1 effort at least one data set was able to used to calculate the material properties discussed. However, it is important to note that while the original displacement data was dubious, the ultimate stress and load-displacement curves were consistent within each group where variations of peak stress and ultimate displacement were less than 8%. This consistency was noted to hold where multiple specimen were measured with the DIC and as such the baseline information data from this initial round of testing was deemed acceptable. In addition to load and displacement data, visual observations regarding damage and failure were noted, while DIC data were also used for damage and failure type correlation. Overall, increased severity of the flaw reduced ultimate load as seen in Figure 31.

Control

Tensile and compression tests were carried out on control 0° and ±45° laminates with no intentional defects introduced. Figure 32 shows the stress-strain curves used for correlation. The unflawed 0° coupons exhibited a nearly linear material response up to failure where testing was stopped in both tension and compression. However, ±45° coupons were initially linear before softening and some load redistribution took place. Testing was continued to ensure that the entire load redistribution phase was captured before complete failure.

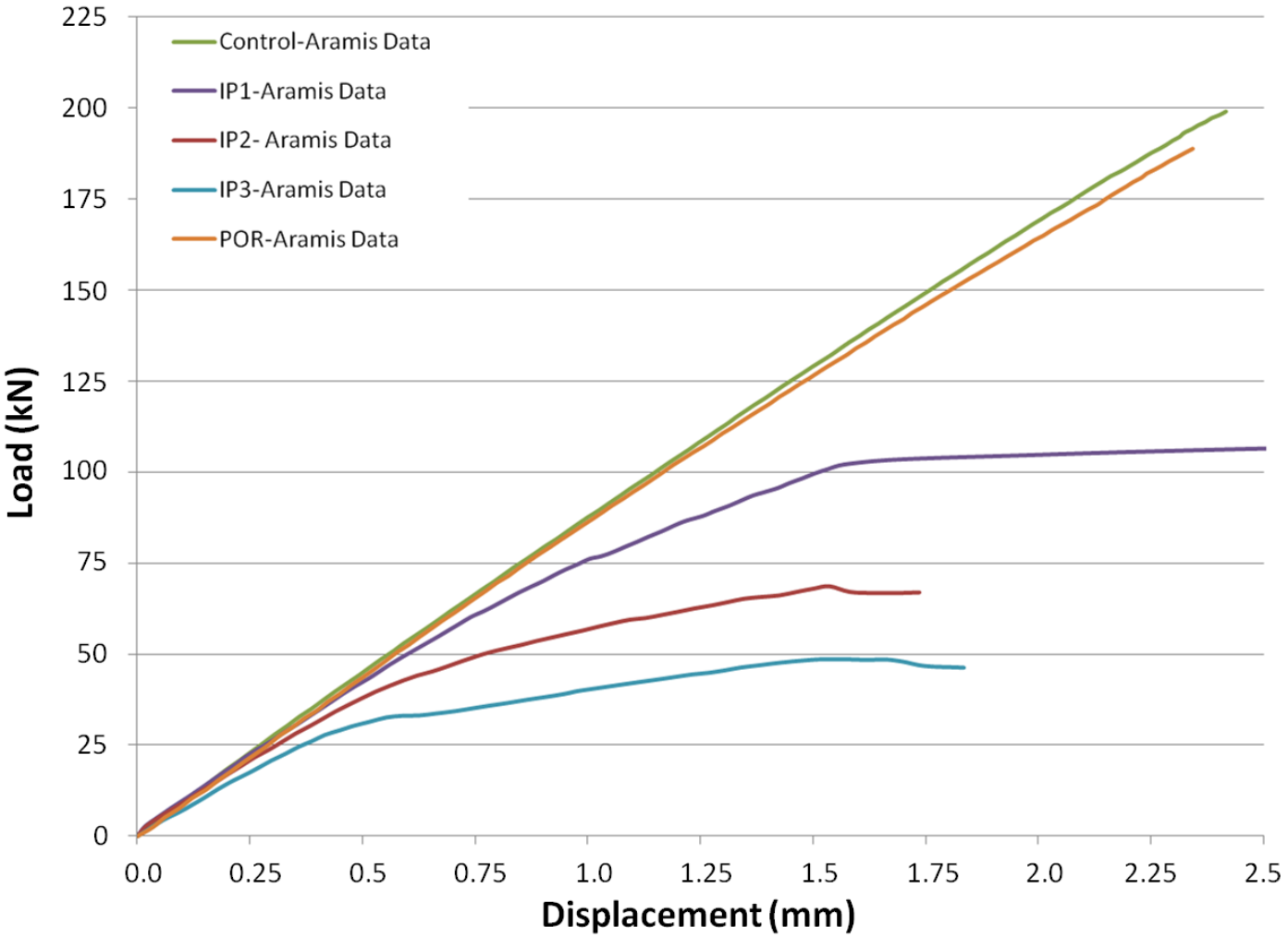

Figure 31: Load-displacement data taken from representative samples during BMT.

As outlined below in more detail, material properties were calculated and compared to the MSU-CMD. The data indicate that the highest strength was observed with the 0° tensile control group with an average of peak stress of 990 MPa while it was approximately 580 MPa for the 0° compressive group. Failures were initiated by matrix cracking followed by ply delamination, load redistribution and ultimately ply failure. Shear stress was approximately the same for both tension and compression at 112 and 124 MPa, respectively, as would be expected based on the observed matrix failures in the ±45° laminates. In addition, a representative sampling of results from the DIC and associated strain field of the 0° control is shown in Figure 33 below. This image shows the uniformity of the strain field on the surface of the coupon just prior to failure with some initial fiber breakage indicated by the small area of increased strain on the left of the lower edge.

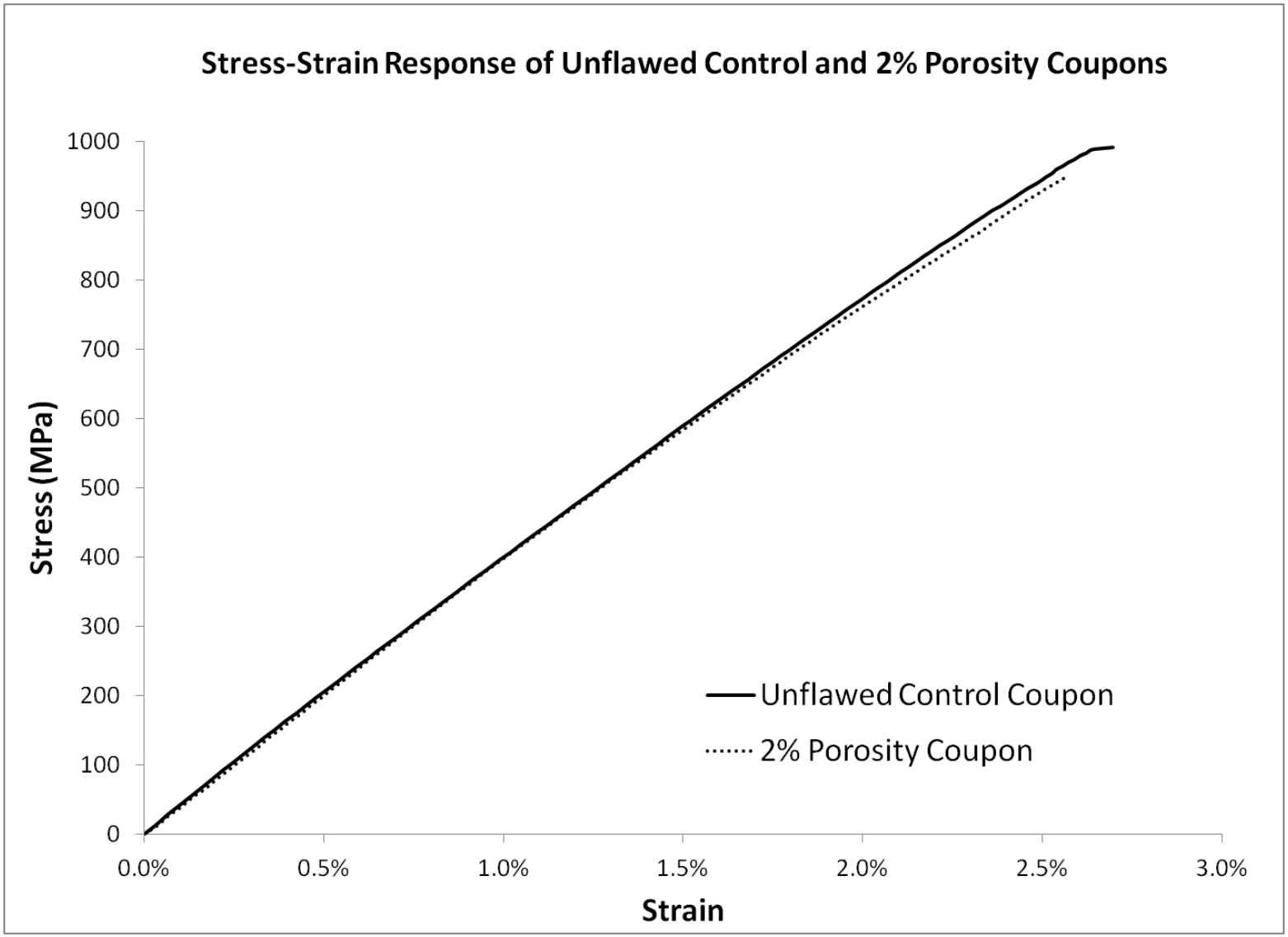

Figure 32: Stress-strain of unflawed control and 2% porosity coupons tension utilized for analytical/experimental correlations.

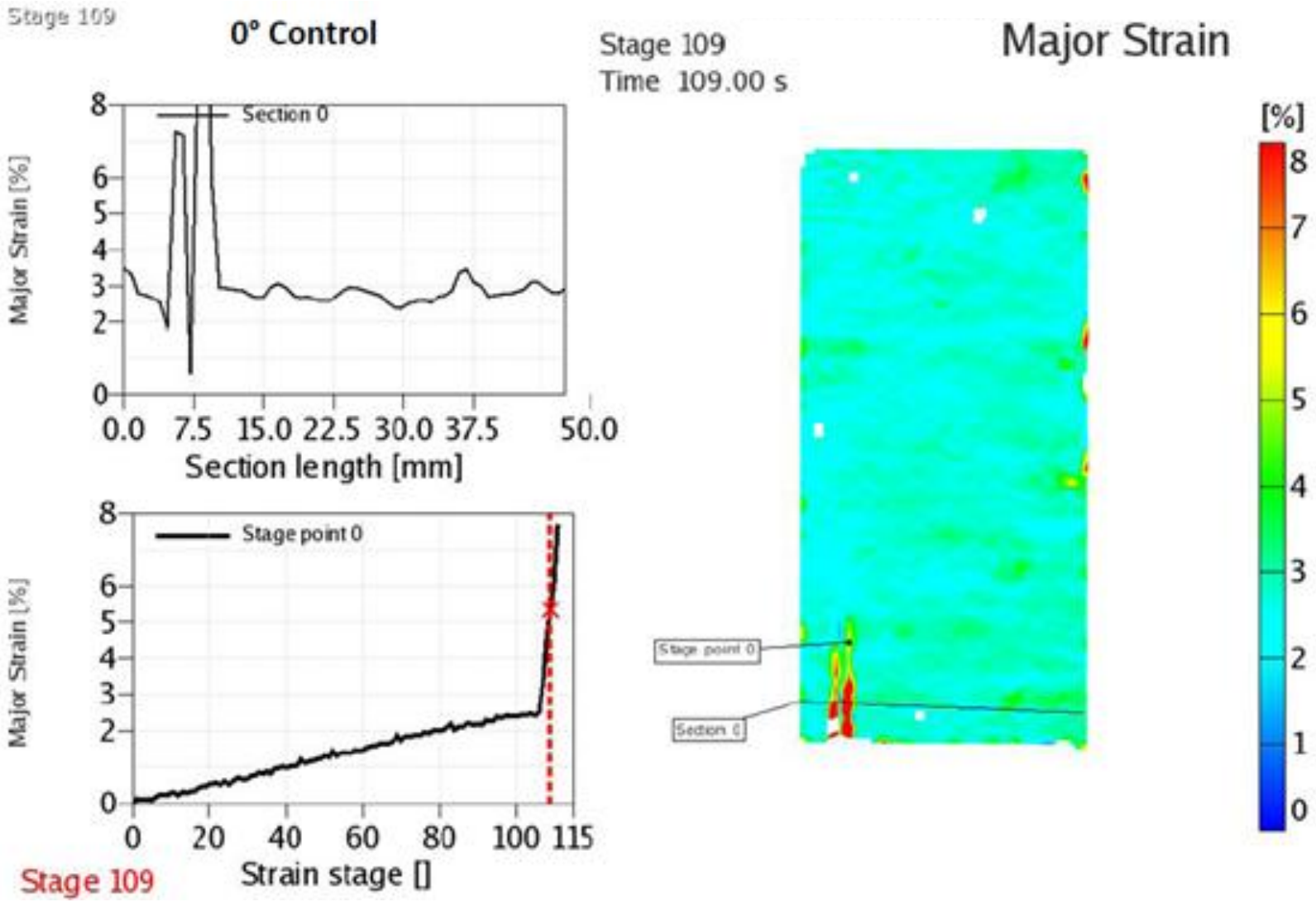

Figure 33: Representative images near failure of 0° control laminate tested in tension from the DIC system.

Comparison to MSU-CMD: Material properties for each coupon were calculated and averaged for each flaw group as noted above and are shown below in Table 3 and Table 4. Standard deviations are offered for ultimate stress to indicate the consistency of each test. However, since the accurate displacement data was limited, standard deviations are not offered for other properties as they would be meaningless with only one or two datasets per test group being gathered. Given this limitation and to ensure accuracy of these values, comparisons were made between the control results and the results of similar tests published in the MSU-CMD. In particular, modulus of elasticity and maximum strain were chosen as points of comparison as they were critical for analytical inputs and correlation.

An overview of comparisons of the MSU-CMD and BMT is shown below in Table 5. These comparisons indicated that while the material properties compare acceptably for tension, the compressive group failure strains from the BMT appeared dubious. This was likely due to the unrestrained method of testing in compression which resulted in bending and buckling in the BMT specimens. While the modulus values appeared to be reasonable in an initial response, the stress-strain curves overall showed an unlikely amount of softening when compared to similar material systems in compression. As such, the material properties from the MSU-CMD were utilized for analytical inputs where it was deemed crucial to have accurate data. These data were also used in initial comparisons to the unflawed controls.

It is worth noting that the DIC images did indicate that a small amount of bending was occurring in these unflawed control compression tests. However, much less bending

was noted in the flawed specimen, indicating that damage was occurring at the flawed area prior to bending occurring. While this bending was not eliminated completely, the reduction indicated that both these data and the flawed tension data may be utilized for the purposes herein and may be used as correlation points for the comparison of different analytical tools.

Porosity

Specimens containing porosity were analyzed with a scanning electron microscope (SEM) to determine the volume of porosity included, which was found to be approximately 1.8% (Figure 34) (Riddle et al., 2011). As noted in Table 3 and Table 4 above, samples with porosity were shown to have decreases in ultimate stress (84-94%) and strains at failure (82-98%) compared to the control samples. Confirmation of this result may be observed by comparing the control and porosity strain fields (Figure 34 and Figure 35) and the stress-strain curve shown in Figure 32 above, which indicate lower strains approaching failure. It should must be noted that unless otherwise identified, all images show 0° fibers in the vertical direction. Comparison of these two strain fields also appear to indicate that there are more concentrations of higher strain in the porous laminate. While these are likely to be associated with areas of increased porosity, further testing would require this association to be determined conclusively.

Table 3: Static properties for laminates tested in tension and calculated percentage of control laminates.

Tension	Control		Porosity		IP 1		IP 2		IP 3		OP 1		OP 2A		OP 4A	
	0°	±45°	0°	±45°	0°	±45°	0°	±45°	0°	±45°	0°	±45°	0°	±45°	0°	±45°
Ultimate Stress (MPa)	990	112	950	103	521	108	344	109	226	107	417	84	742	101	752	102
Standard Dev	(40)	(2.0)	(19)	(1.5)	(24)	(4.1)	(43)	(1.1)	(24)	(4.7)	(26)	(5.3)	(79)	(2.2)	(43)	(2.8)
% Control	--	--	96%	93%	53%	97%	35%	98%	23%	96%	42%	75%	75%	91%	76%	91%
Strain at Failure (%)	2.64%	2.61%	2.54%	3.32%	1.66%	3.23%	1.66%	3.07%	1.66%	2.41%	4.77%	4.91%	4.92%	4.06%	4.56%	4.43%
% Control	--	--	96%	127%	63%	124%	63%	118%	63%	92%	181%	188%	186%	156%	173%	170%
Modulus of Elasticity (GPa)	41.1	16.2	39.6	16.6	39.6	18.7	34.8	16.8	24.1	16.6	17.3	5.9	30.8	16.1	31.2	15.3
% Control	--	--	96%	103%	96%	115%	85%	104%	59%	100%	42%	36%	75%	100%	76%	94%
Poisson's ratio	0.27		--		--		--		--		--		--		--	

Table 4: Static properties for laminates tested in compression and calculated percentage of control laminates.

Compression	Control		Porosity		IP 1		IP 2		IP 3		OP 1		OP 2A		OP 4A	
	0°	±45°	0°	±45°	0°	±45°	0°	±45°	0°	±45°	0°	±45°	0°	±45°	0°	±45°
Ultimate Stress (MPa)	582	124	491	125	257	165	216	181	216	139	95	43	227	90	207	86
Standard Dev	(28)	(1.2)	(20)	(1.5)	(23)	(2.8)	(10)	(5.0)	(9.0)	(3.0)	(13)	(2.1)	(3.4)	(7.5)	(5.7)	(0.78)
% Control	--	--	84%	101%	44%	133%	37%	147%	37%	112%	16%	35%	39%	72%	36%	70%
Strain at Failure (%)	1.76%	1.16%	1.44%	1.06%	0.84%	0.59%	0.84%	0.51%	0.92%	0.82%	0.70%	1.11%	1.04%	0.94%	0.92%	0.84%
% Control	--	--	82%	91%	48%	51%	48%	44%	52%	71%	40%	96%	59%	81%	52%	72%
Est. Modulus of Elasticity (GPa	37.2	15.5	36.5	16.4	34.2	25.4	30.9	28.7	29.4	19.7	8.2	4.5	23.1	12.4	23.4	11.9
% Control	--	--	98%	106%	92%	164%	83%	185%	79%	127%	22%	29%	62%	80%	63%	77%
Poisson's ratio	0.28		--		--		--		--		--		--		--	

Table 5: Comparison of control BMT results to published MSU-CMD results in tension and compression. (* indicates exact material match not available and a similar material system used.)

Test	Tension				Compression			
Material Orientation	0°		±45°		0°		±45°	
Data Source	CMD	BMT	CMD	BMT	CMD	BMT	CMD	BMT
Modulus of Elasticity (GPa)	41.1	40.6	14.9	16.2	38.4*	37.2	14.4*	15.5
Strain at Failure (%)	2.7	2.6	2.9*	2.6	2.4	1.8	1.6	1.6

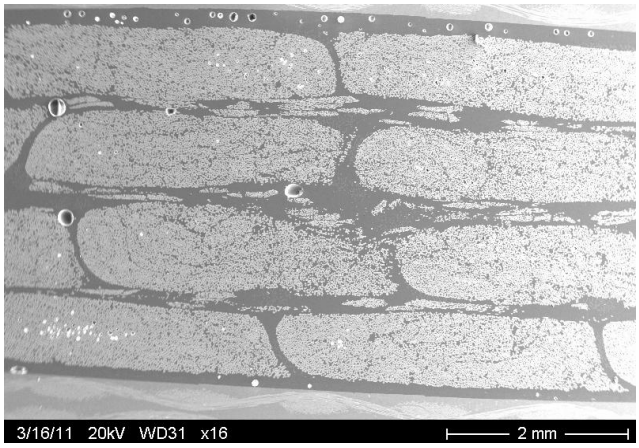

Figure 34: Scanning electron microscopy (SEM) image of porosity sample tested.

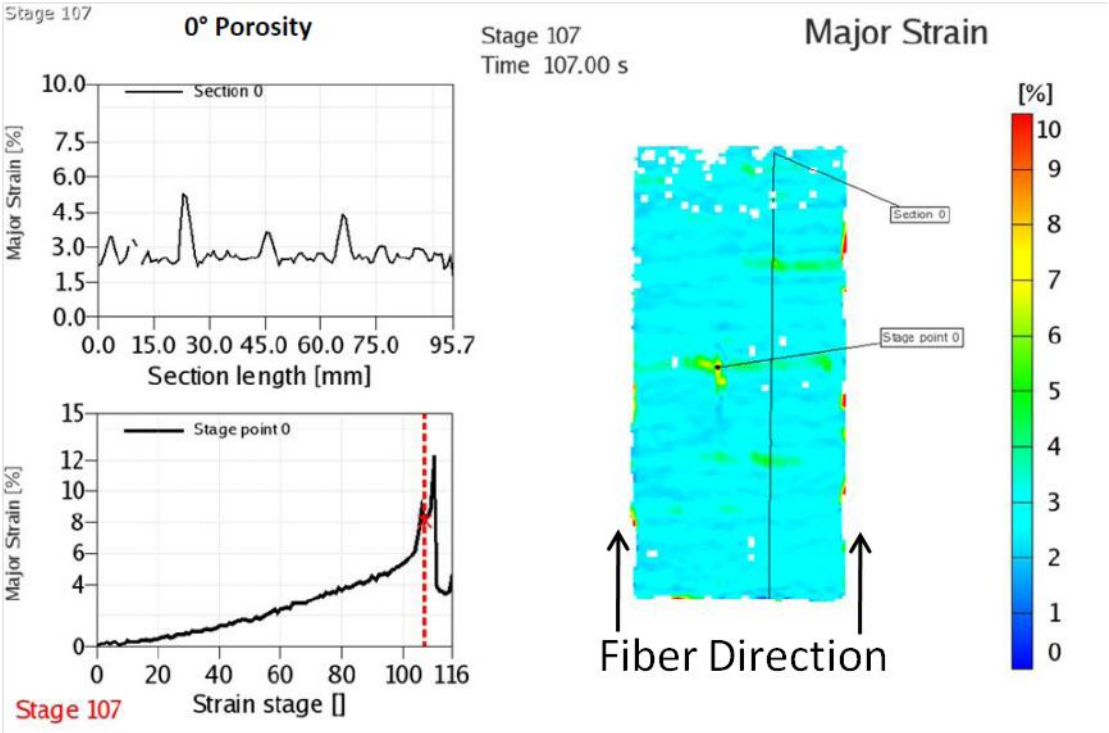

Figure 35: Representative DIC image near failure of 0° porosity laminate tested in tension.

The exception to the observation of reduced ultimate stress was the ±45° group. when tested in compression, which was found to be higher in ultimate stress (101%) even though the strain at failure was reduced (91%). Also of interest was the observed increase in estimated modulus of elasticity for both ±45°groups (103-106%) compared to the control. This increase indicated that shear failure occurred prior to the cracks that are likely to originate and propagate throughout included pores. Or the increase could indicate that the stiffness was increased due to the resin's increased brittleness with increased porosity as noted above (Judd, 1978). While these initial findings were of interest and appeared to agree with previous results where applicable, additional testing at various porosity levels was deemed necessary for the later rounds to determine critical levels of porosity. It must, however, be noted that these data conclusively state that approximately 2% porosity did decrease results with both a 6-16% strength decrease and a 2-18% reduction in the strain at failure. These conclusions were in agreement with previous research noted above. Further, the decrease in strength and increase in modulus of elasticity for the ±45° compression groups did not appear to differ enough from the control groups to warrant further testing. As with the other groups tested, these ±45° groups tended to fail from edge effects resulting negligible differences in material properties from control groups.

IP Wave Results

Test results for the IP wave groups are also noted in Table 3 and Table 4. Results from test observation and the DIC suggest that each of the IP wave groups was noted to have similar damage progression (Figure 36). First failures were noted in areas where

fibers were not continuous through the length of the sample. Through further review of the test data, images, and digital image correlation data, it was apparent that initial damage occurred in each wave at low loading levels on the ends of the samples where fibers ended on the coupon edge (Figure 37). Due to the wave pattern introduced when the samples were cut to make the coupon specimen, fibers through the wave were cut resulting in discontinuous fibers along the sample edge where initial failure was noted (Figure 38). As strain levels increased, cracks initiated in the resin between the tows of the wave before delaminating and progressing through the entire wave section, and they ultimately resulted in fiber failure. These matrix cracks were noted to start at the point there the fiber appeared to be at the largest misalignment angle. The DIC images indicated that the strain accumulated in the wave area progressing transversely from the angled fiber toward the peak of the wave. Fiber breakage appeared to initiate at the point where the strain accumulations from each side of the wave met. These observations combined with the strains at failure indicate that damage accumulation was at lower strains than the control group and was the result of shear in the area of the wave. As noted and detailed below, the amount of shear was directly related to the magnitude of the fiber misalignment angle.

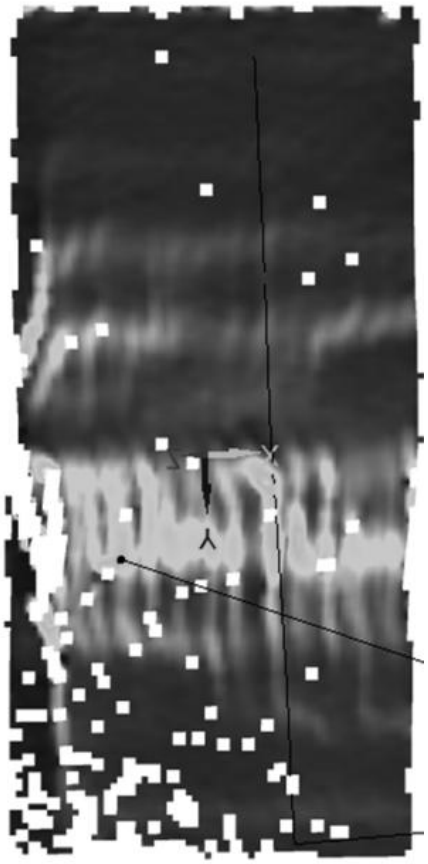

Figure 36: DIC image of initial matrix cracking of 0° (vertical) fibers with IP wave shown below in Figure 37 in tension with distinct strain perturbation around wave.

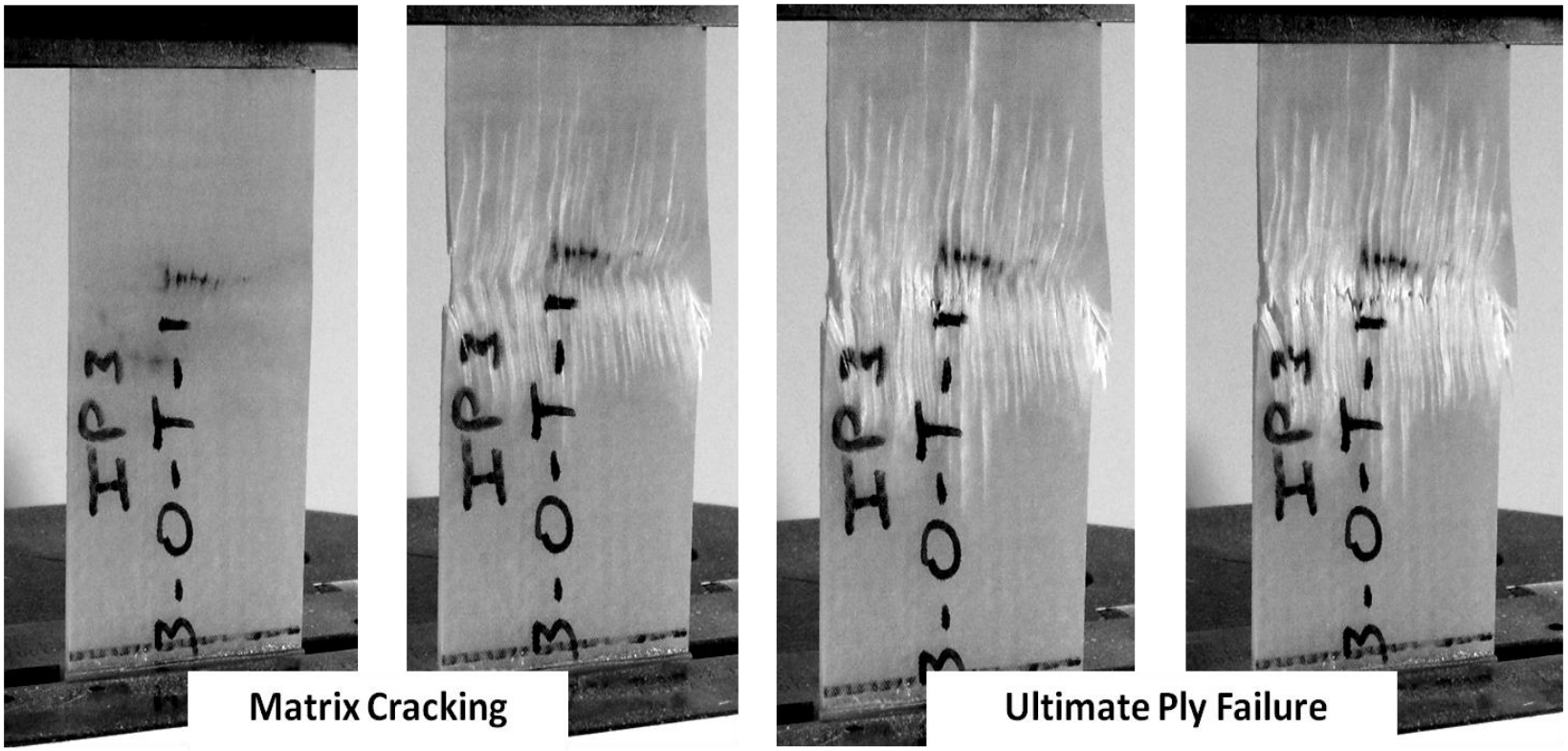

Figure 37: Damage progression of IP Wave 1 with initial damage accumulating at the areas where fibers are not continuous through the length of the sample.

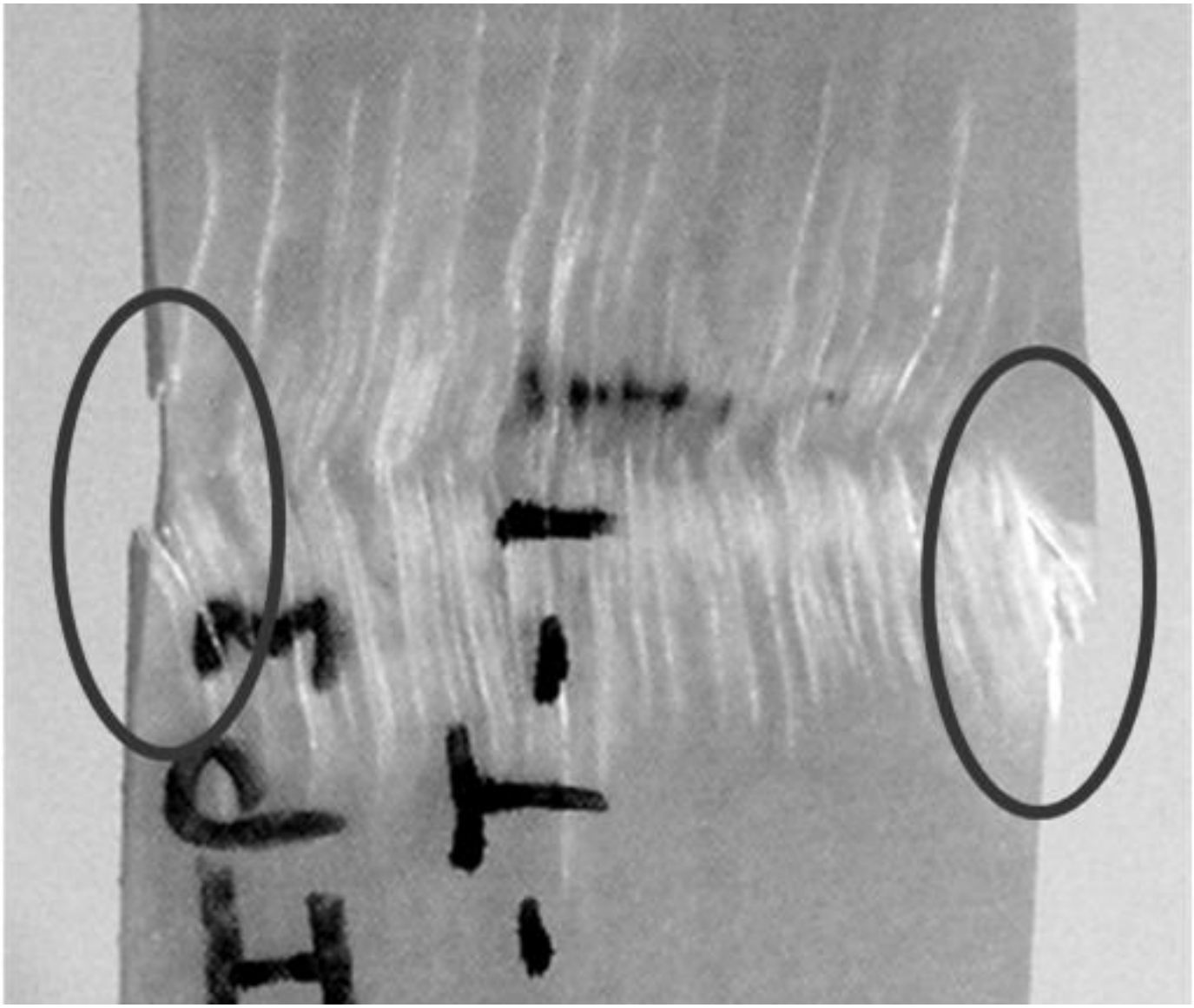

Figure 38: Close up of Figure 37 showing initial failures were noted at the edges were fibers were discontinuous as circled.

Ultimate stress values for the each of the 0° IP wave groups tested in tension were found to have a significant decrease in ultimate stress: 54% down to 25% of the control for waves IP1 through IP3, respectively. As noted in Table 1, the amplitude and wavelengths for each of these waves varied, and even though IP1 had the highest ultimate stress, it also had the largest amplitude. Furthermore, IP2 has larger amplitude and wavelength than IP3, while the ultimate stress for each was approximately the same, though IP2 had a larger strain at failure than IP3. Based on previous research, similarity of the results was expected between the IP2 and IP3 groups, as the fiber angles were similar in the two groups.

It is also interesting to note that the stiffness for these groups was 85-96% of the control. Thus, initial stiffness was similar to the control even though the ultimate stresses and strains were notably lower. This was likely due to the load matrix "locking" the fibers into place at the ends of each wave before the matrix cracking noted above. Very similar results and trends were also noted for the 0° IP wave groups tested in compression. Overall, IP waves resulted in reduced material properties when included in 0° laminates.

The ±45° groups tested in tension were noted to have a similar damage progression as the 0° wave groups as noted in ultimate stress values very similar to the control group (96-98% of control) and the strains at failure were found to be relatively consistent with the control (92-112%). Of note was the stiffness increase compared to the control group (103-115%), likely for the same reasons given for the 0° IP groups noted above, which resulted in significantly lower values for Poisson's ratio. The

±45°compression results were rather remarkable, as the ultimate stress for all IP wave groups was significantly higher compared to similar control groups (127-185%) even though strains at failure were lower (48-52%). This resulted in significantly stiffer ±45° laminates causing a negative Poisson's ratio for the IP wave groups in compression. These results are due to the increase load-carrying ability of the laminates caused by the fibers in the wave approaching 0°. However, both IP2 and IP3 had the same fiber angle though the ultimate stresses in each were different: 181 and 139 MPa, respectively. This difference may be from unexpected responses during manufacture that resulted in differences between initial imparted amplitudes, wavelengths, fiber angles, and the fiber content of the final laminate. Variation of these parameters was confirmed by Riddle et al. (2011) through the non-destructive testing of these coupons. In short, while properties decreased in 0° laminates including IP waves, laminates including ±45° performed as well or better than control, eliminating the need for further analysis. In addition, these data offer reasonable convergence points for the analytical models efforts as discussed and compared in following chapters.

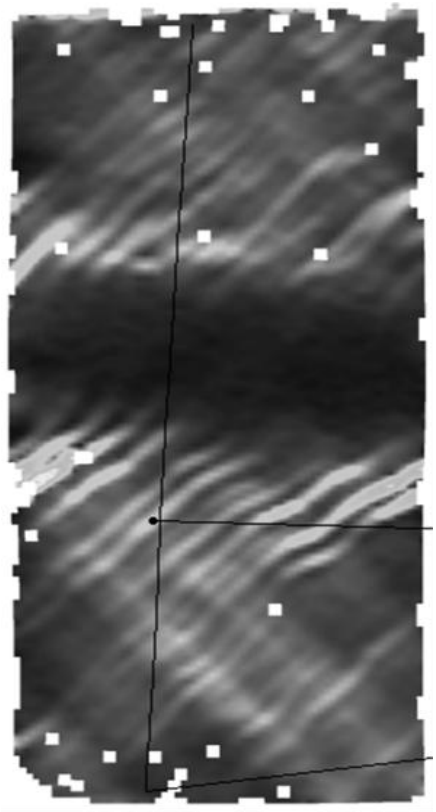

Figure 39: DIC image of ±45° IP wave specimen in tension with similar strain perturbation as Figure 36.

Variations in IP Wave Laminates: As reported by Riddle et al. (2011), there was variation of the IP waves included in each of the four layers of the coupons tested. A medical imaging CT scanner was used to generate three dimensional renderings of test specimen, allowing for precise measurement of the actual flaw geometry introduced into the coupons. This measurement allowed for an understanding of the exact flaw tested. It was of critical importance to have accurate measurements of the introduced flaws in developing analytical/empirical damage correlations. For example, waves may be measured on the surface, but there was no guarantee that the sub-surface layers contained a flaw with the same geometry. As shown in Figure 40, not only did the sub-surface

layers have varying geometries, but the peaks of the wave, as indicated by the dotted purple line, also were not aligned. In order to best approximate the wave pattern for each coupon, Riddle et al. took the average amplitude, wavelength, and fiber misalignment angle for each of the layers to be used as inputs for analytical modeling efforts described herein. These data were then used to determine the average off-axis fiber angle for the entire laminate which was the parameter utilized in all models below.

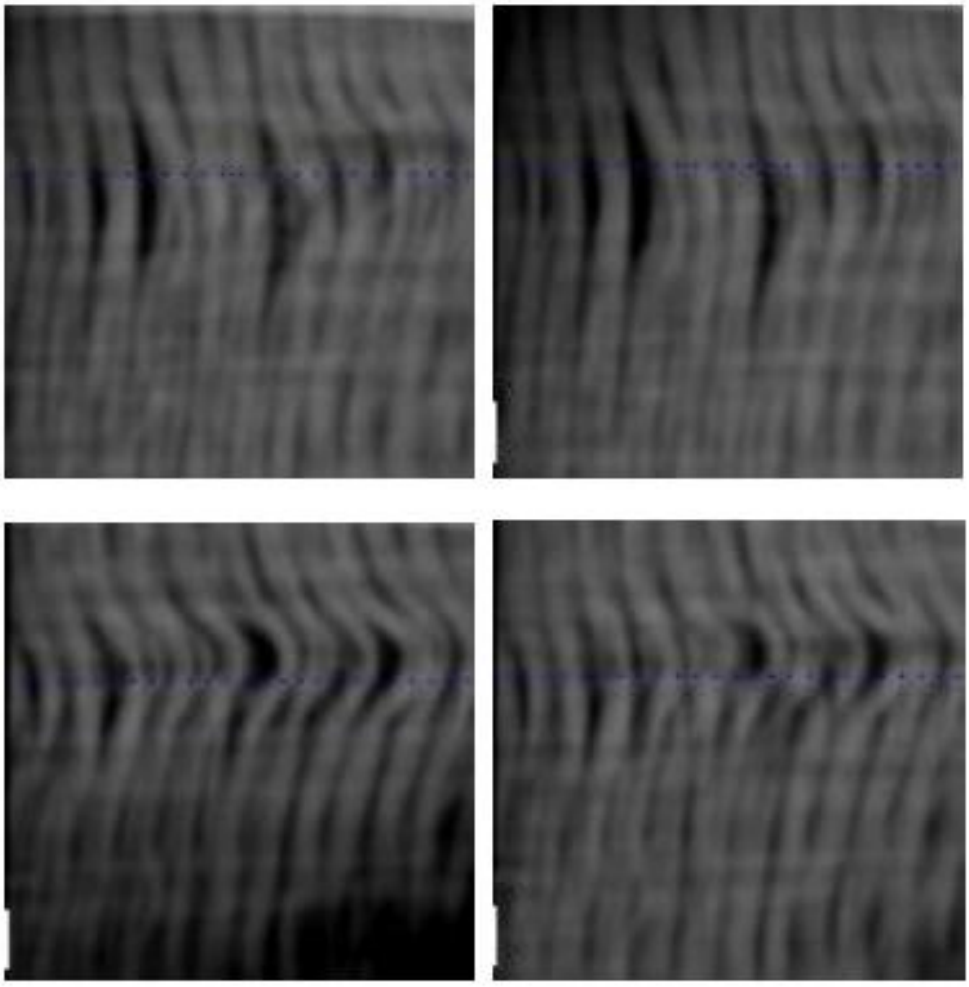

Figure 40: Each of the four layers of an as-tested IP wave with variations in geometry and alignment.

Baseline Correlation Justification: It is important to note that among several conclusions, Riddle (2013) was able to conclude that the fiber misalignment angle for waves was the critical parameter for ultimate strength degradation. In short, there were direct correlations to decreases in strength with increases in fiber misalignment angle. Based on this conclusion, and to assure compatibility, the fiber misalignment angle parameter was utilized throughout. Considering the variations noted in the coupons, the values listed in Table 1 were updated as shown for the each model of the IP wave 1 case that has been utilized as the baseline correlation model below. As seen in Figure 41, this particular wave offered consistent results through this BMT effort when the raw load-displacement data are compared.

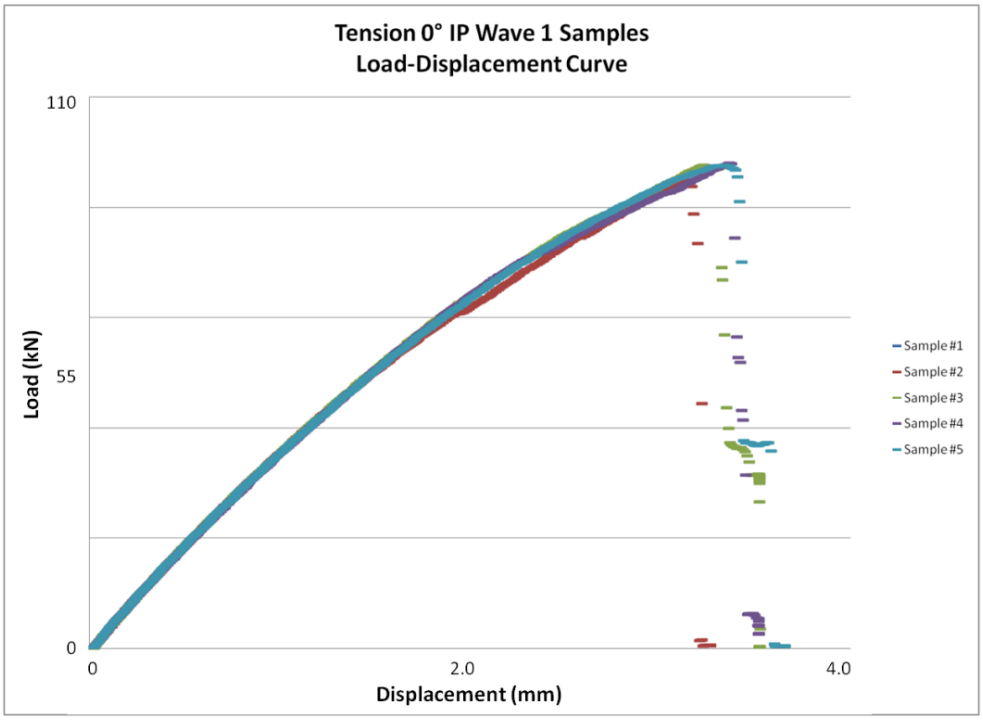

Figure 41: Load-displacement data from all Round 1 IP wave 1 coupons.

As noted above, these displacement data were taken with the LVDT and include any displacements in the entire testing system. While these displacements are not accurate enough for calculating strain, they are useful in determining consistency of the data for this particular flaw. Variation for each specimen was determined by calculating the standard deviation of peak stress and associated strain for each flaw case. The strain variations were then adjusted by the ratio of DIC strain to LVDT strain. As such, a variation for tension of ±0.15% strain and ±58 MPa was determined comparing values at peak stress based on the variability noted in these data. This variability is noted in Figure 42 below with windows indicating the associated variability of stress and strain for each case. Similar calculations were performed for all cases and were found to be within the 10% acceptance criteria noted in the systematic approach utilized noted above and as such are not shown in the correlations below.

In addition to the consistency of the results, the IP wave 1 case had decreases in material strength, and significant degradation was noted, making the result that this case was optimal for baseline use. Further, it was decided that since this case had a fiber misalignment angle close to 30°, it would be a good median case and allow for variations to approximately 15° and 45° following the systematic approach. The resulting stress-strain curves, utilizing the DIC data from this test group, for this IP wave case in tension and compression are found below in Figure 42. Data beyond failure and maximum stress was gathered to begin to establish a material understanding that may be applied to future work with larger substructures and structures. While only this one data set was initially available from the Round 1 effort, confirmation of these results was achieved in Round 2

as outlined by Riddle (2013). As such, this geometry and these results were utilized as the baseline model for experimental/analytical correlation of each modeling type outlined below.

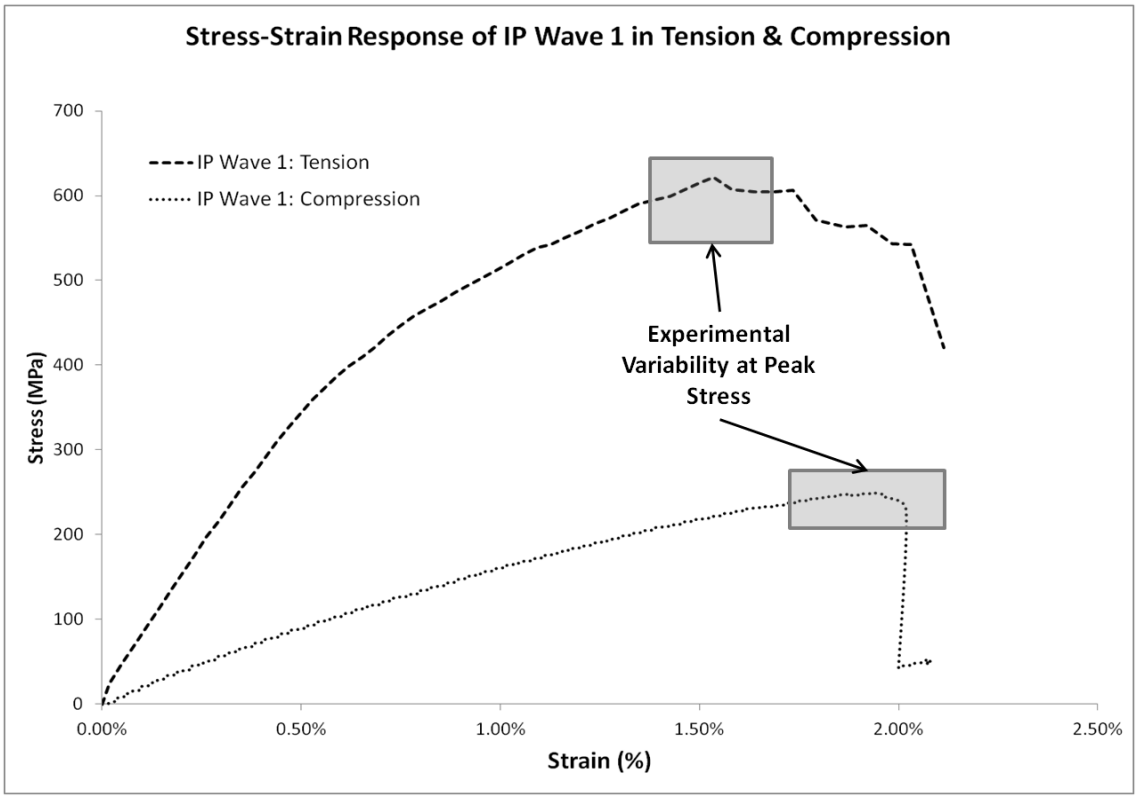

Figure 42: Stress-strain of IP Wave 1 in tension and compression utilized for baseline model correlations with associated experimental variability.

OP Waves Results

Test results for the OP wave groups are also noted in Table 3 and Table 4 above. Results from test observation and the DIC suggest that each of the OP wave groups was noted to have similar damage progression. Also like the behavior of IP waves, as strain levels increased, cracks initiated in the resin between the layers at the ends of the wave before delaminating. However, unlike the behavior of IP waves, after delamination and

significant fiber straightening, the failure area for the OP wave specimens was concentrated at the peak area of the wave. This was due to the fibers being pulled straight and the center of bending being at the peak of the wave. It must be noted that the wave forms for all of the OP wave 1 group delaminated during testing. This resulted in an extreme decrease in the ultimate stress and stiffness results of the OP1 groups in both tension and compression. As such, OP wave 1 was deemed unusable for correlation in both tension and compression.

The two other cases, OP wave 2A and OP wave 4A, were found to have a more consistent response. Ultimate stress and strain at failure values for the OP wave 2A and OP wave 4A 0° and ±45° tension groups were decreased compared to the control but were increased compared to the IP waves. Thus, moduli of elasticity values were similar to the control due to load being transferred more consistently through the wave than seen with IP waves due to the configuration described above. Given the consistency of these waves in tension, the OP wave 4A case was utilized for correlation. However, compression testing of the OP waves proved to be very difficult, as large wavelengths necessitated a long unsupported gage length. This resulted in significant bending as the load transferred through the wave. As such, significant decreases in calculated moduli of elasticity, ultimate strength, and strain at failure were noted and results were considered unusable for correlation given these responses.

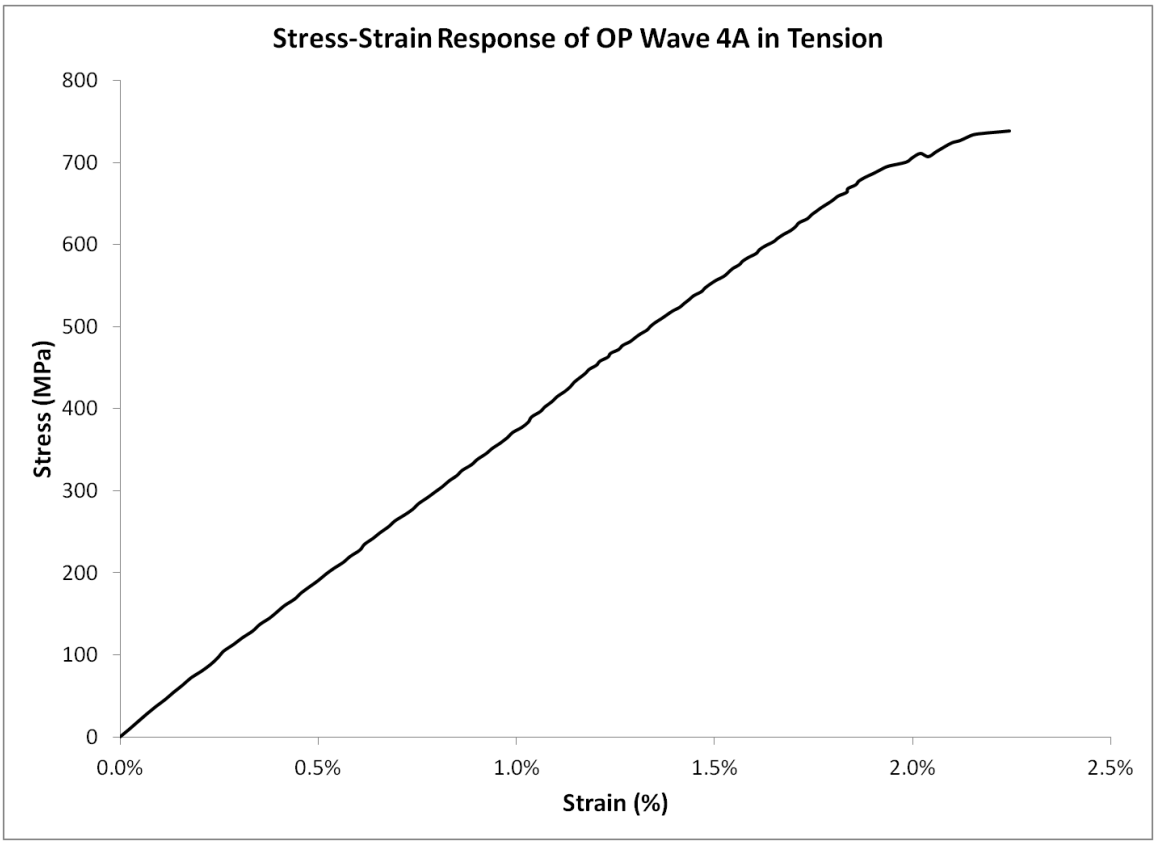

Figure 43: Stress-strain of OP Wave 4A in tension utilized for initial OP wave model correlations.

Physical Testing Conclusions

Static test results have been presented from approximately 150 tests including four test groups, each of different defect type, in both tension and compression (Table 2). Testing parameters for each of the defect types were determined as part of the Flaw Characterization study and were representative of wind turbine blade laminates with scaling as necessary for coupon level testing. In general, the static testing performed has allowed for initial analysis and will allow for convergence points for initial analytical models. Use of the DIC system allowed for confirmation of the calculated strain and

damage progression through strain field measurement during testing. Damage progression was found to vary for each defect type, but was found to generally involve matrix cracking, ply delamination, load redistribution, and ultimately ply failure.

More specifically, the following items were observed and concluded from this portion of the BMT:

1. Porosity was found to have a similar decrease in tensile strength (93% of control) compared to previous research even though this previous research was not performed utilizing specific wind turbine blade materials.
2. IP waves included in 0° laminates resulted in decreasing tensile properties (54-25% of control) as fiber misalignment angle increased due to increased shear response.
3. IP waves in ±45° laminates indicated an increase in compressive strength (112-133% of control). This observation may be due to the fibers in the wave approaching 0° and, therefore, gained an increased load-carrying ability.
4. OP testing was hampered by asymmetry and delamination of the wave forms utilized; however, the data confirmed similar associations between strength and fiber misalignment angle.
5. Strength decreases (74-25% of control) with the increase of fiber misalignment angle (9-48°, respectively) within 0° laminates.
6. Due to the strengths remaining static or increasing, the ±45° groups may be excluded from further testing.

7. Independently amplitude and wavelength are insufficient for wave characterization.
8. When compared to MSU-CMD, some variations did exist, and the MSU-CMD data were utilized for unflawed controls in compression. Otherwise, all data appear consistent and reasonable to be used for the purposes herein.

Multi-Angle Laminate Physical Testing and Results

As an add-on to the Round 1 testing, Multi-Angle Laminate (MAL) testing was performed to enable analytical and experimental correlation with a more complex load-displacement curve. In short, the more complex laminate would likely have more damage accumulation through the test and would require a higher level of accuracy from associated models. While this testing was not originally planned, it was determined that this additional testing was necessary to ensure the linear elastic model stiffness validation in Chapter 4 was effective.

MAL Tension Results and Discussion

Tensile tests were carried out on MAL's with fiber orientation of [0°, +45°,-45°,0°] with no intentional defects introduced. Material properties were calculated as outlined by ASTM D 3039 which was used as a guideline for this testing and resulting analysis. Similar to BMT above, modulus of elasticity was calculated and compared to similar material lay-ups in the MSU-CMD: 33.2 and 32.1 MPa, respectively. In addition, maximum strain values were compared and found to be 2.6% and 3.0%, respectively.

Peak load and strain-at-failure was fairly consistent for each specimen, with differences of approximately 3% and 12%, respectively. The peak average stress of approximately 561 MPa was lower than 990 MPa noted in the BMT above. This is easily explained with the change to the Multi-Angle laminate from the uni-directional laminate used in the BMT. In conclusion, these data appeared reasonable and sufficient for the purpose of providing additional unflawed data for correlation and thus, further discussion of these salient observations may be found below within the Chapter 4 analytical/experimental correlations.

MAL Compression Results and Discussion

Based on the same logic for performing the tensile tests above, compressive tests were carried out on MAL's with fiber orientation of [0°, +45°,-45°, 0°] with no intentional defects introduced. Material properties were calculated as outlined in several ASTM standards that were used as guidelines for this testing and resulting analysis. Similar to BMT above, modulus of elasticity and average maximum strain were calculated; 33.0 MPa and 1.32%, respectively. Direct material comparisons were not able to be made due to lack of compression testing of a similar laminate within the MSU-CMD. However, when these values are compared to tension values noted above, similar trends are observed between this material system and others within the MSU-CMD. In short, between tension and compression, stiffness values are very similar. The maximum strain values in compression were found to be approximately 60% of the maximum strain in tension, comparing absolute values, while in this case it was found to be 51%. However, maximum strains in compression were noted within the MSU-CMD to vary as

much as 26% within the same material system due to inherent difficulties in compression testing of composite materials. While the strain value appears to be slightly low, it does appear reasonable when compared in this fashion. Peak stress and strain-at-failure were fairly consistent, with differences of approximately 3% and 12%, respectively. Likewise, the peak average stress of approximately 312 MPa was lower than 582 MPa noted in the BMT above. This is easily explained with the change to the Multi-Angle laminate from the uni-directional laminate used in the BMT. Below, Figure 44 confirms the same two variations from the uni-directional tests in BMT: a small increase in softening up to failure and then, a short load redistribution before ultimate failure. Similar to the tensile tests, a damage progression section was noted in the curves between the initial failure and the ultimate failure, allowing for more accurate assessment of experimental and analytical convergence. As with tension above, these data appeared reasonable and sufficient for the purpose of providing additional unflawed data for correlation and thus, further discussion of these salient observations may be found below within the Chapter 4 analytical/experimental correlations.

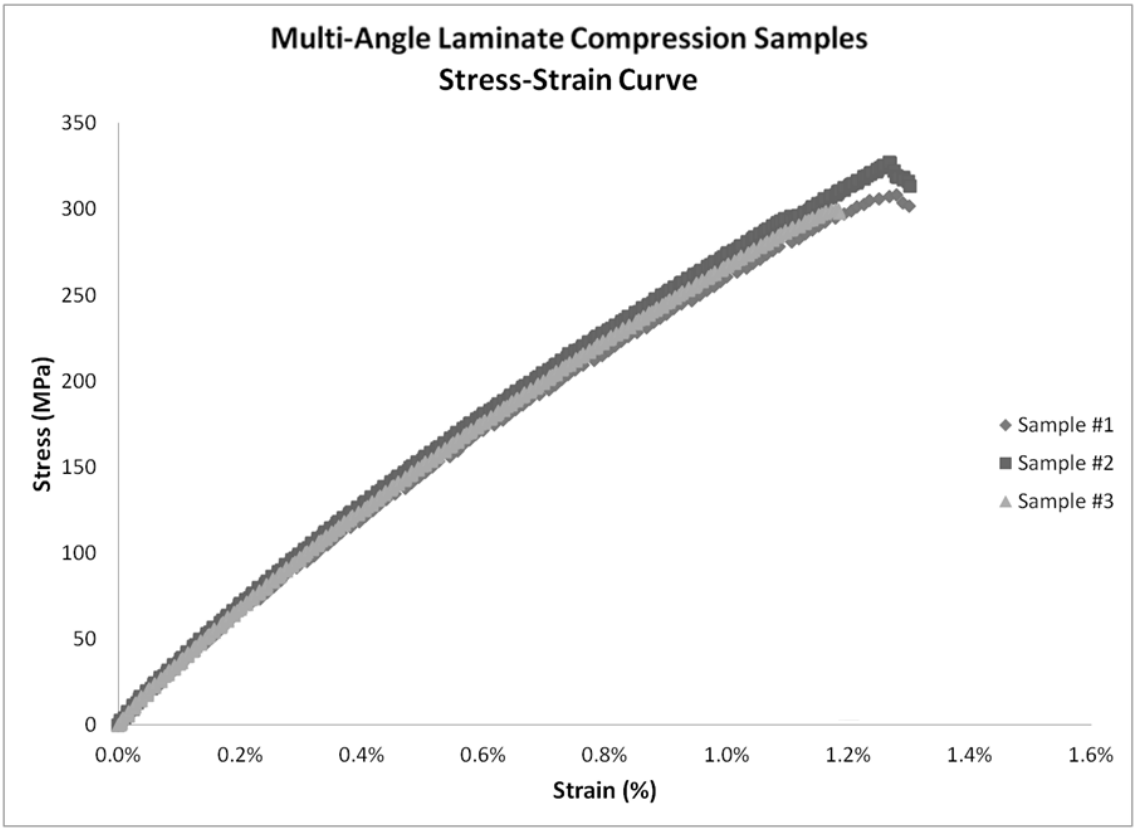

Figure 44: Multi-Angle laminate compression testing stress-strain curves.

Delamination Testing Results and Discussion

As noted above, delamination damage analysis of composites is common and widely performed due to much lower strengths compared to in-plane strength. Failure occurs as the result of delamination, which must be considered as part of an accurate analytical tool. This is especially true for discrete damage modeling where cohesive elements are placed between layers so that crack propagation may occur not only within the layer but also between layers. This discrete approach is discussed in more detail below. Also as noted above, double cantilever beam (DCB) and end notched flexure

(ENF) tests were performed to determine critical strain energy release rates in Mode 1 and Mode 2, respectively.

An increasing crack resistance behavior was noted due to fiber bridging as the crack propagated through each sample (Table 6). This result was due to secondary cracking and fiber bridging consistent with previous testing found in the MSU-CMD. Only initial cracking was considered for ENF testing, and these values are found below in Table 7. Representative load-displacement curves may be found below (Figure 45 and Figure 46). Initial values are fairly consistent and appear reasonable for use in delamination prediction in modeling efforts as outlined below. Data were collected utilizing a primarily 0° uni-directional material to attain the lowest possible values for G_{Ic} and G_{IIc}. Thus, results were conservative when applied to cases with other level associated fiber angles. These data correlated well with MSU-CMD published values and were utilized in complex modeling efforts for analytical/experimental correlation, specifically for discrete damage modeling as outlined further below.

Table 6: Mode I critical strain energy release rate determined from DCB testing.

Sample	Initial GIc	Secondary GIc	Final GIc	Units
DCB_01	295	506	720	J/m^2
DCB_02	287	651	854	J/m^2
DCB_03	320	659	843	J/m^2
AVERAGE	301	605	806	J/m^2

Table 7: Mode II critical strain energy release rate determined from ENF testing.

Sample	GIIc	Units
ENF_01	1321	J/m^2
ENF_02	1883	J/m^2
ENF_03	1367	J/m^2
AVERAGE	1524	J/m^2

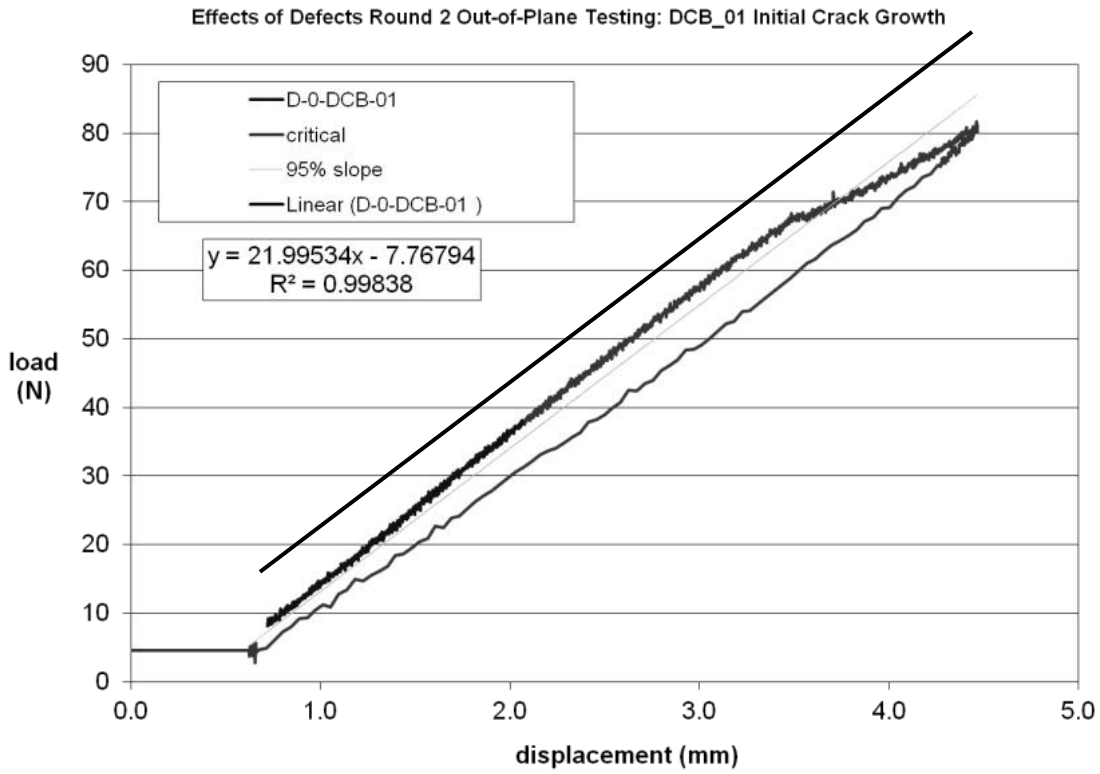

Figure 45: Representative load-displacement results from a Double Cantilever Beam (DCB) test during initial crack progression.

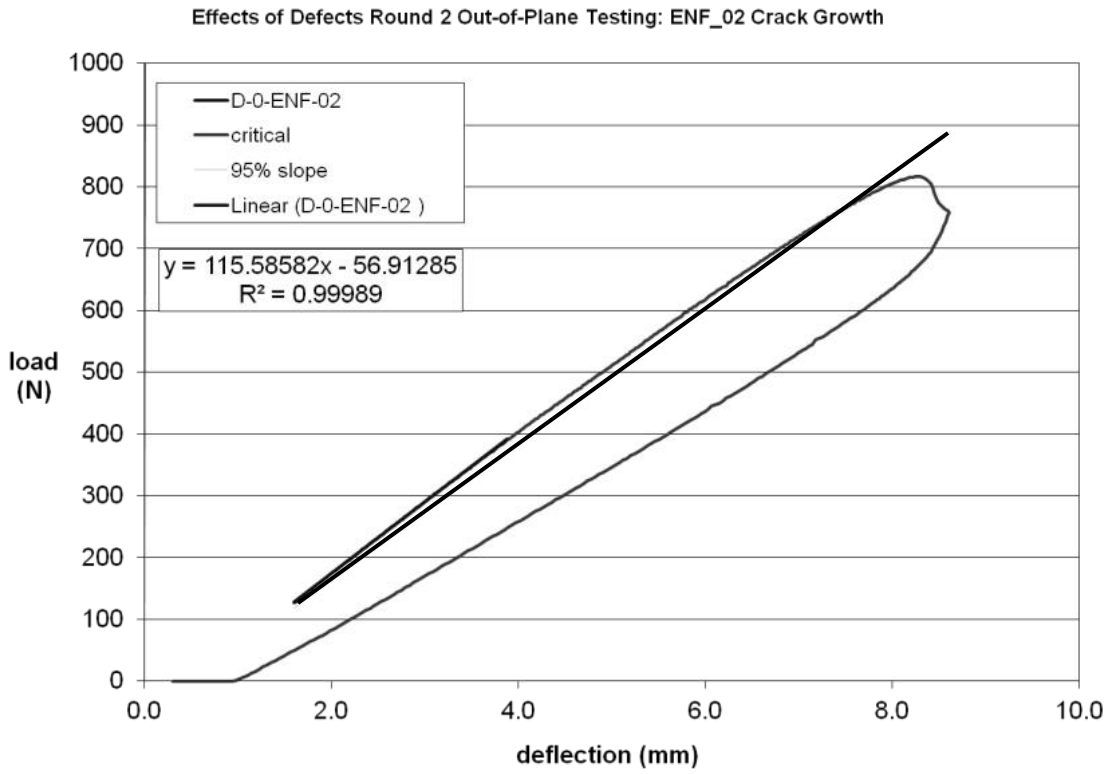

Figure 46: Representative load-displacement results from a End-Notch Flexure (ENF) test during crack progression.

Round 3 BRC Validation Blades

Two complete 9 m blades were manufactured under the Validation Blade subtask of the BRC. As eloquently outlined by Rumsey, these two blades were manufactured at TPI Composited, Inc., located in Warren, RI to allow damage tolerance and damage progression to be assessed as part the Effects of Defects study (2013). In addition, these blades were used for inspection validation to assess the capabilities of several non-destructive inspection techniques before being shipped to the National Renewable Energy Laboratory/National Wind Technology Center (NREL/NWTC) Structural Testing Laboratory (STL), in Boulder, Colorado, where the two blades were subjected to a series

of proof and fatigue tests to failure. The two blades followed the standard Sandia National Laboratory BSDS blade design (Berry and Berg, 2008) and the only intended variation between the two blades was the material and width of the spar cap: the first was fiberglass, and the second was carbon fiber.

With assistance from the MSUCG, manufacturing defects were added, largely in the spar cap, to each of the two blades using the techniques above. Riddle offers a detailed justification of flaw size and placement in each of the two blades (2013). The same three defect types were used, porosity, IP waves, and OP waves, and flaw placement was added to the manufacturing documents to insure consistency and quality (Figure 47). IP waves were added to the spar cap layers prior to blade layup and great care was taken to ensure consistent wave shape and placement into the mold (Figure 48). OP wave forms were added between layers during layup, and porosity was injected through the vacuum bag shortly after infusion. This method of porosity introduction was utilized in Rounds 2 and 3 of the BMT to allow for localized areas of porosity (Riddle, 2013).

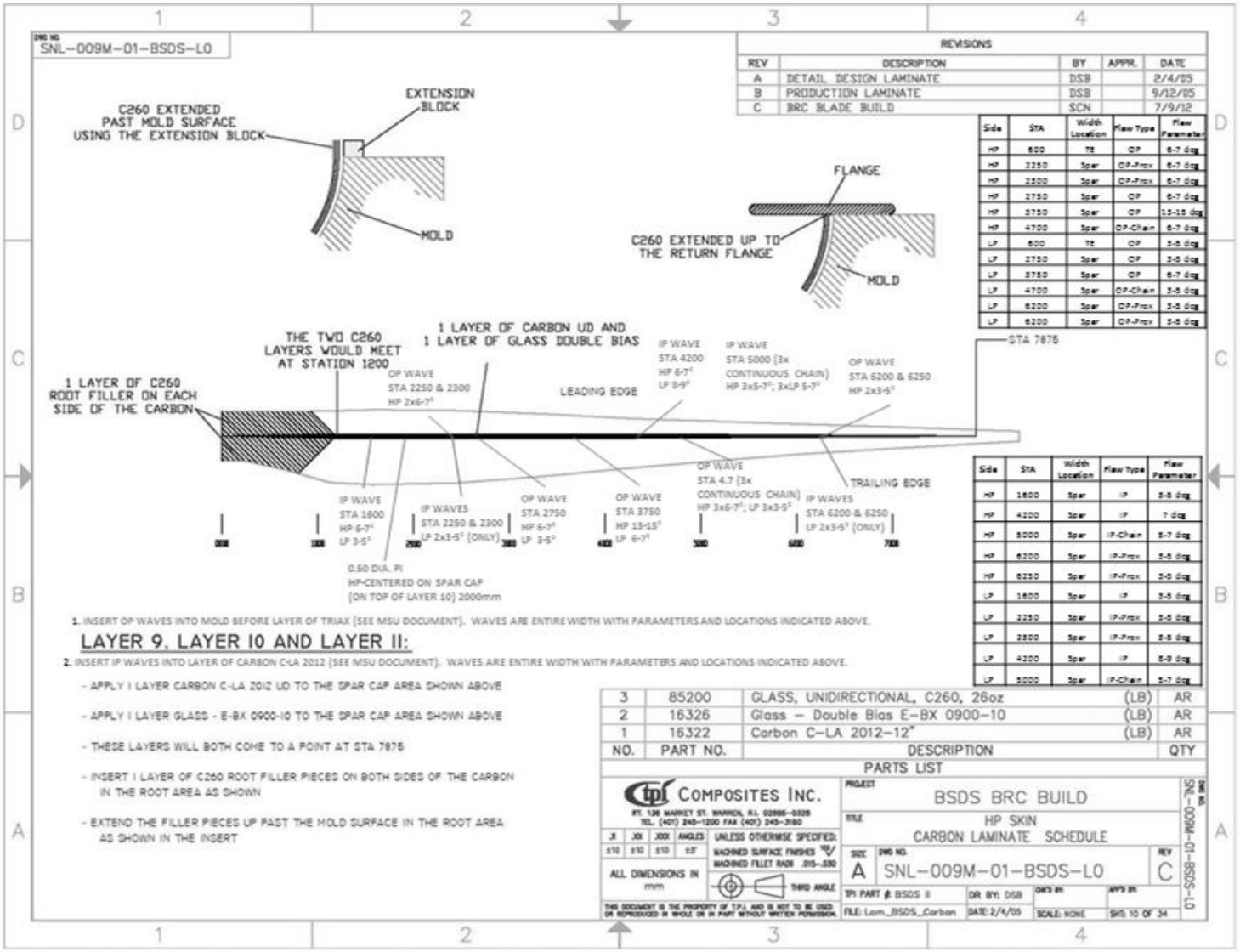

Figure 47: A representative page of the 36 layup drawings to build the BRC validation blades.

Figure 48: The group effort required to place and align the spar cap without disturbing the IP waves (Rumsey, 2013).

A test plan was created by NREL/NWTC staff, with three objectives (NREL/NWTC, 2013):

1. Determine structural properties of the blade through fatigue testing.
2. Determine fatigue strength and failure mode of the blade.
3. Investigate NDI technologies for damage detection structural health monitoring.

Test loads were outlined and modified as necessary through the test effort. The blade was placed as shown in Figure 49. The blade was then instrumented for continuous NDI, including painting key areas as determined by Riddle for DIC data collection (2013). During fatigue testing, periodically the testing was stopped to allow for DIC imaging (Figure 50) to attempt to capture damage progression resulting from the manufacturing flaws added to the blade before failure (Figure 51).

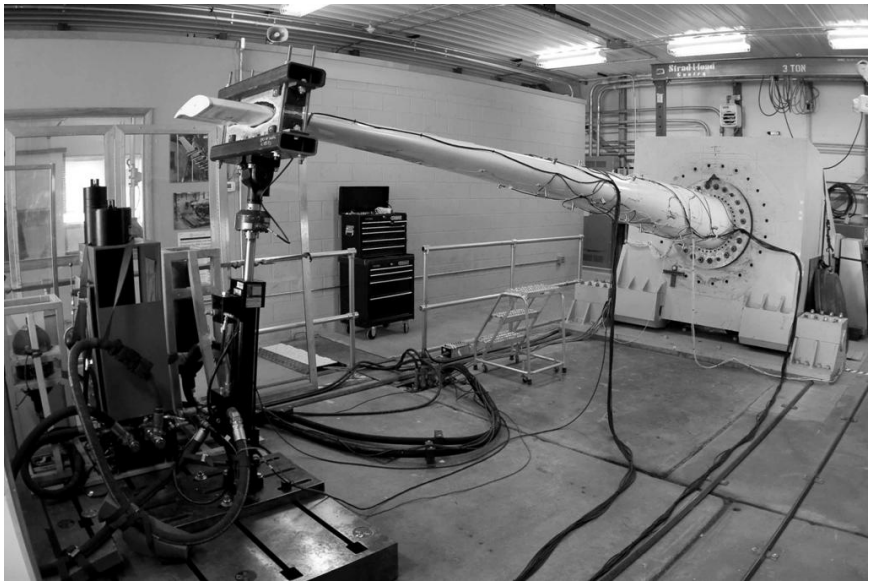

Figure 49: The test layout with the actuator on the left and root fixture on the right (NWTC/NREL, 2013).

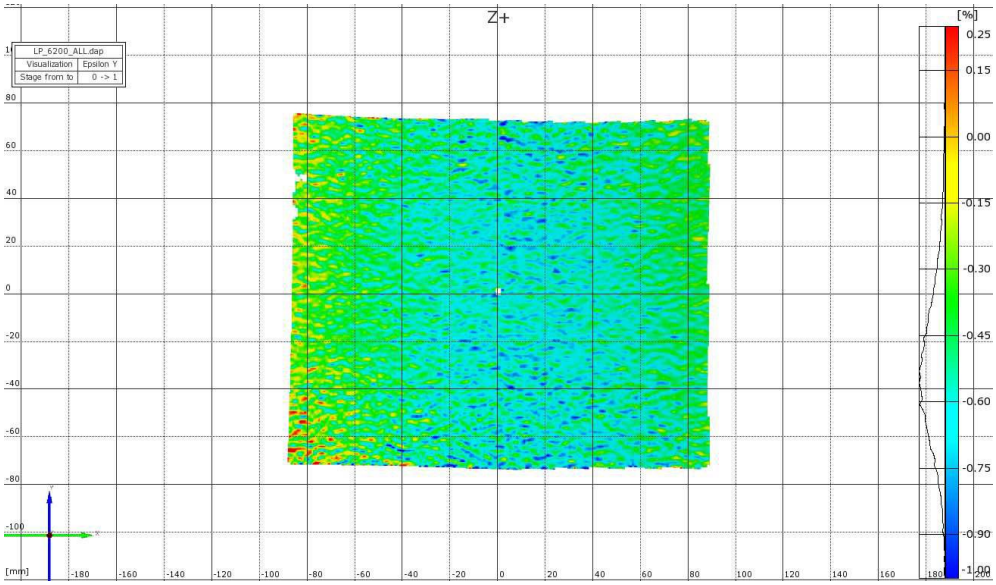

Figure 50: Representative image strain field of area shown below in Figure 51.

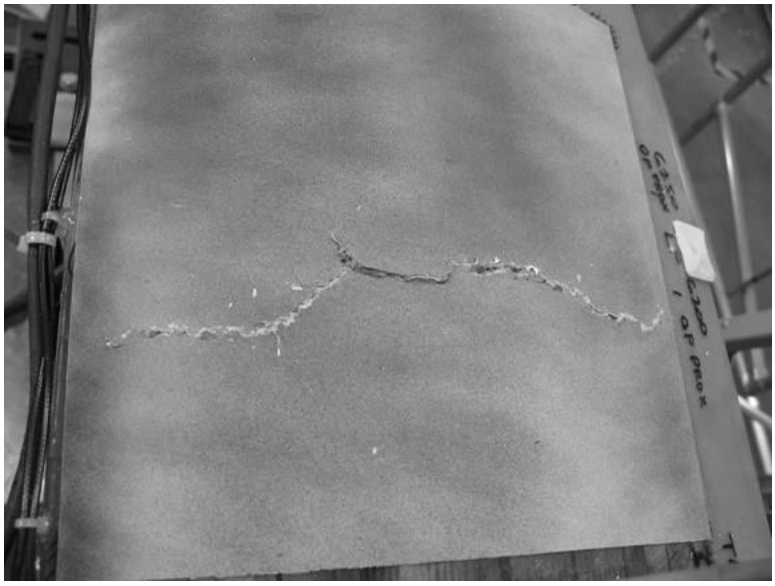

Figure 51: Fatigue failure of BRC blade near an OP wave placed in the spar cap (see Riddle, 2013 for more detail).

After each image set was captured with the DIC, the data were processed and analyzed to determine if strain concentrations and/or average strain increased. While average strain was noted to increase throughout the test due to either increased static loading during imaging, or increased fatigue cycles, few consistent strain concentrations were identified. The exception was a complex OP wave on the high pressure (tensions) side at location 3750 (HP3750). Damage was identified in this area by both acoustic emissions and DIC (Figure 52). As noted above, typical observed damage progression of an OP wave in tension was initial delamination from the wave form and then between layers which reduced interlaminar shear allowing the fibers straighten and carry significant load before failure. The progression pattern for the HP3750 flaw location appeared similar. While this area was noted to have an increased strain concentration fairly early in the loading schedule, damage progression was slow and only showed an

increase in concentration, not an increase in size. Further, the OP wave introduced into the spar cap in this area was not easily identifiable in any DIC image, so correlation between the flaw and the damage progression was not possible. Other areas imaged showed only increases in average strain as noted and as such no sufficient data were gathered to allow for analytical/experimental correlation. This may be explained by noting that the spar cap was bonded directly to the shear web which was the likely load-carrying member in this assembly and overshadowed the localized strain concentration of the defects. Overall, test results from the DIC were inconclusive and no direct damage progression was noted from the manufacturing flaws resulting in no correlation data. It is recommended that future work take place at the new MSUCG Structural Testing Facility to bridge the gap from coupon to blade testing which would likely allow for more complete understand of the effects of defects on a substructure and structure.

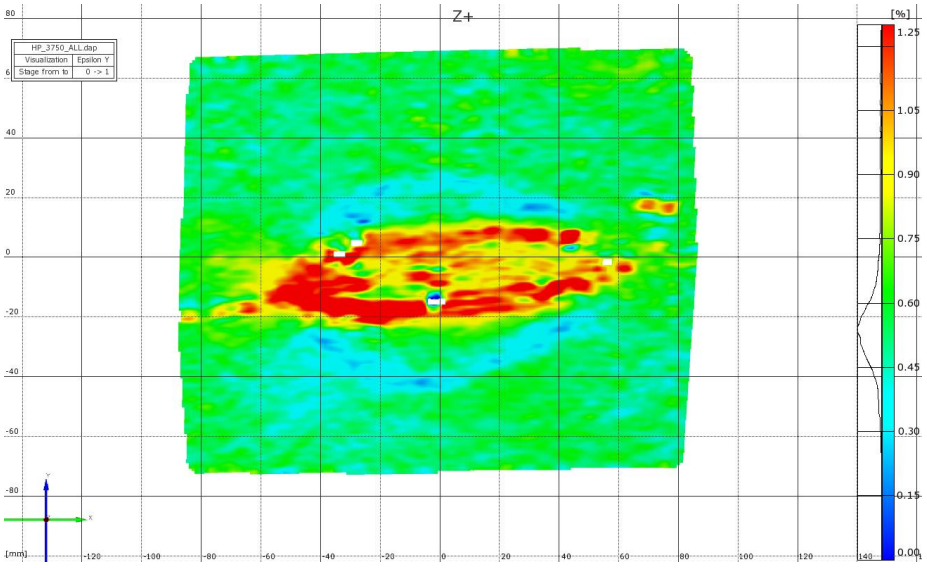

Figure 52: Strain field of HP3750 showing high strain concentration after initial damage before ultimate failure.

CONTINUUM MODELING INTRODUCTION AND LINEAR ELASTIC MODULUS VALIDATION

Introduction

A systematic approach, outlined in this chapter, was employed to compare different continuum damage modeling (CDM) methods. All of these modeling methods utilized material properties and responses generated in the Benchmark Material Testing (BMT) effort outlined in the previous chapter. As noted above, a CDM approach does not directly model damage, but instead degrades material properties of specific elements based on the stress condition calculated in that element. This material property degradation then allows for the global material response to be analyzed.

As noted above, there are many different material property degradation methods, and are they commonly based on various different failure criteria or specifications of a material response. With the former methods, once damage initiation has occurred, the element follows a damage evolution criterion before completely failing and usually being deleted. In the latter case, elements follow a path of degradation or are assumed to have zero load-carrying capacity based on calculated stress/strain conditions.

Several different CDM methods were used to generate and run models with increasing computational difficulty to prove the capabilities and expose the deficiencies of each model type. Where applicable, flaw complexity was increased within a model type based on acceptable correlations of less complex cases. Linear elastic models were run first with neither damage criteria, nor non-linear material response, nor any sort of

material defect to confirm accurate correlation to initial stiffness response. Once this was achieved, the Hashin failure criteria were added to porosity, IP, and then OP wave models (Hashin, 1983). This Abaqus (Daussault Systems, v6.12, 2012) built-in capability allows for prediction of damage onset based on fiber and matrix properties before following an energy based damage evolution law after damage initiation.

Next, the linear elastic model was modified with user-defined failure criteria where mixed stress/strain based failure criteria were implemented. Instead of a damage evolution law, material properties were directly degraded once failure had occurred to reduce material properties. Several different property reduction schemes were investigated with varying degrees of correlation though, in short, it was found that degrading properties to zero was an overestimation. Finally, a user-defined material card was implemented to match the non-linear shear response. Given the fiber misalignment found in both IP and OP waves, shear between the tows and layers, respectively, was observed to be the critical failure mode. Thus, generation of a non-linear response allowed for better approximation than the standard linear approximation could.

These models were created, run, and correlated to responses outlined in the Benchmark Material Testing (BMT) efforts, and modified to improve correlation. While correlation was found rather easily in some cases, other cases required significant modification, or tuning, of input parameters. In some cases, correlation was able to be achieved by small amounts of acceptable parameter tuning as viscous regularization, maximum element degradation, and shear stress coefficients. These acceptable tuning parameters, in most cases, were adjusted to assist with convergence, and the subsequent

effects on the model were able to be traced. In other cases, material properties, such as modulus of elasticity, were modified as a final approach to attempt correlation. Adjustment of these types of parameters was considered unacceptable tuning, and while correlation may have been achieved, the model type was considered a failure for prediction. Each case is presented in detail in the Chapters below, and a discussion is offered for each correlation. Acceptable modification of certain input parameters is justified or the model type is found to be inaccurate where modification does not improve results or is unacceptable as described above in the explanation of the systematic approach in Chapter 2.

Linear Elastic Modulus Validation

A continuum based, linear elastic model was created and utilized to ensure that a standard model could match the modulus of elasticity of control samples from the BMT. This was considered a continuum based approach because the individual materials (fiber and matrix) are not modeled separately, but are instead modeled with smeared properties. Two model types with different laminates were run and correlated in tension and compression: a $[(0)_4]$ laminate, and a $[0/\pm45/0]$ laminate. In both cases, analytical/experimental correlation was achieved that confirmed the ability of the models to predict initial material stiffness response without the need for tuning any parameters.

Methods

A standard linear elastic model with no damage or failure criterion was developed. Geometry was set up to match the intended coupon size (100 mm x 50 mm) established during the BMT. A 2D model (Figure 53), with quadrilateral, plane stress shell elements (S4R) was generated in Abaqus where each element was generated to be consistent with the nominal fiber tow width (1.0 mm). Displacement and boundary conditions were applied at the top and bottom, respectively, to match the BMT testing conditions and, as such, full field calculations were made to match the BMT data for load-displacement and stress-strain correlations.

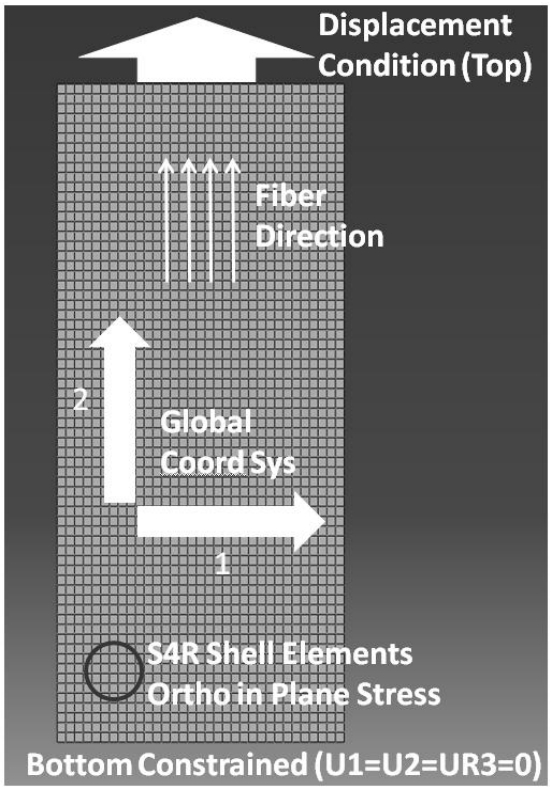

Figure 53: The 2D model setup utilized in the linear elastic validation models.

Even though a 2D model was utilized, the *SHELL SECTION* keyword option was utilized to specify the laminate through the thickness as shown in the snippet of code below. Use of the *COMPOSITE* option allowed for various properties for each theoretical layer of the specified element set, *PLATE*, with the specified *GLOBAL* orientation:

```
*SHELL SECTION,COMPOSITE,ELSET=PLATE,ORIENTATION=GLOBAL
1.0,1,PPG,0.0
1.0,1,PPG,0.0
1.0,1,PPG,0.0
1.0,1,PPG,0.0
```

The properties for each layer are defined on each line: thickness (1.0 mm), number integration points through the thickness (1), material name (PPG), and rotation from defined 1-direction (0.0), respectively. Thus, the total laminate thickness modeled was 4 mm. This model was then easily adapted to match the [0/±45/0] laminate by simply changing the middle layers to +45.0 and -45.0, respectively:

```
*SHELL SECTION,COMPOSITE,ELSET=PLATE,ORIENTATION=GLOBAL
1.0,1,PPG,0.0
1.0,1,PPG,45.0
1.0,1,PPG,-45.0
1.0,1,PPG,0.0
```

Elastic material properties that were generated from the BMT discussed above were utilized (Table 8). Since no damage or failure criterion were utilized, only the elastic properties were necessary for this effort. Note that a summary of the key points of the code are presented here, while complete code may be found below in the Appendices.

Several assumptions were made to simplify this modeling effort. First, it was assumed that all fibers were parallel and uniform in the intended direction with reference

to the widthwise edge. It was also assumed that all the fibers were parallel and aligned through the thickness. These assumptions greatly simplified the modeling approach even though they were a possible source of the variation noted within the BMT. In addition, perfect bonding between the layers was assumed.

Table 8: Material properties generated as outlined in BMT section.

	E_1	E_2	v_1	G_{12}	G_{13}	G_{23}
Tension (GPa)	40.6	16.3	0.27	16.8	16.8	16.8
Compression (GPa)	38.4	14.4	0.28	14.4	14.4	14.4

Results and Correlation

Two distinct models of unflawed control geometries were run as outlined above: a $[(0)_4]$ laminate and a $[0/\pm45/0]$ laminate both in tension and compression. Load-displacement and stress-strain data were generated for each case and used to compare and correlate, respectively, to BMT results. Results and correlation for each are outlined below.

$[(0)_4]$ Laminate:

As these were the first modeling efforts of this research, several steps were taken to ensure that proper modeling details, such as mesh density, were being considered to assure convergence. These steps also allowed for comparison of boundary conditions and assured model integrity. Given the simplicity of the model, it was confirmed that these criteria were achieved with a square element size having an edge length equivalent to the width of a fiber tow (nominally 1.0 mm). While equivalent results were achieved

with a coarser mesh, this finer density was utilized with the intention of keeping it consistent through all analytical approximations in this program. Processing times with this finer mesh were still short and were less than 1 minute in length.

BMT results clearly showed that coupon failure was fairly sudden and complete. Fiber failures were noted starting from the edges or near the grips, and brooming out across the entire coupon. When fiber failure was initially noted, a small amount of load transfer was also seen in the stiffness reduction up to failure. The purpose of this initial model was to correlate initial response, which was achieved as seen in Figure 54 and Figure 55 below. Visually, the model indicated stress concentrations (Figure 54) in the same areas where first fiber failure was noted in BMT. These stress concentrations are the result of the boundary conditions which constrain the model from reducing width on the ends to match the grip conditions during BMT. A comparison of the stress-strain curves (Figure 55 and Table 9) indicates energy was conserved as the areas under both curves are approximately equal. In addition, the initial stiffness matched to within approximately 0.2%, ensuring that this is a reasonable starting point for the systematic modeling approach.

Similar to the tensile case, the model was also run in compression. Stress-strain results indicate similar initial correlation, confirming the model's capability to accurately predict initial response to within approximately 2.8% of the actual value from the BMT (Table 9). As noted earlier, the coupons tested in compression had softening beginning at approximately 0.2% strain. As such, the linear elastic does not match, nor was it expected

to, once this softening occurs due to lack of either a damage definition or non-linear elastic response in compression.

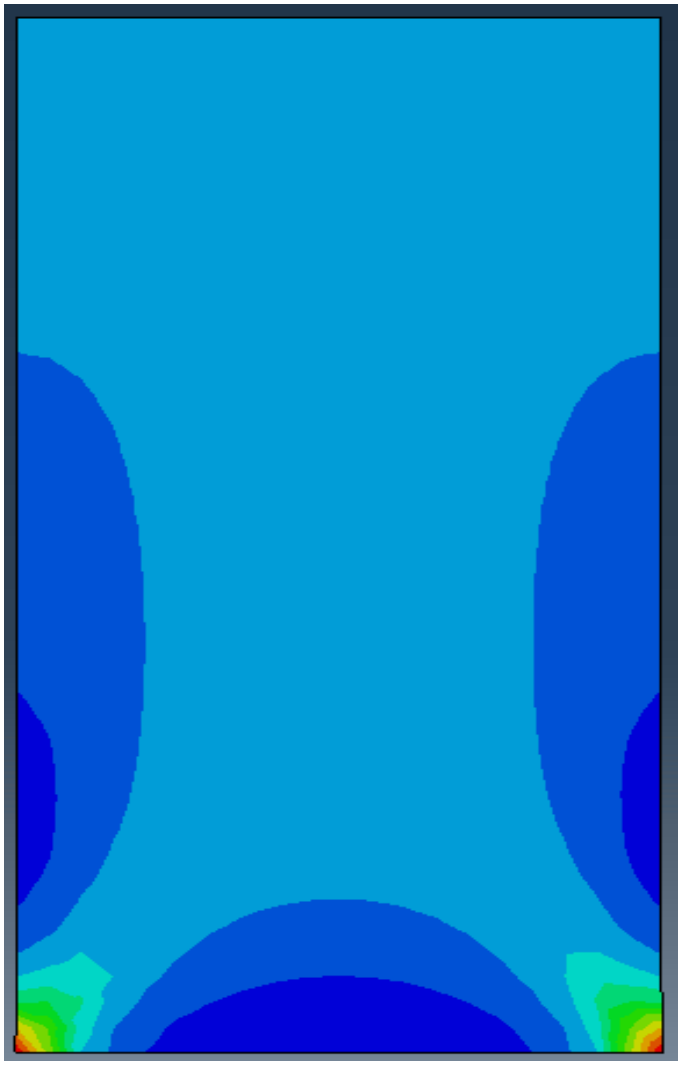

Figure 54: Linear elastic model ($[(0)_4]$ laminate) longitudinal stress response with increased stress due to the boundary conditions constraining the top and bottom edges to match the grip conditions during BMT.

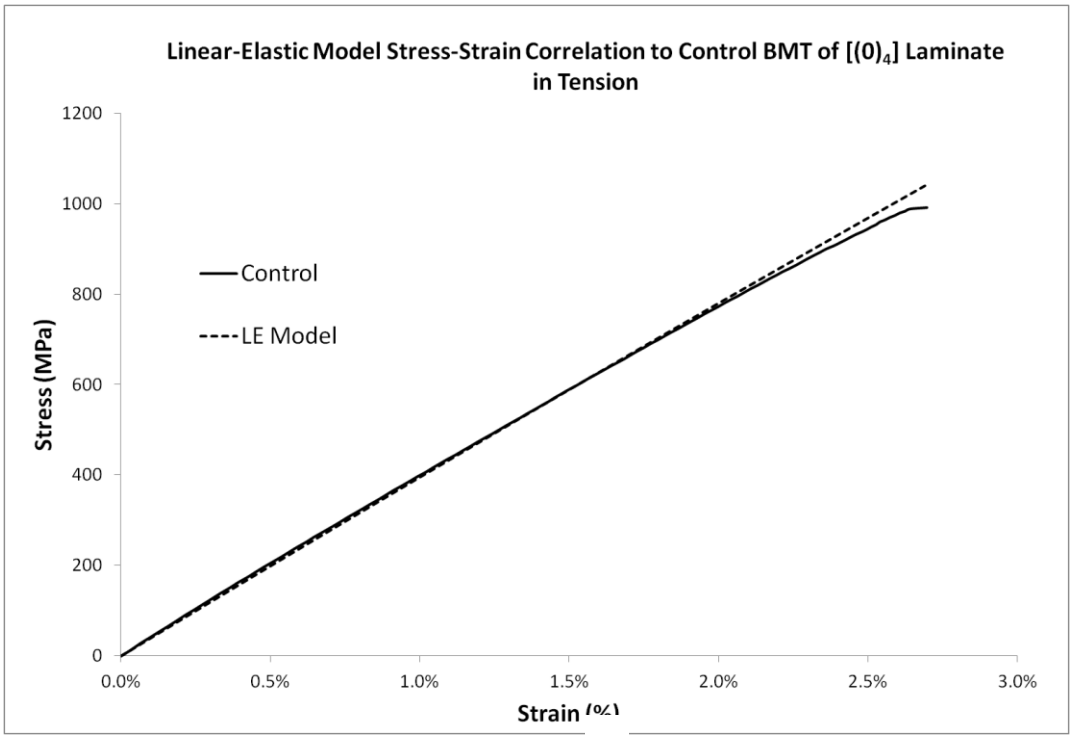

Figure 55: Comparison of $[(0)_4]$ laminate BMT Control and linear elastic model in tension results indicating good correlation.

Table 9: Comparison of actual experimental and analytical predictions for initial linear elastic models.

	Tension				Compression			
	$[(0)_4]$		[0/±45/0]		$[(0)_4]$		[0/±45/0]	
	Actual	Predicted	Actual	Predicted	Actual	Predicted	Actual	Predicted
Modulus of Elasticity (GPa)	40.6	40.5	38.0	39.1	38.4	39.6	28.9	30.3
% difference	*-0.2%*		*2.8%*		*3.1%*		*4.9%*	

[0/±45/0] Laminate

The linear elastic model was modified to add shear by sandwiching a ±45° between 0° plies. During the BMT it was observed that stiffness was less and there was more significant softening in both tension and compression compared to the four ply 0° laminate, as seen in Table 9. The only adjustment made to the analytical model was to

change the orientations of the two middle layers of the laminate; no material properties were modified. Initial stiffness values correlated well, indicating that the calculated modulus by the model was accurate for both tension and compression with variations of 3.1% and 4.9%, respectively.

Linear Elastic Modulus Validation Discussion and Conclusions

Beginning the three round, systematic approach, an initial linear elastic model validation was performed to ensure that this basis for many of the following models was able to accurately match the generally linear response of unflawed specimen from the BMT. Two laminates were tested and modeled with increasing complexity and different elastic moduli to ensure the model was able to accurately predict laminate stiffness with different laminate orientations, which was deemed necessary given the focus on fiber misalignment flaws. In both laminate cases for tension and compression, initial modulus was matched with a linear elastic model up to damage initiation. No failure criteria were included and, as such, it was not expected that the models would predict the material response once any softening occurred. These results confirmed that the models were able to accurately predict the initial stiffness response of the different laminate cases with material data from the BMT. While these models offered a jumping-off point for the systematic approach of this work, they were deemed insufficient for damage progression modeling due to the lack of a failure criterion and/or damage response. Due to the lack of failure and/or damage parameters, flawed geometries were not considered with this initial approach, but in each case modeled flaws were run linear elastically to ensure initial

modulus matched prior to invoking any failure criteria. As such, addition of these parameters was the next logical step in predicting material response, and several different methods have been implemented, as outlined in the Chapters below, to attempt more complete correlation.

LINEAR ELASTIC CDM WITH HASHIN FAILURE CRITERIA

Introduction

Continuing with Round 1, the continuum based, linear elastic model initially utilized above was modified to include damage progression built into Abaqus for the elastic-brittle nature of fiber-reinforced composites. This tool utilized the Hashin failure criteria, and damage was characterized by implementing a stiffness degradation that neglects the plastic deformation commonly missing in the response of fiber-reinforced composites. This approach required the user to specify an initial linear elastic response, a damage initiation criterion, and a damage evolution response. Initially, two different models were created and utilized to model the effects of porosity and an IP wave. In both cases, analytical/experimental correlation was made, and in the case of porosity, was sufficient and showed prediction potential. In the case of the IP wave, correlation was acceptable in certain regions depending on the amount and type of acceptable tuning of model variables indicating additional work with this technique was worthwhile. As such, an OP wave case was generated, and run very similarly to the IP wave case, with results similar to those that were found in the BMT. Finally, additional wave cases and a case with different material, a carbon fiber uni-directional, were generated and compared with BMT results. In all cases, the model was able to consistently correlate to the BMT results as did for the initial IP wave case, not only indicating the promise of this technique but also verifying the systematic approach of increasing flaw complexity taken herein. In

short, the initial IP wave cases showed to be a good baseline for preliminary technique correlation.

Methods

The standard linear elastic model used above was modified and the Hashin failure criteria were added. Again, geometry was set up to match the intended coupon size (100 mm x 50 mm) established during the BMT. To determine if initial correlations were reasonable, 2D models (Figure 56) were generated with both unflawed and IP wave geometries, with quadrilateral, plane stress shell elements (S4R), in Abaqus where each element was generated to be consistent with the nominal fiber tow width (1.0 mm). The IP wave modeled had an amplitude (A) of 3.8 mm, a wavelength (λ) of 47.6 mm, and average off-axis fiber angle of 28.7°. Local coordinate systems were defined for the elements oriented to form the wave such that the fiber direction remained consistent through the wave, and the material properties were modeled to correctly match these properties. Displacement and boundary conditions were applied at the top and bottom, respectively, to match the BMT testing conditions and as such, full field calculations were made to match the BMT data for load-displacement and stress-strain correlations.

In reviewing the test data, images, and DIC data, it was apparent that initial damage occurred in each wave at low loading levels on the ends of the samples where fibers ended on the coupon edge. Due to the wave pattern introduced, when the samples were cut, fibers through the wave were cut resulting in discontinuous fibers along the sample length. Based on this observation, it was assumed that these portions of the

laminate were not of interest when considering the goal of isolating defects. Thus, the geometry shown in right of Figure 56 was utilized for all of the IP wave modeling efforts

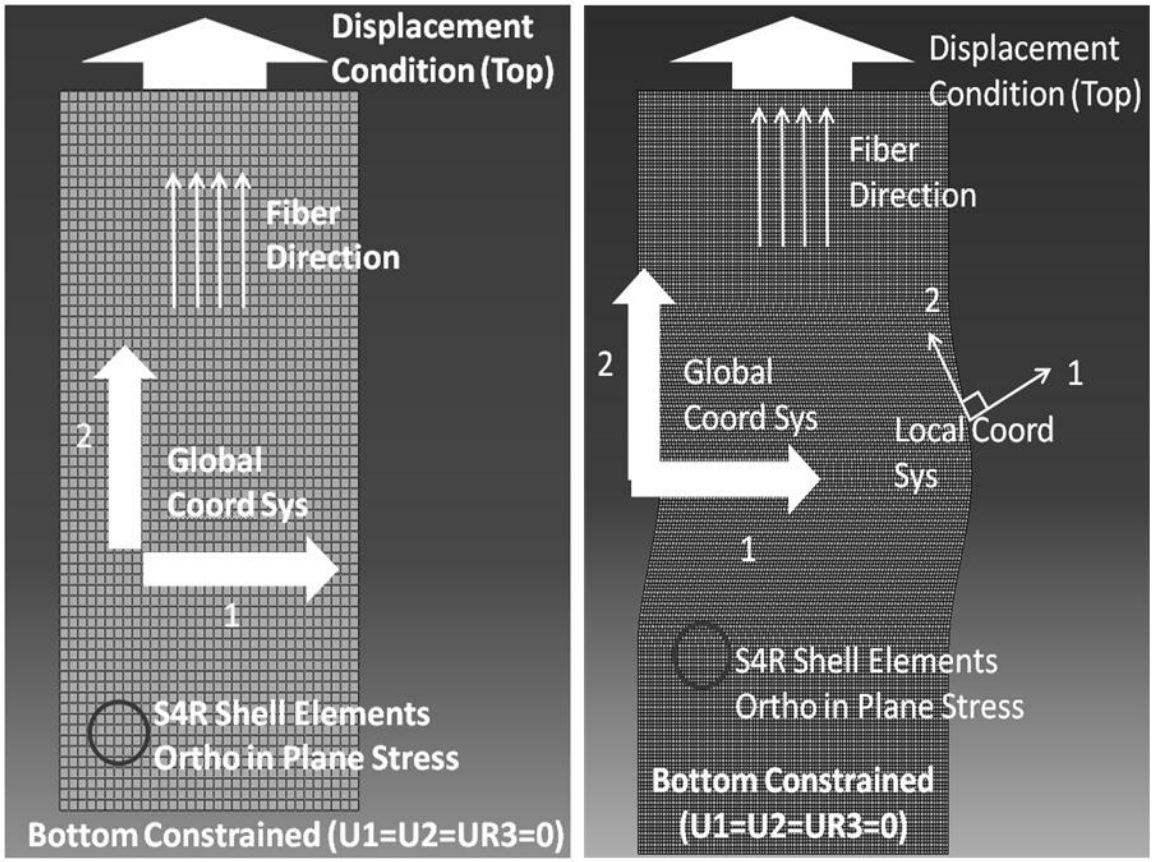

Figure 56: The 2D model setup utilized in the Control (left) and IP wave (right) linear elastic models with Hashin failure criteria.

herein, while similar models with differing geometries were utilized for the unflawed controls as seen above in the left of Figure 56.

Even though a 2D model was utilized, the *SHELL SECTION* keyword option required specifying the laminate through the thickness as shown in the snippet of code below. Use of the *COMPOSITE* option allowed for a various properties for each

theoretical layer of the specified element set, *PLATE*, with the specified *LOCAL* orientation:

```
*SHELL SECTION,COMPOSITE,ELSET=PLATE,ORIENTATION=LOCAL
1.0,1,PPG,0.0
1.0,1,PPG,0.0
1.0,1,PPG,0.0
1.0,1,PPG,0.0
```

The fiber orientation of each element, *LOCAL*, was specified in a *DISTRIBUTION TABLE* with respect to the model edge. The properties for each layer are defined on each line: thickness (1.0 mm), number integration points through the thickness (1), material name (PPG), and rotation from defined 1-direction (0.0), respectively. Thus, the total laminate thickness modeled was 4 mm. Elastic material properties that were generated from the BMT discussed above were utilized. Note that a summary of the key points of the code are presented here, while complete code may be found below in the Appendices.

Several assumptions were made to simplify this modeling effort. First, it was assumed that all fibers were parallel and uniform in the intended direction with reference to the widthwise edge, including through the IP wave. It was also assumed that all the fibers, for both the unflawed and IP wave geometries, were parallel and aligned through the thickness. These assumptions greatly simplified the modeling approach even though they were a possible source of the variation noted within the BMT. In addition, perfect bonding between the layers was assumed. In the case of the IP wave, it was assumed that the initial failures and debonds of the discontinuous edge fibers had negligible effect on the material response and were disregarded for this effort.

Hashin Failure Criteria Summary and Approach

Abaqus has a built-in a Progressive Damage and Failure for Fiber-Reinforced Materials (Analysis User's Manual v6.12, 2012) that is intended to be used for elastic-brittle, anisotropic materials. Three criteria must be specified to define the material stiffness degradation of this CDM: initial elastic response, damage initiation criteria, and damage evolution response. The initial elastic response was easily defined as a linear elastic material with a plane stress orthotropic material stiffness matrix, as in Chapter 4 above. However, damage initiation must also be defined for the four included mechanisms:

Fiber tension ($\hat{\sigma}_{11} \geq 0$): $$F_f^t = \left(\frac{\hat{\sigma}_{11}}{X^T}\right)^2 + \alpha\left(\frac{\hat{\tau}_{12}}{S^L}\right)^2 \quad (1)$$

Fiber compression ($\hat{\sigma}_{11} < 0$): $$F_f^c = \left(\frac{\hat{\sigma}_{11}}{X^C}\right)^2 \quad (2)$$

Matrix tension ($\hat{\sigma}_{22} \geq 0$): $$F_m^t = \left(\frac{\hat{\sigma}_{22}}{Y^T}\right)^2 + \left(\frac{\hat{\tau}_{12}}{S^L}\right)^2 \quad (3)$$

Matrix compression ($\hat{\sigma}_{22} < 0$): $$F_m^c = \left(\frac{\hat{\sigma}_{22}}{2S^T}\right)^2 + \left[\left(\frac{Y^C}{2S^T}\right)^2 - 1\right]\frac{\hat{\sigma}_{22}}{Y^C} + \left(\frac{\hat{\tau}_{12}}{S^L}\right)^2 \quad (4)$$

where X^T is the longitudinal tensile strength, X^C is the longitudinal compressive strength, Y^T is the transverse tensile strength, Y^C is the transverse compressive strength, S^L is longitudinal shear strength, S^T is transverse shear strength, α is a shear stress contribution coefficient that determines contribution to fiber tensile initiation, and $\hat{\sigma}_{11}$, $\hat{\sigma}_{22}$, $\hat{\tau}_{12}$ are stress tensor components where the nominal stress is modified with a damage operator, *M*:

$$M = \begin{bmatrix} \frac{1}{1-d_f} & 0 & 0 \\ 0 & \frac{1}{1-d_m} & 0 \\ 0 & 0 & \frac{1}{1-d_s} \end{bmatrix} \quad (5)$$

where d_f, d_m, and d_s are damage variables for fiber, matrix, and shear damage, respectively, derived from the damage variables of the stress scenarios noted in the four mechanisms listed above. If the modified stress tensor components meet the criteria for any of the four mechanisms, then damage is initiated. The damage variables become non-zero, the damage operator, *M*, modifies the nominal stress, and appropriate stiffness degradation begins. Instead of continuing with the stiffness matrix of a plane stress orthotropic material, the degraded material response is then calculated:

$$\sigma = \mathrm{C_d}\varepsilon \quad (6)$$

where: $$\mathrm{C_d} = \frac{1}{D}\begin{bmatrix} (1-d_f)E_1 & (1-d_f)(1-d_m)\nu_{21}E_1 & 0 \\ (1-d_f)(1-d_m)\nu_{12}E_2 & (1-d_m)E_2 & 0 \\ 0 & 0 & (1-d_s)GD \end{bmatrix} \quad (7)$$

and: $$D = 1 - (1-d_f)(1-d_m)\upsilon_{12}\upsilon_{21} \quad (8)$$

where, again, d_f , d_m, and d_s each reflected the current state of fiber, matrix, and shear damage, respectively, E_1, E_2, and *G* are the directional and shear moduli of elasticity, respectively, and ν_{12} and ν_{21} are Poisson's ratios.

To address issues associated with mesh dependency, Abaqus has adjusted the constitutive law to express a stress-displacement relation utilizing characteristic length. As shown in Figure 57, the damage variable for each of the four failure mechanisms

behaves such that stress increases linearly (*OA*) through the elastic region up to damage initiation (*A*) at which point the slope is linearly negative (*AC*). In cases where unloading occurs (*B*), a secant is used (*OB*) to account for damage that has occurred, and the same path is then used for reloading. For each of the four failure mechanisms, the energy dissipated due to failure, G^c, must be specified to determine the area of the *OAC* triangle.

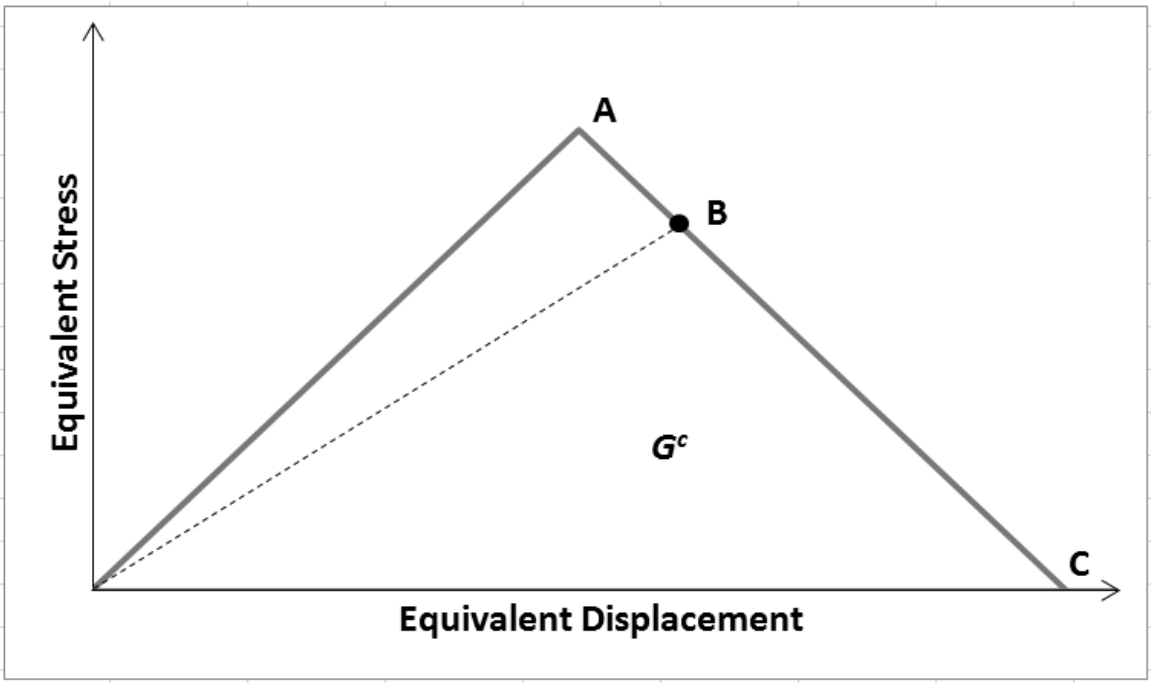

Figure 57: Equivalent stress and equivalent displacement where initial linear elastic is along *OA*, damage initiates at *A*, damage evolution is along *AC*, and G^c is the energy dissipated due to failure.

In addition to the damage evolution criteria, an upper bound, d_{mzx}, may be set to handle elements with severe damage. This upper bound allows for the maximum degradation, shown as *C* in Figure 57, to be effectively reduced by limiting d_{max} to a value between 0 and 1, where 0 is damage onset and 1 is complete failure. Element

deletion then occurs for each element that reaches d_{max} and the element is thereby removed from the mesh. Element deletion may also be turned off keeping elements in the computation where C_d for the element remains at the minimum value for the remainder of the computation.

To assist with convergence issues that are common with implicit analysis when modeling material softening and stiffness degradations, viscous regularization may be introduced. This causes the tangent stiffness matrix to always be positive for the small time increments required for convergence of these model types. In short, the viscous damage variable, $\dot{d}_v$, is calculated:

$$\dot{d}_v = \frac{1}{\eta}(d - d_v) \tag{9}$$

where η is the viscosity coefficient representing the relaxation time of the viscous system and d is the damage variable evaluated in the inviscid model. As such, the stiffness matrix, C_d, is then calculated using these viscous adjusted values.

Hashin Failure Criteria Code Inputs

As such, damage initiation was defined by inputting the six material strength criteria (longitudinal, transverse, and shear, each in both tension and compression) and the shear stress coefficient in the code as:

**DAMAGE INITIATION, CRITERION=HASHIN, ALPHA=α*
X^T, X^C, Y^T, Y^C, S^L, S^T

Damage evolution was adjusted by specifying the energy dissipated, G^c, at failure for each of the four failure mechanisms (fiber and matrix, each in both tension and compression):

**DAMAGE EVOLUTION, TYPE=ENERGY, SOFTENING=LINEAR*
G^c_{ft}, G^c_{fc}, G^c_{mt}, G^c_{mc}

Element deletion was controlled within the *SECTION CONTROLS* keyword of the input file. It is simply an on/off switch that allows for maximum degradation to be set between 0 and 1:

**SECTION CONTROLS, ELEMENT DELETION=YES, MAX DEGRADATION=1.*

Damage stabilization, generally a tuned input, was controlled by specifying the four viscosity coefficients (fiber and matrix, each in both tension and compression):

**DAMAGE STABILIZATION*
η_{ft}, η_{fc}, η_{mt}, η_{mc}

Hashin Failure Criteria Model Inputs

Elastic material properties that were generated from the BMT discussed above were utilized as shown in Table 10.

Table 10: Material properties generated as outline in BMT section.

	E_1	E_2	v_1	G_{12}	G_{13}	G_{23}
Tension (GPa)	40.6	16.3	0.27	16.8	16.8	16.8
Compression (GPa)	38.4	14.4	0.28	14.4	14.4	14.4

For the 2% porosity case, the material properties were reduced based on Kerner's (1956) approach to determine material properties utilizing the rule of mixtures when

voids are included within a material. Assuming a constant thickness with 2% porosity by volume, adjusted modulus of elasticity, E_C, was calculated:

$$E_C = E_f V_f + E_m V_m + E_p V_p \tag{10}$$

where E is modulus and V is fiber volume for fiber, matrix, and porosity. As such, the material properties from Table 10 were then modified based on the 2% porosity case resulting in properties shown in Table 11. It is important to note that the standard properties from Table 10 were utilized for the IP wave case.

Table 11: Material properties adjusted using Kerner's rule of mixtures approach to predict properties for 2% included porosity.

Rule of Mixtures Reduction	E_1	E_2	v_1	G_{12}	G_{13}	G_{23}
Tension (GPa)	39.8	16.0	0.27	16.5	16.5	16.5
Compression (GPa)	37.6	14.1	0.28	14.1	14.1	14.1

The specific inputs necessary for damage initiation for this model were also generated from the BMT or were taken as listed in the MSU-CMD as shown in Table 11. In addition to these values, several others were estimated based on BMT data and were deemed acceptable tuning inputs (Figure 12). These included element deletion, maximum degradation factor, shear coefficient, and damage evolution criteria. While these were deemed acceptable to tune, these modifications were evaluated and justified. For this initial model, element deletion was turned on with a maximum degradation factor set to 1, meaning that elements were deleted upon reaching failure criteria. Similarly, the shear coefficient was set to 1 based on Hashin (1980). In the case of the fracture energies necessary for damage evolution, initial values were generated utilizing Irwin's approach:

$$G^c = G_{Ic}^2/E \quad (11)$$

where BMT values were utilized for energy release rate (G_{Ic}), and both longitudinal and transverse moduli of elasticity (E) were utilized in tension and compression. Since these energy values were an approximate in order to generalize a start point, it was intended that they then be modified to improve analytical/experimental correlation as necessary. In all cases, modifications are noted and justified below; cases where justification or correlation was not possible are deemed unacceptable and noted as such.

Table 12: Starting damage initiation and evolution parameters for both models with Hashin failure criteria.

Property	X^T	X^C	Y^T	Y^C	S^L	S^T	G^c_{Lt}	G^c_{Lc}	G^c_{Tt}	G^c_{Tc}
Value	990	582	60	162	112	124	16.0	16.9	39.9	45.1
Units	MPa						kN/mm			

Results and Correlation

Two distinct models were run as outlined above: one with reduced properties to match the porosity case and one with an IP wave added to the coupon geometry. Load-displacement and stress-strain data were generated for each case and used to compare and correlate, respectively, to BMT results. Processing times for each of these models ranged from 1 to 16 minutes in length. Based on the systematic approach outlined above, the initial case after porosity correlation was an IP wave, in tension and compression, before moving on to assess correlation for other cases. Results and correlation for each are outlined below.

Porosity

Porosity coupon samples from the BMT results clearly showed that coupon failure was fairly sudden and complete. Fiber failures were noted starting from the edges or near the grips and brooming out across the entire coupon. As noted in the BMT section above, areas of strain concentration were noted in the DIC images. Since the porosity geometry was not directly modeled, and a true continuum approach degrading material properties was utilized, the model cannot capture this physical response (Figure 58). However, the material response was captured as seen in the stress-strain correlations in Figure 59 indicating energy conservation. When fiber failure was initially noted, a small amount of load transfer was also seen in the minor stiffness reduction up to failure. Up to this point, the model matched the modulus of elasticity of the BMT porosity case and was quite linear. The model did not capture the initial small failures, likely associated with localized porosity pockets as noted in the DIC images, and as such the model over-predicted the stiffness beyond strains of approximately 1.25% when coupon samples began to degrade. Instead, the model continued to predict linearly up to approximately 2.25% strain where damage begins and failure was noted at just over 2.5% strain. The model was conservative, as it under-predicts the load and strain at failure; however, the variation was slight: 2.54% compared to 2.56% and 927 MPa compared to 947 MPa, the latter of both as noted during the BMT.

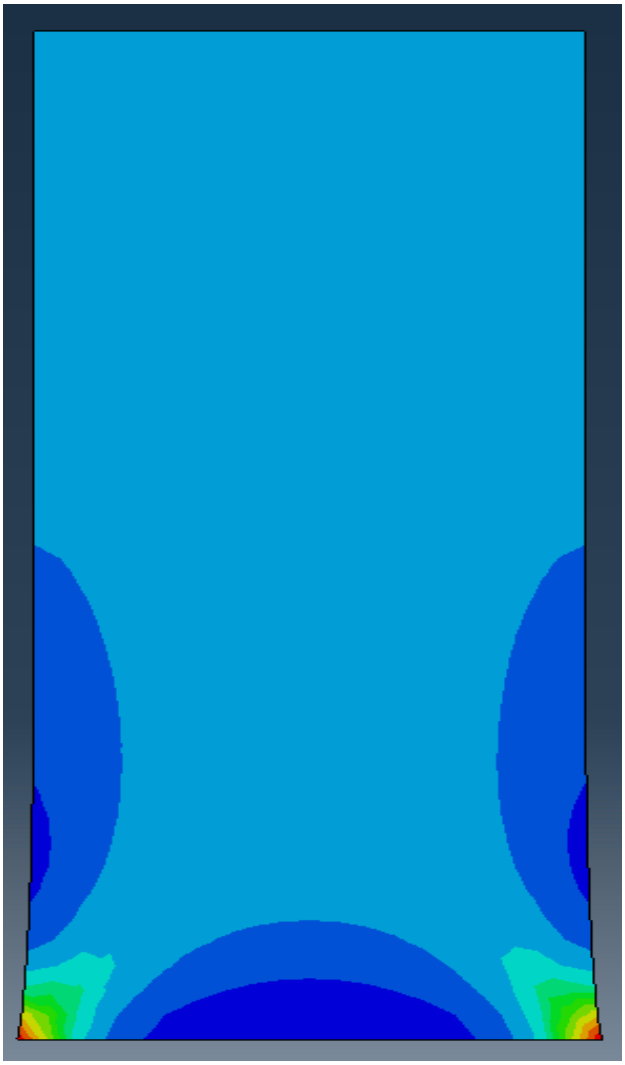

Figure 58: Linear elastic with Hashin failure criteria model longitudinal response that matches the linear elastic response up to failure shown in BMT above.

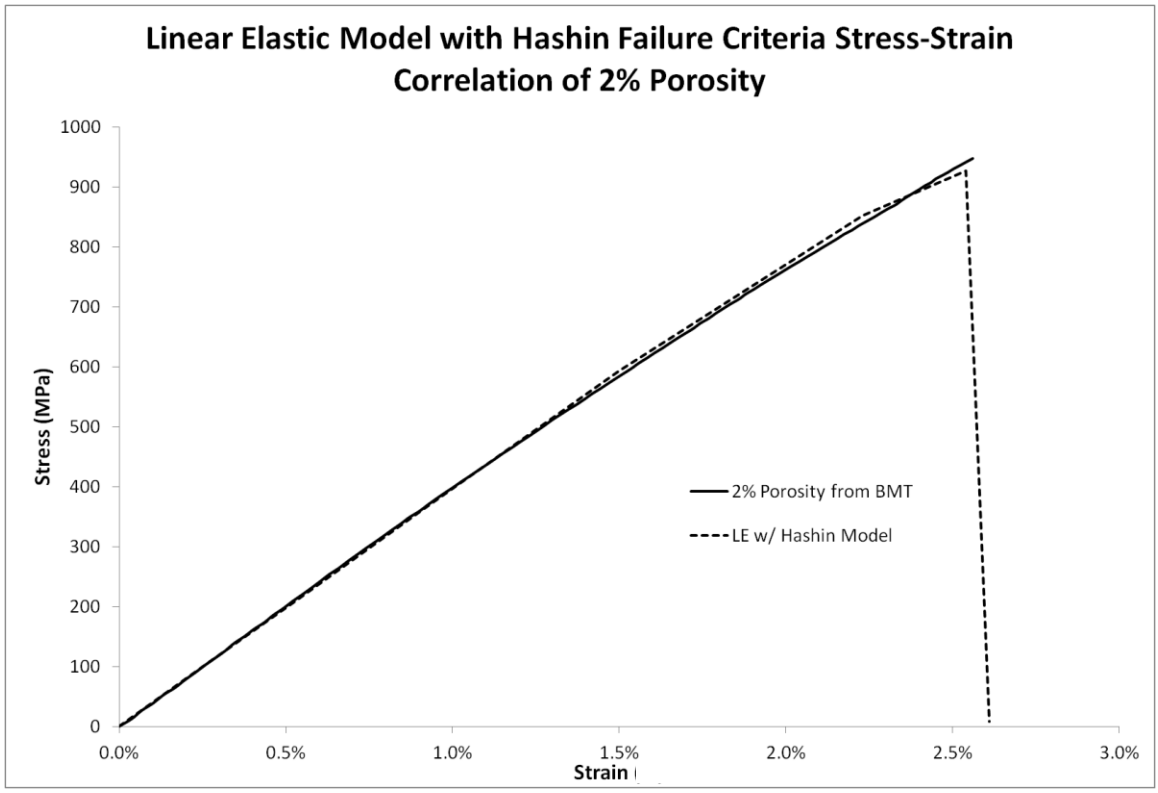

Figure 59: Comparison of 2% Porosity BMT and linear elastic with Hashin failure criteria model in tension results indicating good correlation.

In order to achieve the correlation noted in Figure 59, the damage evolution criteria were tuned in two ways to match the rapid failure seen in the BMT. The first method was to first reduce all the fracture energy inputs that specify the damage evolution to 10.0 kN/mm. This resulted in the as-modeled curve shown in Figure 59 above. In addition, to understand the impact of the damage evolution criteria, the model was then run with only the damage initiation criteria. The results were identical to the reduced fracture energy case, in short, indicating that the model was not utilizing these inputs. This non-utilization was due to the default of the elements being deleted and having no load-carrying capacity after initiation similar to rapid failure noted in the BMT.

In short, for the porosity case in tension, only accurate damage initiation criteria are necessary, given the proper element choice.

Compression models with porosity were analyzed as well; however, similar to the controls tested, the porosity samples were noted to have a significant amount of bending. Unlike the wavy specimen, the porosity samples did not have a flaw that was critical enough to Since the MSU-CMD does not contain data for flawed specimen, no correlation was available for porosity in compression. As such, this model was run for in compression, but until a robust compression data set is available correlation is not possible.

Several considerations were made based on variability when considering modeling approaches for porosity. Discrete modeling of each case is not only extremely intensive and computationally expensive but also requires *a priori* knowledge of the flaw sizes, locations, proximity effects, and shapes. Given each of these difficulties, discrete modeling of porosity was not considered for this work, and given the acceptable correlation achieved with this approach, combined with the closeness of the material response to the unflawed case, no additional consideration was deemed necessary for porosity.

IP Wave

Based on the systematic approach outlined above, the initial flaw case considered was an IP wave, first in tension and then in compression. Results in tension allowed for further analysis of additional IP waves, but in compression correlation was not achieved and further analysis was not performed as justified below.

IP Wave in Tension: IP wave tension coupon samples from BMT results clearly showed that coupon failure was less sudden than for the unflawed controls or porosity specimens. Initially, shear damage was noted in the area of the fiber misalignment, generally in the area of peak fiber misalignment, and it progressed both transversely perpendicular to the fiber and longitudinally parallel to the fiber along the wave. First fiber failure was noted in the areas where this damage progressed together and met from both sides of the wave. This progression was visualized with the use of DIC which allowed for initial visual comparison to analytical solutions and is shown in Figure 60 (right and left, respectively) for the linear elastic Hashin failure criteria model. As shown, the model was able to capture the peak area of strain where damage occurred at the peak fiber misalignment angle, and the damage then progressed toward the edges perpendicular to the fiber direction and longitudinally to the wave peak between the two areas of fiber misalignment. It should be noted that this initial comparison is qualitative and visual only. While it shows that the model was able to accurately predict the damage progression, quantitative comparison is also needed for adequate correlation. Similar to above, quantitative analytical/experimental correlation was performed utilizing stress-strain curves. With the inputs noted above, the response matched the initial stiffness of this IP wave fairly well as shown in Figure 61. However, the IP waves of this magnitude showed initial softening and degradation in the wave around 0.25%. The model slightly over-predicted the stiffness but then corrects for it at approximately 0.5% strain where damage initiation was first noted. The damage evolution then under-predicted the load-carrying capacity of the laminate, indicating that maximum stress was about 500 MPa at

approximately 0.8% strain, which was well below the actual 621 MPa at 1.6% observed in the BMT. As a result, it is clear that the model under predicts the dissipated energy (Figure 61).

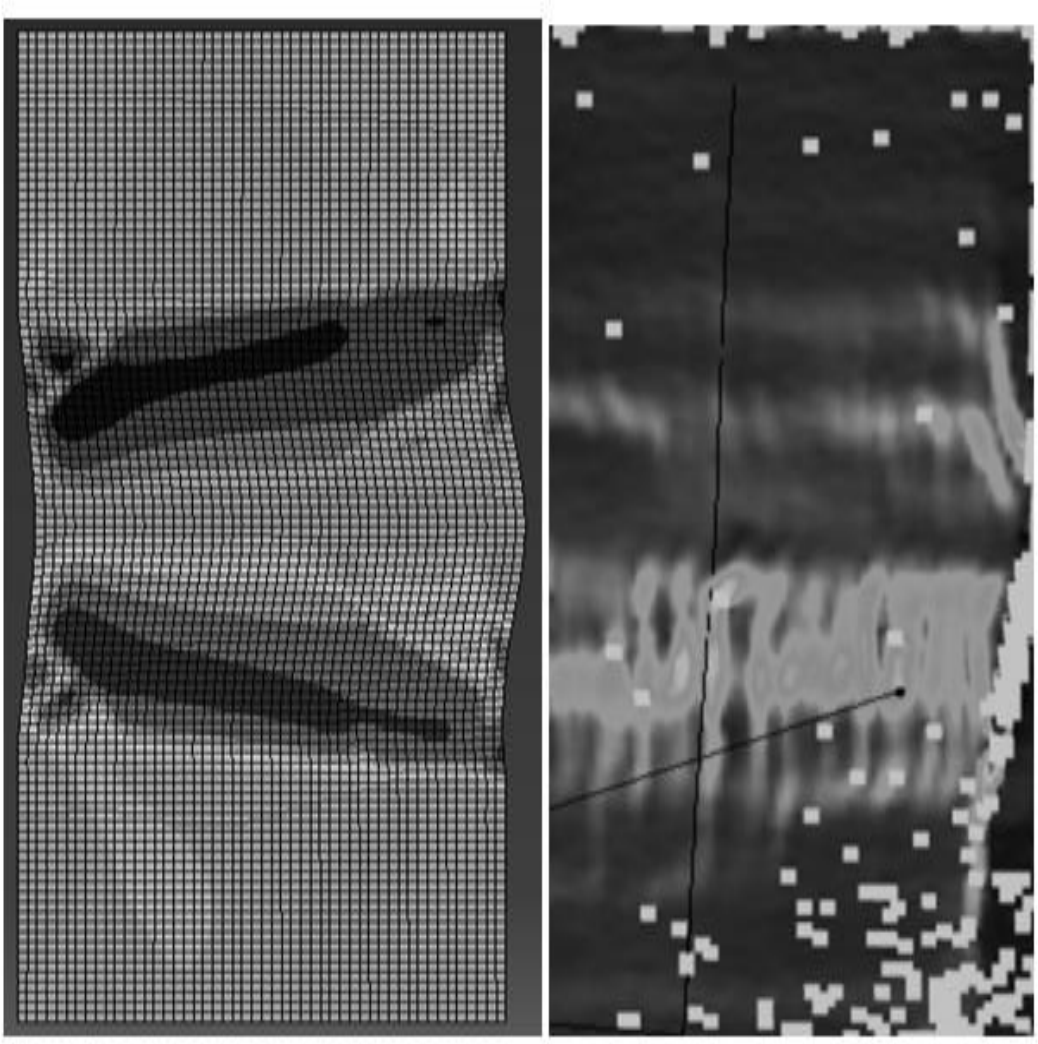

Figure 60: Shear strain field comparison of linear elastic with Hashin failure criteria solution (left) and DIC image (right) in tension.

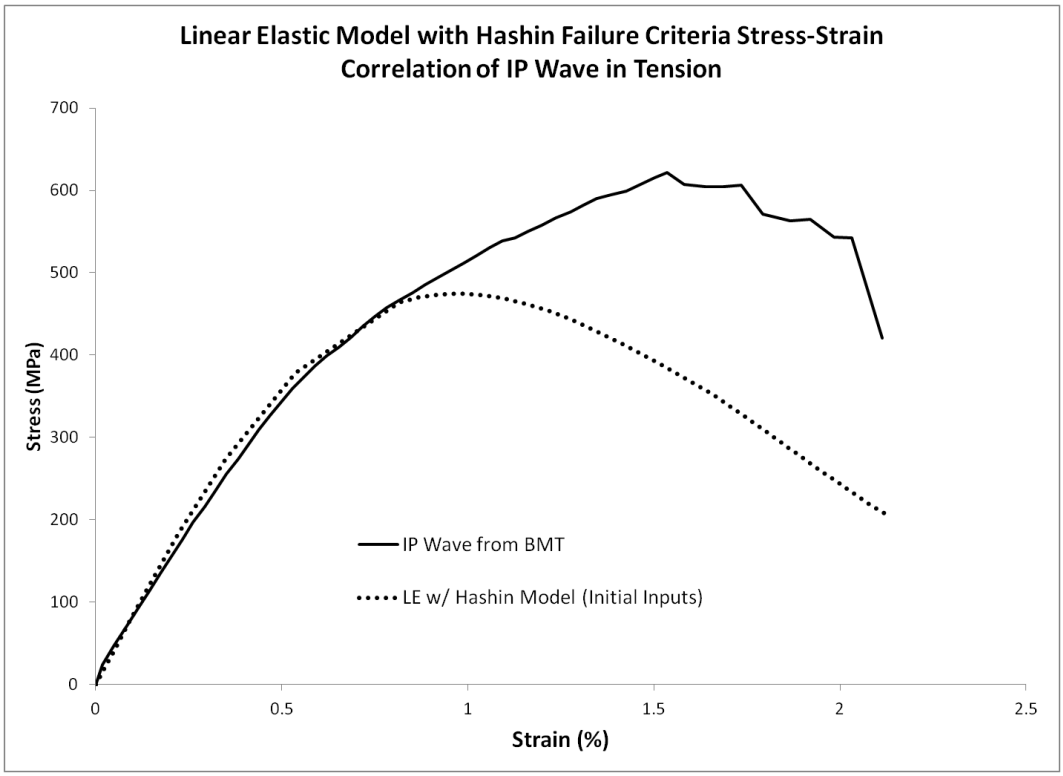

Figure 61: Stress-strain comparison of IP wave BMT and linear elastic with Hashin failure criteria model in tension results indicating good correlation.

Given this difference, the damage initiation and evolution criteria were both modified in an attempt to improve accuracy. Several modification steps were performed to understand the implications of adjusting these parameters and each parameter, as such, was modified individually. It was found that increasing the longitudinal shear stress for initiation, S^L, by 10% to 123 MPa, and doubling all of both tensile fracture energies from the values listed in Table 12 energies yielded the best correlations; 33.8 and 90.2 kN/mm, respectively.

Other parameters were modified in attempts to understand the model implication of each one. This included the energy values associated with damage evolution which

were found not to have an effect on the results. The values were increased by two orders of magnitude and were set to zero; the results were identical to those shown in Figure 61. This result was likely due to the element deletion occurring before the evolution could take place. Element deletion was then turned off, which then led to convergence problems and as such the damage evolution values were left as originally input. In short, it appeared that damage initiation occurred, followed by element deletion and a load redistribution to the surrounding elements during the next step. It was noted for this IP wave case that element deletion first occurred in the area where the stresses from each side of the wave met at the peak of the wave and migrated toward the area of maximum misalignment angle from there.

A similar test was performed for the damage stabilization viscous damping parameters. While the general shape of the resulting curve did not change drastically, it was found that as the viscous parameter increased from zero to one, the shape became smoother. However, there were convergence issues at the zero value, which were equivalent to the stabilization being turned off. As such, small values of 0.05 were utilized for all of the viscous parameters, and this value was left constant throughout.

While improved correlation (Figure 62) was achieved with the adjustments noted above, discrepancies were still evident, particularly in the under-prediction of the strain at maximum stress (1.25% at 600 MPa). From this point, the model showed decreasing load-carrying capacity up to the point where it matched the final failure of approximately 550 MPa at just over 2% strain. In short, this model was able to predict aspects of the damage progression of the IP wave and conserve energy, but it was not an exact match.

However, given the variation of the waves through the thickness of the BMT coupons noted above as being compared to an idealized model where all layers are exactly identical, an exact match cannot be expected. Basically, the model was predicting the idealized case whereas the coupons have some variability that result in the stress-strain curve not being as smooth as it is after the point of maximum stress. This analytical approach cannot capture such a response unless time were to be taken to model this geometry exactly as noted in the BMT section above. Further analysis in this way has been left as future work though additional wave cases were considered below.

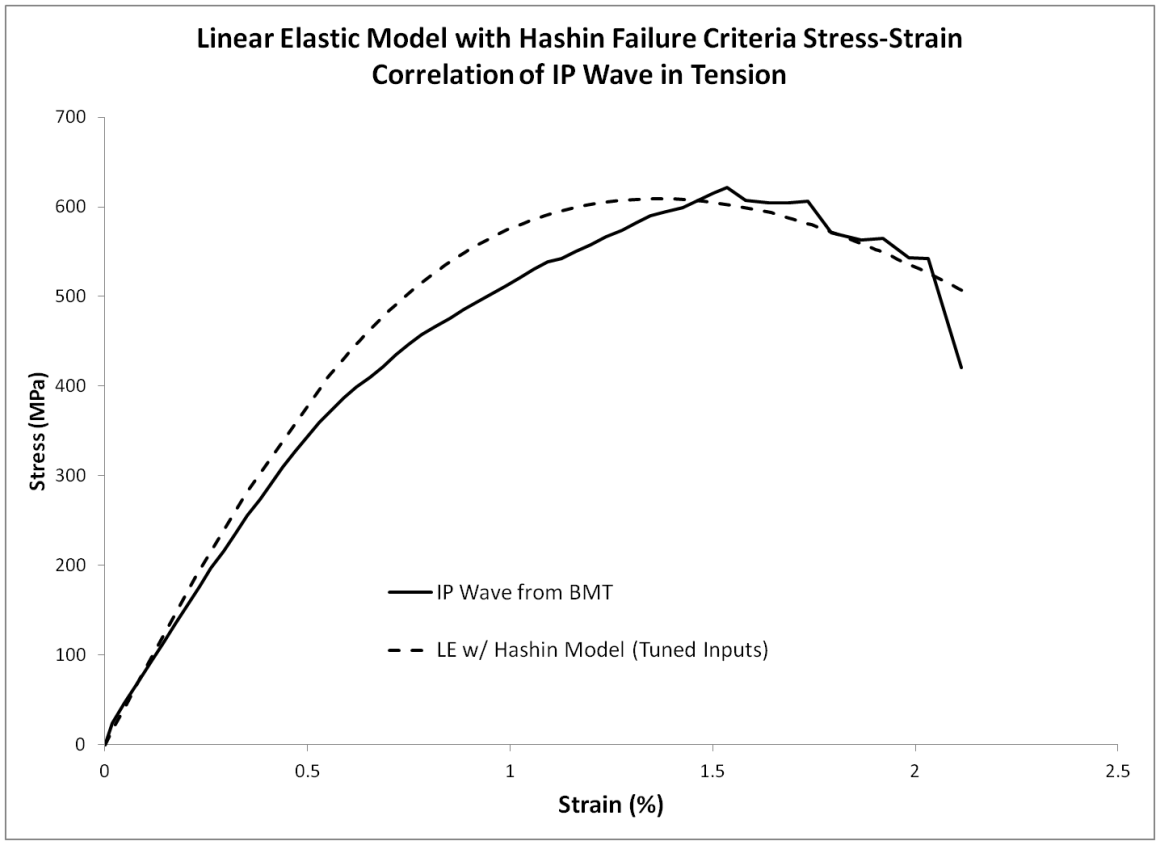

Figure 62: Stress-strain comparison of IP wave BMT and linear elastic with Hashin failure criteria model in tension results indicating good correlation.

IP Wave in Compression: The model was also run for the same IP wave in compression. The boundary conditions were slightly modified such that the straight fiber sections of the model were constrained to prevent transverse displacement, thereby, effectively reducing the gage section. Initial inputs were used as listed in Table 10 and Table 12 above with compression data replaced for the material properties. Correlation was not as straight-forward for the compression case, compared to tension, as the damage progression was not visualized as easily during BMT. Visually, it was more difficult to determine a consistent pattern of damage progression up to ultimate failure than it was to determine a consistent pattern for tension. The DIC images showed increasing strain, and minimal out-of-plane bending that appeared relatively uniform across the entire surface, while the model predicted strain predominantly accumulating in the wave area (Figure 63). As noted above, the gage section for the compression tests was significantly smaller than it was for tension, and this smaller section reduced the amount of area that the DIC was able to capture. Since the flaw dominated this area, only a small amount of unflawed area was imaged at the top and bottom. While this may have affected the range of strains, it should not have affected the way the wave was imaged. It is also likely that the variations of the wave geometry and placement noted above resulted in the more uniform strain field visualized with the DIC. These significant differences, though qualitative, were not able to be minimized without an unreasonable amount of tuning of the model and material properties.

Even with the poor qualitative correlation, resulting stress-strain curves were still compared (Figure 64) as future testing may allow improved damage progression

resolution at a later date. The model was able to match not only the initial stiffness but also the initial softening that occurred. However, at just under 1% strain it began to deviate from the BMT results before flattening out at approximately 200 MPa with only a slight amount of stress reduction occurring beyond 2% strain. This very slight negative slope continued, and a drop to only 150 MPa was noted at 5% strain. In short, the model was not able to capture the entire damage progression, nor was dissipated energy equal to the BMT results.

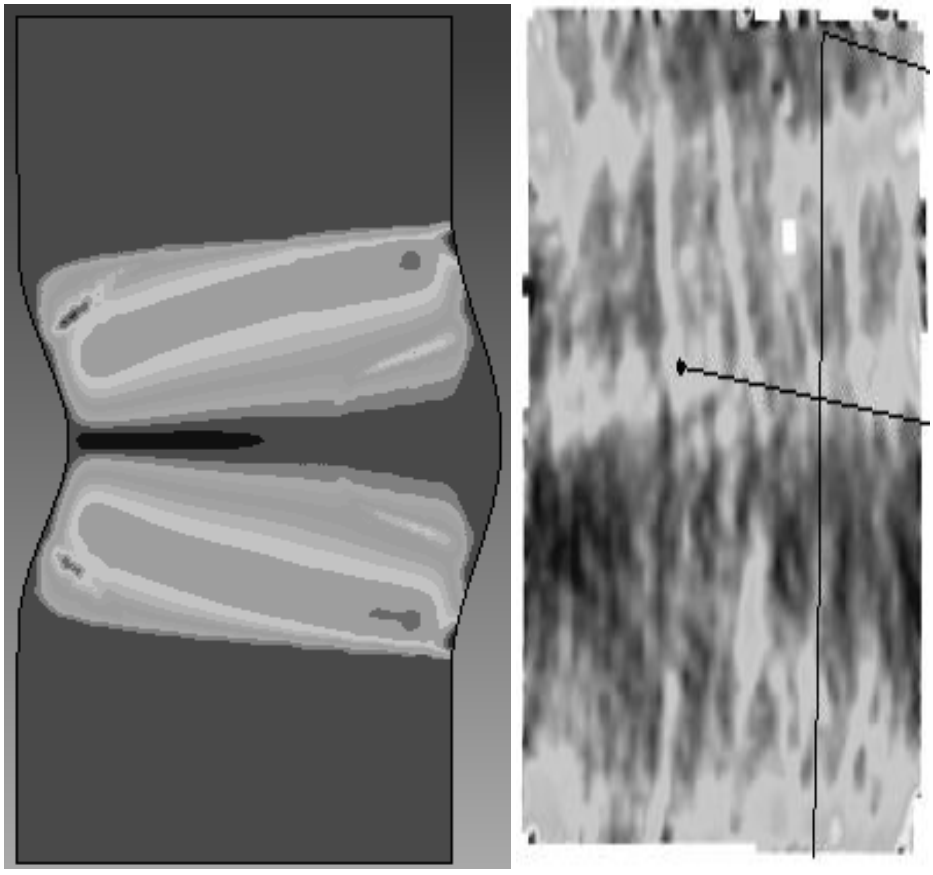

Figure 63: Shear strain field comparison of linear elastic with Hashin failure criteria solution (left) and DIC image (right) in compression.

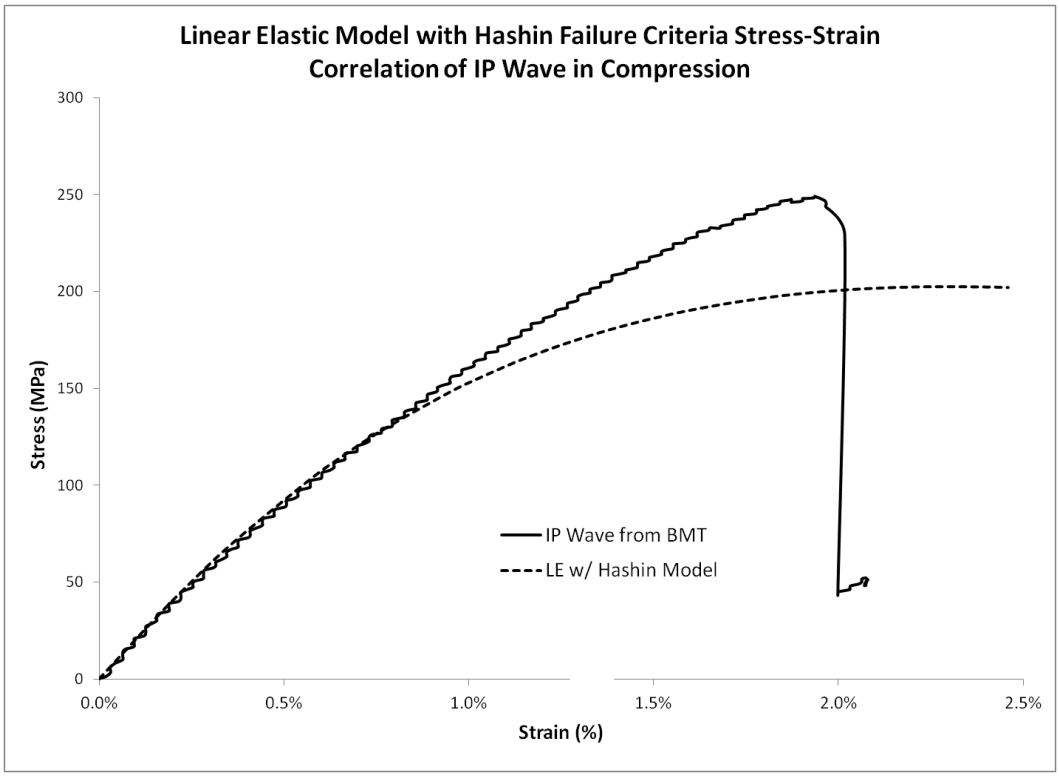

Figure 64: Stress-strain comparison of IP wave BMT and linear elastic with Hashin failure criteria model in compression results indicating reasonable initial correlation.

As above, damage initiation and evolution inputs were adjusted to bound their effects with minimal effect on the model and the adjustments indicated that this effect was due to the geometry. Further evidence of these effects may be seen when looking at the calculated stress field (*S11*) where Figure 65 shows a peak tensile and compressive stress on each side of the coupon at the inflection point of the wave. In short, the model predicted an in-plane rotation that was not observed during the BMT and indicates that further analysis would be needed for correlation of this model in compression. As such, further correlation of this method was not performed or considered for other compression

cases, though model runs have performed as a baseline attempt that may be improved upon with additional future testing.

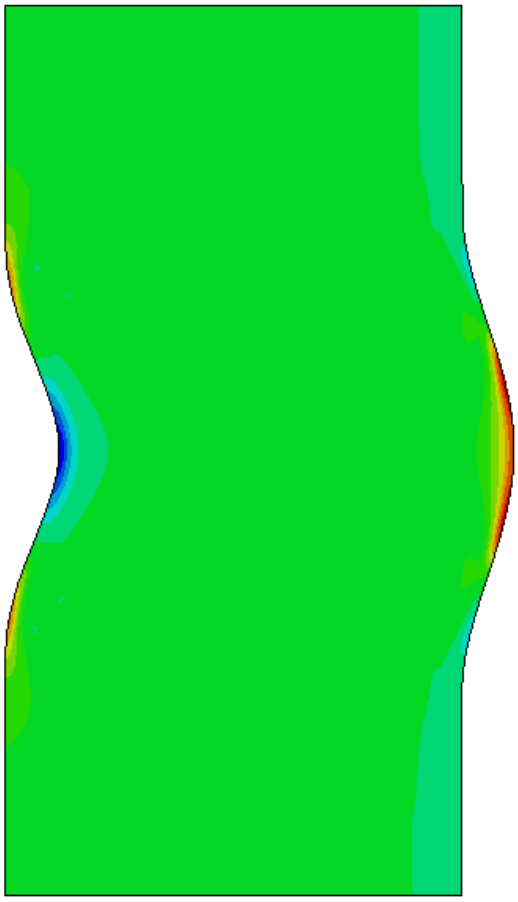

Figure 65: Stress field (*S11*) of linear elastic with Hashin failure criteria model of IP wave in compression with peak stresses noted at the wave inflection points on each side.

OP Wave

Methods: Given the reasonable correlation of the IP wave in tension shown above, it was deemed worthwhile to continue the systematic approach of increasing flaw complexity. Thus, an OP wave model was generated and correlated in both tension and compression. As noted in the BMT, the compression case does not have any correlation

data and was generated only as a baseline to be correlated in the future when such data becomes available. Similar to the IP wave, this OP wave model was setup in 2D (Figure 66) and was rotated about the global 1-direction such that the wave goes through the thickness (50 mm). As shown in Figure 66, the geometry was set up to match the intended coupon size (100 mm x 4 mm), with quadrilateral, plane stress shell elements (S4R) in Abaqus where each element was generated to be consistent with the nominal fiber tow width (1.0 mm). To match the BMT method, a wave form with rotated properties was created and was generalized based on the as-manufactured OP wave. The OP wave modeled had an amplitude (A) of 2.9 mm, a wavelength (λ) of 22.8 mm, and average off-axis fiber angle of 19.4°. Local coordinate systems were defined for the elements oriented to form the wave such that the fiber direction remained consistent through the wave, and the material properties were modeled to correctly match these properties. To match the BMT method, a wave form with rotated properties was created and was generalized based on the as-manufactured OP wave. Displacement and boundary conditions were applied at the top and bottom, respectively, to match the BMT testing conditions and as such, full field calculations were made to match the BMT data for load-displacement and stress-strain correlations.

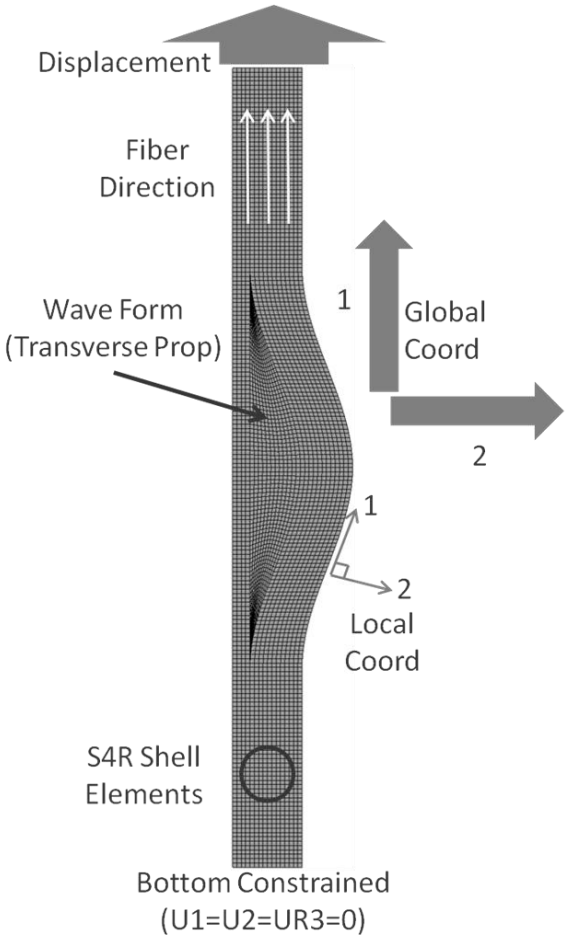

Figure 66: The 2D model setup utilized in the OP wave linear elastic models with Hashin failure criteria.

The model was modified to also have a single layer utilizing the *SHELL SECTION* keyword option with the 50 mm thickness noted above for both the wave and straight portions of fiber. A separate section with rotated properties was added for the wave form. Elastic material properties that were generated from the BMT discussed above were utilized (Table 10). Damage initiation, evolution, and stabilization parameters noted in Table 12 were utilized for this Hashin failure criteria approach. Note that a complete code for this model may be found below in the Appendices.

Several assumptions were made to simplify this modeling effort. First, it was assumed that all fibers were parallel and uniform in the intended direction with reference to the widthwise edge, including through the IP wave. It was also assumed that all the fibers, for both the unflawed and IP wave geometries, were parallel and aligned through the thickness. These assumptions greatly simplified the modeling approach even though this is a possible source of the variation noted within the BMT. In addition, perfect bonding between the layers was assumed.

Results and Correlation: OP wave tension coupon samples from BMT results clearly showed coupon failure was less sudden than in the unflawed controls or porosity specimens. OP wave compression was not analyzed due to buckling failures associated with the asymmetry associated with the wave. In tension, each of the layers was noted to initially delaminate from the form and the surrounding layers in the area of the wave. After this occurred, the wave continued to straighten, and little softening was noted when compared to the softening noted in the IP waves. Fiber failure was similar to what was noted in unflawed, straight fiber controls: sudden failure at the peak of the wave with significant brooming. DIC was utilized, though the edge of the coupons were not captured due to difficulties speckling the edge surface and identifying the coupon edges. As shown in Figure 67, the entire flat surface of the coupon was imaged, and the image showed that the strain was minimal in the area of the wave once the layers delaminated and were in the straightening phase. The DIC data indicated that the strain concentrated at the base of each side of the wave, and as the coupon extended, much of that extension was the result of the fibers in the wave straightening. This was evident even though a

nominally 1.0 mm thick layer of material was between the wave form and the misaligned layers on the surface being imaged.

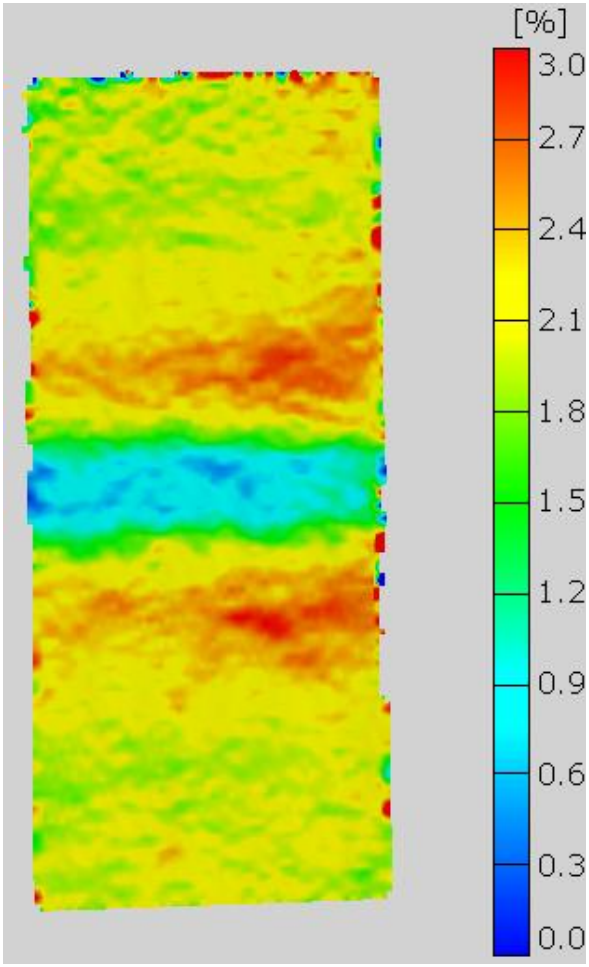

Figure 67: Strain field captured with DIC on flat back surface of OP wave coupon test indicating peak strains on each side of the wave.

While direct correlation was not able to be achieved given the rotation between the DIC and this model approach, it was clear from the model results (Figure 68) that the initial strain concentrations were in the areas of interaction between the wave form and misaligned fibers. Further analysis indicated that elements are first deleted in this area by

the model which matched the observed damage progression. As the stress increased in the elements in this area, the model responded by deleting them consistently through the damage progression phase. During this phase, the undamaged elements were able to continue to carry the load, as they occurred during the softening phase noted in the BMT.

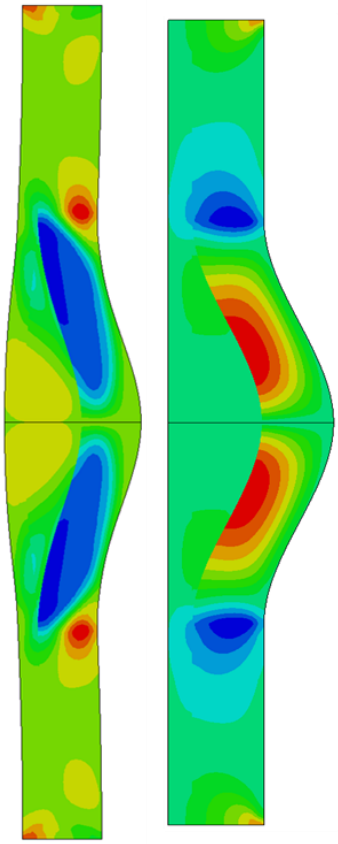

Figure 68: Stress field (*S12*) of linear elastic with Hashin failure criteria model of OP wave in tension (left) compression (right).

As above, quantitative correlation was performed by comparing the full-field stress-strain data from the BMT to the model results and dissipated energy was noted to be approximately equal (Figure 69). Unlike the IP wave above, the correlation shown did not require any modification of the damage initiation criteria, possibly as a result of

including the use of delamination test results for these data. Since this case was actually considering the interlaminar delamination, it followed that these data allowed for accurate modeling. Overall, the correlation was good for this case and would warrant additional comparisons in tension. Unfortunately, due to data corruption, no additional datasets exist for the OP waves in tension with this same glass material; however, a carbon OP wave case in tension is discussed below. The model was also run for the compression case (as shown in Figure 68, right) and while the compression case seemed reasonable, there are no data for comparison, and so no correlation was made; however, the model is ready when future data become available.

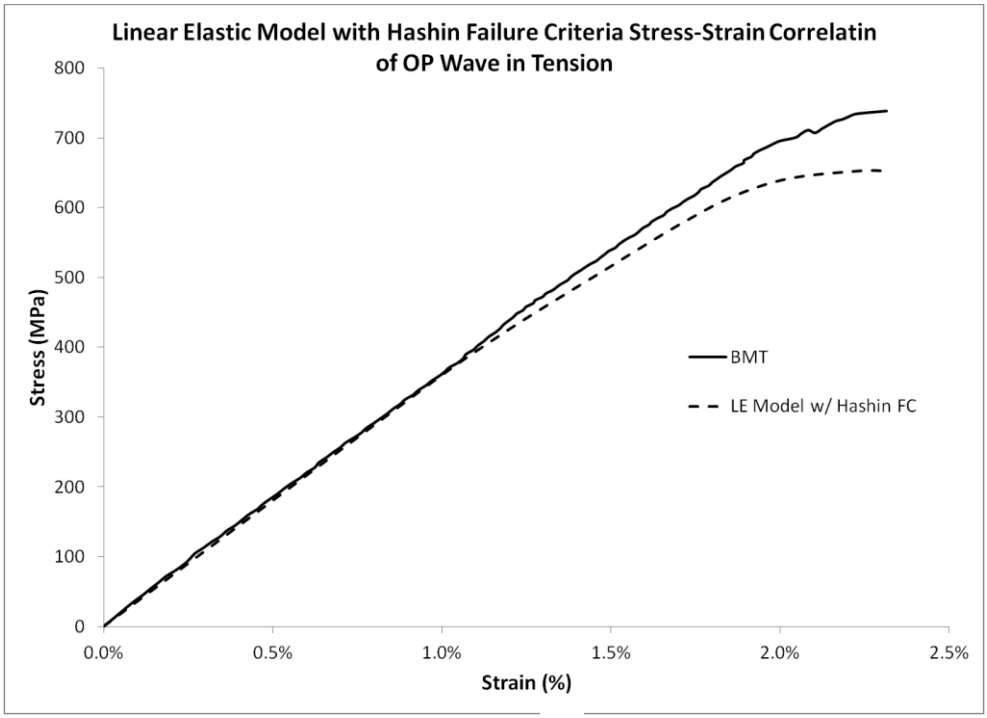

Figure 69: Stress-strain comparison of OP wave BMT and linear elastic with Hashin failure criteria model in tension results indicating good overall correlation.

Additional IP Waves in Tension

Given the reasonable correlation to the IP wave case above, two other IP wave cases were correlated. These two cases were chosen as they offered bounds, with fiber misalignment angles of approximately 16° and 48°, to the first case of approximately 29°. The approach was to use the tuned model from the first case and to determine the predictive capability of this model by not adjusting any of the parameters. Models for each different angle were generated in a similar fashion as Figure 56 above, but with different amplitudes, wavelengths, and fiber misalignment angles. Otherwise, the models were identical for these cases. It must also be noted that qualitative visual damage progression appeared virtually identical to the initial IP wave case (Figure 63) for each case correlated here. As such, further discussion was not warranted.

While the initial case above, over-predicted the load-carrying capacity after initially matching the stiffness, it very closely matched the appropriate stress at the ultimate failure strain. Neither of these bounding cases matched this result, but they both showed similar variations (Figure 70). The 16° case matched the initial stiffness and, similar to the initial 29° case, over-predicted the load-carrying capacity before ultimately under-predicting the ultimate failure stress by just over 10%. The 48° case also matched the initial stiffness and over-predicted the load-carrying capacity. However, instead of being conservative this case also over-predicted the ultimate failure stress by almost 40%.

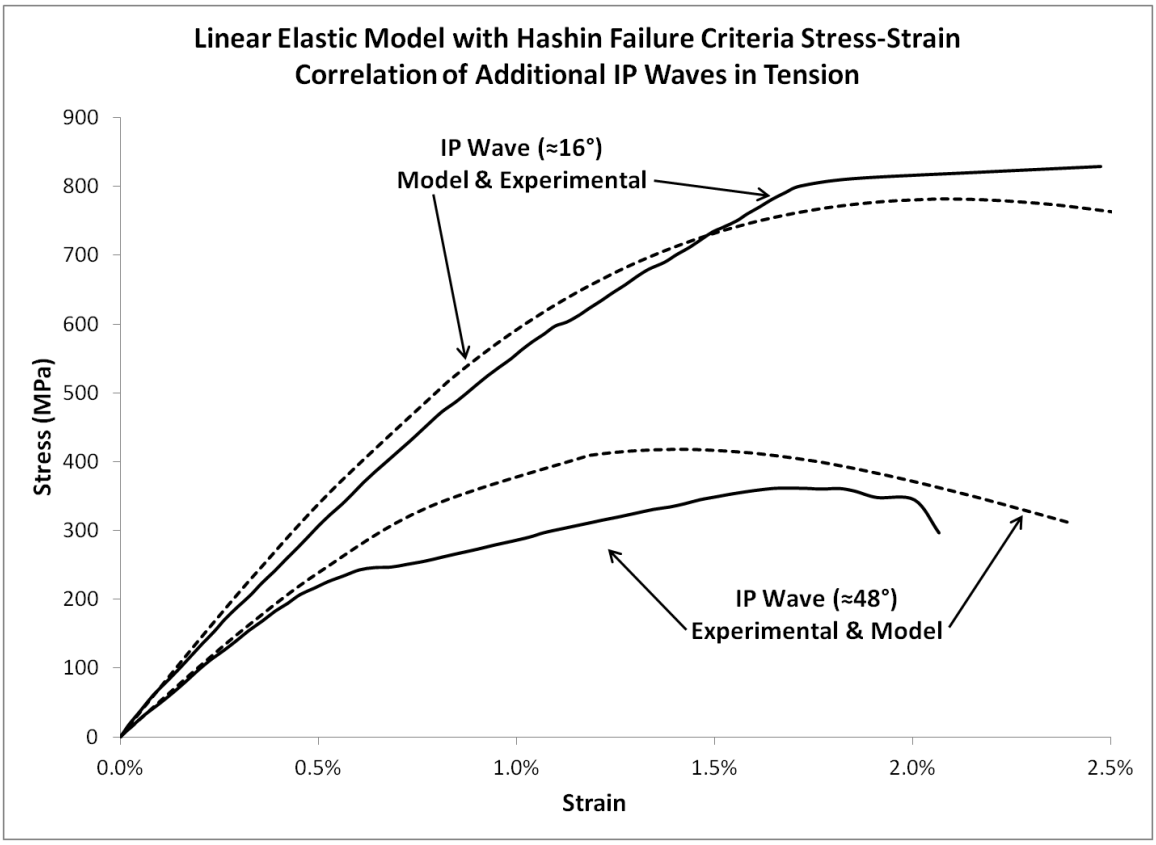

Figure 70: Stress-strain comparison of 16° and 48° IP waves cases in tension results indicating reasonable overall correlation and prediction.

While each model varied in its ability to predict ultimate failure stress, each case was consistently able to match initial coupon moduli. Exact response was not matched from that point on, but that response resulted from two of the stated assumptions. The first assumption is fundamental to the continuum approach: since the material in the model was generalized, exact failure modes were not able to match and as such an exact correlation cannot be expected. In addition, when combined with the assumption of uniformity not actually seen in the coupons, the resulting correlations appeared quite reasonable, and it appeared that this model did have some predictive capability in these

bounding cases. To drastically improve the results, and likely improve the predictive capabilities, a more complex model would be needed that addresses one, if not both, of these assumptions, which is left as future work. The two compression cases were run, but, as noted above, correlations were not performed. Overall, this model indicated that for IP waves in tension, this approach is able to offer correlation and has reasonable predictive capabilities.

Carbon Fiber IP Waves in Tension

Following the systematic approach and to further test the predictive capability of this modeling approach, the same model was run with the initial IP wave case (Figure 56, right) changing the material to a uni-directional carbon fiber. Material properties and damage parameters were gathered from the BMT and from Soden et al. (1998) who characterized two typical uni-directional carbon fiber/epoxy composites quite extensively. These material properties are shown below in Table 13, while the damage parameters are listed in Table 14. It is worth noting that at the time of this publication comprehensive carbon data for this material system and IP wave results were not able to included in the BMT. As such, comparisons between fiberglass and carbon fiber composites utilizing these outside carbon data were justified to determine consistency and predictive capability of this model against general trends known to exist between these common materials.

Table 13: Carbon fiber material properties generated as outlined in BMT section and from Soden et al. in italics (1998).

	E_1	E_2	v_1	G_{12}	G_{13}	G_{23}
Tension (GPa)	83.9	5.8	0.29	*5.5*	*5.5*	*5.5*

Table 14: Starting damage initiation and evolution parameters for carbon fiber models with Hashin failure criteria.

Property	X^T	X^C	Y^T	Y^C	S^L	S^T	G^c_{Lt}	G^c_{Lc}	G^c_{Tt}	G^c_{Tc}
Value	1200	900	40	200	110	110	7.7	20.4	112.0	67.0
Units	MPa						kN/mm			

As expected, the qualitative comparison of the strain accumulation leading to damage was consistent between for the carbon fiber (Figure 71) and that noted above for glass (Figure 60, left). This was largely expected due to the consistent damage progression noted with this technique. Quantitative comparison (Figure 72) indicated that the carbon IP wave model was approximately twice as stiff as the experimental coupon which matched the initial difference in longitudinal modulus. The model predicted softening to then begin at approximately 500 MPa which was higher than the roughly 400 MPa seen in the glass experiment and model. At this point, damage was noted in the carbon model and continued to progress until it reached a peak stress of approximately 640 MPa at approximately 0.8% strain. This level of strain matched common trends where carbon fibers generally have a strain at failure of approximately half of glass. Some load-carrying capacity was noted beyond this point, but the model predicts reduction in residual strength up to approximately 1.5% strain. Overall, this carbon model offered a jumping off point and appeared to vary from the glass experiment and model typically based on normal comparisons of glass and carbon fibers. Future

work to compare to actual carbon fiber IP wave coupons is highly recommended with a full array of material and damage properties generated for same carbon material as tested. This will ensure that the carbon model is accurate.

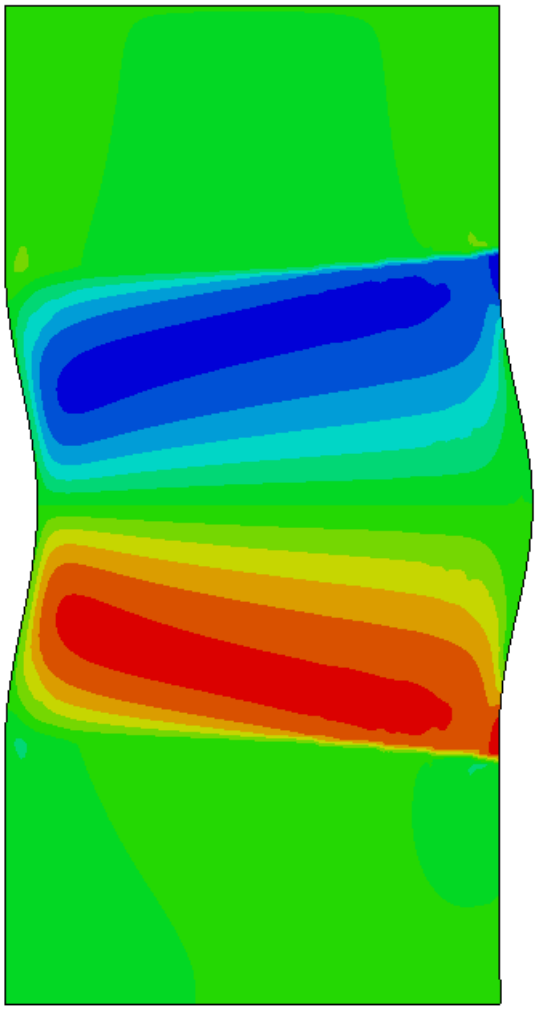

Figure 71: Shear strain field of linear elastic model with Hashin failure criteria for carbon fiber material.

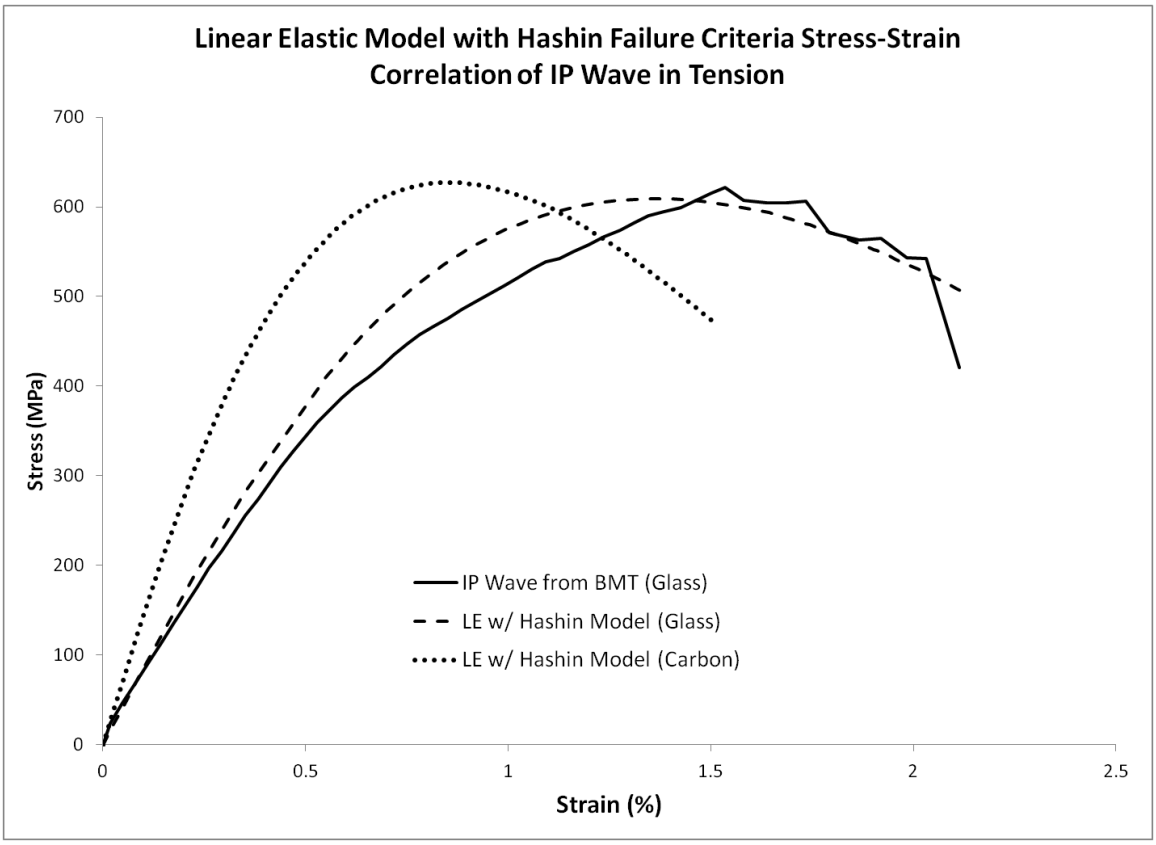

Figure 72: Stress-strain comparison of fiberglass composite from BMT and model with Hashin failure criteria with predicted carbon response for IP wave with same Hashin model.

Hashin Failure Criteria Approach Summary and Conclusions

A continuum based, linear elastic model was modified to include damage progression built into Abaqus for the elastic-brittle nature of fiber-reinforced composites. This tool utilized Hashin failure criteria, and damage was characterized by implementing a stiffness degradation that neglects the plastic deformation commonly missing in the response of fiber-reinforced composites. Material properties and baseline damage initiation and evolution criteria were determined from BMT and were used as initial

model inputs. Correlation to BMT testing was performed and justifiable tuning of these latter parameters was utilized to better understand the effects on the results and to improve prediction. Two models were built and run: one for a 2% porosity case, the other for an IP wave case. Each had varying correlation results.

The method of reducing the input material properties for porosity based on Kerner's rule of mixtures approximation, combined with a linear elastic model utilizing Hashin damage initiation criteria, resulted in good correlation in tension. In compression, a result that appears reasonable was achieved with the model; however, no correlation data exists due to the complexity of compression testing. Given these results, and the fact that this model was truly a CDM, no additional methods were considered on the coupon level. Since correlation was achieved, and since the model was simple to set up, and was computationally inexpensive to run, additional examination of the porosity cases was deemed unnecessary, as further testing would be required. However, it is suggested that this testing be performed and further correlations at larger scales be performed as future work.

Similarly, the IP wave in tension showed reasonable correlation initially, though the model over-predicted damage. The damage inputs were then adjusted, and the model then slightly under-predicted the strain at which the peak stress occurred, but it captured the damage progression and load transfer portion of the curve quite well. In addition, qualitative observations comparing the test and the model match well All of these results indicate that the model does have some predictive capabilities, as material properties and initial damage inputs were based on unflawed controls from the BMT. While correlation

was reasonable in tension, it was not achieved in compression, as the model predicts rotations not seen in the BMT. For the IP wave case, it is suggested that future work include utilizing this model, as its testing offers correlation points at larger scales such as a flaw included in a structure. In addition, further testing to better understand the effects in compression is recommended to model these damage progression cases.

Other wave types and fiber misalignment angles were then modeled to determine model capabilities. First, OP waves modeled utilizing the tuned parameters from the initial IP wave case, though the perspective of the model was rotated. The results indicated that good correlation was achieved in tension, though visual damage progression was more difficult to analyze. A compression model was created and run; however, correlation is left to future work at such a time when OP wave compression results become available. Next, two bounding IP waves were modeled in tension with the tuned parameters and correlated to assess the accuracy, consistency, and predictive capability of the model. While neither case correlated as well as the initial IP wave case, both were reasonable and as such this model indicates that for IP waves in tension, this approach was able to offer correlation and has reasonable predictive capabilities. Further predictive capabilities were checked by changing material to a carbon fiber and comparing to the initial IP wave case with glass. Comparisons were reasonable given normal comparative trends from fiberglass to carbon fiber composites.

Overall, this linear elastic model with the Hashin failure criteria were found to have reasonable correlation in tension, but correlation was not achieved in compression. Further work has been identified and may be warranted, given the ease of working with

this model and its light computational expense. Comparison to other modeling approaches is offered in detail below.

LINEAR ELASTIC CDM WITH USER-DEFINED FAILURE CRITERIA

Introduction

Based on the increase in complexity from Round 1 to Round 2 of the three round systematic approach, an approach was attempted to offer the user more control compared to what was offered by the built-in Hashin failure criteria. A similar linear elastic model was created but the Hashin failure criteria were replaced with a subroutine with user-defined failure criteria. This method calculated the material response with a damage check subroutine at each iteration and allowed for a mixture of stress and strain based criteria to be utilized. Once damage has been initiated, the subroutine specifies a material property degradation scheme based on the type of failure that has occurred. A model was created and utilized to predict the effects of an IP wave. Analytical/experimental correlations were made and a significant amount of tuning, largely of the material property degradation scheme, was performed in an attempt at convergence. Given the amount of tuning necessary that still resulted in poor correlation, this modeling approach was found to be insufficient for predicting material response of an IP wave in tension or compression.

Methods

The standard linear elastic model used above was modified and a material degradation subroutine with user-defined failure criteria were utilized. Similar to the models above, the geometry was set up to match the intended coupon size (100 mm x 50

mm) established during the BMT. A 2D model (Figure 73) was generated with an IP wave geometry, with quadrilateral, plane stress shell elements (S4R), in Abaqus where each element was generated to be consistent with the nominal fiber tow width (1.0 mm). The IP wave modeled had an amplitude (A) of 3.8 mm, a wavelength (λ) of 47.6 mm, and average off-axis fiber angle of 28.7°. Local coordinate systems were defined for the elements oriented to form the wave such that the fiber direction remained consistent through the wave, and the material properties were modeled to correctly match these properties. Displacement and boundary conditions were applied at the top and bottom, respectively, to match the BMT testing conditions and as such, full field calculations were made to match the BMT data for load-displacement and stress-strain correlations.

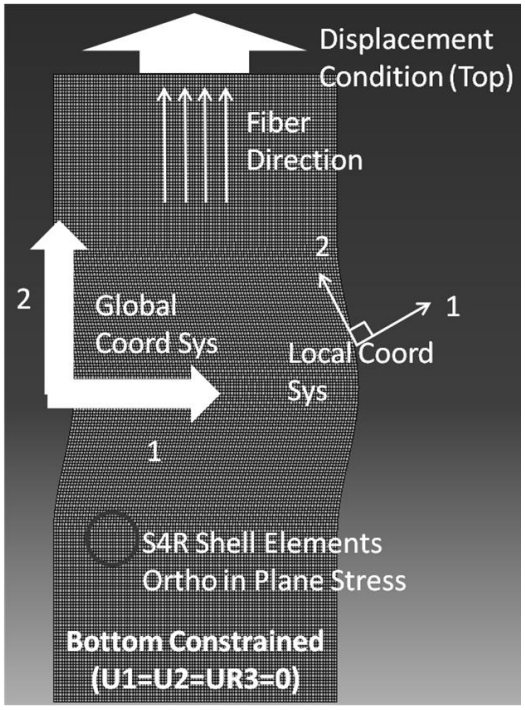

Figure 73: The IP wave model utilized in the linear elastic models with the user-defined failure criteria.

In reviewing the test data, images, and DIC data, it was apparent that initial damage occurred in each wave at low loading levels on the ends of the samples where fibers ended on the coupon edge. Due to the wave pattern introduced when the samples were cut, fibers through the wave were cut, resulting in discontinuous fibers along the sample length. Based on this observation, it was assumed that these portions of the laminate were not of interest when considering the goal of isolating defects. Thus, the geometry shown in Figure 73 was utilized for all of the IP wave modeling efforts in this Chapter.

Even though a 2D model was utilized, the *SHELL SECTION* keyword option was utilized to specify the laminate through the thickness as shown in the snippet of code below. Use of the *COMPOSITE* option allowed for various properties for each theoretical layer of the specified element set, *PLATE*, with the specified *LOCAL* orientation:

```
*SHELL SECTION,COMPOSITE,ELSET=PLATE,ORIENTATION=LOCAL
1.0,1,PPG,0.0
1.0,1,PPG,0.0
1.0,1,PPG,0.0
1.0,1,PPG,0.0
```

The fiber orientation of each element, *LOCAL*, was specified in a *DISTRIBUTION TABLE* with respect to the model edge. The properties for each layer were defined on each line: thickness (1.0 mm), number integration points through the thickness (1), material name (PPG), and rotation from defined 1-direction (0.0), respectively. Thus, the total laminate thickness modeled was 4 mm. Elastic material properties that were generated from the BMT discussed above were again utilized. Note that a summary of the

key points of the code is presented here, while complete code may be found below in the Appendices.

Several assumptions were made to simplify this modeling effort. First, it was assumed that all fibers were parallel and uniform in the intended direction with reference to the widthwise edge. It was also assumed that all the fibers were parallel and aligned through the thickness. These assumptions greatly simplified the modeling approach even though they were a source of the variation noted within the BMT. In addition, perfect bonding between the layers was assumed. In the case of the IP wave, it was assumed that the initial failures and debonds of the discontinuous edge fibers had negligible effect on the material response and were disregarded for this effort.

Subroutine Approach and Summary

Simple CDM's have been utilized in finite element analyses that account for damage in the fiber and matrix, independently. Utilizing a simple material property degradation model, Chang and Chang (1987) presented a progressive damage model for laminated composites with a circular hole in tension. Convergence between stress and failure analyses were performed utilizing classical lamination theory considering material nonlinearity and property degradation resulting from damage, respectively. Nonlinear finite element analysis was performed and agreement was found between the analytical and experimental data. In the stress analysis, the equilibrium equation and stress-strain relations were derived. The equilibrium equation took into account that once the laminate was damaged, a redistribution of the stresses and strains resulted in degraded material properties. Thus, the equilibrium equation was solved at each step utilizing a

Newton-Raphson iteration scheme. The failure criteria were defined based on the failure mechanisms resulting from damage: matrix cracking, fiber-matrix shearing, and fiber breakage. Based on these criteria, a property reduction model was implemented reducing certain properties to zero upon failure. Numerical procedures were written based on the following procedural logic:

1. Increase the applied load from P^{n-1} to P^n by a small increment ΔP.
2. Calculate incremental strains, $\Delta\varepsilon_{ij}$, and incremental stresses, $\Delta\sigma_{ij}$, from derived stress-strain relations and equilibrium equations.
3. Update the total stresses, σ^n_{ij}.
4. Calculate in-plane stresses in each ply by coordinate transformation.
5. Assess damage using failure criteria equations.
6. Return to the first step if no damage is found or continue to the following steps if damage occurs.
7. Stop, if damage has propagated across the laminate and no more load can be added.
    a. Continue, otherwise.
8. Update material properties by applying property degradation model.
9. Redistribute stresses and strains in the laminate by applying equilibrium equations.
10. Return to step (4).

Following this logic, Chang and Chang's results agreed with the analytical and experimental data from seven independent laminates. Later, Chang and Lessard (1991)

performed similar work on damage tolerance of laminated composites in compression with a circular hole. Based on this research, Abaqus created a user subroutine to model damage progression for a circular hole within a composite laminate that achieves in good agreement. Similar input code files were written to run IP wave models in Abaqus utilizing the decision tree shown below in Figure 74. This decision tree was derived from the logic noted above, and the steps that are standard inputs are indicated with darker backgrounds while the user-subroutine steps are shown lighter.

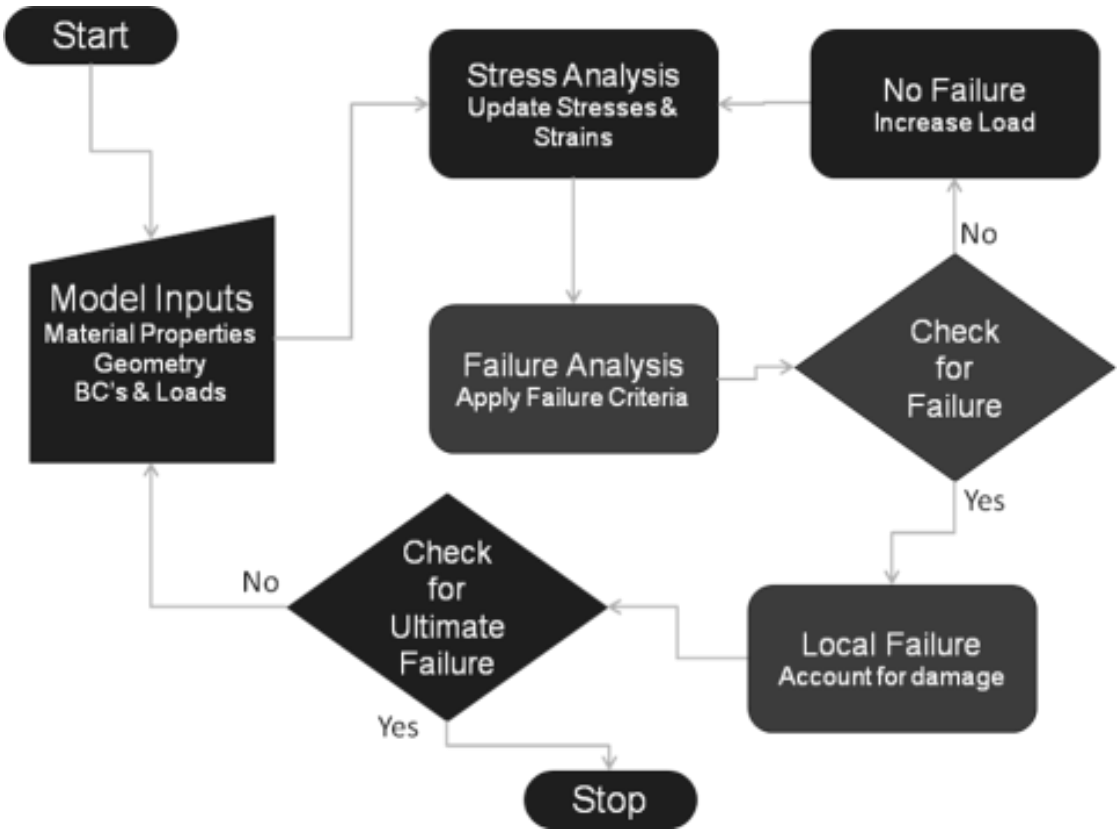

Figure 74: Decision tree for progressive damage modeling utilized in this modeling.

User-defined Failure Criteria Approach

As shown above in Figure 74, the standard input file built and meshed the model, while the subroutine checked for damage at each increment. Three individual types of damage were estimated: matrix cracking damage, fiber-matrix compression damage, and fiber failure damage. Based on detection of each of these, or a combination of damage types, specific material properties were reduced to zero (0) based on the assumption of brittle failure with no energy absorption (Table 15). In short, if damage was detected, the material properties were adjusted, or the loop was stopped if ultimate failure occurred. If damage was detected but not ultimate failure, the material properties were degraded depending on the type of failure as outlined in Table 15 below.

Table 15: Progressive damage outline and degradation approach.

Material Failure Type	Elastic Property Adjustments for Each Failure Type				Failure Value			Notes
					#1	#2	#3	
No Failure	E_x	E_y	v_{xy}	G_{xy}	0	0	0	Full Properties
Matrix Cracking Damage	E_x	0	0	G_{xy}	1	0	0	Used in Tensile and Compressive cases
Fiber-Matrix Compression Damage	E_x	E_y	0	0	0	1	0	Fiber Compresses & Matrix Cracks; Compression Only
Fiber Failure Damage	0	0	0	0	0	0	1	Fiber Buckles or Breaks; All properties drop to zero
Combined Matrix Cracking & Fiber-Matrix	E_x	0	0	0	1	1	0	Fiber is still intact and able to carry some load.
Combined Matrix Cracking & Fiber	0	0	0	0	1	0	1	All properties drop to zero
Combined Fiber-Matrix & Fiber	0	0	0	0	0	1	1	
All Combined Failure Modes	0	0	0	0	1	1	1	

To determine the failure values, user-defined failure criteria integrating both maximum stress and strain criteria were implemented into the subroutine. A modified maximum stress failure criterion was implemented with the inclusion of a maximum strain criteria to accurately model ultimate fiber failure. As such, matrix cracking damage was estimated by:

$$\left(\frac{\sigma_{22}}{Y_T}\right)^2 + \left(\frac{\tau_{12}}{S_T}\right)^2 = 1 \quad (1)$$

where σ_{22} and Y_T are transverse stress and transverse strength, respectively, and τ_{12} and S_T are shear stress and strength, respectively. It must be noted that this same equation was utilized for both tensile and compressive cases, and the associated material properties are changed for each case (Table 14). While the fiber-matrix compression damage case appeared to be necessary only in compression loading cases, with the given geometries these failure criteria were utilized in both tensile and compressive cases:

$$\frac{\sigma_{11,C}}{Y_C} + \frac{\tau_{12}}{S_T} = 1 \quad (2)$$

where $\sigma_{11,C}$ and Y_C are fiber compressive stress and strength, respectively. Finally, two different equations were utilized depending on whether fiber failure is in tension or compression, respectively:

$$\frac{\varepsilon_{11,T}}{\bar{\varepsilon}_T} = 1 \quad (3)$$

$$\frac{\sigma_{22,C}}{X_C} = 1 \quad (4)$$

where $\varepsilon_{11,T}$ and $\bar{\varepsilon}_{11,T}$ were calculated for ultimate tensile strain and compressive stress, respectively. Utilization of the maximum strain criterion in tension was based on the consistency of strain at failure of these materials as determined in the BMT and MSU-CMD. Integration of this criterion was a fundamental motivation in utilizing this user-defined technique.

Thus, at each increment the subroutine ran through these failure criteria equations that utilize the stress and strain data of that increment. Resulting values of these

equations range from zero (0) to one (1) with failure occurring when the value was equal to one (1). As the failure indices were calculated to be one (1), failure has occurred in that element and the material properties were adjusted based on the failure type as noted in Table 15 above. For example, if a matrix failure occurred, the failure indices included in the user subroutine calculated that Failure Value #1 became equal to one (1). As a result, the elastic properties for that element only include E_x and G_{xy} as these are fiber dominated. The loop continued with the degraded properties until fiber failure or a combination of failures occurred resulting in no material properties for that element.

User-Defined Failure Criteria Subroutine Code

The standard code portion for this method was fairly simple and only requires three portions of code. These were:

**ELASTIC,TYPE=LAMINA, DEPENDENCIES=3*
E_{11}, E_{22}, v_{12}, G_{12}, G_{13}, G_{23}, *T*, FV_1
FV_2, FV_3
⋮
{These lines are repeated for every possible combination of FV's; 8 in this case.}
**DEPVAR*
3,
**USER DEFINED FIELD*

where the material type was identified (**ELASTIC*), the first six inputs were elastic material properties, *T* was the temperature which was left as zero in this case, and *FV* were each of the failure values that were calculated in the subroutine. As such, the input lines were repeated for each possible combination of failure value options, which was 8 in this case, as outlined above in Table 15. Next, the number of dependent variables (**DEPVAR*) was declared to match the number of failure values utilized (3) which also

matched the number of *DEPENDENCIES* noted. Finally, the subroutine was called into use with the **USER DEFINED FIELD* keyword command which must occur in the material property definition as shown here. This keyword is one of over 50 different user subroutines available in Abaqus and allows the user to define changes in material response based on the loading or stress state in the solution. In this case, field variables were updated based on changes in state variables based on material point data as outlined in the subroutine explanation below.

Defining the subroutine is a more complex and detailed undertaking than the standard code was in this case, as a separate FORTAN source code file must be written. It is important to note that only portions of the code that are specific to this technique are discussed, while the specifics of FORTRAN are left to the reader. Complete code may be found in the Appendices and more comprehensive explanations of subroutines and use in Abaqus may be found in the Abaqus User Subroutines Reference Manual (2012).

First, the subroutine interface with the standard code and the specific material parameters must be established:

```
      SUBROUTINE USDFLD(FIELD,STATEV,PNEWDT,DIRECT,T,CELENT,TIME,DTIME,
     1 CMNAME,ORNAME,NFIELD,NSTATV,NOEL,NPT,LAYER,KSPT,KSTEP,KINC,
     2 NDI,nshr,coord,jmac,jmtyp,matlayo,laccflg)
C
      INCLUDE 'ABA_PARAM.INC'
C
      PARAMETER(XC=5.8D2,YT=6.6D1,YC=3.5D1,ST=1.24D2,ET=2.6D-2)
C
      CHARACTER*80 CMNAME,ORNAME
      CHARACTER*3  FLGRAY(15)
      DIMENSION FIELD(NFIELD),STATEV(NSTATV),DIRECT(3,3),T(3,3),TIME(2),
     * coord(*),jmac(*),jmtyp(*)
      DIMENSION ARRAY(15),JARRAY(15)
```

The material and strength parameters were the damage criteria taken from the BMT as discussed in the next section below. It is worth noting that while each of the *USDFLD* parameters was turned on in the first several lines of this code, only those listed in Table 16 are utilized.

Table 16: Variables defined and passed between the subroutine and standard code utilized in this routine.

Variable	**Definition**
DIRECT (3,3)	Material direction cosines relative to GLOBAL
T(3,3)	Material direction cosines relative to elements
TIME(2)	Time step of current increment
CMNAME	Material name
ORNAME	Local orientation name
FIELD(NFIELD)	Variables to be defined and passed out
STATEV(NSTATV)	Variables to be updated
COORD	Material point coordinates
JMAC	Variables passed into the GETVRM() to access an output variable
JMTYP	
MATLAYO	
LACCFLG	

Next, the failure variables were initialized and the stresses were retrieved from the previous increment:

```
EM     = STATEV(1)
EFS    = STATEV(2)
DAMAGE = STATEV(3)
CALL GETVRM('S',ARRAY,JARRAY,FLGRAY,jrcd,
$     jmac, jmtyp, matlayo, laccflg)
S11 = ARRAY(1)
S22 = ARRAY(2)
S12 = ARRAY(4)
ET = ARRAY(4)
```

Finally, the crucial portion of the code was reached where the stresses were used to check for failure in each of the cases, or each dependent variable is determined. A simple *IF* loop was utilized for each of the Equations 1-4 noted, with 3 and 4 being manually swapped out for tension and compression, respectively. For example, matrix cracking damage was coded:

```
IF (MC .LT.  1.D0) THEN
  MC = (S22/YC)**2 + (S12/ST)**2
  STATEV(1) = MC
ENDIF
```

where *MC* is the name for the matrix cracking damage variable. The loop first determined that if the matrix cracking damage variable was less than one, the loop then recalculated with the updated stresses, *S22* and *S12*, before updating the appropriate state variable. No calculation was necessary if the value was one because failure already occurred. Finally, the state variables were used to update the field variables which were then passed back to the standard code, and the code was ended:

```
FIELD(1) = 0.D0
FIELD(2) = 0.D0
IF (MC .GT.  1.D0) FIELD(1) = 1.D0
IF (FMD .GT.  1.D0) FIELD(2) = 1.D0
FIELD(3) = FFD
STATEV(3) = FIELD(3)
RETURN
END
```

User-Defined Failure Criteria Subroutine Model Inputs

When compared to the Hashin failure criteria above, this modeling approach requires fewer inputs, and they are more easily taken directly from the BMT. As such,

elastic material properties that were generated from the BMT discussed above were utilized (Table 10). The specific inputs necessary for damage initiation for this model were also generated from the BMT or were as listed in the MSU-CMD as shown in Table 18 below. In all cases, modifications of these inputs are noted and justified in the discussion below, or in cases where justification was not possible, they are deemed unacceptable and are noted as such.

Table 17: Material properties generated as outline in BMT section.

	E_1	E_2	v_1	G_{12}	G_{13}	G_{23}
Tension (GPa)	40.6	16.3	0.27	16.8	16.8	16.8
Compression (GPa)	38.4	14.4	0.28	14.4	14.4	14.4

Table 18: Failure criteria inputs as determined from BMT.

Property	X^C	Y^T	Y^C	S^T	ε^T
Value	582	60	162	124	2.6%
Units	MPa				Strain (%)

Results and Correlation

A model was run with an IP wave added to the coupon geometry utilizing a user-defined material property-driven damage progression as outlined above. Load-displacement and stress-strain data were generated and used to compare and correlate, respectively, to BMT results. Processing times for all runs of this model ranged from 2.5 to 8 minutes in length. Continuing with the systematic approach outlined above, the initial case considered was an IP wave, first in tension and then in compression. Correlation was not achieved in either tension or compression and further analysis was not performed as detailed below.

IP Wave in Tension

As noted above, IP wave tension coupon samples from BMT results clearly showed coupon failure was less sudden than for the unflawed controls or porosity specimens. Initially, shear damage was noted in the area of the fiber misalignment, generally in the area of peak fiber misalignment, and it progressed both transversely perpendicular to the fiber and longitudinally parallel to the fiber along the wave. First fiber failure was noted in the areas where this damage had progressed together and had met from both sides of the wave. This progression was visualized with the use of DIC which allowed for initial visual comparison to analytical solutions, and it is shown in Figure 75 (right and left, respectively) for the linear elastic user-defined failure criteria model. As shown, the model captured the area of strain accumulation where damage occurs at the peak fiber misalignment angle. The strain accumulation then progressed toward the edges perpendicular to the fiber direction and longitudinally to the wave peak between the two areas of fiber misalignment. It should be noted that this initial comparison is qualitative and visual only.

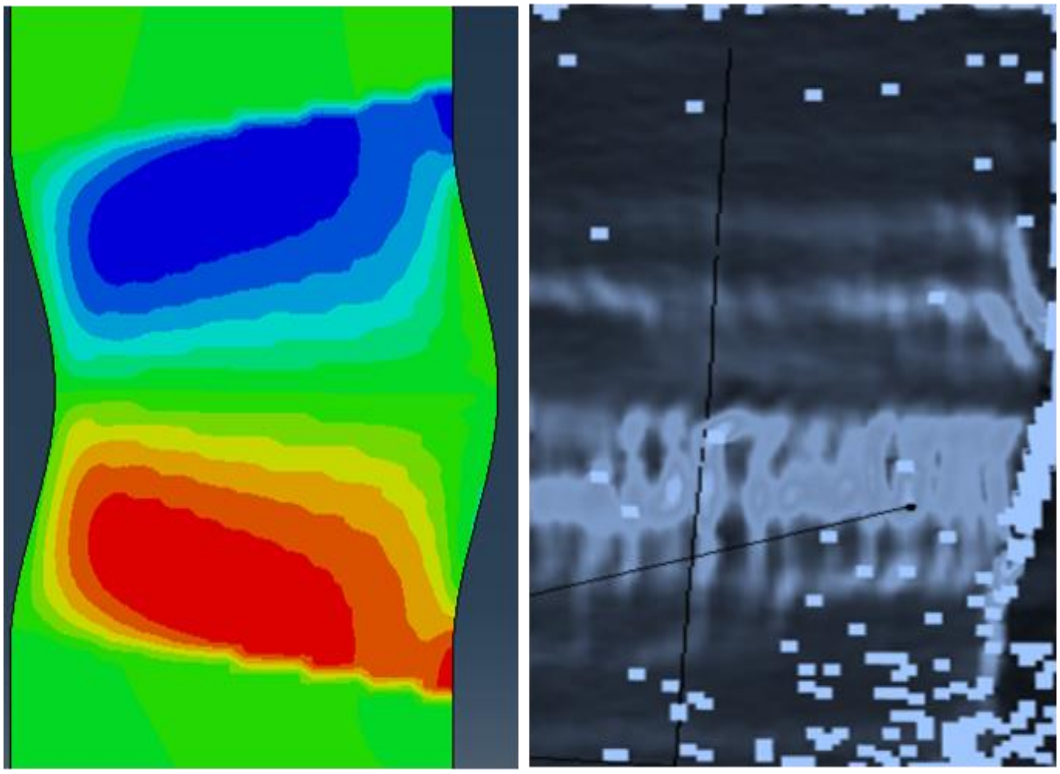

Figure 75: Shear strain field comparison of linear elastic with user-defined failure criteria solution (left) and DIC image (right) in tension.

While strain accumulation seemed to be occurring in the same areas, the model may not have actually calculated that damage had occurred in these areas, as was likely the case here. Again, similar to above, quantitative analytical/experimental correlation was performed utilizing stress-strain curves (Figure 76). These indicate that amount of dissipated energy is approximately equal between the experimental and analytical. With the inputs noted above, the response matched the initial stiffness of this IP wave fairly well as shown in Figure 76. However, this correlation was noted for only a very short duration, and as the experimental IP wave coupon began to soften, the model showed no sign of softening. The model instead predicted a continued response up to approximately

0.5% strain where the stress reached approximately 480 MPa which was more than 30% greater than the stress in the coupon at this strain. At this point, initial matrix failure occurred in a large portion of the wave area and the transverse properties were reduced to zero. Load redistributed occurred and the stress climbed to approximately 610 MPa at just under 1.0% strain where additional failures of each type occur. This stress matched the peak stress noted in the BMT for this IP wave geometry; however, the coupon did not see this level of stress until approximately 1.8% strain. At this point, the model predicted reduced load-carrying capacity up to approximately 1.7% strain, where all load-carrying capacity was lost. This trend appeared to match the coupon response after the coupon reached peak stress before ultimate failure. So while it appeared that the model was able to match the coupon response initially and at the end, what occurred in between shows the model was unrealistic. In addition, the model predicted damage to occur at three distinct points, indicating that the model was not able to capture the smaller scale damage. As damage occurred in the coupons, it generally occurred within small areas incrementally with only two large events, initial softening and peak stress. The model did not capture these responses in the same way and caused action to be taken to improve the modeled response.

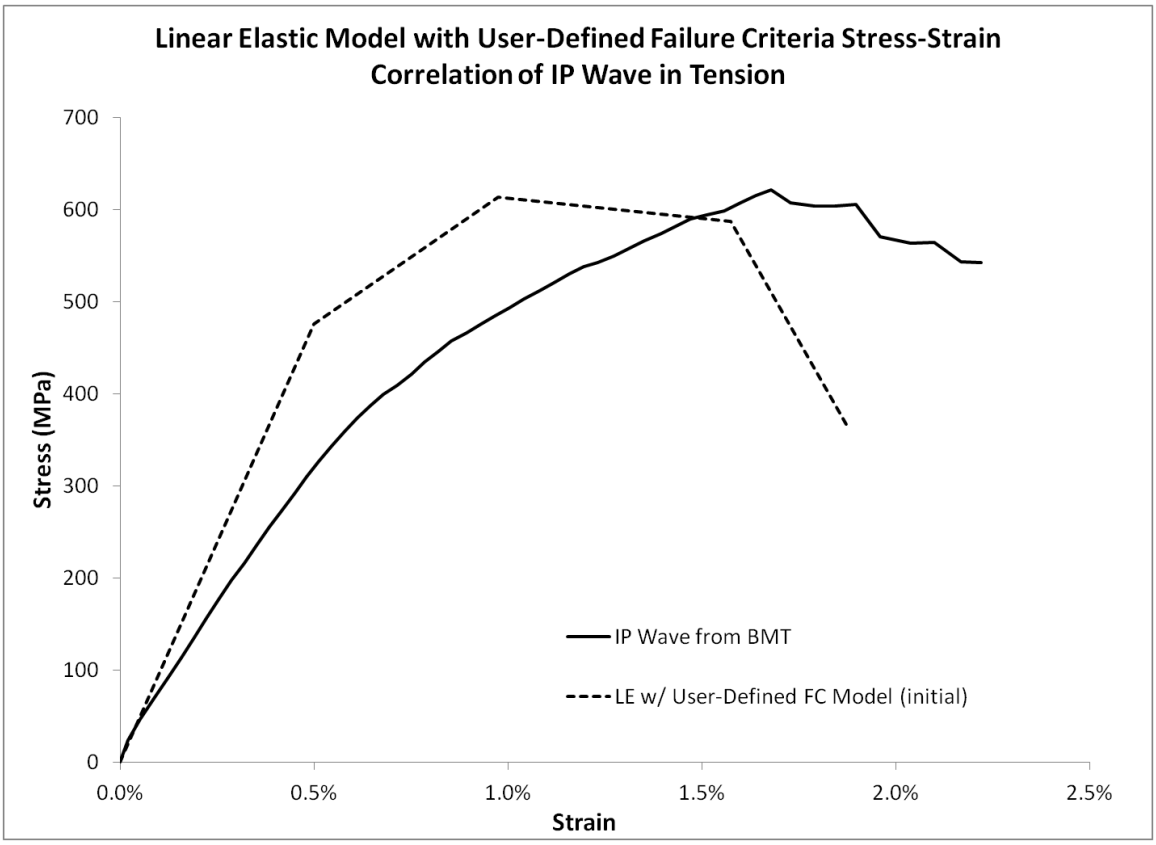

Figure 76: Stress-strain comparison of IP wave BMT and initial linear elastic with user-defined failure criteria model in tension.

To attempt to improve the model's predictive capability, first steps were taken to ensure that the model was performing correctly from a coding standpoint. In particular, time increment size and mesh sensitivity were checked, both of which resulted in a doubling of run times up to approximately 6-8 minutes. First, the time increment was dropped by an order of magnitude (from 0.1 to 0.01) and the maximum time increment allowed was set to the same value to ensure that the small increment was consistent throughout the analysis. No change in the predicted response was noted. Next, the mesh size was incrementally reduced such that the width criteria went from 2 to 4, meaning

that instead of 2 elements along an element edge, they were increased to 4. This increase also saw no noticeable change in the model results.

It was anticipated that this technique would allow for more user control of the model and as such model tuning would be easier to perform and justify. The easiest method to achieve this was to adjust the partial material property degradations, as these parameters were not directly identified in the BMT, nor were they utilized and confirmed in other modeling approaches. As noted above, when a failure was detected, certain material properties were degraded to zero. It may be argued that this degradation was inaccurate and that there was usually some continued load-carrying capacity up to final failure of a particular element. To determine the effects of this degradation, several partial degradation cases were attempted. For matrix cracking and fiber-matrix compression damage, material properties were dropped to 25% and 50% of original values instead of zero. These reductions were also adjusted for the combined case of the two damage types; however, fiber failure was left to degrade all properties to zero as this was a final failure event for each element. As would be expected, the 50% values saw a more drastic change than the 25% values, though neither was as significant as hoped (Figure 77). Overall, the stress-strain response improved, but not at the level seen in other techniques. Additional work could be performed to attempt improved correlation, but this would likely take considerable upfront time in further assessment of model setup and failure criteria. In short, future work is recommended with additional investigation into development of the FORTRAN user-subroutine.

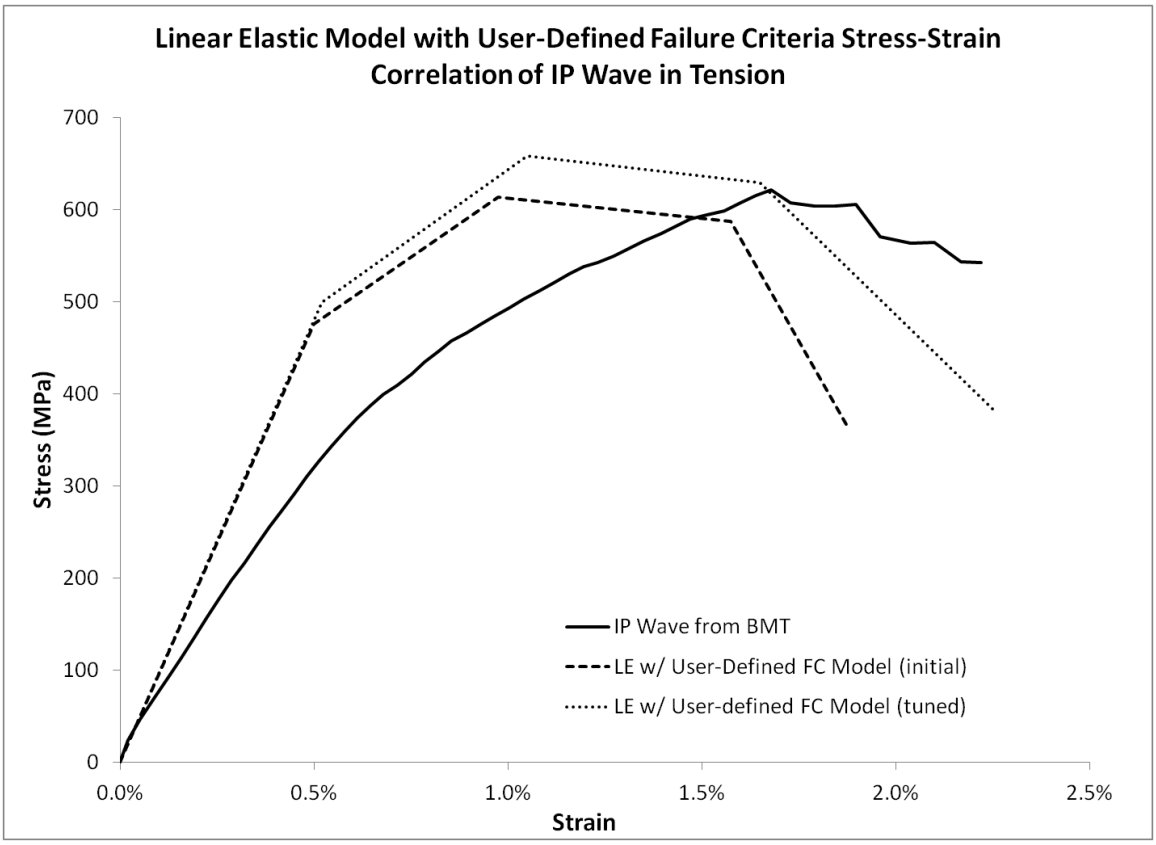

Figure 77: Reprint of stress-strain curve from Figure 76 with addition of tuned linear elastic with user-defined failure criteria model in tension.

IP Wave in Compression

Following the systematic approach, the model was also run for the same IP wave in compression, though the boundary conditions were slightly modified such that the straight fiber sections of the model were constrained to prevent transverse displacement, thereby effectively reducing the gage section. Initial inputs were used as listed in Table 17 and Table 18 above with compression data replaced for the material properties. As noted, analytical/experimental correlation was not as straightforward for the compression case as it was for the tension case, due to the damage progression not being visualized as

easily during BMT. As noted above, the gage section for the compression tests was significantly smaller than it was for tension reducing the amount of area the DIC was able to capture. Since the flaw dominated this area, only a small amount of unflawed area was imaged at the top and the bottom. However, as noted in Figure 78 and in the BMT above, matrix failure was visually noted at both edges initially before progressing across the wave, due to the shear stress increasing with load. As the load increased, the wave effectively pushed transversely, causing rotations that increased stress from the left edge around the peak of the wave to the base of the wave at the right edge. The model was able to capture this effect; however, instead of the effect's happening in a progressive manner as noted by the softening of the coupon response in Figure 79, the model predicted failure abruptly at a higher amount of dissipated energy. Up to the point that softening began, the model matched the initial stiffness. Similarly to the tensile case, the model did not account for this softening, and stress increased up to approximately 260 MPa, which matched within 10% the peak stress of the coupon. However, the strain at this point for the model was approximately 1.5% instead of nearly 2.0% for the coupon, and at this point the model predicted little additional load-carrying capacity. Even with the 25% reduction in the estimated strain at peak stress, this model appeared to correlate better than the tensile case. However, further consideration was not warranted due to the strain at peak stress mismatch, combined with the lack of correlation of the shear-induced softening associated with the IP wave geometry. Additional work could be performed to attempt improved correlation, but this would likely take considerable upfront time in further assessment of model setup and failure criteria.

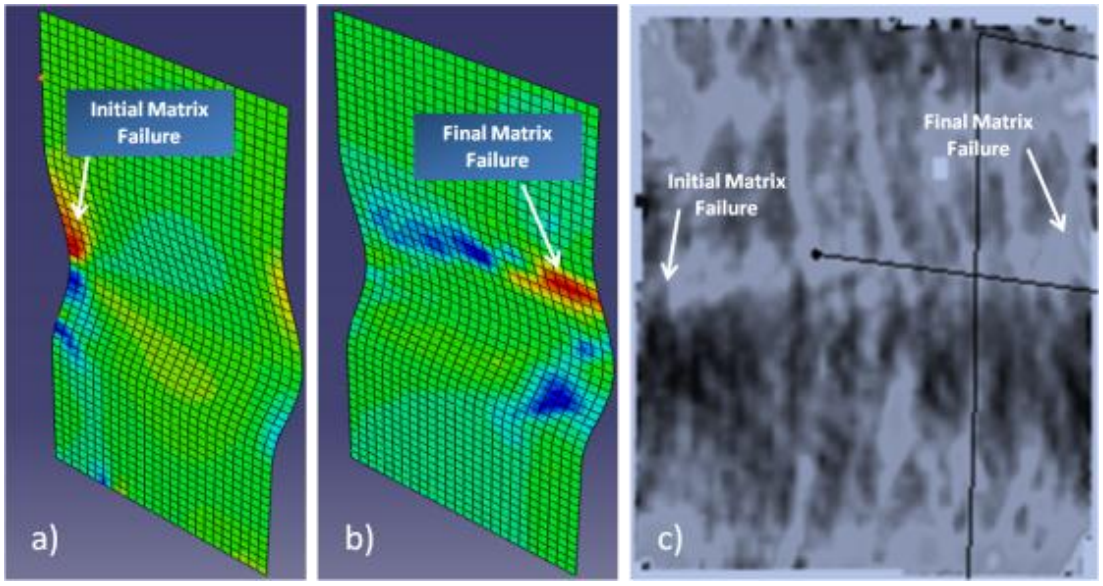

Figure 78: Visual comparison of analytical and experimental compression results where a) indicates initial matrix failure point, b) indicates last matrix failure point before buckling, and c) shows similar behavior from the DIC data.

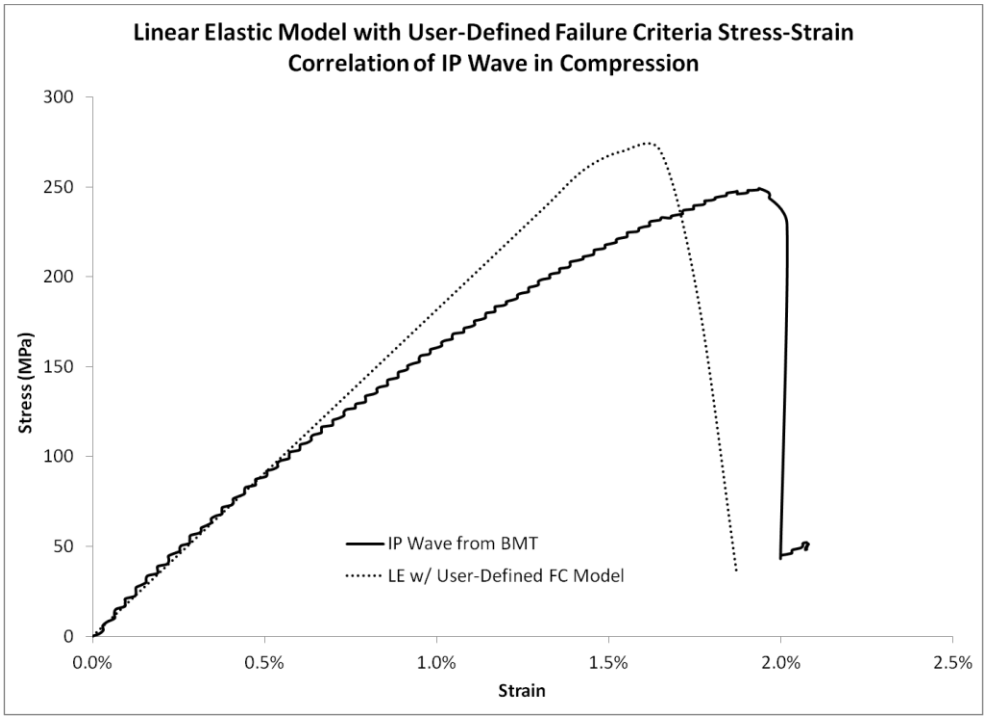

Figure 79: Stress-strain comparison of IP wave BMT and initial linear elastic with user-defined failure criteria model in compression.

User-Defined Failure Criteria Subroutine
Approach Summary and Conclusions

A continuum based, linear elastic model was modified to include a user-defined failure criteria in Abaqus utilizing a user subroutine. The subroutine was written to include combined modified maximum stress criteria with a maximum strain criterion for fiber failure in tension. An IP wave case was developed and run in both tension and compression with material properties and damage criteria that were determined from BMT and used as model inputs. Correlation to BMT testing was performed and justifiable tuning of parameters was utilized to better understand the effects on the results and to improve model correlation and damage prediction.

The IP wave case in tension was found to have reasonable visual correlation with strain accumulations noted in the same areas. However, the model did not match the BMT results quantitatively, indicating that while the strain accumulated in the same places, the resulting responses were different. To improve the model's correlation, attempts were made to adjust the time increment, mesh density, and material degradation. Only the latter showed an improvement in correlation, but not within reasonable limits. As such, further assessment in tension was not deemed worthwhile. The same wave modeled in compression was also found to have reasonable visual correlation with matrix failures occurring in similar progression. Similar to the tension case, the model predicted damage to happen in large amounts instead of incrementally. With the model's under-prediction of the strain at peak stress, further consideration for the compression case was deemed unnecessary.

Overall, this linear elastic model with user-defined failure criteria were found to have poor correlation. Additional work could be performed to attempt improved correlation, but this would likely take considerable upfront time in further assessment of model setup and failure criteria. In addition, the amount of potential work does not seem warranted, given the reasonable and acceptable correlations achieved with other techniques. As such, this is left as possible future work, and in this case this technique was considered insufficient, resulting in no further consideration. However, given the dominance of the shear response in the fiber wave, a different approach was attempted in a similar vein utilizing a user-defined material as outlined in Chapter 7 below. Comparison to this and other modeling approaches is offered in detail below.

CDM WITH NON-LINEAR SHEAR AND TRUNCATION

Introduction

As part of Round 2, to continue improvement of the IP wave case compared to the other CDM approaches above, a similar model was created with a user material card (UMAT) to allow input of specific non-linear shear response with manual truncation at a specified strain. Investigation of the DIC data for all wave cases indicates that the initial damage response was due to shear between the misaligned fibers of the wave. Given this shear response and lack of initial softening noted in the previous cases, this model type was investigated as a possible solution. In short, the subroutine determines state of shear and updates the shear properties based on the tabulated shear stress-strain relationship developed from shear tests during the BMT. Some may consider that this method alone is not a damage model; however, given the method of degrading the shear properties, the author contests that this method is clearly a typical material property degradation model. As indicated by VanPaepegem et al. (2006), unrecoverable damage or plasticity occurs through the shear response. As such, this method degrades the shear material properties based on the shear response that generalizes this noted damage and plasticity. Analytical/experimental correlations were made and correlations were noted at initial low strain levels where the model was able to predict initial softening but then diverged from the BMT results.

Methods

The standard linear elastic model used above was modified and a material degradation subroutine with user-defined failure criteria were utilized. Similar to the models above, the geometry was set up to match the intended coupon size (100 mm x 50 mm) established during the BMT. A 2D model (Figure 80) was generated with an IP wave geometry in Abaqus where each element was generated to be consistent with the nominal fiber tow width (1.0 mm). The mesh was used to model four layers of a 4-node bilinear, plane stress shell element (CPS4) for the continuum elements constituting the fiber tows and surrounding matrix, which was a variation from the S4R elements used in the previous CDM models to simplify the coding required for this particular approach. The IP wave modeled had an amplitude (A) of 3.8 mm, a wavelength (λ) of 47.6 mm, and average off-axis fiber angle of 28.7°. Local coordinate systems were defined for the elements oriented to form the wave such that the fiber direction remained consistent through the wave and the material properties were modeled to correctly match these properties. Displacement and boundary conditions were applied at the top and bottom, respectively, to match the BMT testing conditions, and as such, full field calculations were made to match the BMT data for load-displacement and stress-strain correlations.

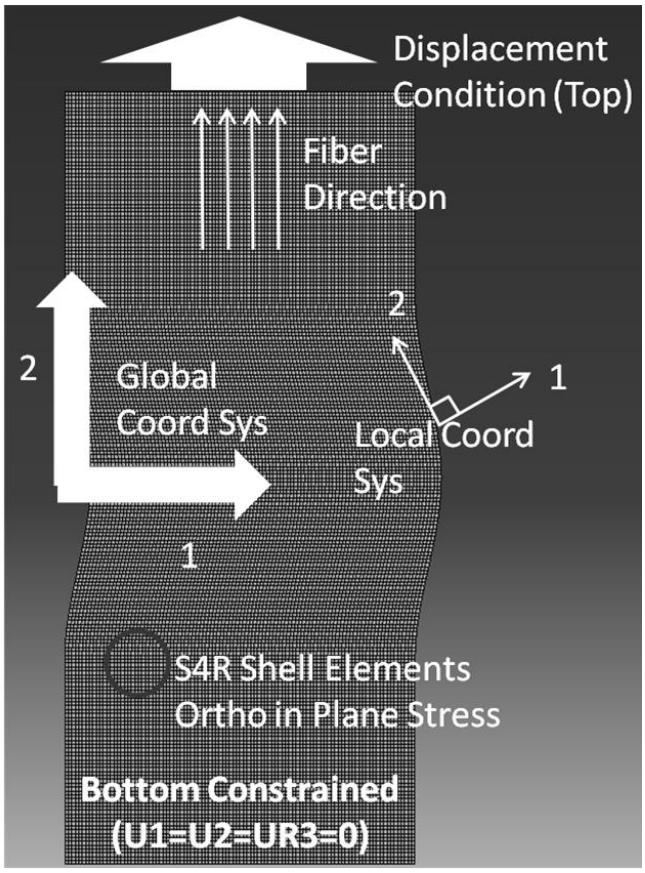

Figure 80: The 2D model setup utilized in the Abaqus linear elastic models.

In reviewing the test data, images, and DIC data, it was apparent that initial damage occurred in each wave at low loading levels on the ends of the samples where fibers ended on the coupon edge. Due to the wave pattern introduced when the samples were cut, fibers through the wave were cut, resulting in discontinuous fibers along the sample length. Based on this observation, it was assumed that these portions of the laminate were not of interest when considering the goal of isolating defects. Thus, the geometry shown in Figure 80 was utilized for all of the IP wave runs outlined in this Chapter.

Even though a 2D model was utilized, the *SOLID SECTION* keyword option was utilized to specify the laminate with a specified thickness as shown in the snippet of code below:

```
*SOLID SECTION,ELSET=PLATE, MATERIAL=PPG,ORIENTATION=LOCAL
4.0
```

This method smears all of the layers of the laminate into a uniform laminate of the specified element set, *PLATE*, with the specified *MATERIAL* named PPG in this case. Elastic material properties that were generated from the BMT discussed above were again utilized. The fiber orientation of each element, *LOCAL*, was specified in a *DISTRIBUTION TABLE* with respect to the model edge. Thus, the total laminate thickness was specified on the second line at 4 mm in this case. Note that a summary of the key points of the code are presented here, while complete code may be found below in the Appendices.

Several assumptions were made to simplify this modeling effort. First, it was assumed that all fibers were parallel and uniform in the intended direction with reference to the widthwise edge. It was also assumed that all the fibers were parallel and aligned through the thickness. These assumptions greatly simplified the modeling approach even though they were a source of the variation noted within the BMT. In addition, perfect bonding between the layers was assumed. In the case of the IP wave, it was assumed that the initial failures and debonds of the discontinuous edge fibers had negligible effect on the material response and were disregarded for this effort.

Non-Linear Shear Approach and Summary

Each of the modeling techniques discussed above utilized a shear modulus value and assumed that this shear and other material property responses were linear. However, during the BMT it was determined that misaligned fibers, for both IP and OP waves, led to a material response that was dominated by shear between the fibers in the wave for tension and compression. Further, testing showed that the shear response was non-linear as seen in Figure 81, and significant plastic response was noted. Thus, shear non-linearity was deemed significant and a non-linear constitutive law was developed for the bulk material using a user-defined material subroutine (UMAT) in Abaqus. In this case, the subroutine determines shear properties based on the tabulated shear stress-strain relationship in Figure 81. Using this relationship, after an element reached a stress-strain state that varied from the initial state, the secant modulus was determined by the subroutine and updated into the material card.

Shear stress-strain data from the actual materials, established in the BMT, were utilized in the UMAT. However, model convergence was not initially achieved due to the negative stiffness after significant shear failure shown at approximately 2.2% in Figure 81. Thus, an assumed non-negative shear response was approximated along with the lines of secant modulus used to map the shear response (Figure 81). It is noted that the strain negative stiffness was with extensive matrix damage and was outside the range of these tests as it was beyond the load-carrying capacity. The approximation of a stiffness reduction due to constant stress was deemed acceptable to approximate a non-negative shear response that allowed easy model convergence.

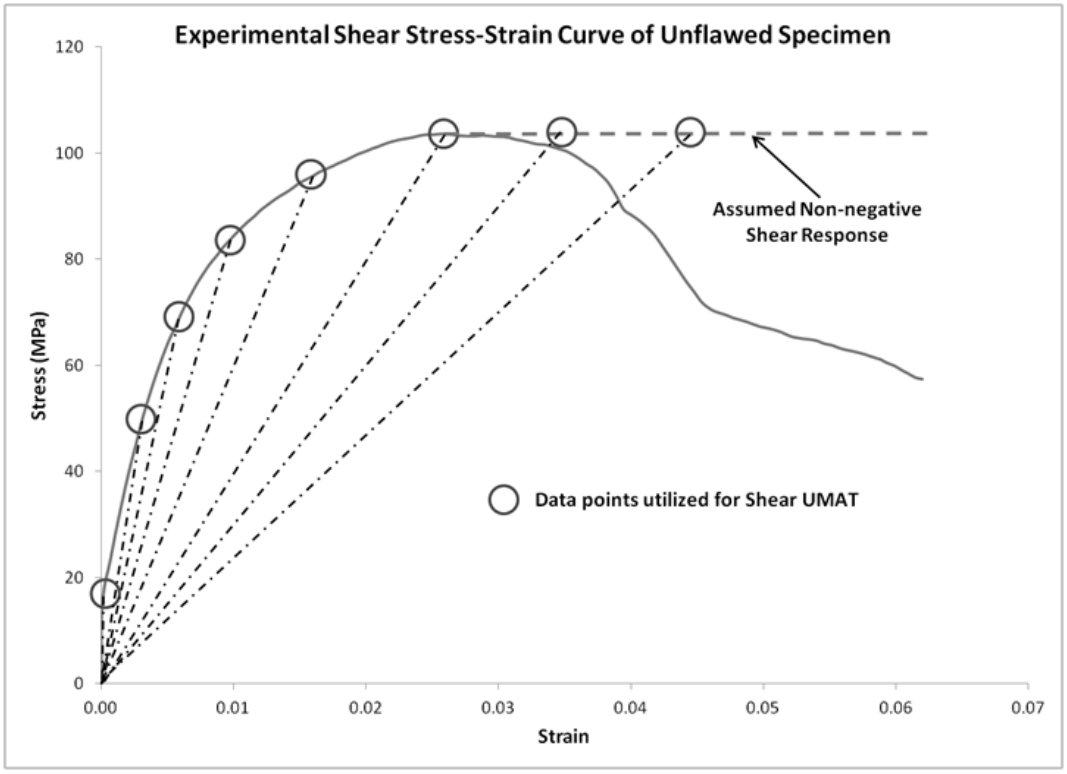

Figure 81: Shear stress-strain relationship of unflawed specimen with tabulated data points indicated for UMAT.

It is worth noting that recently several studies have indicated that the use of secant modulus in this way is inaccurate and results in an under-prediction of stiffness based on loading-unloading-reloading (LUR) tests as shown in Figure 82, right (VanPaepegem et al., 2006; Mandell and Samborsky, 2013). However, since the secant method captured the quasi-static, monotonic loading performed in all of the BMT as seen in the left of Figure 82, removal of the observed hysteresis from consideration, whether due to plasticity or matrix damage, was deemed reasonable. Further, when noting the impact on the modeled results, the secant method offered a worst case scenario which bounded the problem between over-predicting shear modulus response in the linear case and under-

predicting the response in the secant method case. This under-prediction of stiffness by the secant modulus is clearly evident when the right and left images of Figure 82 as noted by the reduction in slope during loading compare the LUR curve. Given the comparative nature of the work herein, further investigation of the LUR implications is left as future work.

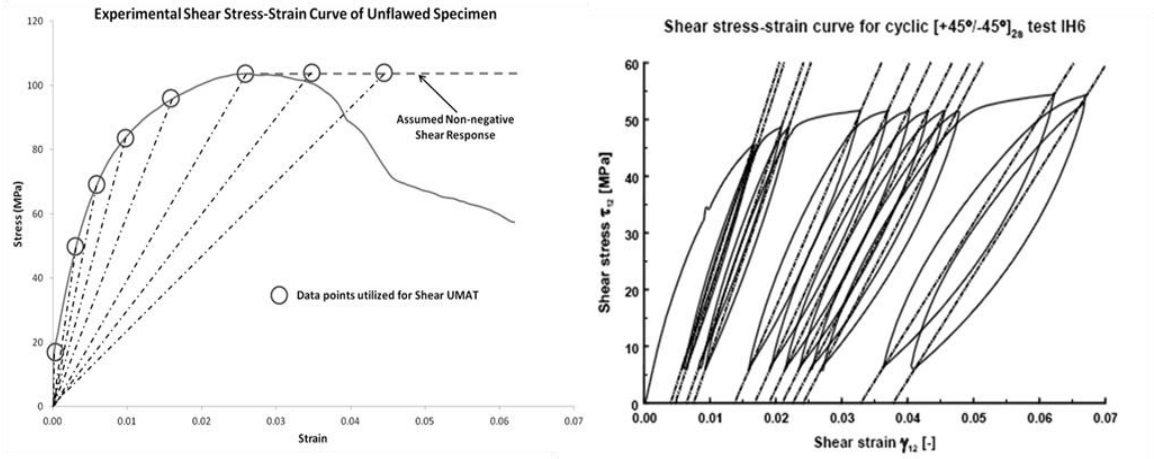

Figure 82: Shear stress-strain curve from BMT utilized for UMAT utilizing secant modulus (left) and LUR response indicating less reduction in stiffness (right) (VanPaepegem et al., 2006).

Finally, since Abaqus does not allow the use of multiple subroutines to be called independently, the results of this method were truncated at an overall strain to match the general unflawed control case, or approximately 2.5% strain. The displacement condition was able to be set to this strain in each case to ensure actual failure condition was exceeded by the model to allow truncation. While this method was not ideal, it was clear in all cases that the model was convergent or divergent well before this point is reached.

UMAT Subroutine Code

While this approach was rather simple in theory, the coding wass rather complex and required use of a general and powerful toolset within Abaqus. In fact, Abaqus warns that "use of this [UMAT] subroutine generally requires considerable expertise. You are cautioned that the implementation of any realistic constitutive model requires extensive development and testing. Initial testing on a single-element model with prescribed traction loading is strongly recommended (Abaqus User Subroutines Reference Manual 1.1.36, 2012)." The UMAT subroutine was used to define the constitutive behavior of a material at material calculation points of elements where specified. It required that the stresses and solution-dependent state variables be updated in each increment and that a material Jacobian matrix be provided. It is important to note that only portions of the code that are specific to this technique are discussed, while the specifics of FORTRAN are left to the reader. Complete code may be found in the Appendices and more comprehensive explanations of subroutines and use in Abaqus may be found in the Abaqus User Subroutines Reference Manual (2012).

To implement the UMAT, the **USER MATERIAL* keyword specified the linear material properties and the tabulated stress-strain data:

```
*MATERIAL, NAME=PPG
*USER MATERIAL,CONSTANTS=20
PROPS(1)=E11,PROPS(2)=E22,PROPS(3)=N12,PROPS(4)=G12,
PROPS(5-12)=SHEAR STRAINS,PROPS(13-20)=SHEAR STRESSES
```

where *CONSTANTS* defined the number of material inputs which may be changed to match the non-linear shear constitutive case being approximated. These *CONSTANTS*

were then the data to be taken and used in the UMAT subroutine. Generally, the subroutine looked like:

```
      SUBROUTINE UMAT(STRESS,STATEV,DDSDDE,SSE,SPD,SCD,
     1 RPL,DDSDDT,DRPLDE,DRPLDT,
     2 STRAN,DSTRAN,TIME,DTIME,TEMP,DTEMP,PREDEF,DPRED,CMNAME,
     3 NDI,NSHR,NTENS,NSTATV,PROPS,NPROPS,COORDS,DROT,PNEWDT,
     4 CELENT,DFGRD0,DFGRD1,NOEL,NPT,LAYER,KSPT,KSTEP,KINC)
C
      INCLUDE 'ABA_PARAM.INC'
C
      CHARACTER*80 CMNAME
      DIMENSION STRESS(NTENS),STATEV(NSTATV),
     1 DDSDDE(NTENS,NTENS),DDSDDT(NTENS),DRPLDE(NTENS),
     2 STRAN(NTENS),DSTRAN(NTENS),TIME(2),PREDEF(1),DPRED(1),
     3 PROPS(NPROPS),COORDS(3),DROT(3,3),DFGRD0(3,3),DFGRD1(3,3)
      ⋮
      RETURN
      END
```

where specific variables used are defined in Table 19 and the material parameters were taken from the BMT as discussed in the next section.

Table 19: Variables defined and passed between the subroutine and standard code utilized in this routine.

Variable	**Definition**
DDSDDE	Jacobian matrix where Δσ and Δε are stress and strain increments, respectively
STRESS	Stress tensor passed in and updated to be passed out at end of routine
STATEV	Array of solution-dependent state variables.
SSE	Specific elastic strain energy
SPD	Plastic dissipation
SCD	Creep dissipation
NPROPS	User specified array of material constants; stress-strain data in this case
NOEL	Element number
NPT	Integration point number
NTENS	Size of the array to be used in each case

The remainder of the code followed one of two paths depending on the material state. A simple *IF* statement was used to determine whether the material state was within or outside of the initial linear shear stress defined. If it was still within this initial state, the routine recalculates the initial values and moves on to the next element, whereas if it fell outside, the routine kicked into action. In this latter case, the Jacobian material matrix at each integration point of each element was first calculated and then updated:

```
 IF(SHEAR.GE.GAMMAMAX(NOEL,NPT)) THEN
      CALL UMAT_SHEAR_STIF(SHEAR,GAMMA,TAU,GG12,G12,STRESS3)
      IF(STRAIN1(3).LT.0.D0) STRESS3=-STRESS3
ELSE
      G12=TAUMAX(NOEL,NPT)/GAMMAMAX(NOEL,NPT)
      STRESS3=G12*STRAIN1(3)
ENDIF

DDSDDE(1,1) =  DD11
DDSDDE(1,2) =  DD12
DDSDDE(1,3) =  0.D0
DDSDDE(2,1) =  DD12
DDSDDE(2,2) =  DD22
DDSDDE(2,3) =  0.D0
DDSDDE(3,1) =  0.D0
DDSDDE(3,2) =  0.D0
DDSDDE(3,3) =  G12
```

and was then used to determine stresses for each integration point of each element:

```
C    STRESS CALCULATION
STRESS(1)= DDSDDE(1,1)*STRAIN1(1) + DDSDDE(1,2)*STRAIN1(2)
STRESS(2)= DDSDDE(2,1)*STRAIN1(1) + DDSDDE(2,2)*STRAIN1(2)
      STRESS(3)= STRESS3

      GAMMATMP(NOEL,NPT)=SHEAR
      TAUTMP(NOEL,NPT)=DABS(STRESS3)
    RETURN
    END
```

Once this stress calculation was complete, these values were then used to update the state variables depending on the the material stress-strain state:

```
SUBROUTINE UMAT_SHEAR_STIF(SHEAR,GAMMA,TAU,GG12,G12,STRESS3)
    IMPLICIT REAL*8(A-H,O-Z)
    DIMENSION GAMMA(*),TAU(*),GG12(*)

    IF   (SHEAR.LT.GAMMA(1)) THEN
        G12=GG12(1)
        STRESS3=G12*SHEAR
    ELSEIF(SHEAR.LT.GAMMA(2)) THEN
        G12=GG12(2)
        STRESS3=TAU(1)+G12*(SHEAR-GAMMA(1))
    ELSEIF(SHEAR.LT.GAMMA(3)) THEN
        G12=GG12(3)
        STRESS3=TAU(2)+G12*(SHEAR-GAMMA(2))
    ELSEIF(SHEAR.LT.GAMMA(4)) THEN
        G12=GG12(4)
        STRESS3=TAU(3)+G12*(SHEAR-GAMMA(3))
    ELSEIF(SHEAR.LT.GAMMA(5)) THEN
        G12=GG12(5)
        STRESS3=TAU(4)+G12*(SHEAR-GAMMA(4))
    ELSEIF(SHEAR.LT.GAMMA(6)) THEN
        G12=GG12(6)
        STRESS3=TAU(5)+G12*(SHEAR-GAMMA(5))
    ELSEIF(SHEAR.LT.GAMMA(7)) THEN
        G12=GG12(7)
        STRESS3=TAU(6)+G12*(SHEAR-GAMMA(6))
    ELSEIF(SHEAR.LT.GAMMA(8)) THEN
        G12=GG12(8)
        STRESS3=TAU(7)+G12*(SHEAR-GAMMA(7))
    ELSE
        G12=GG12(8)
        STRESS3=TAU(8)+G12*(SHEAR-GAMMA(8))
    ENDIF

    RETURN
    END
```

These values were then fed back into the standard portion of the code to be used for the next increment. It is important to note that this was where the specific shear properties were calculated for each case and if the number of *CONSTANTS*, which corresponded to the *NPROPS* variable, are changed, then this portion of code must also be updated.

Non-Linear Shear UMAT Subroutine Model Inputs

When compared to the Hashin failure criteria above, fewer inputs are needed for this modeling approach, and they are more easily taken directly from the BMT. As such, elastic material properties that generated from the BMT discussed above were utilized (

Table 19). The specific inputs necessary for tabulated stress-strain relationship for this model were also generated from the BMT (Table 20). To reiterate, the specific stress-strain relationship was taken directly from quasi-static, monotonic shear tests utilizing a ±45 laminate tested in tension. The key points identified in Table 21 below were chosen as points where significant changes in slope of the resulting stress-strain relationships were noted. Admittedly, these data were open to some interpretation, and small modifications that still fell on the shear curve shown in Figure 81 were deemed acceptable. In all cases, modifications of these inputs are noted and justified in the discussion below, or in cases where justification was not possible, they are deemed unacceptable and are noted as such.

Table 20: Material properties generated as outline in BMT section.

Standard Properties	E_1	E_2	v_1	G_{12}
Tension (GPa)	40.6	16.3	0.27	16.8
Compression (GPa)	38.4	14.4	0.28	14.4

Table 21: Stress-strain inputs for each state indicated in Figure 81 and used in the routine.

State	**1**	**2**	**3**	**4**	**5**	**6**	**7**	**8**
Strain	0.002	0.003	0.056	0.087	0.0149	0.024	0.0356	0.0454
Stress (MPa)	18.1	49	67.2	80.6	94.3	103.2	103.2	103.2

Results and Correlation

A model was run with an IP wave added to the coupon geometry utilizing a user-defined non-linear shear material response as outlined above. Load-displacement and stress-strain data were generated and used to compare and correlate, respectively, to BMT results. Processing times for all runs of this model ranged from 1.5 to 5 minutes in length. Continuing with the systematic approach outlined above, the initial case considered was an IP wave, first in tension and then in compression. While correlation was achieved for initial portions in each case, the model then diverged from the BMT test results, and as such further analysis was not performed as detailed below.

IP Wave in Tension

As noted above, IP wave tension coupon samples from BMT results clearly showed coupon failure was less sudden than in the unflawed controls or porosity specimens. Initially, shear damage was noted in the area of the fiber misalignment, generally in the area of peak fiber misalignment, and it progressed both transversely perpendicular to the fiber and longitudinally parallel to the fiber along the wave. First fiber failure was then noted in the areas where this damage progressed together and met from both sides of the wave. This progression was visualized as shown in Figure 83, right, with the use of DIC which allowed for initial visual comparison to analytical solutions shown in left and middle images. As shown in the left image of Figure 83, the model captured the area of strain accumulation where damage occurs at the peak fiber misalignment angle and then progresses toward the edges perpendicular to the fiber

direction and longitudinally to the wave peak between the two areas of fiber misalignment. The middle image of Figure 83 shows that instead of the damage progressing completely across the wave, the fibers become nearly straight at the maximum displacement. This matches the coupon testing, though the coupons clearly indicate matrix failure through the wave area and fiber breakage around the peak of the wave due to reaching maximal longitudinal stress. This model does not account for fiber failure as it does not have damage criteria, nor does the UMAT cover the longitudinal or transverse properties which were found to be linear in the BMT. Since this comparison was qualitative and visual, before considering additions or modifications quantitative correlations were made.

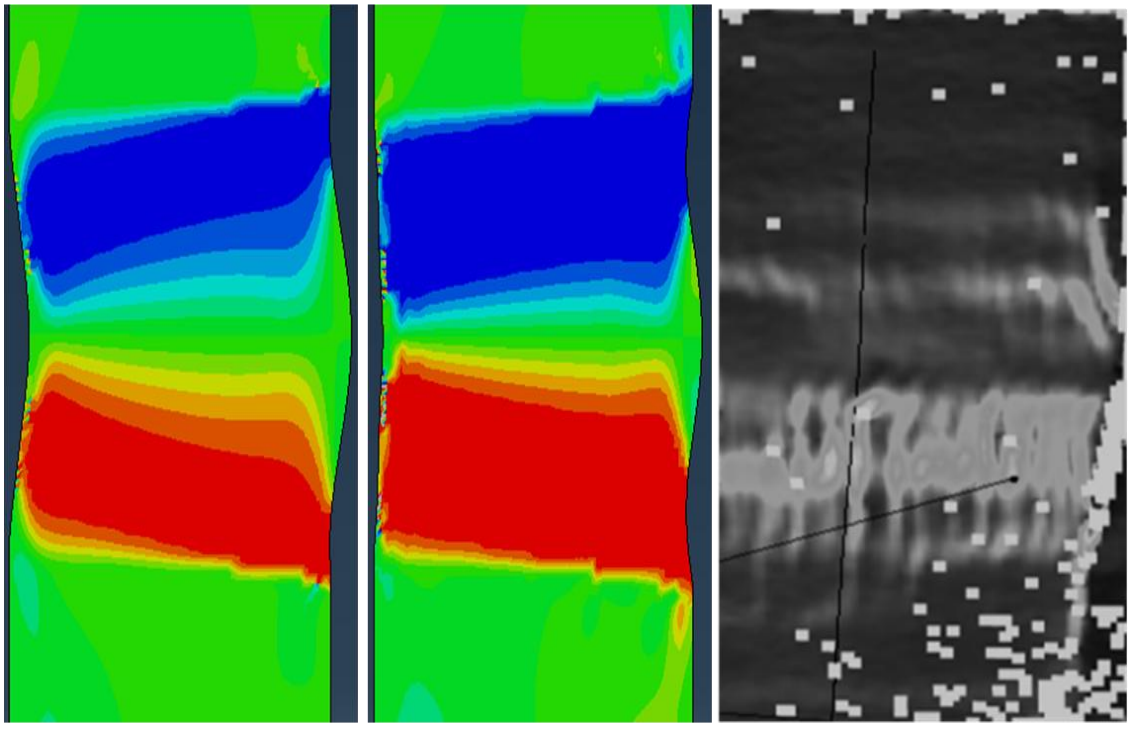

Figure 83: Shear strain field comparison of non-linear shear UMAT model solutions (left and middle) and DIC image (right) in tension.

Quantitative analysis of the non-linear shear UMAT initial IP wave model indicated good initial stiffness correlation as shown in Figure 84. However, when the dissipated energies are compared, the model appears to have excessive amount. At approximately 0.5% strain, the model over-predicted stress by about 10%; however, both the model and coupon at this point begin to show softening due to reduction of the shear modulus. From this point the UMAT model was slightly divergent up to approximately 1.6% strain due to overestimation of the shear response. After this point, however, the model became truly divergent due to increase in stiffness noted above the 1.6% strain. It is interesting to note that this point was also at approximately the same strain where the coupon reached peak stress and began to degrade significantly. Further review of the model indicated that as the model reached the displacement associated with this strain level, the fibers in the wave area were nearly straight, as seen in the middle image of Figure 83 above. Since there was no damage criteria and the fibers were nearly straight almost eliminating the shear between them, the longitudinal modulus became dominant and the modeled stiffness increased accordingly. Further review of the model results insinuated that this stress shift began closer to the 0.9% strain area.

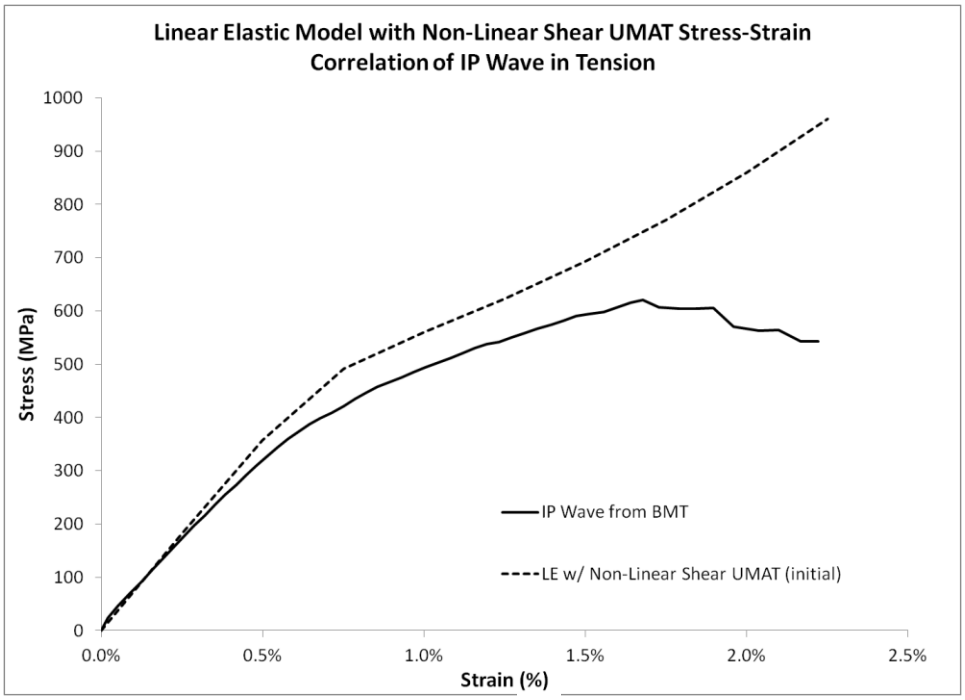

Figure 84: Stress-strain comparison of IP wave BMT and initial non-linear shear UMAT model in tension.

In an attempt to improve the UMAT model's predicted material response, parametric analyses were performed to understand the bounds associated with adjusting the calculated shear modulus. The stress values in Table 21 above were adjusted while the strain values were kept constant, to ensure that the resulting slopes were being adjusted as intended. Two cases were run where the stress values were doubled and halved. As expected, the doubling far over-predicted the stress response of the coupon, while the halving did the opposite. However, the point of divergence was still at approximately 0.9% as noted above in both cases. Further parametric studies were performed to see if this divergence point could be manipulated, but to no avail due to the dominance of the longitudinal modulus. Finally, an incremental analysis was performed,

reducing the stress values in Figure 84 incrementally until the tuned correlation in Figure 85 was achieved at an 11% reduction. A comparison of these stress values was made with the original BMT results and they were found to be too drastic to be accurate and as such while this amount of tuning improved results, they were deemed unacceptable.

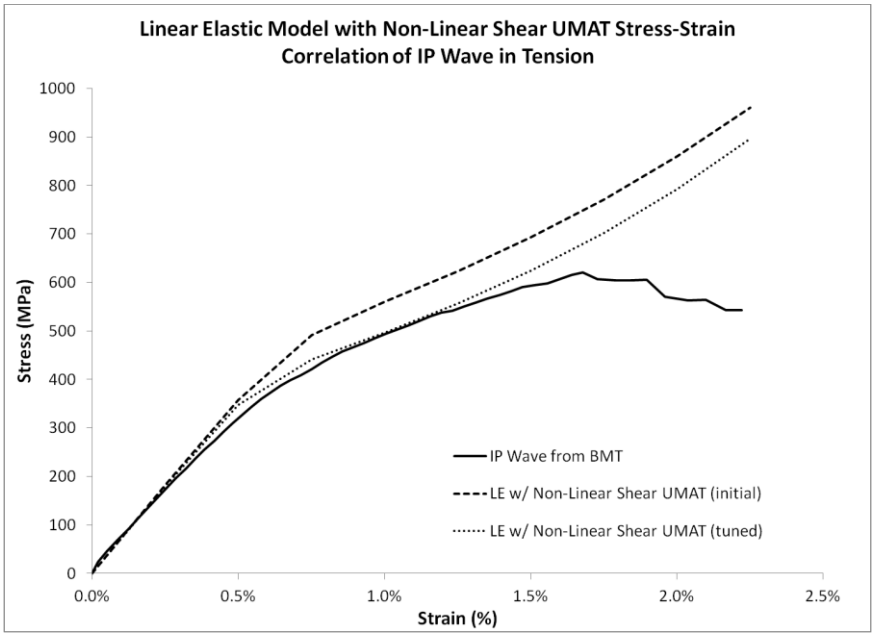

Figure 85: Reprint of stress-strain curve from Figure 84 with addition of an unacceptably tuned non-linear shear UMAT model in tension.

IP Wave in Compression

Following the systematic approach, the model was also run for the same IP wave in compression, though the boundary conditions were slightly modified such that the straight fiber sections of the model were constrained to prevent transverse displacement, thereby effectively reducing the gage section. Initial inputs were used as listed in Table 20 and Table 21 above, with compression data replaced for the material properties. As noted, analytical/experimental correlation was not as straight forward for the compression

case as compared to tension, since the damage progression was not visualized as easily during BMT. As noted above, the gage section for the compression tests was significantly smaller than for tension, reducing the amount of area the DIC was able to capture. Since the flaw dominated this area, only a small amount of unflawed area was imaged at the top and bottom. However, as noted in the BMT above, matrix failure was visually noted at the edges initially before progressing across the wave due to the shear stress increase with increased load. As the load increased, the wave effectively pushed transversely, causing rotations that increased stress from the left edge around the peak of the wave to the base of the wave at the right edge. The model appeared to initially capture this effect as indicated in the left Figure 86 which indicated an early loading where strain accumulated in the wave area before reaching a point where a significant shear failure pushed the wave toward the right, as shown the right image. This right image did not match the result seen experimentally. Further, analysis of the correlated stress-strain curves indicated that this failure was premature at approximately 0.6% strain and a stress of approximately 116 MPa which was less than half of the peak stress noted in the coupon (Figure 87). Once this failure occurred, no additional stress increase was noted in the modeled damage progression and this model was deemed unacceptable due to the fact that an unrealistic non-linear shear constitutive response would have been necessary for correlation. Based on the this unacceptable tuning and the unacceptable tension results above, no adjustments were made to the model to attempt correlation improvement.

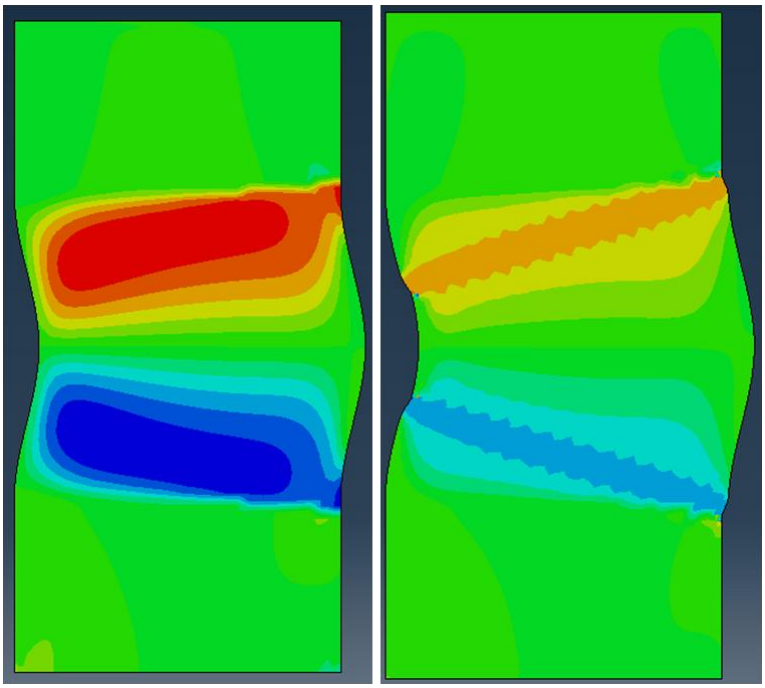

Figure 86: Shear strain field comparison of non-linear shear UMAT model solutions in compression.

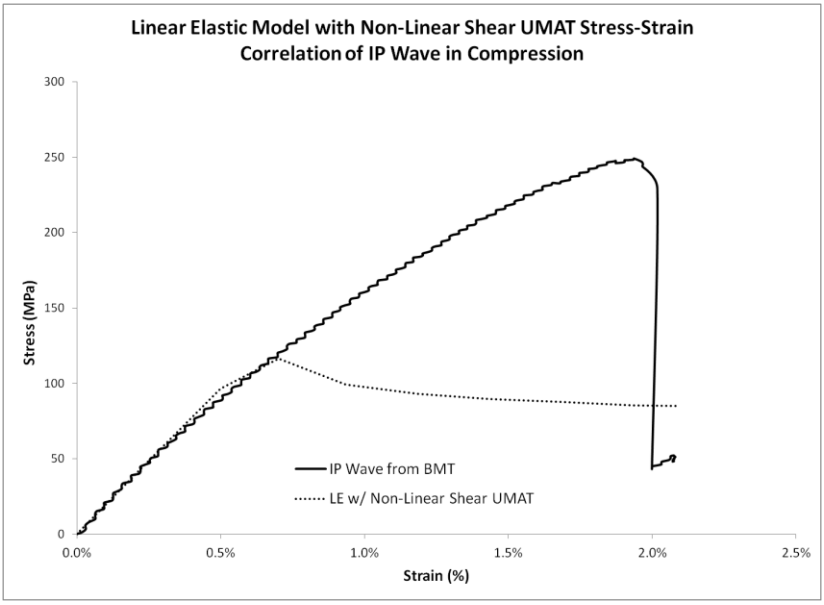

Figure 87: Stress-strain comparison of IP wave BMT and initial non-linear shear UMAT model in compression.

Non-Linear Shear UMAT Approach Summary and Conclusions

A continuum based, linear elastic model was modified to include a user-defined material in Abaqus utilizing a user subroutine. The subroutine was written to determine the state of shear stress for each element in the model to account for the non-linear degrading shear stress noted in the BMT. An IP wave case was developed and run in both tension and compression with material properties, including non-linear shear stresses and strains that were determined from BMT and used as model inputs. Correlation to BMT testing was performed and tuning of parameters was utilized to better understand the effects on the results and to attempt to improve model correlation and damage prediction.

The IP wave case in tension was found to have reasonable visual correlation, and strains accumulations were noted in the same areas. In additional, the model was able to predict initial stiffness and accurate softening associated with degradation in the wave area until the fibers straightened enough for longitudinal modulus to dominate, resulting in divergence between the model and coupon results. To better understand the effects of the non-linear shear relationship with the modeled results, a brief parametric study was performed, but in all cases the longitudinal modulus dominated the model results at the divergence point of approximately 0.9%. A similar initial result was noted in compression before a shear collapse was noted visually in the wave areas that was not seen experimentally. While this resulting visual collapse was not initially unreasonable, it occurred prematurely as indicated in the resulting stress-strain curve. In both cases, acceptable tuning was not able to achieve results that improved correlations.

Overall, this method showed some correlation by matching initial softening in both tension and compression before the model diverged. It must be noted that while this model included a non-linear constitutive shear response, there were no failure criteria. While it seems reasonable, at least in theory, to add failure criteria, Abaqus does not allow for inclusion of built-in failure criteria such as the Hashin criteria utilized above. In addition, inclusion of the user-defined failure criteria approach noted above is not possible, as Abaqus is also limited in that a user-defined material and user-defined field cannot be utilized in the same code. As such, this non-linear shear UMAT method was set aside for combination with the discrete damage method outlined in Chapter 8.

DISCRETE DAMAGE MODEL WITH COHESIVE ELEMENTS

Introduction

Discrete modeling is considered by many to be more consistent with the physical damage of thermosetting polymer reinforced composites. As noted, a continuum approach relies on representing the damage as a change in material properties, whereas observed damage is typically local failure of the constituents (matrix and/or fiber). Constitutive properties do not physically change in a continuum sense and the degradation is a consequence of the local failure. As such, DDM attempts to directly model damage as it would actually occur. It must be noted however, that this method is generally more expensive computationally and is more mesh dependent than CDM. As noted above, with recent increases in computational availability, the use of cohesive elements has proven a viable option for modeling laminated composites without requiring an initial crack be placed in the model (Karayev et al, 2012; Lemanski et al., 2013).

Cohesive elements are typically utilized to model behavior of bonded joints and other material interfaces due to their nature based on the idealization of fracture mechanisms into a cohesive law relating traction to separation across the interface (Abaqus Analysis User's Manual, 2012). There are several ways in which cohesive elements can be utilized largely depending on whether the elements have a zero or a finite thickness. In addition, interactions may be defined or to simplify common nodes may be used, as herein, to place cohesive elements between layers of bulk continuum elements (Figure 88). In all cases, cohesive zones must only be one cohesive element

thick and orientation must be considered. In summary, a layer of zero thickness cohesive elements with specific bi-linear traction-separation criteria are placed in areas of interest such as between layers of the laminate. While previous convention was to utilize cohesive elements only in specific areas, in essence predefining the crack path, computational availability has made it conceivable to place cohesive elements willy-nilly through the model. Thus, damage and crack progression may occur virtually anywhere in the model where the stress state indicates rather than where the user has placed these elements. Given the consistent crack formation and progression in areas of fiber waviness noted in the BMT combined with the Round 2 milestone of developing a DDM, this method was investigated.

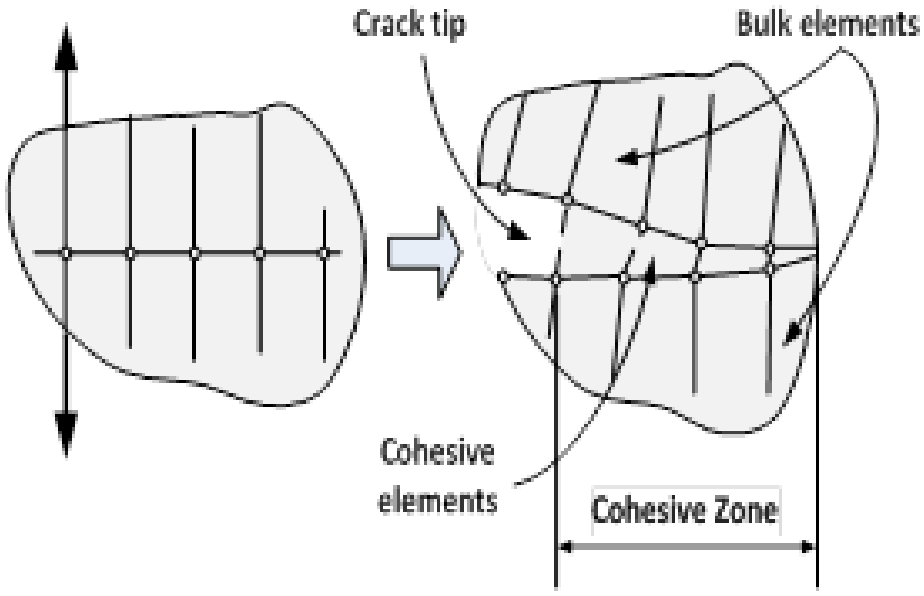

Figure 88: Example of placed cohesive elements resulting in crack progression showing cohesive element failure between the bulk elements (right).

Methods

A model with an IP wave geometry was adapted with cohesive elements between the fiber tows to attempt discrete modeling of damage as it occurs. Similar to the linear elastic models used above, the geometry was set up to match the intended coupon size (100 mm x 50 mm) established during the BMT. A 2D model (Figure 73) was generated with an IP wave geometry, with quadrilateral, plane stress shell elements (CPS4), in Abaqus where each element was generated to be consistent with the nominal fiber tow width (1.0 mm). The IP wave modeled had an amplitude (A) of 3.8 mm, a wavelength (λ) of 47.6 mm, and average off-axis fiber angle of 28.7°. Local coordinate systems were defined for the elements oriented to form the wave such that the fiber direction remained consistent through the wave and the material properties were modeled to correctly match these properties. Displacement conditions were applied at the top and bottom to match the BMT testing conditions by applying a symmetry boundary condition at the mid-plane which aligned with peak of the wave. As such, full field calculations were made to match the BMT data for load-displacement and stress-strain correlations.

In reviewing the test data, images, and DIC data, it was apparent that initial damage occurred in each wave at low loading levels on the ends of the samples where fibers ended on the coupon edge. Due to the wave pattern introduced when the samples were cut, fibers through the wave were cut, resulting in discontinuous fibers along the sample length. Based on this observation, it was assumed that these portions of the laminate were not of interest when considering the goal of isolating defects for the CDM models analyzed above. This was largely based on the assumption that since the CDM's

generalized the material, these areas were likely to effect the model by over-predicting the load-carrying capacity. However, with the cohesive element DDM these areas were physically modeled as discontinuous fiber, and the effects would not adversely affect the results. As shown in Figure 73, these discontinuous fibers were then added back into the model.

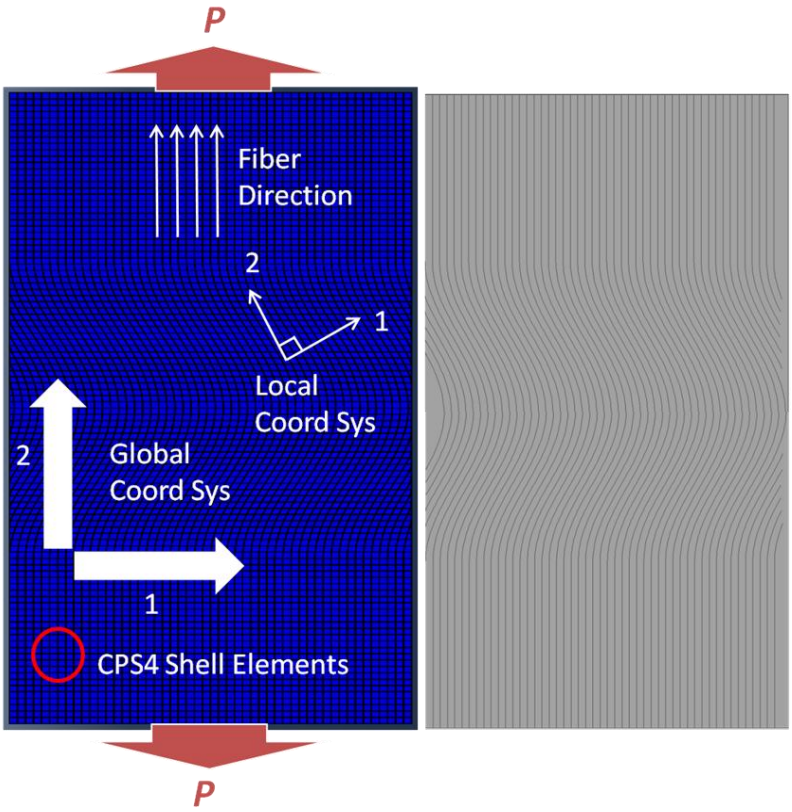

Figure 89: The 2D model setup utilized in the Abaqus DDM with cohesive elements models (left) and the rows of cohesive elements highlighted (right).

To simplify the 2D model that was utilized, the *SOLID SECTION* keyword option was utilized to specify the laminate with a specified thickness as shown in the snippet of code:

**SOLID SECTION,ELSET=PLATE, MATERIAL=PPG,ORIENTATION=LOCAL*
4.0

This method smears all of the layers of the laminate into a uniform laminate of the specified element set, *PLATE*, with the specified *MATERIAL* named PPG in this case. Elastic material properties that were generated from the BMT discussed above were again utilized. The fiber orientation of each element, *LOCAL*, was specified in a *DISTRIBUTION TABLE* with respect to the model edge. Thus, the total laminate thickness was specified on the second line at 4 mm in this case. Note that a summary of the key points of the code are presented here, while complete code may be found below in the Appendices.

Several assumptions were made to simplify this modeling effort. First, it was assumed that all fibers were parallel and uniform in the intended direction with reference to the widthwise edge. It was also assumed that all the fibers were parallel and aligned through the thickness. These assumptions greatly simplified the modeling approach even though they were a source of the variation noted within the BMT. In addition, perfect bonding between the layers was assumed.

Cohesive DDM Approach and Code Summary

As noted above, a layer of zero thickness cohesive elements with specific traction-separation criteria were placed in areas of interest, and a bi-linear criterion was used as shown in Figure 90 below. The initial stiffness, *K*, of the cohesive element is linear up to the damage initiation point at critical separation, Δ_c. From this point to the failure separation, Δ_{fail}, the slope estimates the damage evolution of each the cohesive

element up to failure. At this point, the traction-separation criterion is met for a specific cohesive element, a separation occurs resulting in crack propagation and element deletion. As such, damage progression is able to modeled discretely. It is important to consider that each element is 2D and as such must have traction-separation criteria defined in each direction of the plane utilized. Further, it must be noted that to achieve accurate results, significant time up-front is needed for mesh generation and to determine the cohesive element bi-linear response parameters. Based on the inexact ability to determine these latter parameters, they must be adjusted in an iterative approach resulting in multiple model runs to establish reasonable analytical/experimental correlation. Such parametric studies are necessary to ensure that these cohesive properties do not impact the stiffness and response of the surrounding material in ways other than those intended.

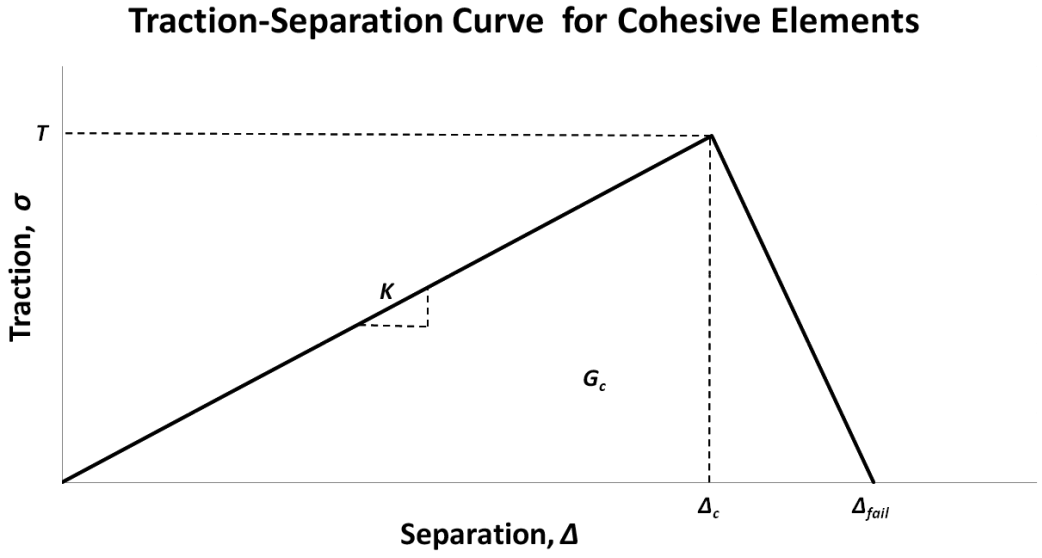

Figure 90: Representation of a cohesive element's bi-linear traction-separation response.

Coding of cohesive elements was relatively straightforward once the mesh and cohesive properties had been defined. Element sets of cohesive elements must be defined and in this case two sets were utilized: one for the discontinuous fiber sections and the other for the rest of the cohesive elements in the model. As such:

```
*COHESIVE SECTION, ELSET=COHESIVE, CONTROLS=EC-1,
MATERIAL=COHESIVE_MAT,
RESPONSE=TRACTION SEPARATION, THICKNESS=SPECIFIED
 0.,4.
*SECTION CONTROLS, NAME=EC-1, ELEMENT DELETION=YES, MAX
DEGRADATION=1.,
VISCOSITY=1E-0.5
```

where **COHESIVE SECTION* was used to define the key properties of the cohesive elements in the element set (*ELSET*). The *CONTROLS* set defined in **SECTION CONTROLS* were called out for the specific element set as were the material properties (*MATERIAL*), the type of cohesive response (*RESPONSE*), and that the *THICKNESS* was specified 4.0 mm for the assumed out-of-plane element thickness. The **SECTION CONTROLS* were named and then *ELEMENT DELETION* was turned on, and the *MAX DEGRADATION* was set such that each element was deleted once it reaches 100% of the specified damage parameters. The *VISCOSITY* parameter was turned on and set very low to help with model convergence while having little impact on the results.

Definition of the material and cohesive properties was then contained within the **MATERIAL* specification:

```
*MATERIAL, NAME=COHESIVE_MAT
*DAMAGE INITIATION, CRITERION=MAXS
T1MAX, T2MAX, T3MAX
*DAMAGE EVOLUTION, TYPE=ENERGY, MIXED MODE BEHAVIOR=BK,
POWER=2.284
```

GIC GIIC, GIIIC
**ELASTIC, TYPE=TRACTION*
K1EFF,K2EFF,K3EFF

where the *NAME* was set to that called out in the **COHESIVE SECTION* above. While the keywords **DAMAGE INITIATION* and **DAMAGE EVOLUTION* were used similarly to the Hashin failure criteria progressive damage method above, these parameters in this case were used to define the *TRACTION SEPARATION* response also called out in the **COHESIVE SECTION* above. As such, the **DAMAGE INITIATION* parameters were the initial cohesive element peak traction parameters for each of the utilized directions in the 2D model used here (the third value in this case is left as zero). Further, the **DAMAGE EVOLUTION* parameters were the critical energy release rates, and **ELASTIC* defined the stiffness of the initial traction.

Cohesive DDM Inputs

When compared to most of the techniques above, this modeling approach needs fewer inputs, and they are more easily taken, or generated, from the BMT. As such, elastic material properties that generated from the BMT discussed above were utilized (Table 22). The specific inputs necessary for the cohesive elements were generated parametrically with the exception of the damage evolution parameters which were based on the results from the BMT delamination testing. Specifically, the final average G_c value was used for damage evolution energy for each mode. Any modifications of these inputs are noted and justified in the discussion below, or in cases where justification was not possible, they are deemed unacceptable are noted as such.

Table 22: Material properties generated as outline in BMT section.

	E_1	E_2	v_1	G_{12}	G_{13}	G_{23}	GIc (J/m^2)	GIIc (J/m^2)
Tension (GPa)	40.6	16.3	0.27	16.8	16.8	16.8	806	1524
Compression (GPa)	38.4	14.4	0.28	14.4	14.4	14.4		

Parametric studies were performed to determine the properties of the cohesive elements using BMT data as noted above (Figure 91). Initial model analyses were performed to determine the cohesive element stiffness, K_{eff}. Analyses were performed at various stiffness values to determine the convergence value of 5E6 N/mm by performing several model runs to determine convergence point (Figure 91a). Similarly, the effects of T_{1max} were determined by analyzing at several different values and it was determined that failure behavior was not dependent on T_{1max} (Figure 91b). However, when a similar test was analyzed for T_{2max} it was quickly apparent that the failure was sensitive to Mode II shear damage, confirming the BMT results of shear dominated failure in the wave (Figure 91c). The peak tractions (T_{1max} = T_{2max} = 110 MPa) were then used in an initial run as shown in Figure 91d to confirm these values and ensure that the cohesive elements were not influencing initial stiffness correlations. Using this information the model was analyzed, and the damage progression and failure shape matched in some initial portions of the stress-strain comparisons. While out-of-plane delamination testing was performed, the strain energy release rates were not utilized in this parametric testing, it is recommended that future work be performed to ensure energy conservation.

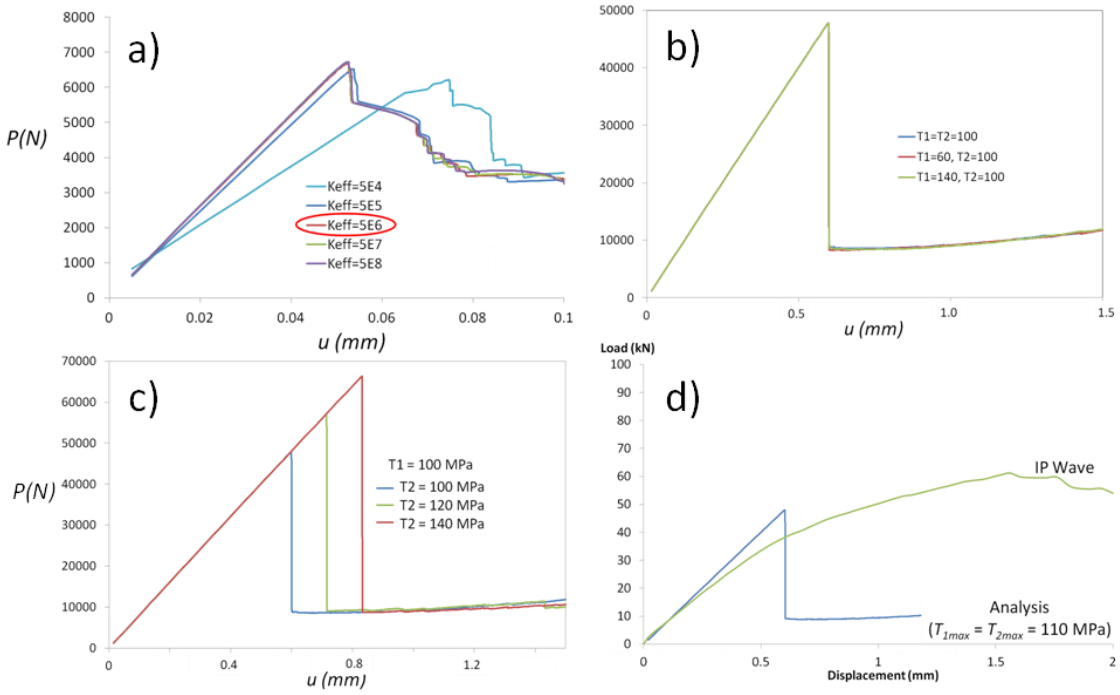

Figure 91: Results of parametric studies to find cohesive element: a) effective stiffness, K_{eff}; b) peak Mode I traction, T_{1max}; c) peak Mode II traction, T_{2max}; and, d) confirmation of peak tractions.

Results and Correlation

A model was run with an IP wave added to the coupon geometry utilizing cohesive elements with traction-separation criteria placed between each of the fiber tows as outlined above. Load-displacement and stress-strain data were generated and used to compare and correlate, respectively, to BMT results. Continuing with the systematic approach outlined above, the initial case considered was an IP wave, first in tension and then in compression. Processing times for all runs of this model were significant compared to the CDMs above and ranged from 160 to over 240 minutes in length. This was due in part to the small increments necessary for convergence. In addition, once a

significant number of cohesive elements failed, overall convergence was difficult and the increment became even smaller. However, little load-carrying capacity was realized after these failures and the model was often able to be stopped at approximately 90 minutes while still allowing reasonable results for correlation. The results that follow were similar to the non-linear shear UMAT, meaning that overall correlation was not achieved in either tension or compression and further analysis was not performed.

IP Wave in Tension

As noted above, IP wave tension coupon samples from BMT results clearly showed coupon failure was less sudden than for the unflawed controls or porosity specimens. Initially, shear damage was noted in the area of the fiber misalignment, generally in the area of peak fiber misalignment, and it progressed both transversely perpendicular to the fiber and longitudinally parallel to the fiber along the wave. First fiber failure was then noted in the areas where this damage progressed together and met from both sides of the wave. This progression was visualized as shown in Figure 92, right, with the use of DIC which allowed for initial visual comparison to analytical solutions shown in the left image. The model captured the area of strain accumulation where damage occurred at the peak fiber misalignment angle and then progressed toward the edges perpendicular to the fiber direction and longitudinally to the wave peak between the two areas of fiber misalignment.

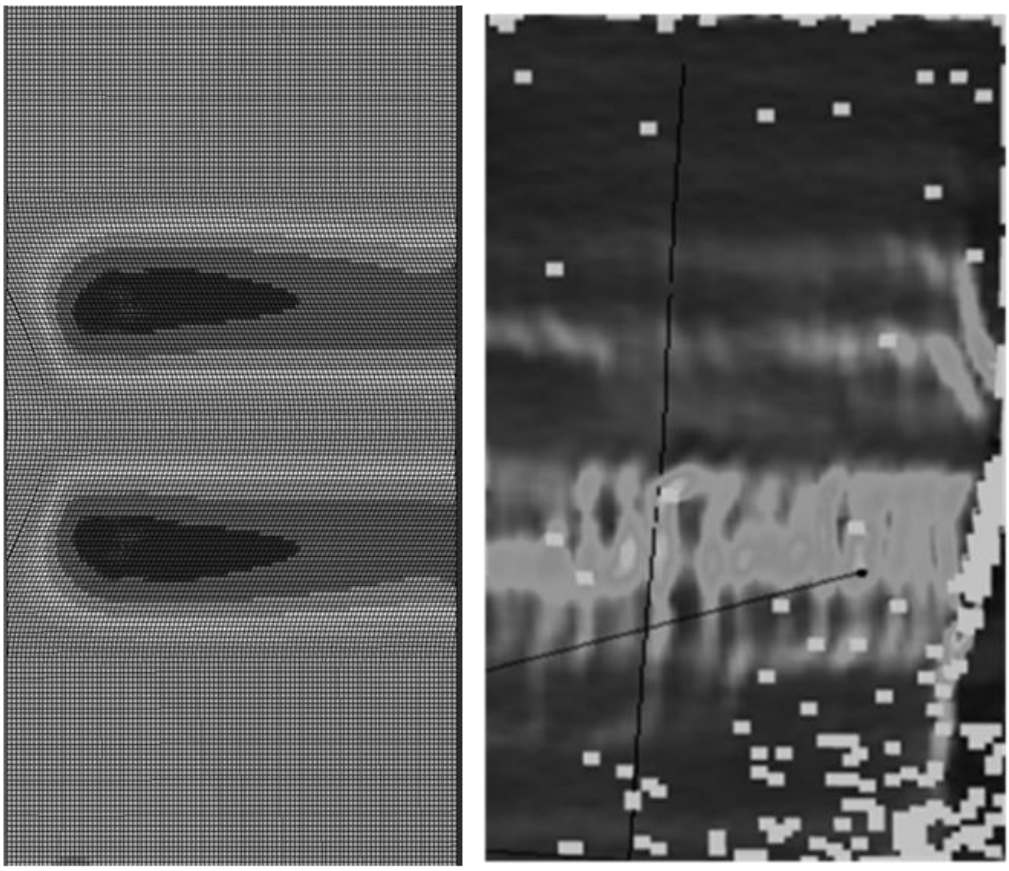

Figure 92: Shear strain field comparison of cohesive element DDM solution (left) and DIC image (right) in tension.

Due to the discrete nature of this model and the fact that damage was physically modeled, additional visual correlation was able to be performed. As noted above, the discontinuous fiber sections of the laminate were introduced into this model and as may be expected the cohesive properties had to be dropped by about 10% (to 100 MPa) in order for damage to initiate early in these areas as seen in the BMT. With this modification, the discontinuous fiber areas broke free prior to other damage at low loads. Then as load increased, delaminations between the fiber tows were noted in the model matching the coupon tests as seen in Figure 93. In both cases, as the fibers straightened,

more cracking was noted between the fiber tows across the entire specimen, though the model increment was noted to be very small as discussed in more detail below. These indicate good analytical/experimental correlation, but since such comparison was qualitative and visual, quantitative correlations were made before considering additions or modifications.

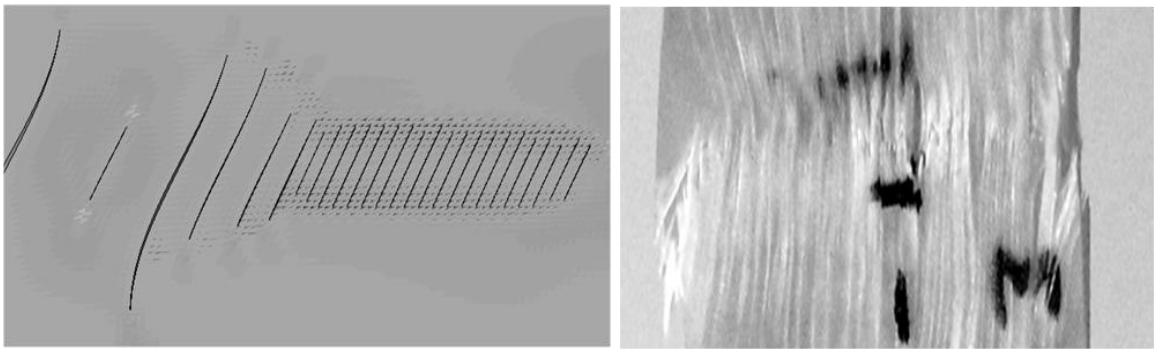

Figure 93: Shear strain field comparison of cohesive element DDM solution (left) and actual coupon image (right) in tension.

Quantitative analysis of the cohesive element DDM with the BMT results indicated good initial stiffness correlation as shown in Figure 93Figure 94. However, it was clear that the model did not predict any material softening, though an initial drop at approximately 0.4% strain was noted when the discontinuous fiber areas delaminated. A shift was noted in the model stress-strain due to the unrecoverable damage, and loading continues with consistent stiffness up to the first significant group of cohesive element failure at just over 0.5% strain before the results were truncated at 1.25% strain. This shift was not noted in the coupon results due to the lack of uniformity of the coupon noted in the BMT, resulting that these initial failures occurred incrementally. It is interesting to note that while the stress-strain indicated that load-carrying capacity

dropped suddenly at this point, the model dropped the solution increment significantly such that virtually every cohesive group failure was captured. The increments became so small that differentiation at the resolution of the stress-strain curve was not possible, but solving at each small increment caused the significant increase in run times noted above. Further analysis of the stress-strain curve correlation shown in Figure 94 clearly indicated that this method alone only captured the a portion of damage progression. Based on the parametric studies performed above and results from other modeling techniques, the use of a DDM with cohesive elements between fiber tows in tension was insufficient for correlation. In short, additional tuning of the cohesive element properties would compromise model accuracy due to influencing results such as initial stiffness thereby actually reducing model accuracy. As such, no additional tuning was attempted.

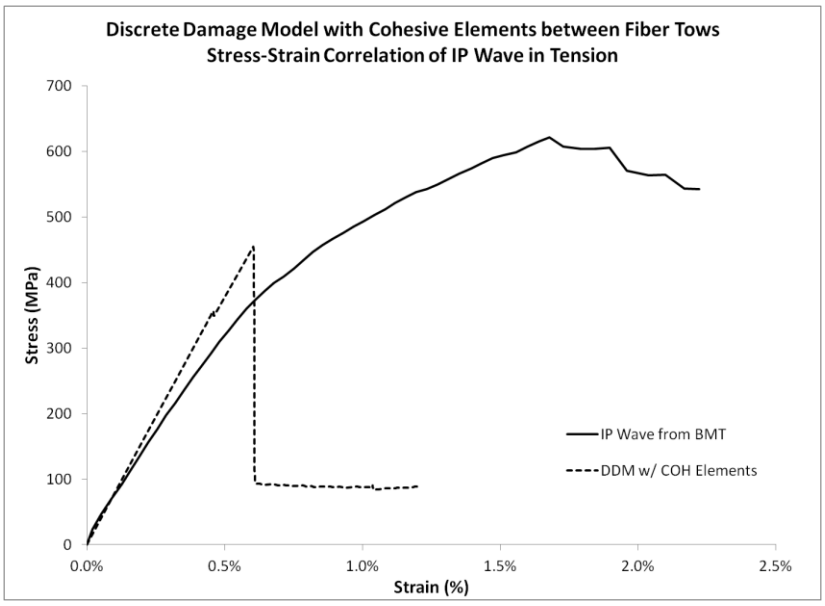

Figure 94: Stress-strain comparison of IP wave BMT and cohesive element DDM in tension.

IP Wave in Compression

Again following the systematic approach, the model was also run for the same IP wave in compression, though the boundary conditions were slightly modified such that the straight fiber sections of the model were constrained to prevent transverse displacement, thereby effectively reducing the gage section. Initial inputs were used as listed in Table 22 above with compression data replaced for the material properties. As noted, analytical/experimental correlation was not as straight forward for the compression case, as compared to tension, since the damage progression was not visualized as easily during BMT. As noted above, the gage section for the compression tests was significantly smaller than for tension reducing the amount of area the DIC was able to capture. Since the flaw dominated this area, only a small amount of unflawed area was imaged at the top and bottom. However, as noted in the BMT above, matrix failure was visually noted at the edges initially before progressing across the wave due to the shear stress increase with increased load. As the load increased, the wave effectively pushed transversely causing rotations and increasing stress from the left edge around the peak of the wave to the base of the wave at the right edge. The model appeared to capture this effect as indicated in Figure 95, though again the modeling of actual damage was noted. Similar to the tension case, an initial delamination of the discontinuous fiber section was noted; however, the delamination occurred at the peak of the wave and progressed toward the roots. This followed intuition and offered possible explanation for the lack of visualization of this effect during coupon loading, which would be even more difficult to see in the coupons due to lack of uniformity noted. The additional cohesive failures

through the entire model run followed a similar path. While this appeared to correlate well, quantitative stress-strain correlation was not easily accomplished (Figure 96). Similar to the tension case, initial stiffness correlated well and a shift was noted with the discontinuous fiber delamination. In addition, once cohesive element failures began the load-carrying capacity dropped almost immediately with the same incrimination shift noted. Based on these similarities to the tension case, correlation was deemed unacceptable and no adjustments were made to the model.

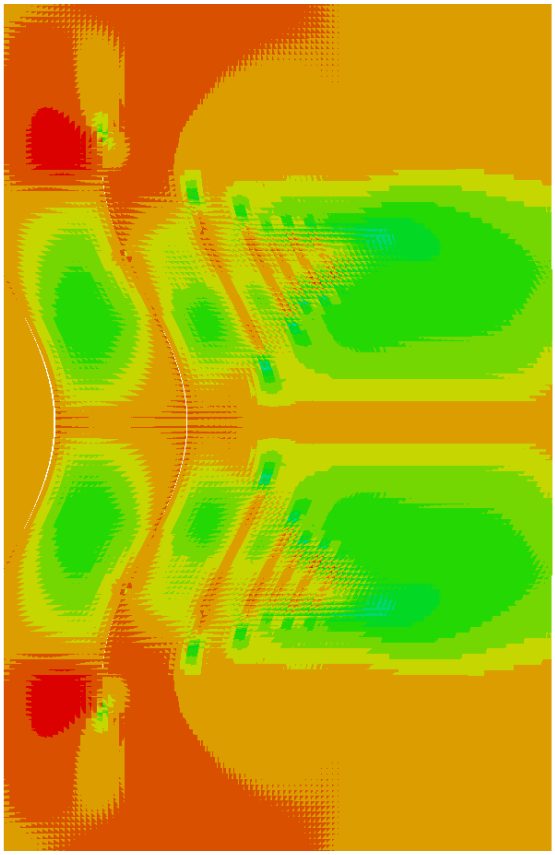

Figure 95: Shear strain field comparison of cohesive element DDM solution (left) and DIC image (right) in compression.

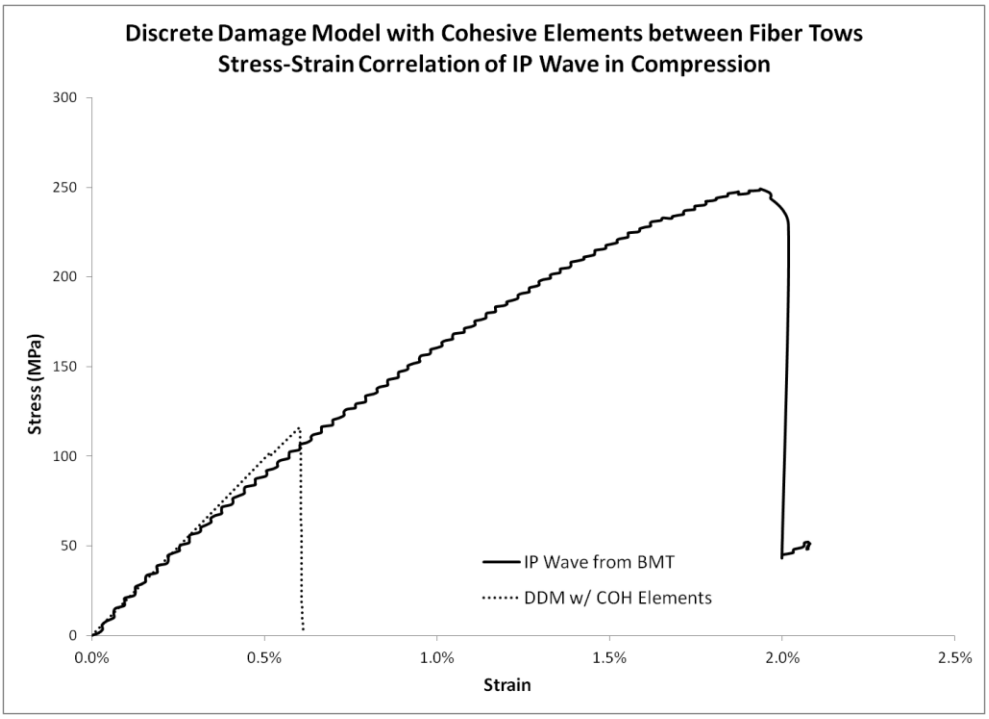

Figure 96: Stress-strain comparison of IP wave BMT and cohesive element DDM in compression.

Cohesive Element DDM Approach Summary and Conclusions

A discrete based was modified to include cohesive elements placed between all fiber tows of an IP wave in Abaqus. The geometry was modified from the CDM cases to include the areas of discontinuous fibers. Material properties were taken from the BMT and specific traction-separation parameters were taken from the delamination BMT, while others were determined parametrically. The IP wave case was developed and run in both tension and compression and was correlated to the BMT.

The discrete nature of the results in both cases lent to easier visual correlation and in compression even appeared to offer explanation of the damage that occurred within the laminate that was not able to be visualized. The model uniformity indicated a slight shift

in the stress-strain curves associated with initial discontinuous fiber areas with a return to initial stiffness, indicating that not including these areas in previous models was perhaps justified. However, inclusion in a DDM is much easier, as the cohesive properties were able to be reduced slightly to compensate for these discontinuities, and it was the compensation that made inclusion easier.

Overall, while initial visual and quantitative analytical/experimental correlations appeared reasonable, both models predicted significant degradation once cohesive element failures initiated under-predicting dissipated energy. Lack of continued load-carrying capacity beyond this point proved that this initial correlation was insufficient for predicting damage response. In addition, based on the parametric study performed, additional tuning of the cohesive element properties was not justifiable or performed, and this approach alone was deemed insufficient. However, it seemed that this response may pair well with the response noted from the non-linear shear UMAT in Chapter 7 above and as such these methods are combined in Chapter 9.

COMBINED NON-LINEAR SHEAR UMAT CDM AND COHESIVE ELEMENT DDM APPROACH

Introduction

In Chapters 7 and 8, a CDM using a non-linear shear response and a DDM using cohesive elements, respectively, were attempted and discussed. In both cases, analytical/experimental correlation was noted in specific areas of the stress-strain response. A user-defined material subroutine (UMAT) was written for the CDM based on the shear response from the BMT. This model was able to capture the initial softening until fiber straightening resulted in divergence with longitudinal modulus becoming dominant. Similarly, the use of cohesive elements realized matrix damage between the fiber tows, but implementation resulted in the under-prediction of both peak stress and strain. In both cases, the models seemed to capture the response, while both lacked the exact damage progression observed in the BMT. It was hoped that by combining them, the interaction of the two model types may result in a consistent, accurate, and predictive analytical tool.

As suggested for Round 3, a model was created that combined the non-linear shear UMAT with cohesive elements placed between the fiber tows throughout the model. This method requires several inputs from the user, including material properties and shear response that in this case were generated in the BMT. Additionally, the cohesive element properties were defined utilizing test results and/or parametric studies as in Chapter 8. Analytical/experimental correlations were made and correlations were

noted with the initial IP wave in both tension and compression. Following the systematic approach, an OP wave and additional IP waves, including a carbon fiber case, were modeled and correlated. Correlation was achieved in each case without additional tuning, indicating the promise of this modeling technique.

Methods

A model with an IP wave geometry was adapted with a non-linear shear UMAT and cohesive elements between the fiber tows to attempt modeling of damage as it occurs. While much of this section is repeated from Chapters 7 and 8, it is included here for continuity and the ease of the reader. Similar to the linear elastic models used above, the geometry was set up to match the intended coupon size (100 mm x 50 mm) established during the BMT. A 2D model (Figure 73) was generated with an IP wave geometry, with quadrilateral, plane stress shell elements (CPS4), in Abaqus where each element was generated to be consistent with the nominal fiber tow width (1.0 mm). The IP wave modeled had an amplitude (A) of 3.8 mm, a wavelength (λ) of 47.6 mm, and average off-axis fiber angle of 28.7°. Local coordinate systems were defined for the elements oriented to form the wave such that the fiber direction remained consistent through the wave and the material properties were modeled to correctly match these properties. Displacement conditions were applied at the top and bottom to match the BMT testing conditions by applying a symmetry boundary condition at the mid-plane which aligned with peak of the wave. As such, full field calculations were made to match the BMT data for load-displacement and stress-strain correlations.

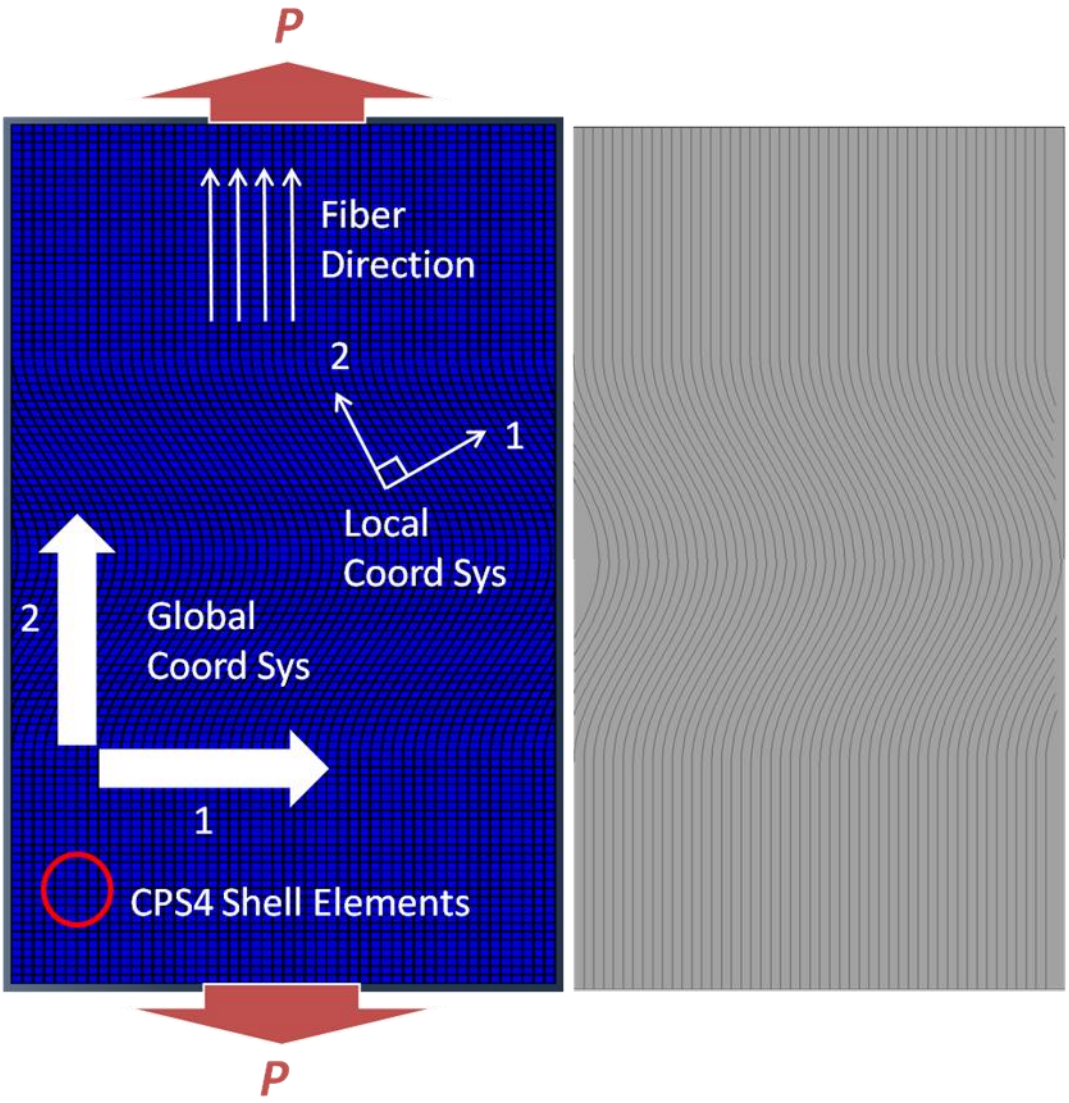

Figure 97: The 2D model setup utilized in the Abaqus DDM with cohesive elements models (left) and the rows of cohesive elements highlighted (right).

In reviewing the test data, images, and DIC data, it was apparent that initial damage occurred in each wave at low loading levels on the ends of the samples where fibers ended on the coupon edge. Due to the wave pattern introduced, when the samples were cut, fibers through the wave were cut, resulting in discontinuous fibers along the sample length. Based on this observation, it was assumed that these portions of the

laminate were not of interest when considering the goal of isolating defects for the CDM models analyzed above. This was largely based on the assumption that since the CDMs generalized the material, these areas were likely to effect the model by over-predicting the load-carrying capacity. However, with the cohesive element DDM these areas were physically modeled as discontinuous fiber, and the effects would not adversely affect the results. As shown in Figure 73, these discontinuous fibers were then added back into the model.

To simplify the 2D model that was utilized, the *SOLID SECTION* keyword option was utilized to specify the laminate with a specified thickness as shown in the snippet of code below:

```
*SOLID SECTION,ELSET=PLATE, MATERIAL=PPG,ORIENTATION=LOCAL
4.0
```

This method smears all of the layers of the laminate into a uniform laminate of the specified element set, *PLATE*, with the specified *MATERIAL* named PPG in this case. Elastic material properties that were generated from the BMT discussed above were again utilized. The fiber orientation of each element, *LOCAL*, was specified in a *DISTRIBUTION TABLE* with respect to the model edge. Thus, the total laminate thickness was specified on the second line at 4 mm in this case. Note that a summary of the key points of the code are presented here, while complete code may be found below in the Appendices.

Several assumptions were made to simplify this modeling effort. First, it was assumed that all fibers were parallel and uniform in the intended direction with reference

to the widthwise edge. It was also assumed that all the fibers were parallel and aligned through the thickness. These generalizations greatly simplified the modeling approach even though they are a source of the variation noted within the BMT. In addition, perfect bonding between the layers was assumed.

Cohesive DDM Approach and Code Summary

As noted above, a layer of zero thickness cohesive elements with specific traction-separation criteria were placed in areas of interest and a bi-linear criterion was used as shown in Figure 90 below. The initial stiffness, *K*, of the cohesive element is linear up to the damage initiation point at critical separation, Δ_c. From this point to the failure separation, Δ_{fail}, the slope estimates the damage evolution of each cohesive element up to failure. At this point, the traction-separation criterion is met for a specific cohesive element, and a separation occurs resulting in crack propagation and element deletion. As such, damage progression is able to be modeled discretely. It is important to consider that each element is 2D and as such must have traction-separation criteria defined in each direction of the plane utilized. Further, it must be noted that to achieve accurate results, significant time up-front is needed to build meshes and determine the bi-linear response parameters. Based on the inexact ability to determine these latter parameters, they must be adjusted in an iterative approach resulting in multiple model runs to establish reasonable analytical/experimental correlation. Such parametric studies are necessary to ensure that these cohesive properties do not impact the stiffness and the response of the surrounding material in ways other than those intended.

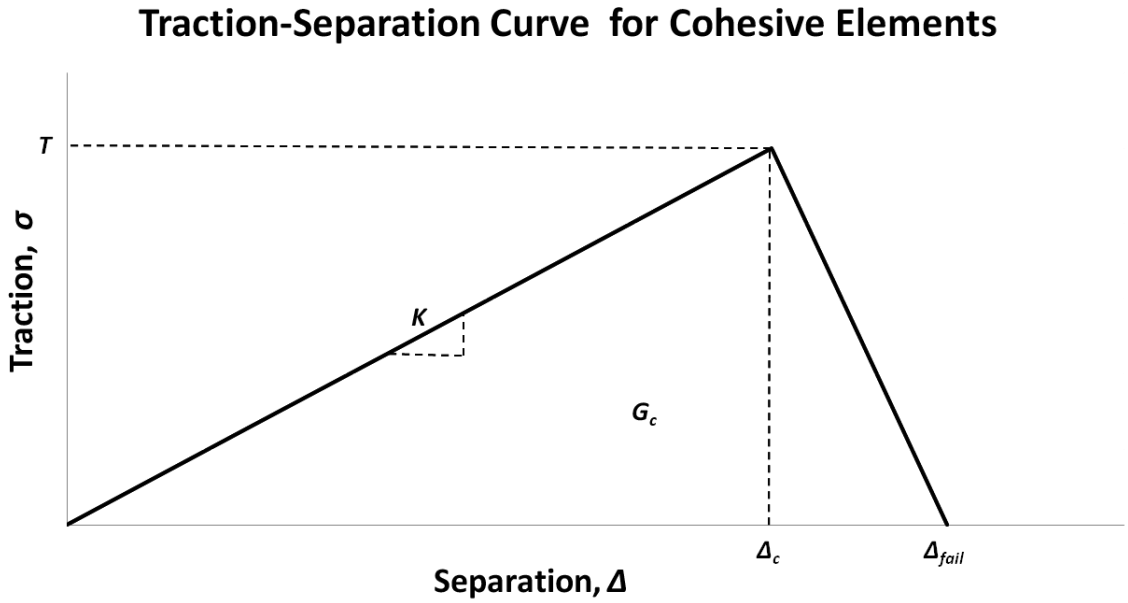

Figure 98. Representation of a cohesive element's bi-linear traction-separation response.

Coding of cohesive elements was relatively straightforward once the mesh and cohesive properties had been defined. Element sets of cohesive elements must be defined and in this case two sets were utilized: one for the discontinuous fiber sections and the other for the rest of the cohesive elements in the model. As such:

```
*COHESIVE SECTION, ELSET=COHESIVE, CONTROLS=EC-1,
 MATERIAL=COHESIVE_MAT,
RESPONSE=TRACTION SEPARATION, THICKNESS=SPECIFIED
 0.,4.
*SECTION CONTROLS, NAME=EC-1, ELEMENT DELETION=YES, MAX
DEGRADATION=1.,
VISCOSITY=1E-0.5
```

where **COHESIVE SECTION* was used to define the key properties of the cohesive elements in the element set (*ELSET*). The *CONTROLS* set defined in **SECTION CONTROLS* were called out for the specific element set as were the material properties (*MATERIAL*), the type of cohesive response (*RESPONSE*), and that the *THICKNESS* was

specified 4.0 mm for the assumed out-of-plane element thickness. The **SECTION CONTROLS* were named and then *ELEMENT DELETION* was turned on, and the *MAX DEGRADATION* was set such that each element was deleted once it reaches 100% of the specified damage parameters. The *VISCOSITY* parameter was turned on and set very low to help with model convergence while having little impact on the results.

Definition of the material and cohesive properties was then contained within the **MATERIAL* specification:

```
*MATERIAL, NAME=COHESIVE_MAT
*DAMAGE INITIATION, CRITERION=MAXS
T1MAX, T2MAX, T3MAX
*DAMAGE EVOLUTION, TYPE=ENERGY, MIXED MODE BEHAVIOR=BK, POWER=2.284
GIC GIIC, GIIIC
*ELASTIC, TYPE=TRACTION
K1EFF,K2EFF,K3EFF
```

where the *NAME* was set to that called out in the **COHESIVE SECTION* above. While the keywords **DAMAGE INITIATION* and **DAMAGE EVOLUTION* were used similarly to the Hashin failure criteria progressive damage method above, these parameters in this case were used to define the *TRACTION SEPARATION* response also called out in the **COHESIVE SECTION* above. As such, the **DAMAGE INITIATION* parameters were the initial cohesive element peak traction parameters for each of the utilized directions in the 2D model used here (the third value in this case is left as zero). Further, the **DAMAGE EVOLUTION* parameters were the critical energy release rates, and **ELASTIC* defined the stiffness of the initial traction.

Non-Linear Shear Approach and Summary

Each of the modeling techniques discussed above utilized a shear modulus value and assumed that this shear and other material property response were linear. However, during the BMT it was determined that misaligned fibers, for both IP and OP waves, led to a material response that was dominated by shear between the fibers in the wave for tension and compression. Further, testing showed that the shear response was non-linear as seen in Figure 99 and significant plastic response was noted. Thus, shear non-linearity was deemed significant and a non-linear constitutive law was developed for the bulk material using a user-defined material subroutine (UMAT) in Abaqus. In this case, the subroutine determined shear properties based on tabulated shear stress-strain relationship in Figure 99. Using this relationship, after an element has reached a stress-strain state that varies from the initial state, the secant modulus was determined by the subroutine and updated into the material card.

Shear stress-strain data from the actual materials, established in the BMT, were utilized in the UMAT. However, model convergence was not initially achieved due to the negative stiffness after significant shear failure shown at approximately 2.2% in Figure 99. Thus, an assumed non-negative shear response was approximated along with the lines of secant modulus used to map the shear response (Figure 99). It is noted that the negative stiffness was with extensive matrix damage and was outside the range of these tests as it was beyond the load-carrying capacity. The approximation of a stiffness reduction due to constant stress was deemed acceptable to approximate a non-negative shear response that allowed easy model convergence.

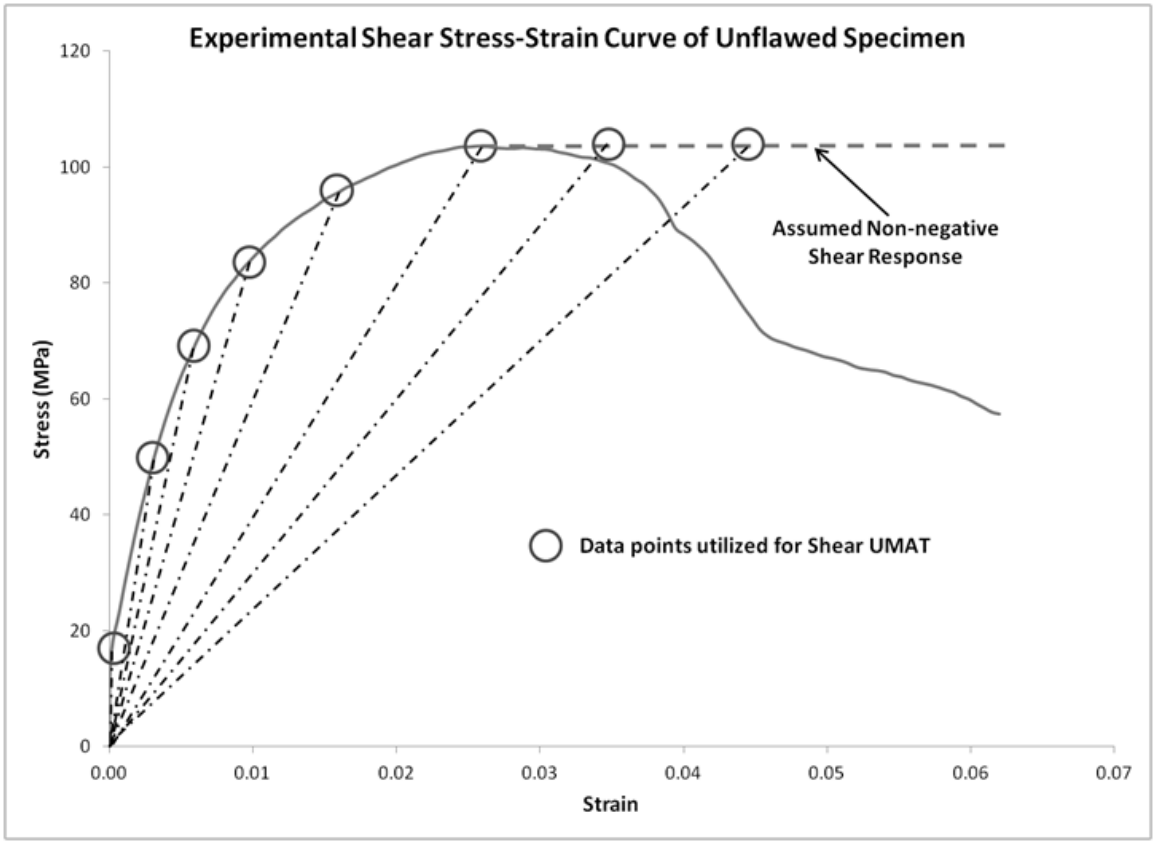

Figure 99: Shear stress-strain relationship of unflawed specimen with tabulated data points indicated for UMAT.

It is worth noting that recently several studies have indicated that the use of secant modulus in this way is inaccurate and results in an under-prediction of stiffness based on loading-unloading-reloading (LUR) tests as shown in Figure 100, right (VanPaepegem et al., 2006; Mandell and Samborsky, 2013). However, since the secant method captured the quasi-static, monotonic loading performed in all of the BMT as seen in the left of Figure 100, removal of the observed hysteresis from consideration, whether due to plasticity or matrix damage, was deemed reasonable. Further, when noting the impact on the modeled results, the secant method offered a worst case scenario which bounded the

problem between over-predicting shear modulus response in the linear case and under-predicting the response in the secant method case. This under-prediction of stiffness by the secant modulus was clearly evident when the right and left images of Figure 100 as noted by the reduction in slope during loading compare the LUR curve. Given the comparative nature of the work herein, further investigation of the LUR implications is left as future work. .

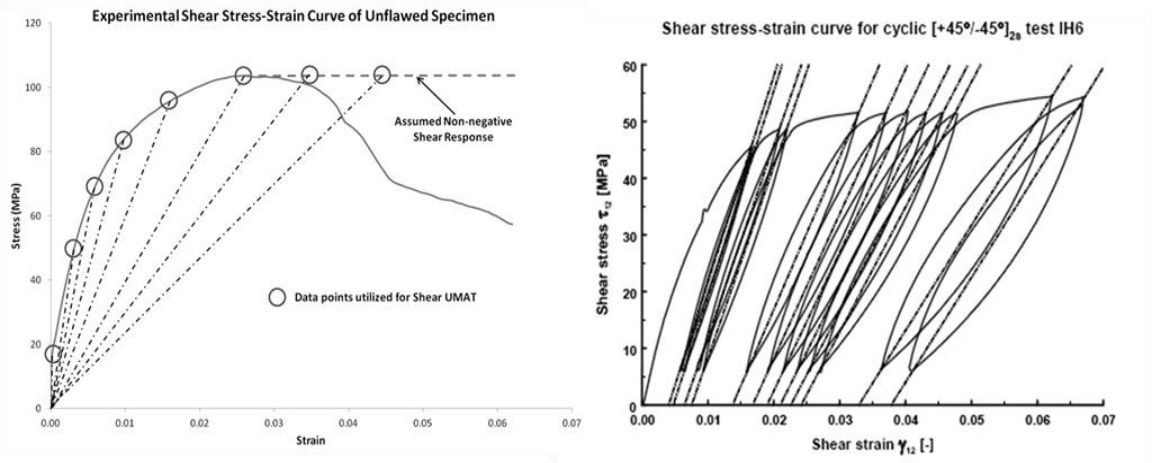

Figure 100: Shear stress-strain curve from BMT utilized for UMAT utilizing secant modulus (left) and LUR response indicating less reduction in stiffness (right) (VanPaepegem et al., 2006).

Finally, since Abaqus does not allow the use of multiple subroutines to be called independently, the results of this method were truncated at an overall strain to match the general unflawed control case, or approximately 2.5% strain. The displacement condition was able to be set to this in each case to ensure that this condition was met. While this method was not ideal, it was clear in all cases that the model was convergent or divergent well before this point was reached.

UMAT Subroutine Code

While this approach was rather simple in theory, the coding was rather complex and required use of a general and powerful toolset within Abaqus. In fact, Abaqus warns that "use of this [UMAT] subroutine generally requires considerable expertise. You are cautioned that the implementation of any realistic constitutive model requires extensive development and testing. Initial testing on a single-element model with prescribed traction loading is strongly recommended (Abaqus User Subroutines Reference Manual 1.1.36, 2012)." The UMAT subroutine was used to define the constitutive behavior of a material at material calculation points of elements where specified. It required that the stresses and solution-dependent state variables be updated in each increment and that a material Jacobian matrix be provided. It is important to note that only portions of the code that are specific to this technique are discussed, while the specifics of FORTRAN are left to the reader. Complete code may be found in the Appendices and more comprehensive explanations of subroutines and use in Abaqus may be found in the Abaqus User Subroutines Reference Manual (2012).

To implement the UMAT, the **USER MATERIAL* keyword specified the linear material properties and the tabulated stress-strain data:

```
*MATERIAL, NAME=PPG
*USER MATERIAL,CONSTANTS=20
PROPS(1)=E11,PROPS(2)=E22,PROPS(3)=N12,PROPS(4)=G12,
PROPS(5-12)=SHEAR STRAINS,PROPS(13-20)=SHEAR STRESSES
```

where *CONSTANTS* defined the number of material inputs which may be changed to match the non-linear shear constitutive case being approximated. These *CONSTANTS*

were then the data to be taken and used in the UMAT subroutine. Generally, the subroutine looked like:

```
      SUBROUTINE UMAT(STRESS,STATEV,DDSDDE,SSE,SPD,SCD,
     1 RPL,DDSDDT,DRPLDE,DRPLDT,
     2 STRAN,DSTRAN,TIME,DTIME,TEMP,DTEMP,PREDEF,DPRED,CMNAME,
     3 NDI,NSHR,NTENS,NSTATV,PROPS,NPROPS,COORDS,DROT,PNEWDT,
     4 CELENT,DFGRD0,DFGRD1,NOEL,NPT,LAYER,KSPT,KSTEP,KINC)
C
      INCLUDE 'ABA_PARAM.INC'
C
      CHARACTER*80 CMNAME
      DIMENSION STRESS(NTENS),STATEV(NSTATV),
     1 DDSDDE(NTENS,NTENS),DDSDDT(NTENS),DRPLDE(NTENS),
     2 STRAN(NTENS),DSTRAN(NTENS),TIME(2),PREDEF(1),DPRED(1),
     3 PROPS(NPROPS),COORDS(3),DROT(3,3),DFGRD0(3,3),DFGRD1(3,3)
      ⋮
      RETURN
      END
```

where specific variables used are defined in Table 23 and the material parameters were taken from the BMT as discussed in the next section.

Table 23: Variables defined and passed between the subroutine and standard code utilized in this routine.

Variable	**Definition**
DDSDDE	Jacobian matrix where Δσ and Δε are stress and strain increments, respectively
STRESS	Stress tensor passed in and updated to be passed out at end of routine
STATEV	Array of solution-dependent state variables.
SSE	Specific elastic strain energy
SPD	Plastic dissipation
SCD	Creep dissipation
NPROPS	User specified array of material constants; stress-strain data in this case
NOEL	Element number
NPT	Integration point number
NTENS	Size of the array to be used in each case

The remainder of the code followed one of two paths depending on the material state. A simple *IF* statement was used to determine whether the material state was

within or outside of the initial linear shear stress defined. If it was still within this initial state, the routine recalculates the initial values and moves on to the next element, whereas if it fell outside, the routine kicked into action. In this latter case, the Jacobian material matrix at each integration point of each element was first calculated and then updated:

```
      IF(SHEAR.GE.GAMMAMAX(NOEL,NPT)) THEN
          CALL UMAT_SHEAR_STIF(SHEAR,GAMMA,TAU,GG12,G12,STRESS3)
          IF(STRAIN1(3).LT.0.D0) STRESS3=-STRESS3
      ELSE
          G12=TAUMAX(NOEL,NPT)/GAMMAMAX(NOEL,NPT)
          STRESS3=G12*STRAIN1(3)
      ENDIF
DDSDDE(1,1) =  DD11
DDSDDE(1,2) =  DD12
DDSDDE(1,3) =  0.D0
DDSDDE(2,1) =  DD12
DDSDDE(2,2) =  DD22
DDSDDE(2,3) =  0.D0
DDSDDE(3,1) =  0.D0
DDSDDE(3,2) =  0.D0
DDSDDE(3,3) =  G12
```

and was then used to determine stresses for each integration point of each element:

```
C     STRESS CALCULATION
STRESS(1)= DDSDDE(1,1)*STRAIN1(1) + DDSDDE(1,2)*STRAIN1(2)
STRESS(2)= DDSDDE(2,1)*STRAIN1(1) + DDSDDE(2,2)*STRAIN1(2)
      STRESS(3)= STRESS3

      GAMMATMP(NOEL,NPT)=SHEAR
      TAUTMP(NOEL,NPT)=DABS(STRESS3)
     RETURN
     END
```

Once this stress calculation was complete, these values were then used to update the state variables depending on the the material stress-strain state:

```
SUBROUTINE UMAT_SHEAR_STIF(SHEAR,GAMMA,TAU,GG12,G12,STRESS3)
      IMPLICIT REAL*8(A-H,O-Z)
      DIMENSION GAMMA(*),TAU(*),GG12(*)
```

```
IF   (SHEAR.LT.GAMMA(1)) THEN
     G12=GG12(1)
     STRESS3=G12*SHEAR
ELSEIF(SHEAR.LT.GAMMA(2)) THEN
     G12=GG12(2)
     STRESS3=TAU(1)+G12*(SHEAR-GAMMA(1))
ELSEIF(SHEAR.LT.GAMMA(3)) THEN
     G12=GG12(3)
     STRESS3=TAU(2)+G12*(SHEAR-GAMMA(2))
ELSEIF(SHEAR.LT.GAMMA(4)) THEN
     G12=GG12(4)
     STRESS3=TAU(3)+G12*(SHEAR-GAMMA(3))
ELSEIF(SHEAR.LT.GAMMA(5)) THEN
     G12=GG12(5)
     STRESS3=TAU(4)+G12*(SHEAR-GAMMA(4))
ELSEIF(SHEAR.LT.GAMMA(6)) THEN
     G12=GG12(6)
     STRESS3=TAU(5)+G12*(SHEAR-GAMMA(5))
ELSEIF(SHEAR.LT.GAMMA(7)) THEN
     G12=GG12(7)
     STRESS3=TAU(6)+G12*(SHEAR-GAMMA(6))
ELSEIF(SHEAR.LT.GAMMA(8)) THEN
     G12=GG12(8)
     STRESS3=TAU(7)+G12*(SHEAR-GAMMA(7))
ELSE
     G12=GG12(8)
     STRESS3=TAU(8)+G12*(SHEAR-GAMMA(8))
ENDIF

RETURN
END
```

These values were then fed back into the standard portion of the code to be used for the next increment. It is important to note that this was where the specific shear properties were calculated for each case and if the number of *CONSTANTS*, which corresponded to the *NPROPS* variable, are changed this portion of code must also be updated.

Combined Approach Model Inputs

As noted in Chapters 7 and 8 above, several material property sets are necessary for the combined approach. It must be noted that the parametric studies noted in Chapter 8 were not re-run, but instead the cohesive element properties were left for possible tuning. Elastic material properties that generated from the BMT discussed above were utilized (Table 24). The specific inputs necessary for tabulated stress-strain relationship for this model were also generated from the BMT (Table 25). The specific inputs necessary for the cohesive elements were generated parametrically with the exception of the damage evolution parameters which were based on the results from the BMT delamination testing. Specifically, the final average G_c value was used for damage evolution energy for each mode.

To reiterate, the specific stress-strain relationship was taken directly from quasi-static, monotonic shear tests utilizing a ±45 laminate tested in tension. The key points identified in Table 24 and Table 25 below were chosen as points where significant changes in slope of the resulting stress-strain relationships were noted. Admittedly, these data were open to some interpretation, and small modifications that still fell within the relationship noted were deemed acceptable. In all cases, modifications of these inputs are noted and justified in the discussion below, or in cases where justification was not possible, they are deemed unacceptable and are noted as such.

Table 24: Material properties generated as outline in BMT section.

	E_1	E_2	v_1	G_{12}	GIc (J/m^2)	GIIc (J/m^2)
Tension (GPa)	40.6	16.3	0.27	16.8	806	1524
Compression (GPa)	38.4	14.4	0.28	14.4		

Table 25: Stress-strain inputs for each state indicated in Figure 99 and used in the routine.

State	1	2	3	4	5	6	7	8
Strain	0.002	0.003	0.056	0.087	0.0149	0.024	0.0356	0.0454
Stress (MPa)	18.1	49	67.2	80.6	94.3	103.2	103.2	103.2

Results and Discussion

A combined continuum/discrete progressive damage model was generated as noted above for IP wave in a coupon geometry. Load-displacement and stress-strain data were generated and used to compare and correlate, respectively, to BMT results. Correlation was also assessed, where applicable, utilizing visualized results from images. Continuing with the systematic approach outlined above, the initial case considered was an IP wave, in tension and compression, before correlation for several other cases as assessed. Processing times for all runs of this model were significant compared to the CDMs above and ranged from 160 to over 240 minutes in length, again due largely to the small increments necessary for convergence. Results and correlation for each are outlined below.

Tensile IP Wave Correlation

During the process of developing this modeling approach, comparisons to experimental data were made to ensure proper validation of the cohesive parameters as noted above. Once these parameters were established and test-based shear response was

applied, visual correlation was noted immediately through the damage progression as seen in Figure 101. In both cases, failure first occurred at the edges where fibers were discontinuous at low loads (Figure 101, left). Next, damage began to accumulate in the area of fiber misalignment as the matrix, or cohesive elements, fail in shear as the fibers try to straighten due to the tensile load (Figure 101, right). Due to the uniformity of model, the areas of failure are much cleaner and less complex compared to the BMT coupon results. However, a more gradual response was noted in the experimental progression due to the material as-tested not being completely uniform as noted by Riddle et al. This work noted that not only did the wave parameters vary in each layer, but also that the center axes of the wave in each layer did not line up exactly on top of one another. These variations were attributed to manufacturing variability and critical parameters were calculated based on the average of the data from each layer.

As seen in Figure 102, the model response matches the experimental and the kinks in the modeled load-displacement data were the result of cohesive failures. Loading took place up to the first failure on one side where the load dropped slightly, while the remaining fibers displaced before taking additional load. This happened again on the other side at the second kink. It is worth noting that while the experimental and analytical curves are similar up to ≈0.5%, the curves do not match exactly. This mismatch was also due to the uniformity of the analytical response resulting in sudden failures, while the experimental data showed a more gradual response. Thus, the curves do not match exactly, but the results that once the initial discontinuous fiber section failures have occurred, the stress-strain points match.

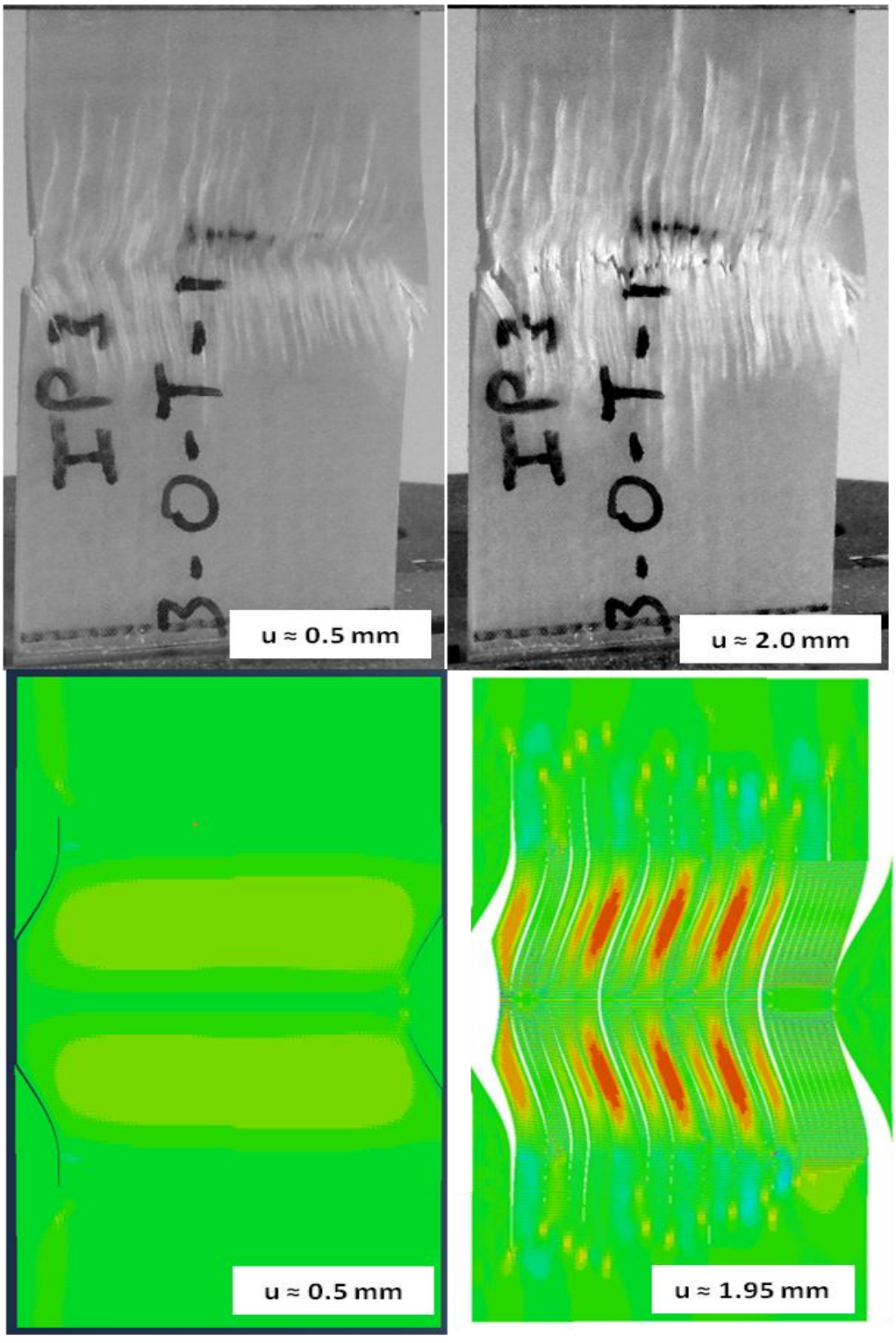

Figure 101: Comparison of damage between analytical (below) and experimental (above) showing onset and final damage left-to-right, respectively.

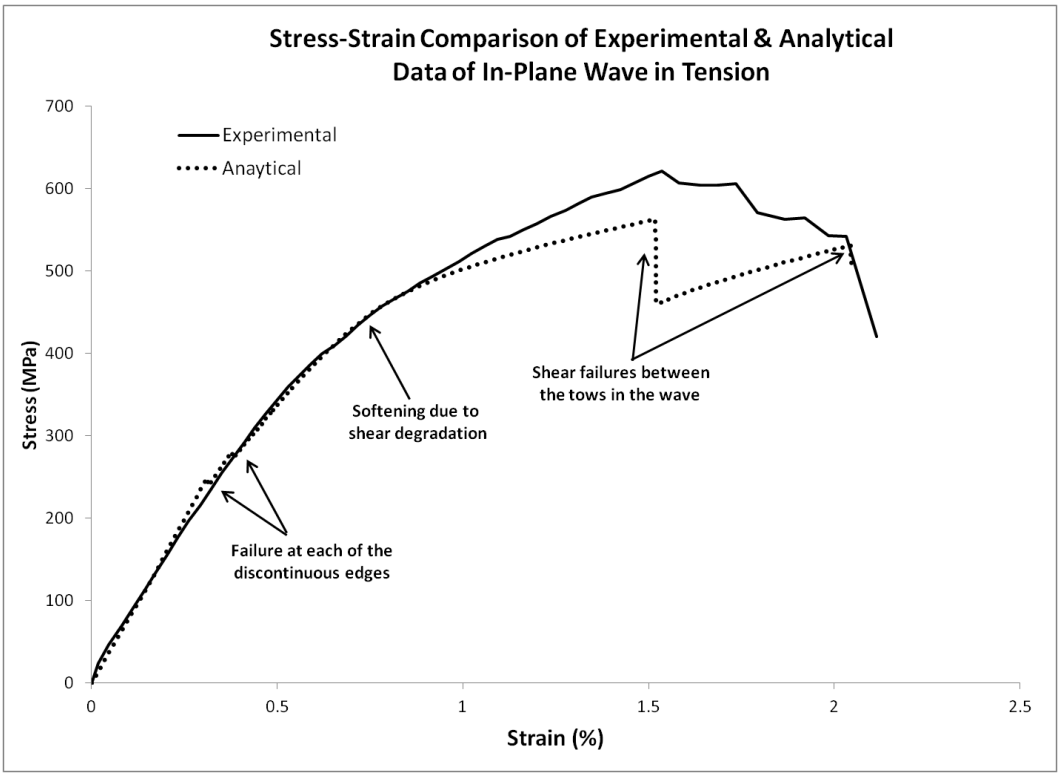

Figure 102: Stress-strain comparison of IP wave BMT and combined model in tension.

From this point, the model matched the softening noted experimentally and indicated the shear response of the UMAT subroutine. While this softening initially matched well up to ≈0.9%, the model then over-predicted the softening response up to the next cohesive failure (≈1.5%). At this third kink, cohesive failure was again noted in the center of the laminate at which point the load-carrying capacity degraded significantly. At this point, load-carrying capacity was still noted before ultimate failure was noted at ≈2%. Thus, as shown, the damage progression noted in the analytical stress-strain curve matched quite well with stress-strain data gathered during the physical testing of the IP wave case.

Compression IP Wave Correlation

Upon completion of tensile correlation, the model was modified and correlation was attempted in compression. The same model was utilized and the material properties were replaced with compression as-tested control results. In addition, the cohesive element damage initiation and damage evolution criteria were updated. Visual comparison was difficult due to difficulty associated with determining the exact damage progression. For example, it was noted that damage occurred in shear around the discontinuous fiber sections, but it was unclear exactly when this initiation occurred. The damage appeared to get worse through the entire test and there was overlapping with matrix failures throughout the fiber misalignment region. This overlapping was likely complicated by the noted variations, and possible delamination, between the layers of the as-tested specimen and delamination. The model, however, showed clearly that failure initially occurs at each of the discontinuous sections before it occurred in shear in the area around the wave as shown in Figure 103. Comparison beyond these generalizations was not possible given the data were not available.

A comparison between the stress-strain curves was then made and correlation was noted (Figure 104). A slight difference in initial stiffness was noted and this difference was attributed to the variation of the IP wave in the compression coupons test. Beyond this, distinct kinks were noted, similar to those in the tensile case, where sections of cohesive zones failed. As above the first two kinks noted were as the discontinuous fiber sections failed (Figure 103, right). Once this initial failure occurred, the main body of the specimen was able to continue to carry increasing load up to the initial failure within the

laminate, as shown in the increased stress area of the right image of Figure 103. After these failures, additional load was carried, before ultimate failure. The model over estimated the load-carrying capacity of the specimen before final failure primarily due to the underestimation of material softening. However, this 10% overshoot can be overlooked as the model predicts ultimate failure at a strain of approximately 1.9%, whereas, the experimental data showed failure at just approximately 2.0%. As such, the model was conservative with respect to strain at ultimate failure and overall the correlation to the experimental data was deemed successful.

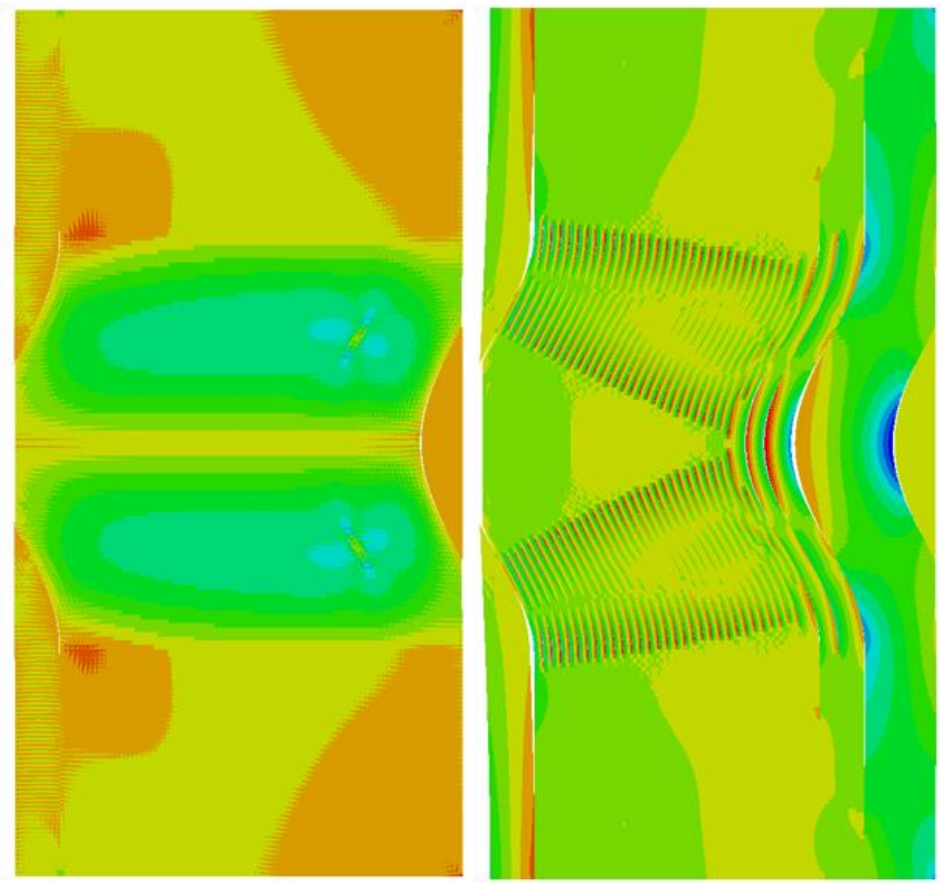

Figure 103: Shear stress of increasing load (left-to-right) noted in the compression of an IP Wave.

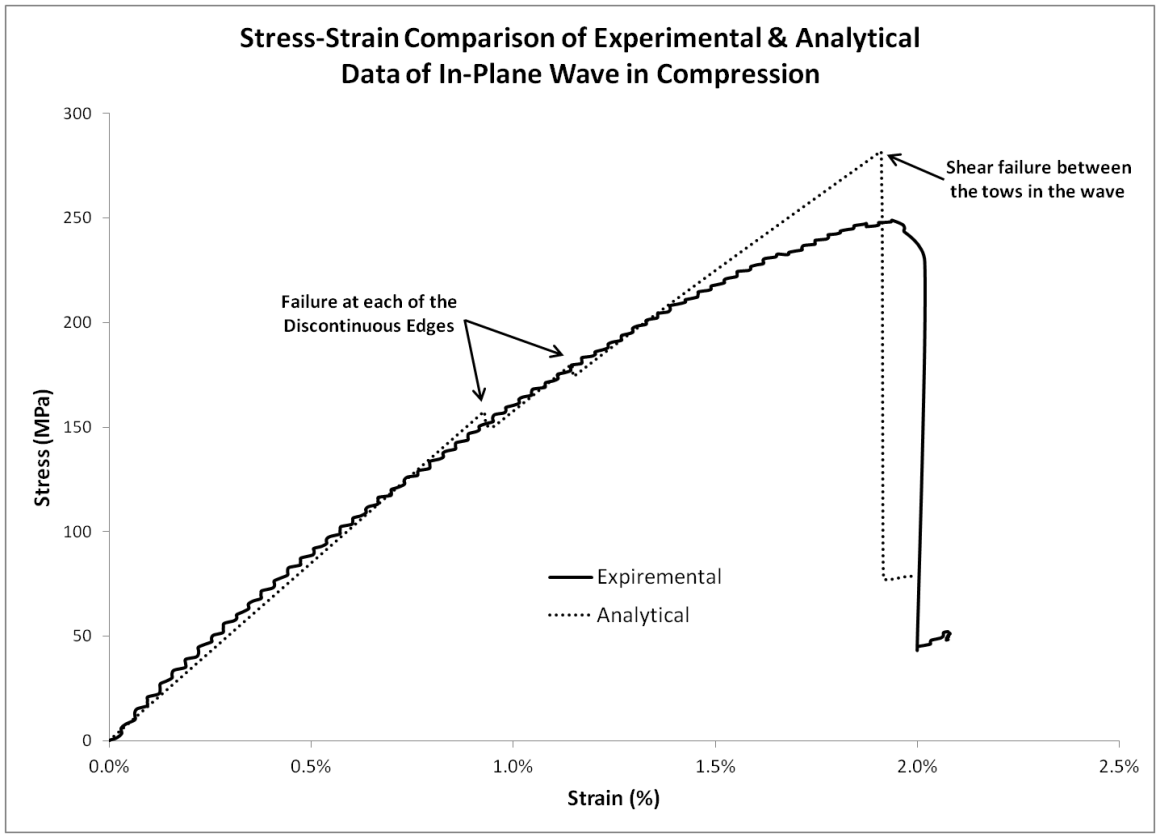

Figure 104: Stress-strain comparison of IP wave BMT and combined model in compression.

Combined Model of OP Wave

Methods: Given the reasonable correlation of the IP wave in tension shown above, it was deemed worthwhile to continue the systematic approach of increasing flaw complexity. Thus, an OP wave model was generated and correlated in both tension and compression. As noted in the BMT, the compression case does not have any correlation data and was generated only as a baseline to be correlated in the future when such data becomes available. Similar to the IP wave, this OP wave model was setup to be 2D and was rotated about the global 1-direction such that the wave went through the thickness

(50 mm). As shown in Figure 105, the geometry was set up to match the intended coupon size (100 mm x 4 mm), with quadrilateral, plane stress shell elements (S4R), in Abaqus where each element was generated to be consistent with the nominal fiber tow width (1.0 mm). To match the BMT method, a wave form with rotated properties was created and was generalized based on the as-manufactured OP wave. The OP wave modeled had an amplitude (A) of 2.9 mm, a wavelength (λ) of 22.8 mm, and average off-axis fiber angle of 19.4°. Local coordinate systems were defined for the elements oriented to form the wave such that the fiber direction remained consistent through the wave, and the material properties were modeled to correctly match these properties. To match the BMT method, a wave form with rotated properties was created and was generalized based on the as-manufactured OP wave. Displacement and boundary conditions were applied at the top and bottom, respectively, to match the BMT testing conditions, and as such, full field calculations were made to match the BMT data for load-displacement and stress-strain correlations.

The model was also modified to have a single layer utilizing the *SHELL SECTION* keyword option with the 50 mm thickness noted above for both the wave and the straight portions of fiber. A separate section with rotated properties was added for the wave form. Elastic material properties, shear response, and cohesive element properties discussed above were utilized and the same assumptions were made.

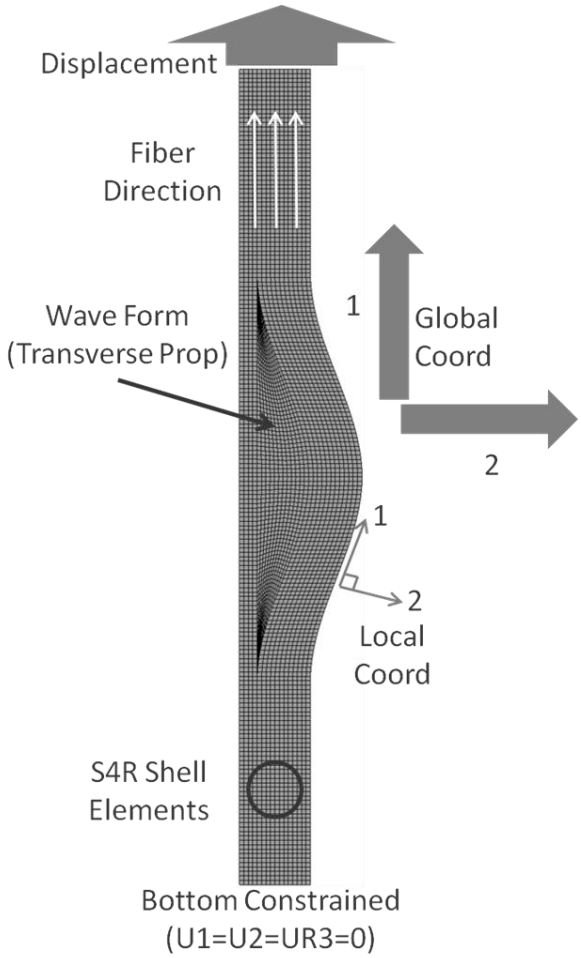

Figure 105: The 2D model setup utilized in the OP wave linear elastic models with Hashin failure criteria.

Results and Correlation: OP wave tension coupon samples from BMT results clearly showed that coupon failure was less sudden than it was for the unflawed controls or porosity specimens. OP wave compression was not analyzed due to buckling failures during the BMT associated with the asymmetry associated with the wave. In tension, each of the layers was noted to initially delaminate from the form and the surrounding layers in the area of the wave. After delamination occurred the wave continued to

straighten, and less softening was noted when compared to the IP waves. Fiber failure was similar to what was noted in unflawed, straight fiber controls; as sudden failure at the peak of the wave with significant brooming. DIC was utilized, though the edge of the coupons were not captured due to difficulties speckling the edge surface and identifying the coupon edges. As shown in Figure 106, the entire flat surface of the coupon was imaged and showed that the strain was minimal in the area of the wave once the layers delaminated and were in the straightening phase. The DIC data indicate both that the strain concentrated at the base of each side of the wave and that, as the coupon extended, much of that extension was the result of the fibers in the wave straightening. This was evident through even through a nominally 1.0 mm thick layer of material between the wave form and the misaligned layers and the surface being imaged.

While direct correlation was not able to be achieved given the rotation between the DIC and this model approach, it was clear from the model results that the initial strain concentrations are in the areas of interaction between the wave form and the misaligned fibers (Figure 107). Further analysis indicated that the damage progression continued with initial cohesive failure occurring after the initial shear response before redistribution allowed for increased load followed by significant delaminations as shown in Figure 108. It was interesting to note that in the progression shown in Figure 108, the strain appeared very consistent and very low in the area of straight fibers below the wave form. These strain concentrations directly matched the DIC results and indicated that this visual analysis was not just qualitative.

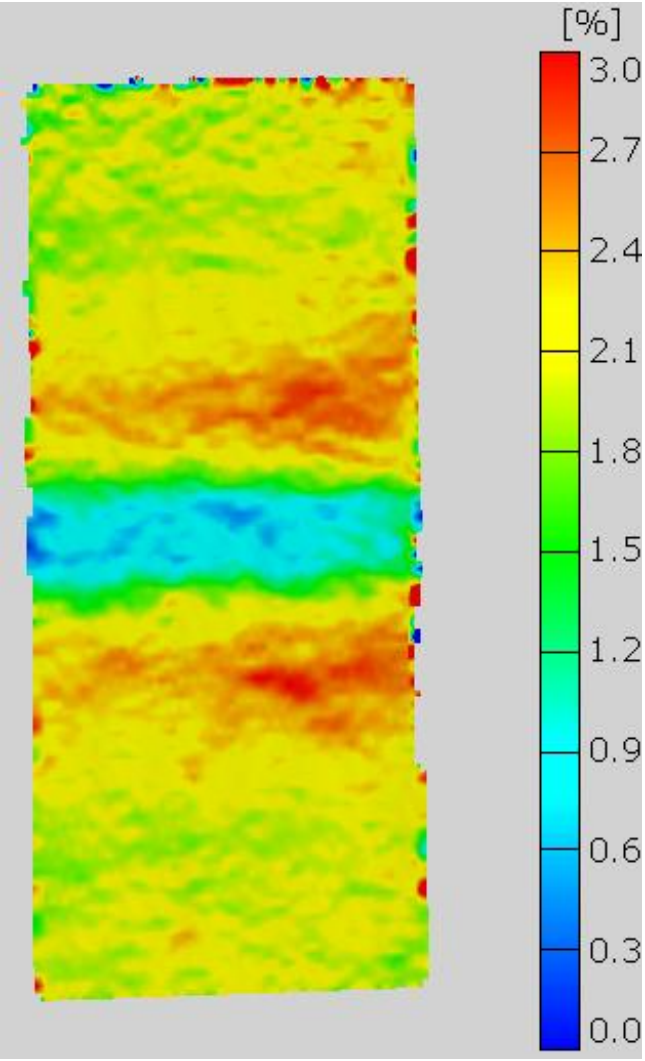

Figure 106: Strain field captured with DIC on flat back surface of OP wave coupon test indicating peak strains on each side of the wave.

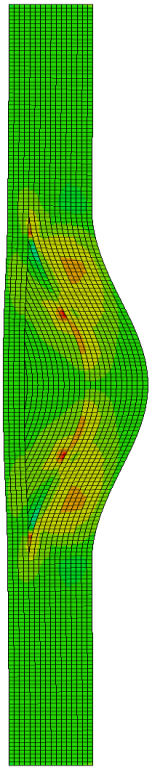

Figure 107: Shear stress field of combined model of OP wave in tension.

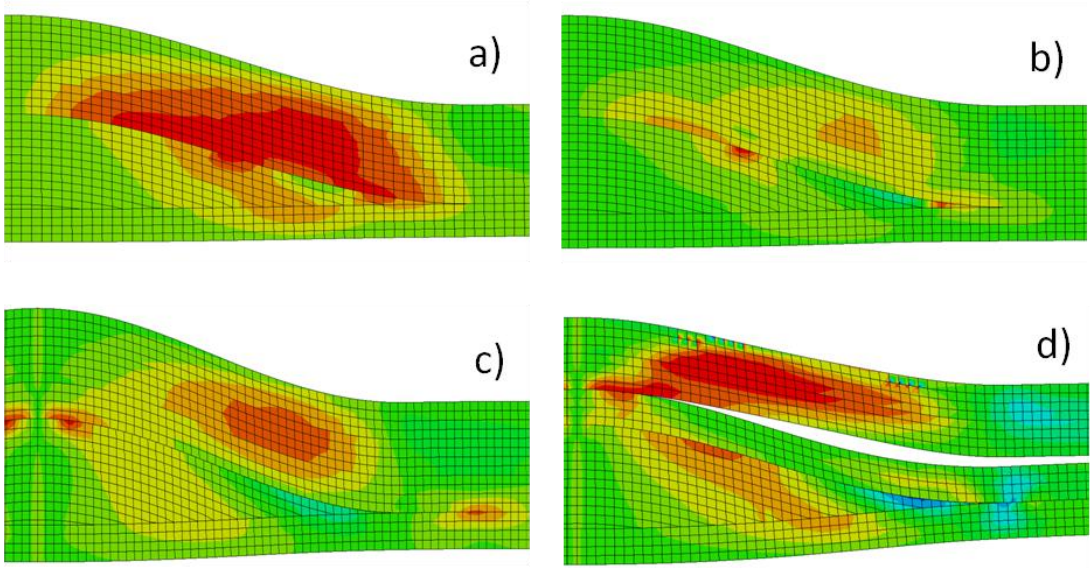

Figure 108: Damage progression of combined model of OP wave in tension indicating a) shear response, b) initial cohesive failure, c) load redistribution, and d) additional delamination and fiber straightening.

As above, quantitative correlation was performed by comparing the full-field stress-strain data from the BMT to the model results (Figure 109). As noted, no changes were made to the input model parameters other than the change in model geometry. The model captured initial stiffness quite well up to approximately 1.5% strain at which point the first cohesive failures were noted, which aligned with the transition from Figure 108a-b. Load redistribution occured and the model predicted the additional load-carrying seen through Figure 108c before additional cohesive failures and manual truncation occurred. While the correlation was not perfect, it matched fairly well. Tuning may be applicable as future work with additional testing and especially with improved understanding of response when this flaw is embedded into a substructure or structure.

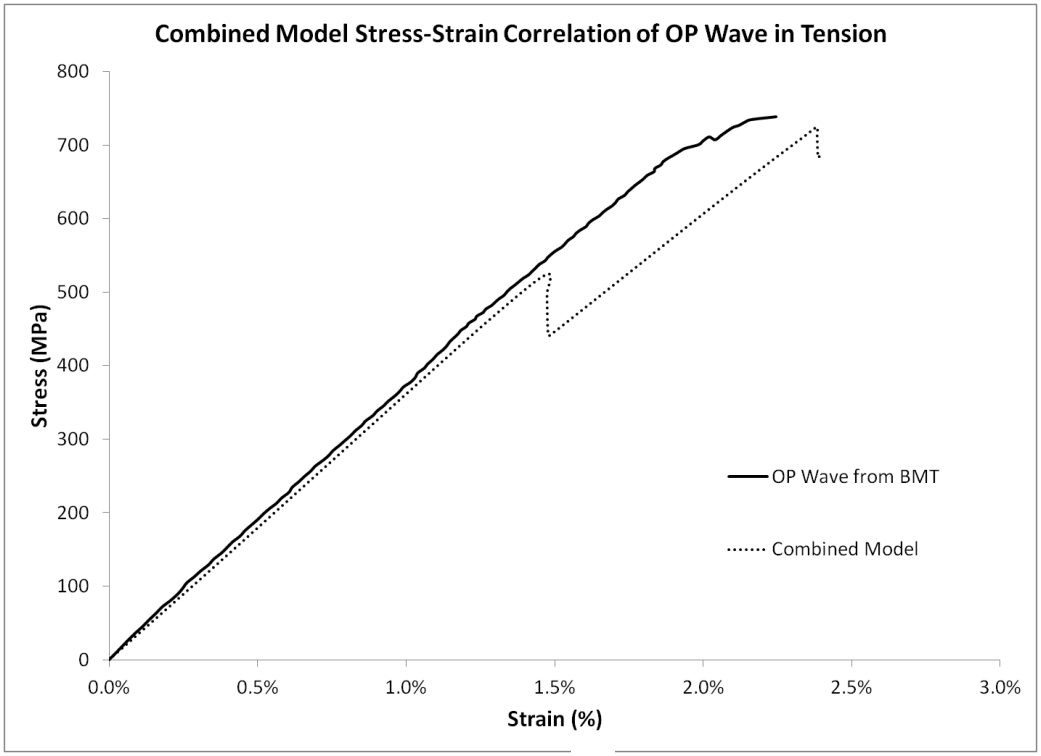

Figure 109: Stress-strain comparison of OP wave BMT and combined model in tension.

OP Wave Compression

The model was also run for the compression case (Figure 110) and while the compression case seems reasonable, there are no data for comparison and so no correlation was made; however, the model is ready when future data become available, and the results of preliminary runs are discussed briefly here. As with all compression cases, the boundary conditions were slightly modified such that the straight fiber sections of the model were constrained to prevent transverse displacement, thereby effectively reducing the gage section. In addition, material property inputs were updated with compression data. Visual results again indicated strain accumulation in the area of interaction between the wave form and misaligned fibers (Figure 110). After this initial shear response, damage progression continued with initial cohesive failure, load redistribution, and multiple cohesive failures including at wave peak as shown in Figure 111. These results appeared to match the visual results noted during BMT compression testing. While the stress-strain results presented in Figure 112 do not have direct corollaries, they appeared reasonable and indicated that this model appeared to be a good jumping off point for future work in this area.

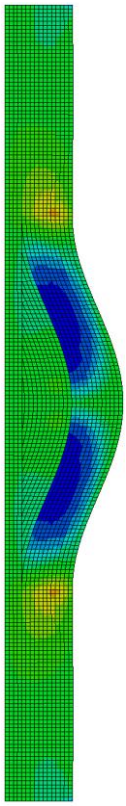

Figure 110: Shear stress field of combined model of OP wave in compression.

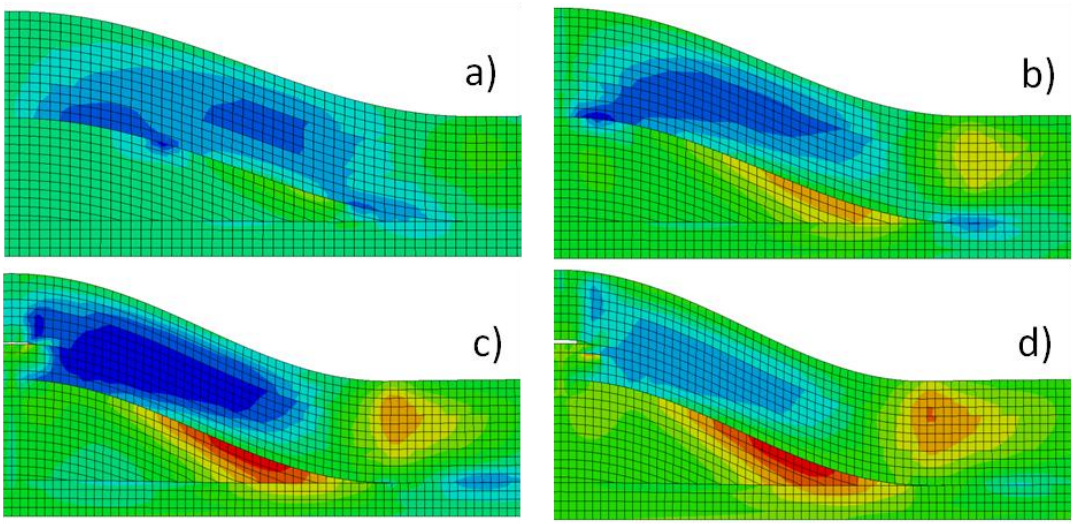

Figure 111: Damage progression of combined model of OP wave in tension indicating a) shear response and initial cohesive failure, b) continued delamination, c) load redistribution, and d) multiple cohesive failures including at wave peak.

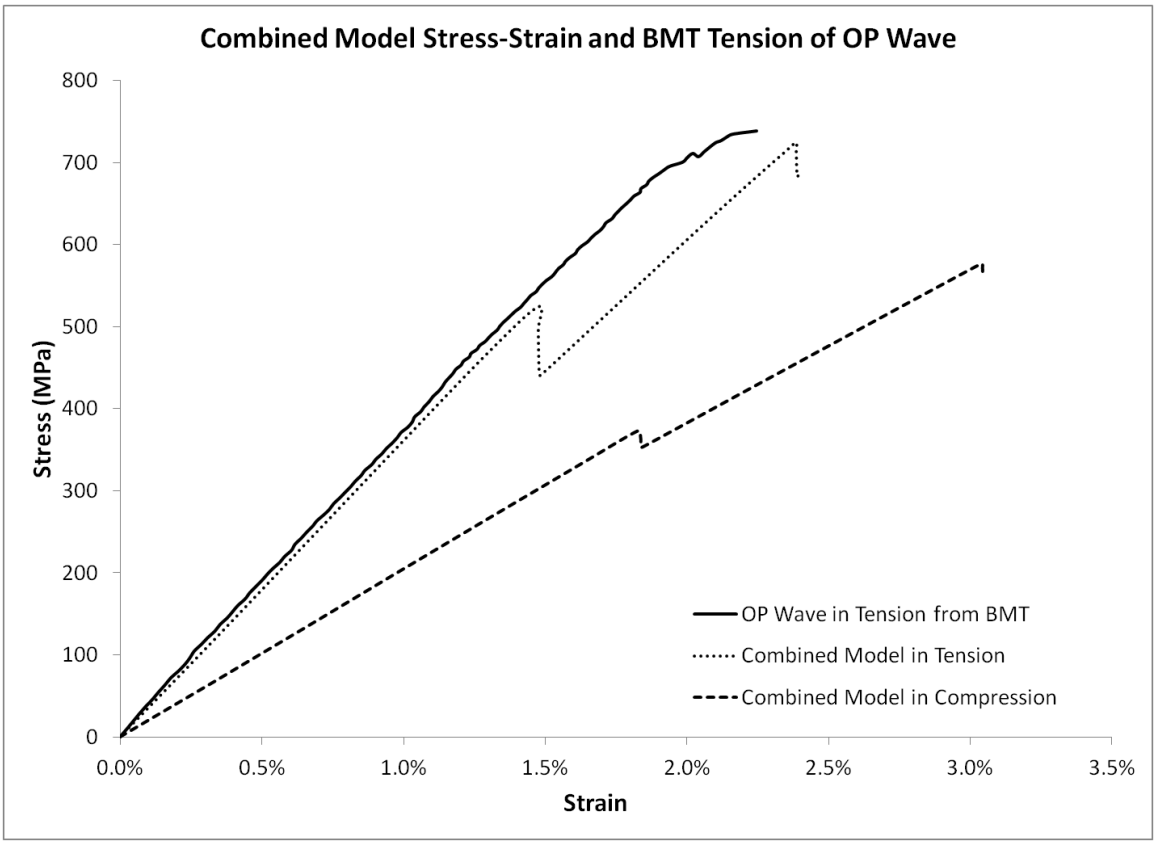

Figure 112: Stress-strain response of combined model in compression shown with OP wave BMT and combined model in tension for comparison.

Additional IP Waves in Tension

Given the reasonable correlation to the IP wave case above, two other IP wave cases were correlated in tension and only in one case in compression. The two cases were chosen because they offered bounds, with fiber misalignment angles of approximately 16° and 48° correlated to the first case of approximately 29°. Only the 16° case was able to be run in compression due to a convergence issue related to increment size associated with the 48° case that was not able to be overcome. The approach was to use the model inputs from the first case to determine the predictive capability of this

model by not adjusting any of the parameters other than geometry. Models for each wave case were generated in a similar fashion as in Figure 97 above, but with different amplitudes, wavelengths, and fiber misalignment angles. Otherwise, the models were identical for these cases and as such the 48° case was not modified to attempt to fix the convergence issue since all other cases ran sufficiently and the increment size was already set very low. It must also be noted that visual damage progression appeared virtually identical to progression in the initial IP wave case for each case correlated here. As such, further discussion was not warranted.

The initial IP wave case above matched initial stiffness, then predicted the discontinuous fibers before over-predicting the softening up to a final failure which did not correlate exactly due to assumed uniformity of the model (Figure 102). Similar initial stiffness results were noted in both the 16° and the 48° IP wave cases (Figure 113). Instead of an over-prediction of the softening, a slight under-prediction was noted in the 16° case, while the 48° case appeared to match the overall softening quite well. As seen in Figure 113, the 16° case had an initial damage kink before softening began resulting in an under-prediction of peak stress of approximately 4.8%. The model then matched, within the same range, the continued load-carrying capacity up to truncation at failure of 2.5% strain. The 48° case told a different story and saw the best correlation of any model case in this entire study through softening. However, shortly after the kinks associated with the delaminating of discontinuous fiber sections, a significant number of cohesive elements failed resulting in a drop in load-carrying capacity, but not in final failure. As such the peak stress was noted at approximately 1% strain and was found to be almost

20% below the peak stress noted in the model at 1.7% strain. After this peak, however, a slight increase in load-carrying capacity was noted up to truncation at failure of 2.4% strain.

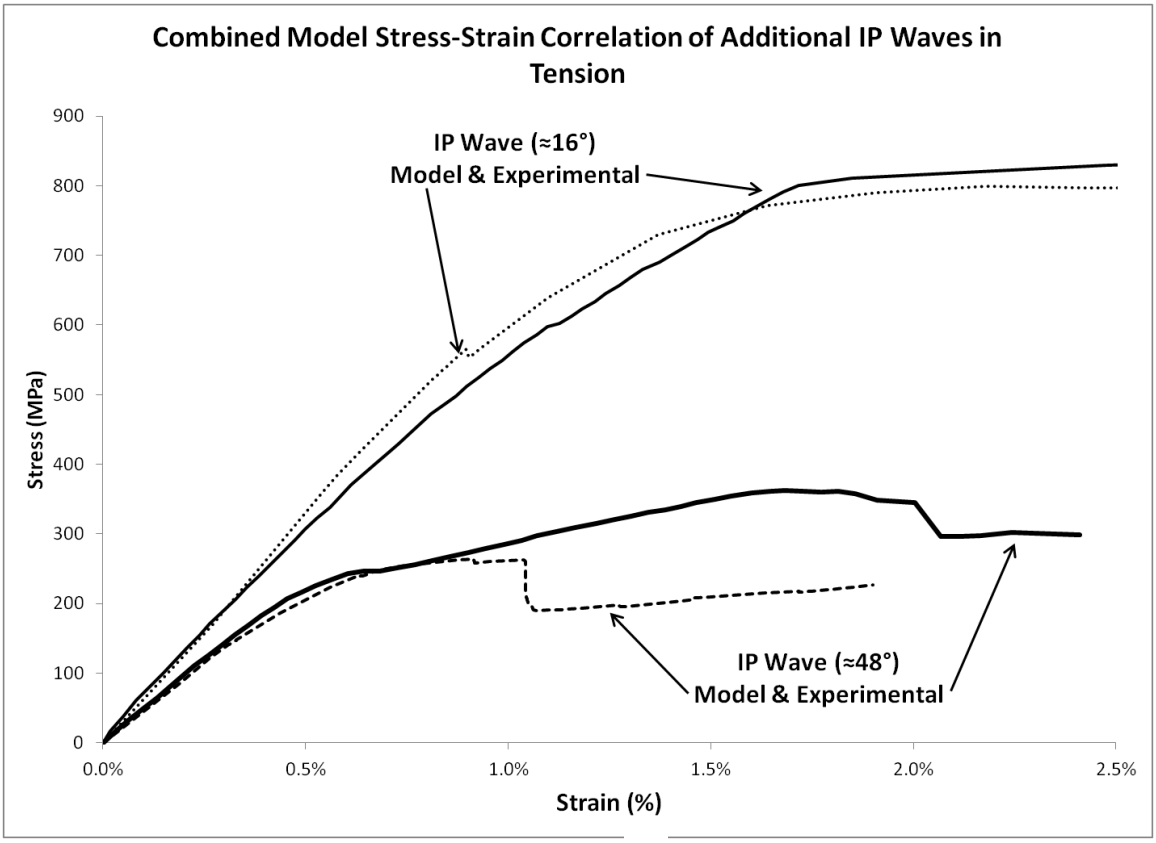

Figure 113: Stress-strain comparison of 16° and 48° IP wave cases in tension with results indicating reasonable overall correlation and prediction.

As noted above only the 16° combined model yielded useful results in compression. The results were very similar to the initial case shown in Figure 104 where stiffness was initially slightly low for the model and was again attributed to variation in the BMT coupons tested. In this case, the only one initial kink was noted and a stiffness change was associated with it. Unlike the initial case, the second kink occurred just

before the peak stress which was over-predicted by approximately 5.1% with a predicted strain of 1.6% instead of the almost 1.8% from the BMT.

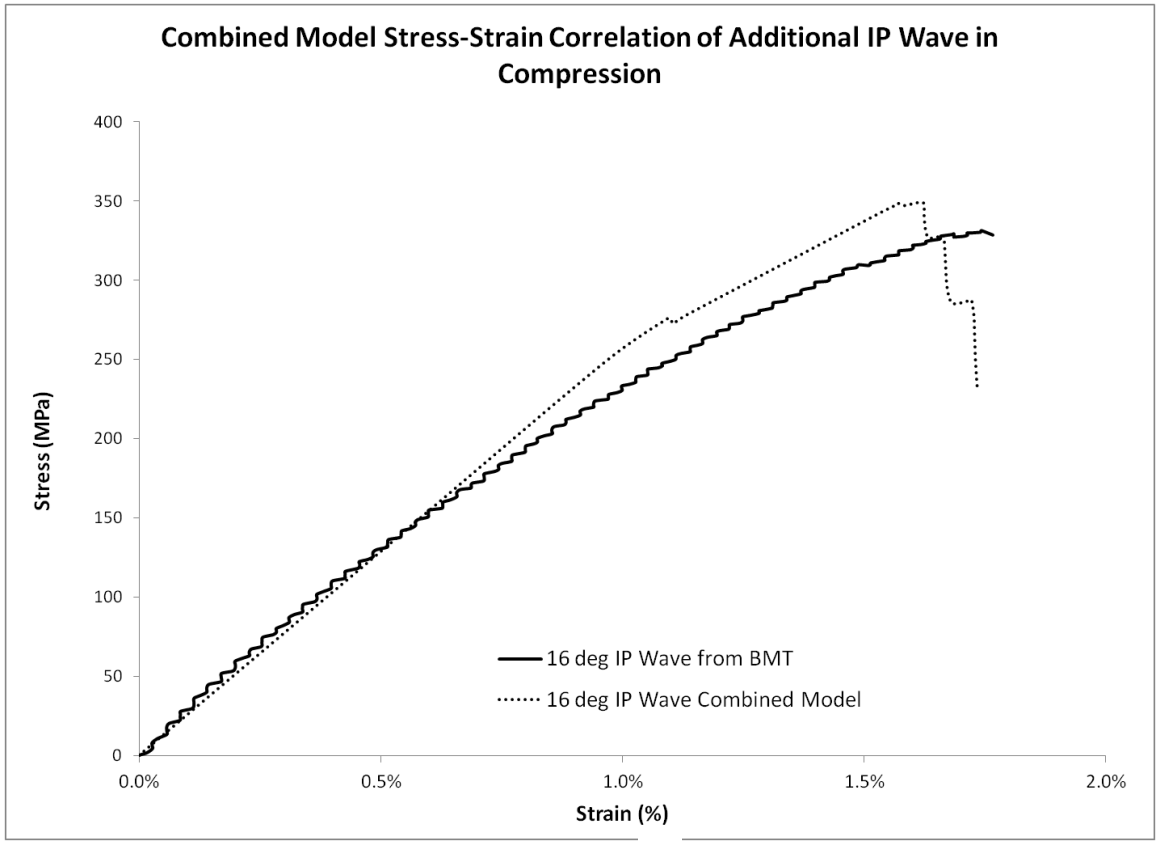

Figure 114 Stress-strain comparison of 16° IP wave case in compression with results indicating reasonable overall correlation and prediction.

While each model showed some variation, each case was able to adequately predict the stress-strain response. The variation in each modeled response was able to adequately be explained by the assumed uniformity of each layer in the model. This uniformity was not actually seen in the coupons and, given this assumption, the resulting correlations appear reasonable warranting that this model does have some predictive capability in these bounding cases. To drastically improve the results, and likely improve

the predictive capabilities, a more complex model would be needed that addresses one, if not both, of these assumptions noted, which is left as future work.

Carbon Fiber IP Waves in Tension

Following the systematic approach and to further test the predictive capability of this modeling approach, the same model was run with the initial IP wave case (Figure 97) changing the material to a uni-directional carbon fiber. Material properties were gather from the BMT and from Soden et al. (1998) who characterized two typical uni-directional carbon fiber/epoxy composites quite extensively. These material properties are shown below in Table 26 while the UMAT stresses and strains are listed in Table 27. The shear stress-strain curves shown in Figure 115 were determined by Soden et al. and utilized in same way as Figure 81 above to generate the tabulated stress and strains shown in Table 27. Figure 115 clearly shows this shear response for two different carbon fiber epoxy composites with subtle variation between the two. Considering these subtle differences, the AS4 data set was utilized the data resolution was finer allowing for easier determination of important stress-strain values. Even though neither of the materials in Figure 115 was the same as the BMT material, this response was determined to be sufficient for this initial comparison. Especially given that at the time of this publication comprehensive carbon data for this material system and IP wave results were not able to be included in the BMT and as such comparisons are made between general trends known to exist between fiberglass and carbon fiber composites.

Table 26: Carbon fiber material properties generated as outlined in BMT section and from Soden et al. in italics (1998).

	E_1	E_2	v_1	G_{12}	G_{13}	G_{23}
Tension (GPa)	83.9	5.8	0.29	*5.5*	*5.5*	*5.5*

Table 27: Stress-strain inputs for each state generated from Figure 115 data and used in the non-linear shear UMAT subroutine.

State	**1**	**2**	**3**	**4**	**5**	**6**	**7**	**8**
Strain	0.005	0.006	0.008	0.010	0.012	0.015	0.020	0.030
Stress (MPa)	29.15	34.98	41.30	47.45	52.39	57.98	63.84	69.47

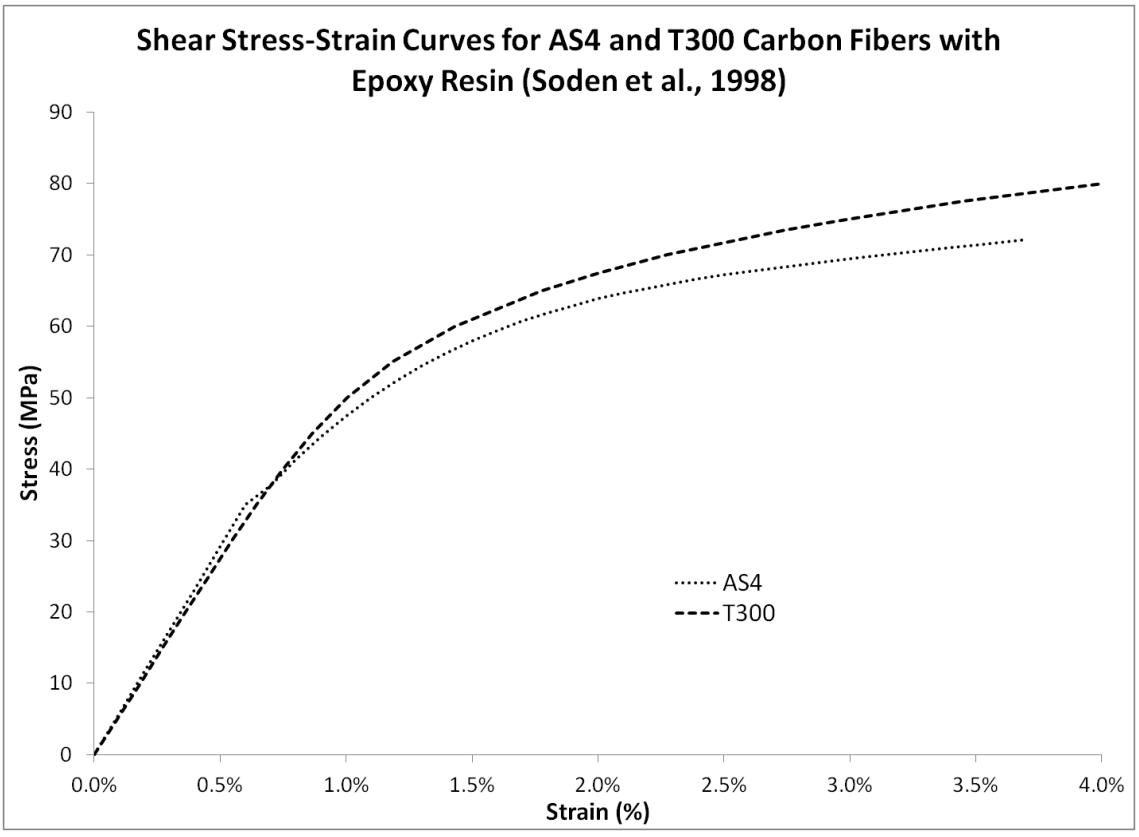

Figure 115: Shear stress-strain relationship of unflawed specimen with tabulated data points indicated for UMAT (Soden et al., 1998).

As expected, the qualitative comparison of the strain accumulation leading to damage was consistent between for the carbon fiber (Figure 116) and that noted above for glass (Figure 101). Initial kinks were noted where edge delaminations occurred before strain accumulated in the wave area leading up to multiple cohesive failures. Quantitative comparison (Figure 117) indicated that the carbon IP wave model was approximately twice as stiff as the experimental coupon which matched the initial difference in longitudinal modulus a similar result as noted with these data in Chapter 5. The model predicted softening to then begin just above 400 MPa which correlated well to the stress at which the glass coupon began to show significant stiffness reduction. The failures at the discontinuous edges were noted at approximately the same strains as the glass model, a result of utilizing the same cohesive damage parameters. A linear response was noted after the second discontinuous edge failure up to peak stress (760 MPa) at approximately 1% strain which was less than the 1.5% noted with glass. At this point, significant cohesive failures occurred then reloading and ultimate failure at approximately 1.5% strain. As noted with the Hashin model in Chapter 5, this carbon model offered a jumping off point to allow and appeared to vary from the glass experiment and model within the typical generalizations between glass and carbon fibers. Future work to compare to actual carbon fiber IP wave coupons is highly recommended with a full array of material and damage properties generated for same carbon material as tested. This will ensure that the carbon model is accurate.

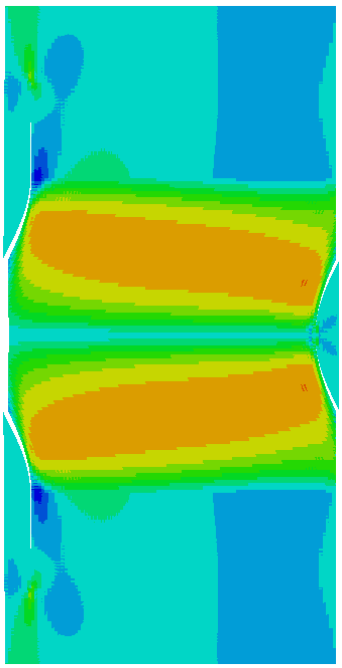

Figure 116: Shear strain field of combined model for carbon fiber material.

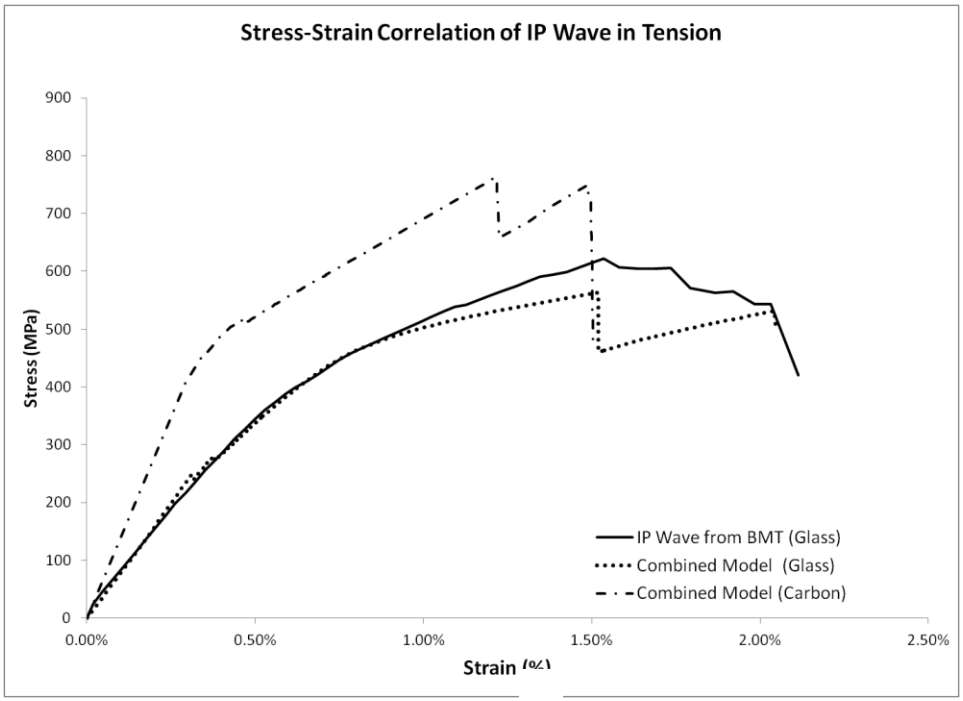

Figure 117: Stress-strain comparison of fiberglass composite from BMT and combined model with predicted carbon response for IP wave with same combined model.

Combine CDM/DDM Approach Summary and Conclusions

A model has been developed that combines both continuum and discrete modeling techniques. To accurately model the continuum portion, a user-defined material subroutine has been created and used with material properties established from experimental testing. Cohesive zone elements were placed between each fiber tow to capture the fracture that occurs in these areas. The model has been analyzed for the same IP wave case that was used for each modeling technique, and reasonable visual damage progression and quantitative stress-strain correlation have been achieved in both tension and compression. The user-defined material subroutine allows for the model to capture shear degradation between key failures and captures cohesive zone failure effectively. While correlation was not exact, due to assumed model uniformity, it matches between the experimental and analytical at all key points through the damage progression.

Other wave types and misalignment angles were then modeled to determine model capabilities. First, OP waves were modeled utilizing the same parameters from the initial IP wave case, though the perspective of the model was rotated and geometry updated. The results indicated that reasonable correlation was achieved in tension and visual damage progression was easier to analyze due to the discrete nature of the cohesive elements. A compression model was created and run with promising results; however, correlation is left as future work at such a time when OP wave compression results become more readily available. Next, two bounding IP waves were modeled and correlated in tension with the unchanged parameters to assess the predictive capability of the model. While both models correlated well and in some areas showed the best

correlation of any model runs, correlation was not perfect and variations in each run were noted. These variations could be the result of insufficient model prediction capability, or perhaps more likely, they are caused by the variations within and between the tested coupons. Establishing this source of error is left as future work. Further predictive capabilities were checked by changing material to a carbon fiber and comparing to the initial IP wave case with glass. Comparisons were reasonable given normal comparative trends from fiberglass to carbon fiber composites.

Overall, this combined continuum/discrete modeling approach was found to have reasonable to very good correlation in all cases for both tension and compression. Further work has been identified and may be warranted given the consistency of this model though the computational expense was high compared to the other techniques discussed herein. A discussion including comparison of this and the other techniques follows in Chapter 10.

REVIEW OF ANALYTICAL/EXPERIMENTAL CORRELATIONS

Damage progression of common manufacturing flaws in composite structures lacks comprehensive understanding and predictive tools. A systematic, three-round (Figure 118), unique comparison of several different modeling techniques was undertaken to establish model consistency, accuracy, and predictive capability. As detailed in Chapters 4-9 above, results from various modeling approaches were correlated with Benchmark Material Testing (BMT) results. A systematic approach was employed to compare different modeling methods discussed herein in increasing complexity of the three rounds as outlined in the Figure 118 work flow diagram.

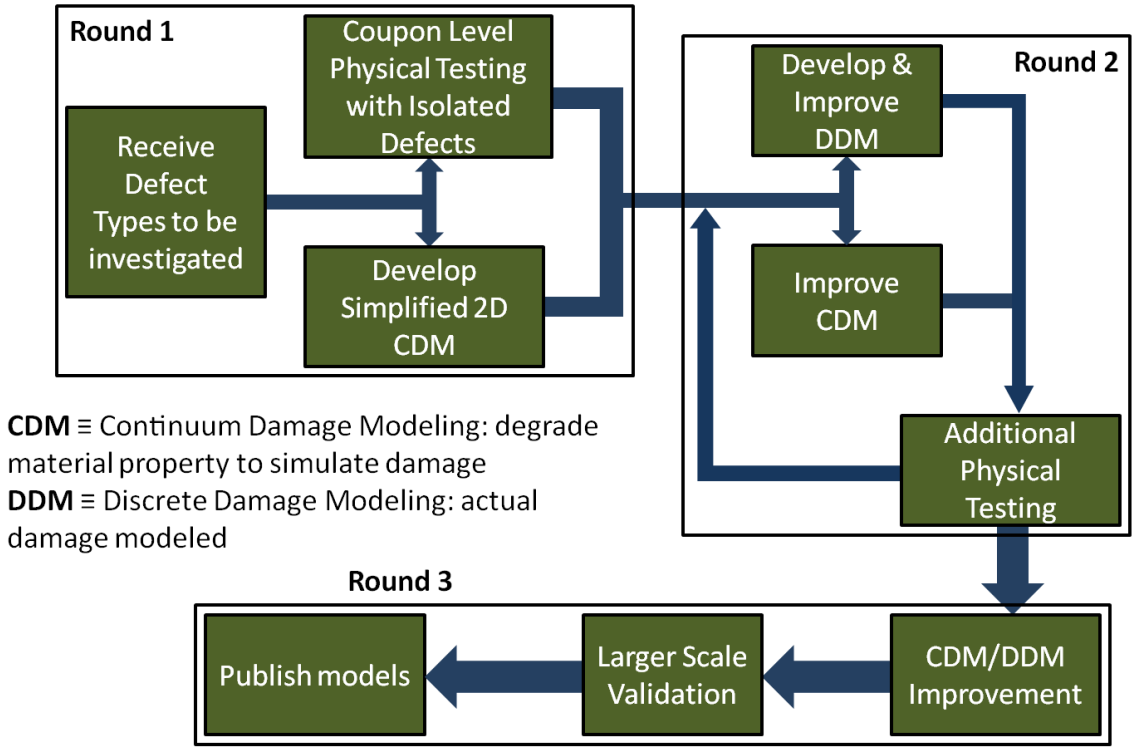

Figure 118: Effects of Defects laminate work flow diagram (reprint).

All of these models utilized material properties and responses generated in the BMT or other justifiable sources. For each different model type, the systematic approach discussed above and noted in Figure 119 was followed. After the model was initially developed, stiffness and an initial IP wave case were correlated. If results were acceptable, flaw complexity was increased to test consistency, accuracy, and predictive capability until the correlation was deemed acceptable or unacceptable. Acceptable modeling methods were able to predict and match flawed material response for multiple flaw types utilizing unflawed material properties and flaw geometries. If these criteria could not be met by a model at any point during the systematic increase in flaw complexity, the model was deemed unacceptable and was discarded.

Unless otherwise noted, the increase in flaw complexity in each case went from controls to porosity to the IP wave baseline case to the initial OP wave case to other IP and OP geometries. Acceptable models were able to predict and match each of these cases, while unacceptable models were only able to predict portions. Figure 120 below shows the correlations of each technique for the IP wave used commonly throughout, while Table 28 offers identification of models run, acceptability of results, and both input parameters and acceptable parameters for tuning for each model. A summary of the results from each Chapter and an identification of the most accurate and consistent model are found below.

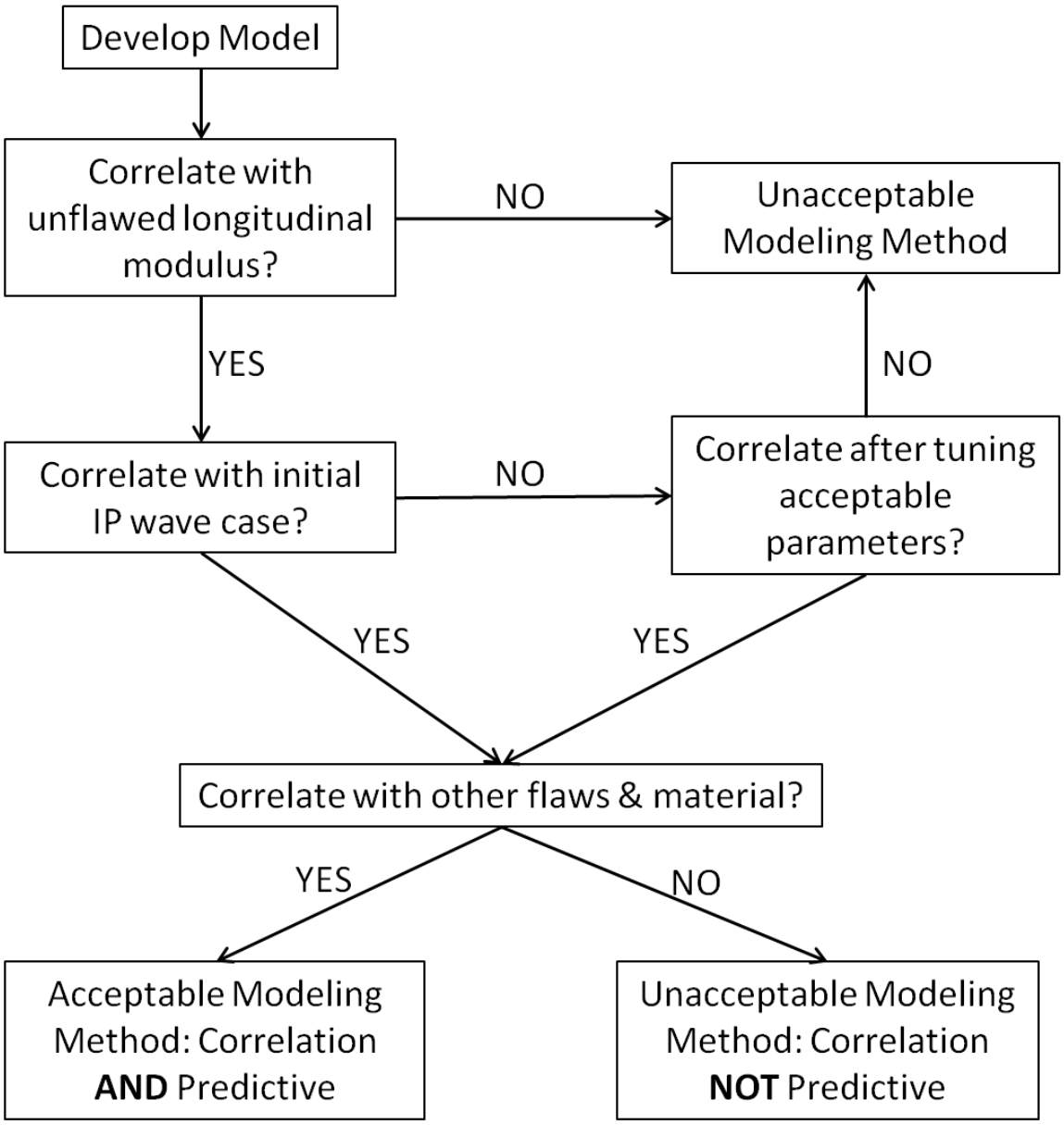

Figure 119: Flow chart depicting systematic approach to determine correlation acceptance and predictive capability (reprint).

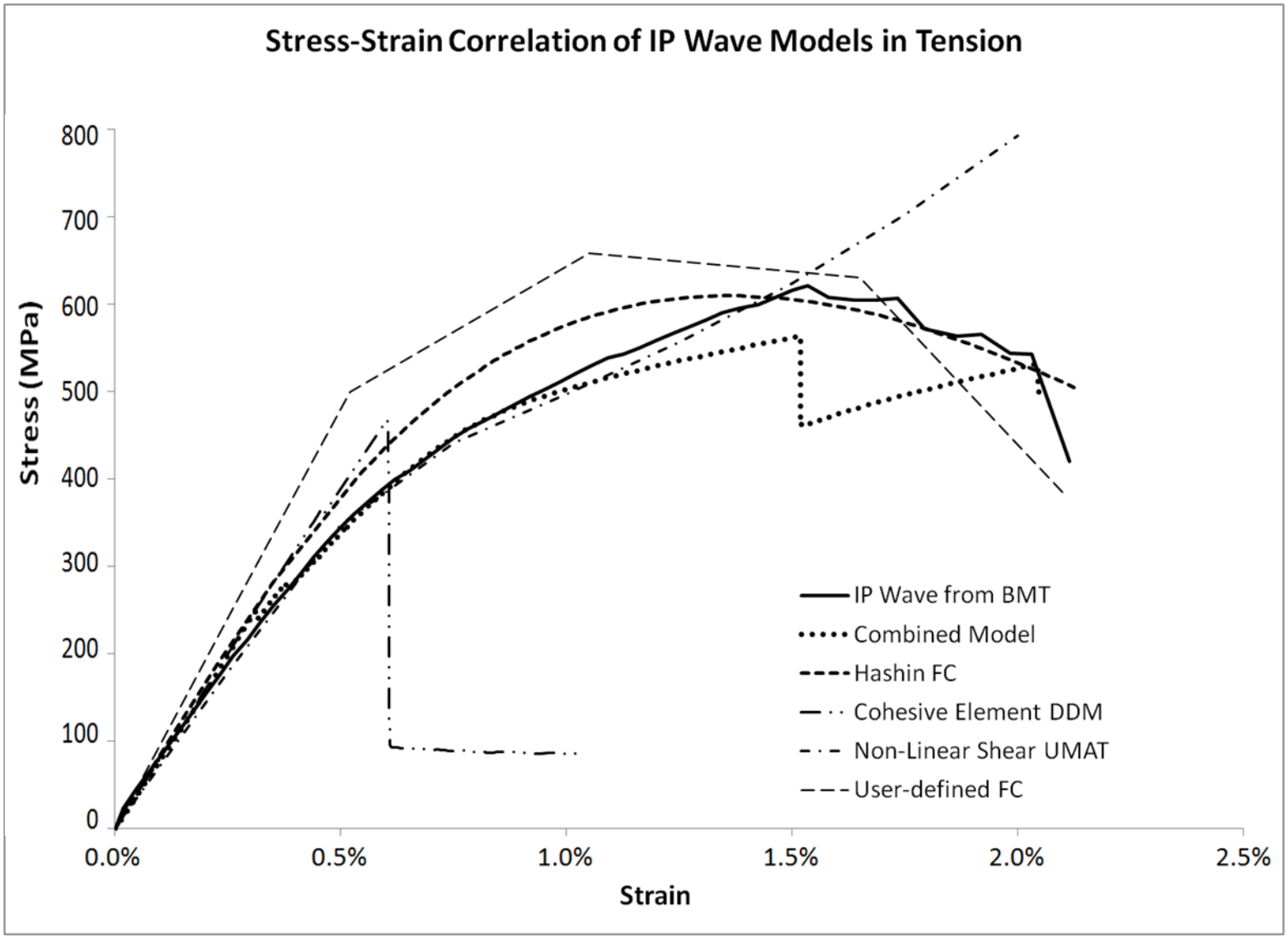

Figure 120: Stress-strain correlations of common IP Wave for each model technique compared to BMT results.

Table 28: Identification of models run, acceptability of results, input parameters, and acceptable parameters for tuning.

			UNFLAWED		POROSITY		IP WAVE		OP WAVE		ADDITIONAL WAVES AND MATERIAL		INPUT PARAMETERS	TUNED PARAMETERS (ACCETABLE)
Model Type	Model	Effects of Defects Round	Tension	Comp	Tension	Comp	Tension	Comp	Tension	Comp	Tension	Comp		
CDM	Linear Elastic	1	MC	MC	NR	NR	NR	NR	NR	NR	NR	NR	ELASTIC PROPERTIES	NONE
	Linear Elastic w/ Hashin Failure Criteria	1	MC	MC	A	M	A	M	A	R	A,M	R	ELASTIC PROPERTIES & DAMAGE INITIATION, EVOLUTION, &	DAMAGE INITIATION, EVOLUTION, & STABILIZATION
	Subroutine w/ User-defined Damage Criteria	2	MC	MC	NR	NR	U	U	NR	NR	NR	NR	ELASTIC PROPERTIES, REDUCED PROPERTIES, & FAILURE CRITERIA	REDUCED PROPERTIES
	Non-Linear Shear	2	MC	MC	NR	NR	U	U	NR	NR	NR	NR	ELASTIC PROPERITES & STRESS-STRAIN FROM UNFLAWED SHEAR RESPONSE	SUBTLE CHANGES TO STRESS-STRAIN
DDM	Cohesive Elements between Tows	2	MC	MC	NR	NR	U	U	NR	NR	NR	NR	ELASTIC PROPERTIES & COHESIVE TRACTION-SEPARATION	COHESIVE TRACTION-SEPARATION
Combined	Non-Linear Shear w/ Cohesive Elements between Tows	3	MC	MC	NR	NR	A	A	A	R	A	A,R	ELASTIC PROPERTIES, STRESS-STRAIN FROM UNFLAWED SHEAR RESPONSE, & COHESIVE TRACTION-SEPARATION	SUBTLE CHANGES TO STRESS-STRAIN & COHESIVE TRACTION-SEPARATION

KEY:
A = ACCEPTABLE CORRELATION (visual correlation and within 10% of Strain at Peak Stress while also within 10% of Peak Stress)
M = MODERATE CORRELATION (visual correlation but marginal quantitative acceptance criteria)
U = UNACCEPTABLE CORRELATION (unacceptable visual and/or quantitative correlation)
R = MODEL RUN BUT NOT CORRELATED (insufficient test data available)
NR = MODEL NOT RUN (due to unacceptable initial case or acceptable overall method)
MC = INITIAL MODULUS CHECK (stiffness of model within 5% of test)

As noted in Table 28, a modulus check (MC) was performed in each case. Next, porosity was modeled using a true CDM approach where material properties were degraded based on amount of included air. Acceptable correlation (A) was achieved in tension, and while results appeared reasonable in compression, correlation was not performed (R) due to lack of consistency of BMT results. Given the property degradation model used, the lack of physical flaw geometry, and the acceptable correlation in tension, no additional runs or correlations were performed for porosity.

With porosity correlations achieved, full attention was paid to the modeling of fiber waviness, a more unique and less investigated subject, as few options exist with predictive capabilities. As noted in Table 28, each technique was initially modeled with the same IP wave case, and if correlation was achieved, additional waves and materials were considered. Correlations were then performed except in cases where BMT results were insufficient, in which case the model was run (R) and correlation was left as future work when results are available. If correlation was deemed unacceptable (U), no additional cases were run.

First, a continuum based, linear elastic model was created and utilized to ensure that a standard model could match the modulus of elasticity of control samples from the BMT (Chapter 4). This was considered to be a continuum based approach because the individual materials (fiber and matrix) are not modeled separately but are instead modeled with smeared properties. Two model types with different laminates were run and correlated in tension and compression: a $[(0)_4]$ laminate and a $[0/\pm45/0]$ laminate. In both cases, analytical/experimental correlation was achieved, confirming the model's

ability to predict initial material stiffness response without the need for tuning of any parameters, verifying the model, and allowing for addition of damage progression.

The continuum based, linear elastic model initially utilized in Chapter 4 above was modified to include damage progression built into Abaqus for the elastic-brittle nature of fiber-reinforced composites as detailed in Chapter 5. This tool utilized Hashin failure criteria, and damage was characterized by implementing a stiffness degradation that neglects the plastic deformation commonly missing in the response of fiber-reinforced composites. This approach required the user to specify an initial linear elastic response, a damage initiation criterion, and a damage evolution response. Initially, two different models were created and utilized to model both the effects of porosity and an IP wave. In both cases, analytical/experimental correlation was made, and in the case of porosity the correlation was sufficient and showed prediction potential warranting no further work. In the case of the IP wave, correlation was acceptable in certain regions depending on the amount and type of acceptable tuning of model variables and thus indicating that additional work with this technique was worthwhile (Figure 120). Following the systematic approach, additional wave cases and a case with different material, a carbon fiber uni-directional, were generated and compared with BMT results as shown by the additional correlations in Table 28. In all cases, the model was able to consistently correlate to the initial IP wave case, not only indicating the promise of this technique but also verifying the systematic approach of increasing flaw complexity taken herein.

In an attempt to offer more user control compared to that in the built-in Hashin failure criteria, a similar model was created, swapping in a subroutine with user-defined failure criteria discussed in Chapter 6. This method calculated the material response with a damage check subroutine at each iteration and allowed for a mixture of stress and strain based criteria to be utilized. Once damage has been initiated, the subroutine specifies a material property degradation scheme based on the type of failure that has occurred. A model was created and utilized to model the effects of an IP wave. Analytical/experimental correlations were made and a significant amount of tuning, largely of the material property degradation scheme, was performed to obtain convergence. Given the amount of tuning necessary, that work still resulted in poor correlation, as seen in Figure 120. This modeling approach was found insufficient for predicting material response of an IP wave in tension or compression, and additional correlations were not deemed worthwhile as indicated in Table 28.

In Chapters 7 and 8, a CDM using a non-linear shear response and a DDM using cohesive elements, respectively, were attempted and discussed. In both cases, analytical/experimental correlation was noted in specific areas of the stress-strain response (Figure 120). To model the non-linear shear response, a user material card (UMAT) was written for the CDM based on the shear response from the BMT. This model was able to capture the initial softening until fiber straightening resulted in divergence as longitudinal modulus became dominant. Similarly, the use of cohesive elements discretely realized matrix damage between the fiber tows, but implementation resulted in under-prediction of both peak stress and strain. In both cases, the models

seemed to capture the response, while both lacked the exact damage progression observed in the BMT, and no additional correlations were attempted (Table 28).

A model was created, as outlined in Chapter 9, that combined the non-linear shear UMAT with cohesive elements placed between the fiber tows throughout the model. This method requires several inputs from the user, including material properties and shear response that in this case were generated in the BMT. Additionally, the cohesive element properties were defined utilizing test results and/or parametric studies as in Chapter 8. Analytical/experimental correlations were made and correlations were noted with the initial IP wave in both tension and compression. Following the systematic approach (Table 28), an OP wave and additional IP waves, including a carbon fiber case, were modeled and correlated showing the best combination of consistency, accuracy, and predictive capability. Correlation was achieved in each case without additional tuning, as shown in Table 28 and Figure 120 indicating the promise of this modeling technique.

It was quite clear that while each model had some strengths, only the Hashin failure criteria and combined models proved to be acceptable and they warranted following the systematic approach beyond the initial IP wave case. Looking at Table 28 made it evident that the Hashin failure criteria and combined model cases were the only two that correlated to the initial IP wave. The Hashin failure criteria results correlated well in tension after some tuning of the damage parameters; however, compression correlation was moderate. On the other hand, the combined model correlated well in both cases. Direct comparison of the results in tension (Figure 121) indicated that the combined model more accurately predicted damage and stress-strain response. However,

the cost for this accuracy was an increase in computational time from 1 to 16 minutes up to a minimum of 90 minutes for the combined approach. In looking back to the compression results and the additional waves/materials discussed in Chapters 5 and 9 above, it became clear that even with the additional computational time, the combined model offered the most consistent, accurate, and predictive results with direct inputs from the BMT.

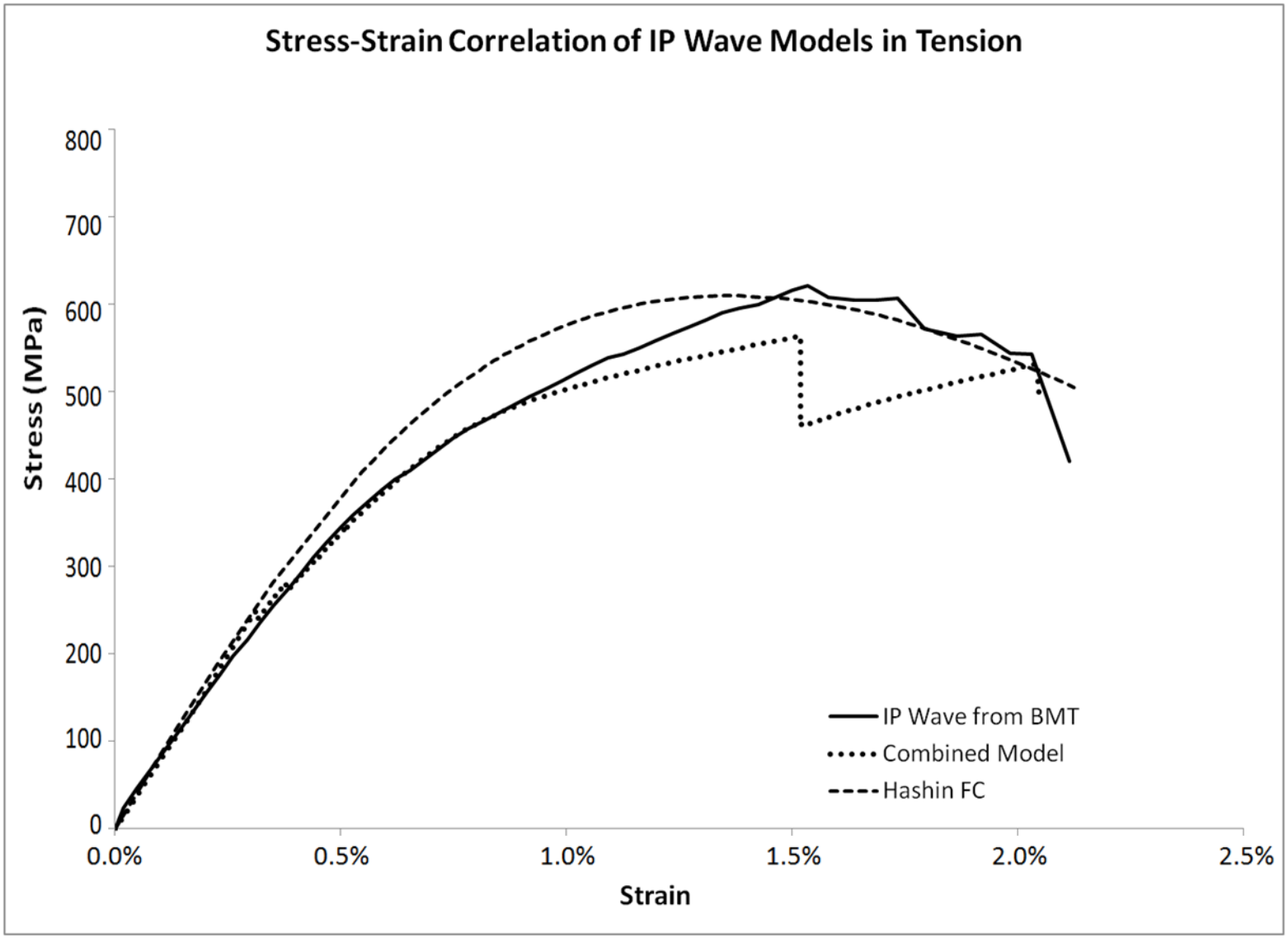

Figure 121: Stress-strain correlations of common IP Wave for Hashin FC and Combined techniques compared to BMT results.

CONCLUSIONS AND RECOMMENDED FUTURE WORK

As noted in the sections and chapters above, a unique comparison of several different analytical approaches to composites has been made with respect to manufacturing for consistency, accuracy, and predictive capability that will allow for improved blade reliability and composite structural assessment. A three-round, systematic approach of increasing complexity was utilized throughout. A benchmark material testing (BMT) program was performed to determine and characterize the material response when typical manufacturing flaws were included in representative wind turbine blade materials. Data from this program were then utilized as inputs and as correlation points for both continuum damage models (CDM) and discrete damage models (DDM). Following the three rounds of the BMT, models increased in complexity before a comparison of all correlations was performed.

The following conclusions may be drawn from the work herein:

1. As the critical parameters, such as fiber misalignment angle or percent of volume content, of typical manufacturing flaws increase in magnitude, material properties degrade, including strength and stiffness.
2. Damage propagates consistently when misaligned fibers are added to the laminate, indicating that these flaw types dominate the material response.
3. Shear dominates the individual ply and laminate response with misaligned fibers due to the interaction of the fibers through the loading profile, resulting in complex, non-linear stress-strain responses.

4. Given the dominance of shear, amplitude and wavelength independently are insufficient for wave characterization: instead, it was confirmed that fiber misalignment angle is an accurate critical flaw parameter.
5. Regardless of model type, initial laminate stiffness is easily calculated analytically when included flaw geometries are modeled discretely with the input of accurate unflawed material properties without any material response or failure criteria definitions.
6. The simple CDM approach with Hashin failure criteria shows good analytical/experimental correlation for porosity when input material properties are degraded utilizing a simple rule of mixtures approximation.
7. The simple CDM approach with Hashin failure criteria shows reasonably consistent, accurate, and predictive analytical/experimental correlation for a variety of fiber wave configurations with input of unflawed material properties and tuned damage properties from an initial case.
8. The more complex CDM approaches with user-defined failure criteria result in inaccurate analytical/experimental correlation within the limits of acceptable parametric tuning.
9. In the more complex CDM approach with non-linear shear UMAT and the DDM approach with cohesive elements placed between fiber tows, analytical approximations are able to capture initial softening, but they diverged from experimental results due to unrealistic responses.

10. A combination of the CDM approach with non-linear shear UMAT and the DDM approach with cohesive elements placed between fiber tows resulted in the most consistent, accurate, and predictive correlation.
11. CDM's require significantly less computational expense than DDM's due to the additional processing power needed to determine damage discretely.
12. Results suggest that analytical tools may be utilized in a predictive fashion to possibly reduce the amount of material testing necessary for quality assurance and qualification.
13. Most likely due to insufficient flaw size, full-scale blade correlation was not possible due to lack of visualized or quantifiable material response in areas of flaw introduction.

In order to address many of the issues raised herein, the items listed and briefly discussed are recommended for future work:

1. Increase scale of models and testing. While progress has been made to understand and model typical manufacturing flaws on a coupon level, an increase in size which utilizes the successful modeling types is recommended. This increase in size should include work to be performed at the MSU Substructure Test Facility. Correlation of models and testing at this level will enable a better understanding of flaw impacts on large structures and, in particular, will bridge the gap more clearly with the BRC validation blade.

2. Characterize additional manufacturing flaw types, materials, and combinations of flaws. While several flaw types were considered and characterized, a continued effort to understand as many flaw types as possible is beneficial. In addition, continued effort allows for continued validation of the models herein, in particular for OP waves in compression and for all waves in carbon fiber.
3. Move models to 3D to assess impact of model uniformity. While assuming a uniform 2D laminate has allowed for reasonable correlations, moving to 3D and modeling each layer independently may allow for improved accuracy of model. Further, investigation into auto-meshing from defect images may allow for faster and easier mesh generation of each layer.
4. Investigate other/combined user-defined options. The work herein investigated two options, but did not fully investigate the options associated with running their FORTRAN subroutines. Further investigation into the use of these user-defined subroutines may lead to a less computationally expensive, but at the same time more consistent, accurate, and predictive analytical tool. While Abaqus states that multiple routines are not possible, an investigation into other coding options is warranted in this area.
5. Reduce run time and improve combined approach. While the combined approach showed the best correlation, it is computationally expensive.

6. Reducing computational expense while improving correlation by possibly incorporating #3 above may improve the predictive capability of the combined CDM/DDM technique.
7. Consider and investigate the implications of loading-unloading-reloading. As noted with the use of the shear stress-strain data, recent research has indicated that unrecoverable damage and/or plasticity result in less stiffness degradation than they do in the secant modulus method. While the work herein appears to have bounded the case, additional work is recommended to understand and assess the impacts of these loading-unloading-reloading implications on the non-linear shear models.
8. Develop multi-scale modeling methodology. The work herein was utilized to compare coupon level analytical approaches. While work to increase scale and improve the techniques herein advances, modeling techniques and approaches must also be advanced to ensure that local damage is accounted for in the global scheme. As such, a multi-scale modeling approach must be considered and applied as part of all future work.

REFERENCES CITED

Abaqus Software and Abaqus Documenation: v. 6.12; Dassault Systemes Simulia Corp, Providence, RI.

Adams, Daniel O'Hare, and Steven J. Bell. "Compression strength reductions in composite laminates due to multiple-layer waviness." *Composites science and Technology* 53.2 (1995): 207-212.

Adams, Daniel O'Hare, and M. W. Hyer. "Effects of layer waviness on the compression strength of thermoplastic composite laminates." *Journal of reinforced plastics and composites* 12.4 (1993): 414-429.

Alfano, G., and M. A. Crisfield. "Finite element interface models for the delamination analysis of laminated composites: mechanical and computational issues." *International journal for numerical methods in engineering* 50.7 (2001): 1701-1736.

Aramis Digital Image Correlation Software and Documentation: v 6.2; Trilion Quality Systems, Plymouth Meeting, PA.

Areias, Pedro, and Ted Belytschko. "Analysis of three-dimensional crack initiation and propagation using the extended finite element method."*International Journal for Numerical Methods in Engineering* 63.5 (2005): 760-788.

ASTM D3039. Standard test method for tensile properties of polymer matrix composite materials .

ASTM D3410-87. Standard Test Method for Compressive Properties of Unidirectional or Cross-ply Fiber Resin Composites, American Society for Testing and Materials .

ASTM D3518. Standard Test Method for In-Plane Shear Response of Polymer Matrix Composite Materials by Tensile Test.

Avery, Darrell P., et al. "Compression strength of carbon fiber laminates containing flaws with fiber waviness." *2004 ASME Wind Energy Symposium, ASME/AIAA, AIAA.* Vol. 174. 2004.

Baley, Christophe, et al. "Application of interlaminar tests to marine composites. A literature review." *Applied composite materials* 11.2 (2004): 99-126.

Barbero, E. J. Introduction to composite materials design; and companion CADEC software package, CRC Press: New York, 1st edition, 1999.

Barbero, Ever J., and Paolo Lonetti. "An inelastic damage model for fiber reinforced laminates." *Journal of Composite Materials* 36.8 (2002): 941-962.

Barenblatt, G. I. "The mathematical theory of equilibrium cracks in brittle fracture." *Advances in applied mechanics* 7.1 (1962): 55-129.

Basu, Shiladitya, Anthony M. Waas, and Damodar R. Ambur. "Prediction of progressive failure in multidirectional composite laminated panels." *International journal of solids and structures* 44.9 (2007): 2648-2676.

Breitzman, T., et al. "Multiscale discrete damage modeling in laminated composites." *ECCM 2010: IV European Conference on Computational Mechanics*. 2010.

Bruggeman, D. A. G. "Calculation of various physics constants in heterogenous substances I Dielectricity constants and conductivity of mixed bodies from isotropic substances." *Annalen der Physik 24.7* (1935): 636-664.

Bogetti, Travis A., John W. Gillespie, and Mark A. Lamontia. "The influence of ply waviness with nonlinear shear on the stiffness and strength reduction of composite laminates." *Journal of Thermoplastic Composite Materials* 7.2 (1994): 76-90.

Borg, Rikard, Larsgunnar Nilsson, and Kjell Simonsson. "Simulation of delamination in fiber composites with a discrete cohesive failure model."*Composites science and technology* 61.5 (2001): 667-677.

Bouchard, Pierre-Olivier, François Bay, and Yvan Chastel. "Numerical modelling of crack propagation: automatic remeshing and comparison of different criteria."*Computer methods in applied mechanics and engineering* 192.35 (2003): 3887-3908.

Boyer, C., A. Béakou, and M. Lemaire. "Design of a composite structure to achieve a specified reliability level." *Reliability Engineering and System Safety*56.3 (1997): 273-283.

Camanho, P. P., and F. L. Matthews. "A progressive damage model for mechanically fastened joints in composite laminates." *Journal of Composite Materials* 33.24 (1999): 2248-2280.

Cairns, D. S., et al. "Design and manufacturing considerations for ply drops in composite structures." *Composites Part B: Engineering* 30.5 (1999): 523-534.

Car, E., et al. "Numerical simulation of fiber reinforced composite materials—two procedures." *International journal of solids and structures* 39.7 (2002): 1967-1986.

Carol, Ignacio, Egidio Rizzi, and Kaspar Willam. "On the formulation of anisotropic elastic degradation. I. Theory based on a pseudo-logarithmic damage tensor rate." *International Journal of Solids and Structures* 38.4 (2001): 491-518.

Carol, Ignacio, Egidio Rizzi, and Kaspar Willam. "On the formulation of anisotropic elastic degradation.: II. Generalized pseudo-Rankine model for tensile damage." *International Journal of Solids and Structures* 38.4 (2001): 519-546.

Cauvin, Alix, and Rene B. Testa. "Damage mechanics: basic variables in continuum theories." *International Journal of Solids and Structures* 36.5 (1999): 747-761.

Chaboche, J-L. "A continuum damage theory with anisotropic and unilateral damage." *La Recherche Aérospatiale* 2 (1995): 139-147.

Chang, Fu-Kuo, and Kuo-Yen Chang. "A progressive damage model for laminated composites containing stress concentrations." *Journal of Composite Materials* 21.9 (1987): 834-855.

Chang, Fu K., Larry Lessard, and Jian M. Tang. "Compression response of laminated composites containing an open hole." *SAMPE Q.* 19.4 (1988): 46-51.

Chang, Fu-Kuo, and Larry B. Lessard. "Damage tolerance of laminated composites containing an open hole and subjected to compressive loadings. I: Analysis." *Journal of Composite Materials* 25.1 (1991): 2-43.

Chen, M. Crisfield, AJ Kinloch, EP Busso, FL Matthews, Y. Qiu, J. "Predicting progressive delamination of composite material specimens via interface elements." *Mechanics of composite materials and structures* 6.4 (1999): 301-317.

Chen, J., and A. New. "Application of decohesive model with mixed damage scale in fracture analysis of composite materials." *Fatigue and Fracture of Engineering Materials and Structures* 24.11 (2001): 761-769.

Christensen, R. M. "Failure criteria for anisotropic fiber composite materials."*Section III, www. FailureCriteria. com* (2008).

Chu, G. D., and C. T. Sun. "Failure initiation and ultimate strength of composite laminates containing a center hole." *Composite materials: Fatigue and fracture.*4 (1993): 35-54.

Costa, Michelle L., Sérgio FM De Almeida, and Mirabel C. Rezende. "Critical void content for polymer composite laminates." *AIAA journal* 43.6 (2005): 1336-1341.

Crisfield, M. A., et al. "Finite element methods and the progressive failure-modelling of composites structures." *Computational Plasticity, CIMNE, Barcelona* (1997): 239-254.

Cui, Weicheng, and M. R. Wisnom. "A combined stress-based and fracture-mechanics-based model for predicting delamination in composites."*Composites* 24.6 (1993): 467-474.

Daniel, I. M. "Failure of composite materials." *Strain* 43.1 (2007): 4-12.

Department of Energy, "20% wind Energy by 2030: Increasing Wind Energy's Contribution to US Electricity Supply." July 2008. DOE/GO-102008-2567.

Dugdale, D. S. "Yielding of steel sheets containing slits." *Journal of the Mechanics and Physics of Solids* 8.2 (1960): 100-104.

Evcil, Ali. "Simulation of Three Dimensional Progressive Damage in Composite Laminates." *Intl Journal of Mechanics, v2* (2008): 67-75.

Federal Aviation Administration: Office of Aviation Research, "Enhanced Reliability Prediction Methodology for Impact Damaged Composite Structures." Washington, D.C. October 1998. DOT/FAA/AR-97/79.

Garnich, Mark R., and Andrew C. Hansen. "A multicontinuum theory for thermal-elastic finite element analysis of composite materials." *Journal of Composite Materials* 31.1 (1997): 71-86..

Gebert, E, "Broken turbine problem found." *National Wind Watch*, 2 June 2012: https://www.wind-watch.org/news/2012/06/02/broken-turbine-blade-problem-found/.

Goswami, Sanjib. "A finite element investigation on progressive failure analysis of composite bolted joints under thermal environment." *Journal of reinforced plastics and composites* 24.2 (2005): 161-171.

Greif, R., and E. Chapon. "Investigation of successive failure modes in graphite/epoxy laminated composite beams." *Journal of reinforced plastics and composites* 12.5 (1993): 602-621.

Guo, Zhan-Sheng, et al. "Critical void content for thermoset composite laminates." *Journal of composite materials* 43.17 (2009): 1775-1790.

Hallett, Stephen R., Ben G. Green, Wen-Guang Jiang, Kin Hei Cheung, and Michael R. Wisnom. "The open hole tensile test: a challenge for virtual testing of composites." *International journal of fracture* 158.2 (2009): 169-181.

Hansen, Andrew C., Jon L. Walker, and Richard P. Donovan. "A finite element formulation for composite structures based on a volume fraction mixture theory." *International journal of engineering science* 32.1 (1994): 1-17..

Hansen, Andrew C., Emmett E. Nelson, and Douglas J. Kenik. "A comparison of experimental data with multicontinuum failure simulations of composite laminates subjected to tri-axial stresses." *Journal of Composite Materials* 47.6-7 (2013): 805-825.

Hashin, Z. "Analysis of composite materials." *J. appl. Mech* 50.2 (1983): 481-505.

Icardi, Ugo. "Assessment of recent theories for predicting failure of composite laminates." *Applied Mechanics Reviews* 60.2 (2007): 76-86.

Judd, Nigel CW. "Voids and their effects on the mechanical properties of composites--an appraisal." (1978).

Kerner, E. H. "The elastic and thermo-elastic properties of composite media."*Proceedings of the physical society. Section B* 69.8 (1956): 808.

Kassapoglou, Christos, "Design and Analysis of Composite Structures." 2nd Ed., Wiley and Sons, Ltd. West Sussex, UK 2013, ISBN: 9781118401606.

Karayev, Kazbek Z., Pierre J. Minguet, Sangwook Lee, Vladimir Balabanov, Nav Muraliraj, T. Walker, E. Nelson, and Don Robbins. "Residual strength evaluation of typical aircraft composite structures with a large notch." In *Proceedings of the 53 AIAA/ASME/ASCE/AHS/ASC Structures, Structural Dynamics and Materials Conference, Honolulu, Hawaii*. 2012.

Krueger, Ronald. *The virtual crack closure technique: history, approach and applications*. No. ICASE-2002-10. INSTITUTE FOR COMPUTER APPLICATIONS IN SCIENCE AND ENGINEERING HAMPTON VA, 2002.

Kim, Youngchan, Julio F. Davalos, and Ever J. Barbero. "Progressive failure analysis of laminated composite beams." *Journal of composite materials* 30.5 (1996): 536-560.

Lambert, J., A. R. Chambers, I. Sinclair, and S. M. Spearing. "3D damage characterisation and the role of voids in the fatigue of wind turbine blade materials." *Composites Science and Technology* 72, no. 2 (2012): 337-343.

Laurin, F., N. Carrere, and J-F. Maire. "A multiscale progressive failure approach for composite laminates based on thermodynamical viscoelastic and damage models." *Composites Part A: Applied Science and Manufacturing* 38.1 (2007): 198-209.

Lekou, D. J., and T. P. Philippidis. "Mechanical property variability in FRP laminates and its effect on failure prediction." *Composites Part B: Engineering* 39.7 (2008): 1247-1256.

Lemanski, S. L., et al. "Modelling failure of composite specimens with defects under compression loading." *Composites Part A: Applied Science and Manufacturing* 48 (2013): 26-36.

Lemaitre, Jean and Rodrigue Desmorat. "Engineering Damage Mechanics: Ductile, Creep, Fatigue and Brittle Failures." Springer, New York: April 24, 2009, ISBN-10: 3540215034.

Long, M. W., and J. D. Narciso. *Probabilistic Design Methodology for Composite Aircraft Structures*. No. 2-51410/7R-001. NORTHROP GRUMMAN CORP DALLAS TX COMMERCIAL AIRCRAFT DIV, 1999.

Luccioni, Bibiana, and Sergio Oller. "A directional damage model." *Computer methods in applied mechanics and engineering* 192.9 (2003): 1119-1145.

Maimí, P., et al. "A continuum damage model for composite laminates: part I–constitutive model." *Mechanics of Materials* 39.10 (2007): 897-908.

Mandell, John F., Daniel D. Samborsky, and Herbert J. Sutherland. "Effects of materials parameters and design details on the fatigue of composite materials for wind turbine blades." *EWEC-CONFERENCE-*. 1999.

Mandell, J. F., D. D. Samborsky, and L. Wang. "Effects of fiber waviness on composites for wind turbine blades." *International Sampe Symposium and Exhibition*. SAMPE; 1999, 2003.

Mandell, J. F., and Samborsky, D. D., "SNL/MSU/DOE June 25 2013 Composite Material Database, Version 22.0." (2013).

McCarthy, C. T., M. A. McCarthy, and V. P. Lawlor. "Progressive damage analysis of multi-bolt composite joints with variable bolt–hole clearances."*Composites Part B: Engineering* 36.4 (2005): 290-305.

Meo, Michele, and E. Thieulot. "Delamination modelling in a double cantilever beam." *Composite Structures* 71.3 (2005): 429-434.

MIL-HDBK-17-1F: Composite Materials Handbook, Volume 1. Polymer Matrix Composites - Guidelines for Characterization of Structural Materials, U.S. Department of Defense, 2002.

Nelson, J.W., Riddle, T.W., and Cairns D.S., "Characterization of Manufacturing Defects Common to Composite Wind Turbine Blades: Effects of Defects.: 52nd AIAA/ASME/ASCE/AHS/ASC Structures, Structural Dynamics and Materials Conference; April 2011, Denver, CO.

Nelson, J.W., Riddle, T.W., Cairns D.S. and Workman, J.E., "Composite Wind Turbine Blade Effects of Defects: Part B—Progressive Damage Modeling of Fiberglass/Epoxy Laminates with Manufacturing Induced Flaws." 53nd AIAA/ASME/ASCE/AHS/ASC Structures, Structural Dynamics and Materials Conference; April 2012, Honolulu, HI.

Oller, S., J. Miquel Canet, and F. Zalamea. "Composite material behavior using a homogenization double scale method." *Journal of Engineering mechanics*131.1 (2005): 65-79.

Ortiz, Michael. "A constitutive theory for the inelastic behavior of concrete."*Mechanics of Materials* 4.1 (1985): 67-93.

Pal, P., and C. Ray. "Progressive failure analysis of laminated composite plates by finite element method." *Journal of reinforced plastics and composites* 21.16 (2002): 1505-1513.

Paquette, J, "Blade Reliability Collaborative (BRC)." Sandia Nation Laboratories, Wind Energy Technology Dept, 2012. SAND2012-5566C: http://energy.sandia.gov/wp/wp-content/gallery/uploads/3-B-3-Paquette-SAND2012-5566C.pdf

Parker, John Wesley. *Development and implementation of a low cost image correlation system to obtain full-field in-plane displacement and strain data [electronic resource]/by John Wesley Parker*. Diss. Montana State University-Bozeman, College of Engineering, 2009.

Peters, W. H., and W. F. Ranson. "Digital imaging techniques in experimental stress analysis." *Optical Engineering* 21.3 (1982): 427-431.

Petrossian, Z., and Michael R. Wisnom. "Prediction of delamination initiation and growth from discontinuous plies using interface elements." *Composites Part A: Applied Science and Manufacturing* 29.5 (1998): 503-515.

Pradeep, D., et al. "Studies on mechanical behavior of glass epoxy composites with induced defects and correlations with NDT characterization parameters."*Journal of Reinforced Plastics and Composites* 26.15 (2007): 1539-1556.

Prusty, B. Gangadhara. "Progressive failure analysis of laminated unstiffened and stiffened composite panels." *Journal of reinforced plastics and composites*24.6 (2005): 633-642.

Puck, A., and H. Schürmann. "Failure analysis of FRP laminates by means of physically based phenomenological models." *Composites Science and Technology* 58.7 (1998): 1045-1067.

Reddy, Y. S. N., C. M. Moorthy, and J. N. Reddy. "Non-linear progressive failure analysis of laminated composite plates." *International journal of non-linear mechanics* 30.5 (1995): 629-649.

Riddle, T.W., Nelson, J.W., and Cairns D.S., "Characterization of Manufacturing Defects Common to Composite Wind Turbine Blades: Flaw Characterization." 52nd AIAA/ASME/ASCE/AHS/ASC Structures, Structural Dynamics and Materials Conference; April 2011, Denver, CO.

Riddle, T.W., Nelson, J.W., Cairns D.S. and Workman, J.E., "Composite Wind Turbine Blade Effects of Defects: Part A - Development of a Protocol for Defect Risk Management and Improved Reliability of Composite Structures." 53nd AIAA/ASME/ASCE/AHS/ASC Structures, Structural Dynamics and Materials Conference; April 2012, Honolulu, HI.

Riddle, T.W., Cairns D.S., and Nelson, J.W., "Effects of Defects Part A: Stochastic Finite Element Modeling of Wind Turbine Blades with Manufacturing Defects for Reliability Estimation." 54nd AIAA/ASME/ASCE/AHS/ASC Structures, Structural Dynamics and Materials Conference; April 2013, Boston, MA.

Riddle, TW, "DEVELOPMENT OF RELIABILITY PROGRAM FOR RISK ASSESSMENT OF COMPOSITE STRUCTURES TREATING DEFECTS AS UNCERTAINTY VARIABLES." PhD Thesis, Montana State University (2013).

Smock, D., "Boeing 787 dreamliner represents composites revolution." Available at: http://www.designnews.com/article/CA6441583.html, 2007.

Soden, P. D., M. J. Hinton, and A. S. Kaddour. "Lamina properties, lay-up configurations and loading conditions for a range of fibre-reinforced composite laminates." *Composites Science and Technology* 58.7 (1998): 1011-1022.

Sungkha777. "Schematic illustration of idealized fiber arrays and their corresponding unit cells."

http://en.wikipedia.org/wiki/File:Schematic_illustration_of_idealized_fiber_arrays_and_their_corresponding_unit_cells.png

Tao, Jianxin, and C. T. Sun. "Influence of ply orientation on delamination in composite laminates." *Journal of Composite Materials* 32.21 (1998): 1933-1947.

Tan, S. C., and R. J. Nuismer. "A theory for progressive matrix cracking in composite laminates." *Journal of Composite Materials* 23.10 (1989): 1029-1047.

Tan, Seng C. "A progressive failure model for composite laminates containing openings." *Journal of Composite Materials* 25.5 (1991): 556-577.

Tan, Seng C., and Jose Perez. "Progressive failure of laminated composites with a hole under compressive loading." *Journal of Reinforced Plastics and Composites* 12.10 (1993): 1043-1057.

Tay, T. E., V. B. C. Tan, and S. H. N. Tan. "Element-failure: An alternative to material property degradation method for progressive damage in composite structures." *Journal of composite materials* 39.18 (2005): 1659-1675.

Tay, T. E., et al. "Progressive failure analysis of composites." *Journal of Composite Materials* 42.18 (2008): 1921-1966.

Wang, L., "Effects of In-plane Fiber Waviness on the Properties of Composite Materials." PhD Thesis, Montana State University (2001).

Wang, J., et al. "Experimental fabrication and characterization of out-of-plane fiber waviness in continuous fiber-reinforced composites." *Journal of Composite Materials* 46.17 (2012): 2041-2053.

Whiteside, M. B., S. T. Pinho, and P. Robinson. "Stochastic failure modelling of unidirectional composite ply failure." *Reliability Engineering and System Safety*108 (2012): 1-9.

Wisnom, Michael R. "Modelling the effect of cracks on interlaminar shear strength." *Composites Part A: Applied Science and Manufacturing* 27.1 (1996): 17-24.

Wisnom, Michael R., Tom Reynolds, and Nigel Gwilliam. "Reduction in interlaminar shear strength by discrete and distributed voids." *Composites Science and Technology* 56.1 (1996): 93-101.

R Wisnom, Michael, and Fu-Kuo Chang. "Modelling of splitting and delamination in notched cross-ply laminates." *Composites Science and Technology* 60.15 (2000): 2849-2856.

Woo, K, Nelson, J.W., Cairns D.S. and Riddle, T.W., “Effects of Defects: Part B—Progressive Damage Modeling of Fiberglass/Epoxy Composite Structures with Manufacturing Induced Flaws Utilizing Cohesive Zone Elements.” 54nd AIAA/ASME/ASCE/AHS/ASC Structures, Structural Dynamics and Materials Conference; April 2013, Boston, MA.

Wu, Yinan, Rajiv Shivpuri, and L. James Lee. "Effect of macro and micro voids on elastic properties of polymer composites." *Journal of reinforced plastics and composites* 17.15 (1998): 1391-1402.

Xiao, Yi, and Takashi Ishikawa. "Bearing strength and failure behavior of bolted composite joints (part II: modeling and simulation)." *Composites science and technology* 65.7 (2005): 1032-1043.

Xie, De, and Anthony M. Waas. "Discrete cohesive zone model for mixed-mode fracture using finite element analysis." *Engineering Fracture Mechanics* 73.13 (2006): 1783-1796.

Zhu, Hong-Yan, et al. "Influence of voids on interlaminar shear strength of carbon/epoxy fabric laminates." *Transactions of Nonferrous Metals Society of China* 19 (2009): s470-s475.

APPENDIX A

INPUT FILE CODES

The Abaqus input and subroutine FORTRAN codes used for the systematic, three-round, unique comparison of several different modeling techniques undertaken to establish model consistency, accuracy, and predictive capability are listed in this appendix. Prior to the listing of each code, a general mesh outline is listed, but is not listed in each case to save space. Only portions of the nodes, elements, and orientations are shown to give the idea, but are not included as these three portions of code consist of at least 62000 lines of code. Note that explanations of each code are offered in the individual chapters above. In addition, the combined code is included where the individual portions of the UMAT subroutine and cohesive elements may be turned off within this code to run each individually. All code was run utilizing Abaqus v6.12.

General Mesh Outline:

```
*NODE,NSET=GLOBAL
     1,  0.0000000E+00,  0.7600000E+01,  0.0000000E+00
     2,  0.9916667E+00,  0.7567490E+01,  0.0000000E+00
     3,  0.1983333E+01,  0.7470518E+01,  0.0000000E+00
     4,  0.2479167E+01,  0.7398334E+01,  0.0000000E+00
     5,  0.3470833E+01,  0.7208116E+01,  0.0000000E+00
     6,  0.3966667E+01,  0.7090897E+01,  0.0000000E+00
     7,  0.4462500E+01,  0.6959585E+01,  0.0000000E+00
     8,  0.5454167E+01,  0.6656991E+01,  0.0000000E+00
     9,  0.6445833E+01,  0.6305514E+01,  0.0000000E+00
    10,  0.7933333E+01,  0.5700000E+01,  0.0000000E+00
⋮
 15140,  0.5454167E+01,  0.1656991E+01,  0.0000000E+00
 15141,  0.5950000E+01,  0.1487006E+01,  0.0000000E+00
 15142,  0.6445833E+01,  0.1305514E+01,  0.0000000E+00
 15143,  0.6941667E+01,  0.1113293E+01,  0.0000000E+00
 15144,  0.7437500E+01,  0.9111670E+00,  0.0000000E+00
 15145,  0.7933333E+01,  0.7000000E+00,  0.0000000E+00
 15146,  0.8429167E+01,  0.4806970E+00,  0.0000000E+00
 15147,  0.8925000E+01,  0.2541970E+00,  0.0000000E+00
 15148,  0.9420833E+01,  0.0000000E+00,  0.0000000E+00
*ELEMENT, TYPE=CPS4,ELSET=CONVENTIONAL4
     1,      1,  10032,     82,     81
     2,  10032,      2,    130,     82
```

```
     3,     2,  10033,     83,    130
     4,  10033,     3,    131,     83
     5,     3,     4,     84,    131
     6,     4,  10034,     85,     84
     7,  10034,     5,    132,     85
     8,     5,     6,     86,    132
     9,     6,     7,     87,     86
    10,     7,  10035,     88,     87
          ⋮
  14905,   15144,   15145,   9082,   9075
  14906,   15145,   15146,   9129,   9082
  14907,   15146,   15147,   9076,   9129
*SOLID SECTION, ELSET=FIBER, MATERIAL=TOW, ORIENTATION=FIBER_ORI
 50.0
*DISTRIBUTION TABLE, NAME=WAVE_ORITAB
COORD3D, COORD3D
*DISTRIBUTION, NAME=FIBER_ORI, LOCATION=ELEMENT, TABLE=FIBER_ORITAB
,         1.,         0.,         0.,         0.,         1.,         0.
1, 0.999908566474915, -0.0135199585929513,     0., 0.0135199585929513,
0.999908566474915,         -0.
2, 0.997743606567383, -0.0671394243836403,     0., 0.0671394243836403,
0.997743606567383,         -0.
3, 0.995632588863373, -0.0933576449751854,     0., 0.0933576449751854,
0.995632588863373,         -0.
4, 0.989609837532043, -0.143778890371323,      0., 0.143778890371323, 0.989609837532043,
-0.
5, 0.985840916633606, -0.167683288455009,      0., 0.167683288455009, 0.985840916633606,
-0.
6, 0.981678426265717, -0.190545096993446,      0., 0.190545096993446, 0.981678426265717,
-0.
7, 0.972541630268097, -0.232728987932205,      0., 0.232728987932205, 0.972541630268097,
-0.
8, 0.967757284641266, -0.251884758472443,      0., 0.251884758472443, 0.967757284641266,
-0.
9, 0.962953865528107, -0.269666314125061,       0., 0.269666314125061, 0.962953865528107,
-0.
10, 0.958221435546875, -0.28602734208107,      0., 0.28602734208107, 0.958221435546875,
-0.
          ⋮
14905,1,0,0,0,1,0
14906,1,0,0,0,1,0
14907,1,0,0,0,1,0
*ORIENTATION, NAME=FIBER_ORI, SYSTEM=RECTANGULAR
FIBER_ORI
3, 0.
          ⋮
[SPECIFIC CODE BEGINS HERE]
```

Hashin Code:

```
[MESH]
        ⋮
*SECTION CONTROLS, NAME=EC-1, ELEMENT DELETION=YES, MAX DEGRADATION=1.
1., 1., 1.
*MATERIAL, NAME=PPG
*DAMAGE INITIATION, CRITERION=HASHIN, ALPHA=1.
990.,112.,60., 162.,112.,124.
*DAMAGE EVOLUTION, TYPE=ENERGY
16.0.,16.9,39.9,45.1
*DAMAGE STABILIZATION
0.1,0.1,0.1,0.1
*ELASTIC, TYPE=ENGINEERING CONSTANTS
 4.06E+06,  1.63E+06.,  1.63E+06.,     0.23,     0.23,     0.63, 1.68E+06, 1.68E+06
 1.68E+06,
*BOUNDARY
SET-5, ZSYMM
*BOUNDARY
IP_WAVE_1-1.BOTTOM, ENCASTRE
*BOUNDARY
IP_WAVE_1-1.TOP, 2, 2
*STEP, NAME=STEP-1, INC=1000
*STATIC
0.01, 1., 1E-09, 1.
*BOUNDARY, OP=NEW
SET-5, ZSYMM
*BOUNDARY, OP=NEW
IP_WAVE_1-1.BOTTOM, ENCASTRE
*BOUNDARY, OP=NEW
IP_WAVE_1-1.TOP, 2, 2, 2.5
*RESTART, WRITE, FREQUENCY=0
*OUTPUT, FIELD
*NODE OUTPUT
CF, RF, U
*ELEMENT OUTPUT, DIRECTIONS=YES
DAMAGEFC, DAMAGEFT, DAMAGEMC, DAMAGEMT, DAMAGESHR, ECDDEN, EDMDDEN, ELDMD,
LE, PE, PEEQ, PEMAG, S, STATUS
*CONTACT OUTPUT
CDISP, CSTRESS
*OUTPUT, HISTORY, VARIABLE=PRESELECT
*END STEP
```

User-defined Code:

```
 [MESH]
          ⋮
*MATERIAL,NAME=PPG
*ELASTIC,TYPE=LAMINA,DEPENDENCIES=3
4.06E+06,  1.63E+06.,  0.23, 1.68E+06, 1.68E+06,  1.68E+06, 0., 0,
0,0
4.06E+06,  1.00E+0.,  0.00, 1.68E+06, 1.68E+06,  1.68E+06, 0., 1,
0,0
4.06E+06,  1.63E+06.,  0.00, 1.00E+0, 1.00E+0,  1.00E+0, 0., 0,
1,0
1.00E+0,  1.00E+0.,  0.00, 1.00E+0, 1.00E+0,  1.00E+0, 0., 0,
0,1
4.06E+06,  1.00E+0.,  0.00, 1.00E+0, 1.00E+0,  1.00E+0, 0., 1,
1,0
1.00E+0,  1.00E+0.,  0.00, 1.00E+0, 1.00E+0,  1.00E+0, 0., 1,
0,1
1.00E+0,  1.00E+0.,  0.00, 1.00E+0, 1.00E+0,  1.00E+0, 0., 0,
1,1
1.00E+0,  1.00E+0.,  0.00, 1.00E+0, 1.00E+0,  1.00E+0, 0., 1,
1,1
*DEPVAR
3,
*USER DEFINED FIELD
*ORIENTATION,NAME=LOCAL
0.,1.,0.,-1.,0.,0.
3,
*SHELL SECTION,COMPOSITE,ELSET=PLATE,ORIENTATION=LOCAL
0.03750,1,PPG,+90.0
0.03750,1,PPG,-90.0
0.03750,1,PPG,+90.0
0.03750,1,PPG,-90.0
*MASS, ELSET=REF
1.0E-5
*EQUATION
2,
TOP,2,1.0,10000,2,-1.0
*MPC
LINEAR,20000,95,97
*ELSET,ELSET=EOUT
338,339
*NSET,NSET=OUTPUT
10000
** ------------------
** ANALYSIS HISTORY
** ------------------
*STEP,INC=200,NLGEOM
*STATIC,DIRECT
```

```
0.05,1.0
*BOUNDARY
NALL,3,5,0.
BOTTOM,1,6,0.
10000,2,,0.2
*RESTART,WRITE,OVERLAY
*NODE PRINT,NSET=OUTPUT
U2,RF2
*NODE FILE,NSET=OUTPUT
U,RF
*EL FILE,ELSET=EOUT
S,E
SDV,FV
*EL PRINT,FREQUENCY=5,ELSET=EOUT
S,E
*END STEP
```

Combined Code:

```
[MESH]
          ⋮
*MATERIAL, NAME=TOW
**ELASTIC, TYPE=ENGINEERING CONSTANTS
**40600.,16300.,16300., 0.23, 0.23, 0.63, 16800., 16800.
**16800.,
*USER MATERIAL,CONSTANTS=20
40600.,4500.,0.27,16800., 0.002,0.003,0.0056,0.0091,
0.0159,0.024,0.0356,0.0454,      25,53,70,83,
96,103,103,103
**----------------------------------------------------------------------------
*COHESIVE SECTION, ELSET=COHESIVE, CONTROLS=EC-1, MATERIAL=COHESIVE_MAT,
RESPONSE=TRACTION SEPARATION, THICKNESS=SPECIFIED
 ,4.
*COHESIVE SECTION, ELSET=COHESIVE2, CONTROLS=EC-1, MATERIAL=COHESIVE_MAT2,
RESPONSE=TRACTION SEPARATION, THICKNESS=SPECIFIED
 ,4.
*SECTION CONTROLS, NAME=EC-1, ELEMENT DELETION=YES, MAX DEGRADATION=1.,
VISCOSITY=1E-05
 1., 1., 1.
**-------------------------------------
*MATERIAL, NAME=COHESIVE_MAT
*DAMAGE INITIATION, CRITERION=MAXS
110.,110.,110.
*DAMAGE EVOLUTION, TYPE=ENERGY, MIXED MODE BEHAVIOR=BK, POWER=2.284
0.706E0, 1.324E0, 1.324
*ELASTIC, TYPE=TRACTION
2.2E6,2.2E6,2.2E6
**-------------------------------------
*MATERIAL, NAME=COHESIVE_MAT2
```

```
*DAMAGE INITIATION, CRITERION=MAXS
55.,55.,55.
*DAMAGE EVOLUTION, TYPE=ENERGY, MIXED MODE BEHAVIOR=BK, POWER=2.284
0.403, 0.751, 0.751
*ELASTIC, TYPE=TRACTION
1.E6,1E6.,1.E6
**----------------------------------------------------------------------------
*RESTART,WRITE,FREQUENCY=10000
** LOAD STEP 1 ----------------------------------------------------------
*STEP, INC=10000,NLGEOM
UNTITLED
*STATIC,STABILIZE=1.E-8
0.01,1.,1.E-9,0.01
*BOUNDARY
GLOBAL,3
LEFT,1
RIGHT,2
*BOUNDARY,TYPE=DISPLACEMENT
RIGHT,1,,1.5
*OUTPUT, FIELD,FREQUENCY=10
*NODE OUTPUT
CF, RF, U
*ELEMENT OUTPUT, DIRECTIONS=YES
LE, PE, PEEQ, PEMAG, S, STATUS
*OUTPUT, HISTORY,FREQUENCY=10
*NODE OUTPUT, NSET=RIGHT
RF1, U1
*NODE PRINT, NSET=RIGHT
RF1, U1
*CONTROLS,PARAMETER=FIELD,FIELD=DISPLACEMENT
0.01,1.
*END STEP
```

Combined UMAT subroutine:

```
      SUBROUTINE UMAT (STRESS,STATEVAR,DDSDDE,SSE,SPD,SCD,
     *RPL,DDSDDT,DRPLDE,DRPLDT,
     *STRAIN,DSTRAIN,TIME,DTIME,TEMPER,DTEMPER,PREDEF,DPREDEF,CMNAME,
     *NDIRSTR,NSHRSTR,NTENS,NSTATEV,
     *PROPS,NPROPS,COORDS,DROT,PNEWDT,
     *CELENT,DFGRD0,DFGRD1,NOEL,NPT,LAYER,KSPT,KSTEP,KINC)

      IMPLICIT REAL*8(A-H,O-Z)
      CHARACTER CMNAME*80
      DIMENSION STRESS(NTENS),STATEVAR(NSTATEV),
     *DDSDDE(NTENS,NTENS),DDSDDT(NTENS),DRPLDE(NTENS),
     *STRAIN(NTENS),DSTRAIN(NTENS),TIME(2),PREDEF(1),DEPREDEF(1),
     *PROPS(NPROPS),COORDS(3),DROT(3,3),DFGRD0(3,3),DFGRD1(3,3)
C----------------------------------------------------------------
```

```
      PARAMETER(NEMAX=30000)
      DIMENSION STRAIN1(3)
      SAVE DD11,DD12,DD22,IFLAG,KINC_SAV
      DIMENSION GAMMAMAX(NEMAX,4),TAUMAX(NEMAX,4)
      DIMENSION GAMMATMP(NEMAX,4),TAUTMP(NEMAX,4)
      SAVE GAMMAMAX,TAUMAX,GAMMATMP,TAUTMP
      DIMENSION GG12(10),TAU(10),GAMMA(10)
      SAVE GG12,TAU,GAMMA
C
C IN THIS, THE HARDENING/SOFTENING OF SHEAR STIFFNESS IS CONSIDERED ONLY.
C ALSO, IT IS ASSUMED THAT THE ORTHOTROPY IS PRESERVED DURING DEFORMATION.
C
      IF(IFLAG.NE.1) CALL UMAT_INIT(IFLAG,PROPS,NPROPS,DD11,DD22,DD12,
     +                         GAMMA,TAU,GG12)
C-------------------------------------------------------------
      IF(KINC.GT.KINC_SAV) THEN
            KINC_SAV=KINC
            DO I=1,NEMAX
            DO J=1,4
                  IF(GAMMATMP(I,J).GT.GAMMAMAX(I,J)) THEN
                  GAMMAMAX(I,J)=GAMMATMP(I,J)
                  TAUMAX(I,J)=TAUTMP(I,J)
                  ENDIF
            ENDDO
            ENDDO
      ENDIF
C-------------------------------------------------------------
C    STRAIN UPDATE
DO I=1,NTENS
STRAIN1(I)=STRAIN(I) + DSTRAIN(I)
END DO

C    PROPERTIES - STIFFNESS MATRIX
      SHEAR=DABS(STRAIN1(3))
      IF(SHEAR.GE.GAMMAMAX(NOEL,NPT)) THEN
            CALL UMAT_SHEAR_STIF(SHEAR,GAMMA,TAU,GG12,G12,STRESS3)
            IF(STRAIN1(3).LT.0.D0) STRESS3=-STRESS3
      ELSE
            G12=TAUMAX(NOEL,NPT)/GAMMAMAX(NOEL,NPT)
            STRESS3=G12*STRAIN1(3)
      ENDIF

      DDSDDE(1,1) =  DD11
      DDSDDE(1,2) =  DD12
      DDSDDE(1,3) =  0.D0
      DDSDDE(2,1) =  DD12
      DDSDDE(2,2) =  DD22
      DDSDDE(2,3) =  0.D0
DDSDDE(3,1) =  0.D0
```

```
DDSDDE(3,2) =  0.D0
DDSDDE(3,3) =  G12

C    STRESS CALCULATION
STRESS(1)= DDSDDE(1,1)*STRAIN1(1) + DDSDDE(1,2)*STRAIN1(2)
STRESS(2)= DDSDDE(2,1)*STRAIN1(1) + DDSDDE(2,2)*STRAIN1(2)
      STRESS(3)= STRESS3

      GAMMATMP(NOEL,NPT)=SHEAR
      TAUTMP(NOEL,NPT)=DABS(STRESS3)
    RETURN
    END
C
C=======================================================================
C
      SUBROUTINE UMAT_INIT(IFLAG,PROPS,NPROPS,DD11,DD22,DD12,
   +                   GAMMA,TAU,GG12)
      IMPLICIT REAL*8(A-H,O-Z)
      DIMENSION PROPS(*),GAMMA(*),TAU(*),GG12(*)

      IFLAG=1

      DO I=1,NPROPS
            WRITE(6,*) I,PROPS(I)
      ENDDO

      E1=PROPS(1)
      E2=PROPS(2)
      P12=PROPS(3)
      P21=P12*E2/E1
      DELTA=1.D0-P12*P21
      DD11=E1/DELTA
      DD22=E2/DELTA
      DD12=P12*DD22

      WRITE(6,*)'G12():'
      NNN=(NPROPS-4)/2
      N1=4
      N2=N1+NNN
      GG12(1)=PROPS(N2+1)/PROPS(N1+1)
      DO I=1,NNN
            GAMMA(I)=PROPS(N1+I)
            TAU(I)=PROPS(N2+I)
            DEL_EPS=PROPS(N1+I+1)-PROPS(N1+I)
            DEL_SIG=PROPS(N2+I+1)-PROPS(N2+I)
            GG12(I+1)=DEL_SIG/DEL_EPS
      WRITE(6,*) I,GG12(I)
      ENDDO
```

```
      RETURN
      END
C
C=======================================================================
C

      SUBROUTINE UMAT_SHEAR_STIF(SHEAR,GAMMA,TAU,GG12,G12,STRESS3)
      IMPLICIT REAL*8(A-H,O-Z)
      DIMENSION GAMMA(*),TAU(*),GG12(*)

      IF    (SHEAR.LT.GAMMA(1)) THEN
            G12=GG12(1)
            STRESS3=G12*SHEAR
      ELSEIF(SHEAR.LT.GAMMA(2)) THEN
            G12=GG12(2)
            STRESS3=TAU(1)+G12*(SHEAR-GAMMA(1))
      ELSEIF(SHEAR.LT.GAMMA(3)) THEN
            G12=GG12(3)
            STRESS3=TAU(2)+G12*(SHEAR-GAMMA(2))
      ELSEIF(SHEAR.LT.GAMMA(4)) THEN
            G12=GG12(4)
            STRESS3=TAU(3)+G12*(SHEAR-GAMMA(3))
      ELSEIF(SHEAR.LT.GAMMA(5)) THEN
            G12=GG12(5)
            STRESS3=TAU(4)+G12*(SHEAR-GAMMA(4))
      ELSEIF(SHEAR.LT.GAMMA(6)) THEN
            G12=GG12(6)
            STRESS3=TAU(5)+G12*(SHEAR-GAMMA(5))
      ELSEIF(SHEAR.LT.GAMMA(7)) THEN
            G12=GG12(7)
            STRESS3=TAU(6)+G12*(SHEAR-GAMMA(6))
      ELSEIF(SHEAR.LT.GAMMA(8)) THEN
            G12=GG12(8)
            STRESS3=TAU(7)+G12*(SHEAR-GAMMA(7))
      ELSE
            G12=GG12(8)
            STRESS3=TAU(8)+G12*(SHEAR-GAMMA(8))
      ENDIF

      RETURN
      END
```